



UNIVERSITÀ DEGLI STUDI DI PALERMO

Dottorato in Ingegneria dell'innovazione tecnologica

Dipartimento dell'Innovazione Industriale e Digitale (DIID)

Ingegneria Chimica, Gestionale, Informatica, Meccanica

Settore Scientifico Disciplinare ING-IND/26

REVERSE ELECTRODIALYSIS HEAT ENGINE: Low-Grade Waste Heat into Electricity

IL DOTTORE

Ing. Francesco Giacalone

IL COORDINATORE:

Prof. ing. Antonio Chella

IL TUTOR

Prof. Ing. Giorgio Micale

CO-TUTORS

Prof. ing. Stefano Brandani

Prof. ing. Andrea Cipollina

CICLO XXI

ANNO CONSEGUIMENTO TITOLO 2019

CONTENTS

<u>CONTENTS.....</u>	<u>I</u>
<u>LIST OF DISSERTATION PUBLICATIONS</u>	<u>VII</u>
<u>INTRODUCTION</u>	<u>1</u>
<u>1 CONVERSION OF LOW GRADE HEAT INTO POWER.....</u>	<u>5</u>
1.1 SALINITY GRADIENT POWER	7
1.1 LOW-GRADE HEAT INTO ELECTRICITY.....	8
1.2 SGP HEAT ENGINE: FUNDAMENTALS	12
1.3 STATE OF THE ART OF SGP ENGINES.....	15
1.4 MOTIVATION AND GOALS OF THIS WORK	17
<u>SECTION I: REVERSE ELECTRODIALYSIS PROCESS</u>	<u>19</u>
<u>2 REVERSE ELECTRODIALYSIS.....</u>	<u>21</u>
ABSTRACT.....	23
2.1 INTRODUCTION	24
2.2 GIBBS FREE ENERGY OF MIXING	26
2.3 RED PROCESS: FUNDAMENTALS	28
2.3.1 ION EXCHANGE MEMBRANES	30
2.3.2 MEMBRANES PROPERTIES	32
2.4 EXPERIMENTAL	38

2.4.1 CORRECTED POWER DENSITY	40
2.4.2 AVERAGE MEMBRANE PERMSELECTIVITY AND RESISTANCES	42
2.5 MODELLING REVERSE ELECTRODIALYSIS.....	46
2.5.1 EQUIVALENT CIRCUIT SCHEME AND ELECTRICAL EQUATIONS	46
2.5.2 WATER AND SALT FLUX THROUGH THE IEMS	49
2.5.3 SALT AND GLOBAL MASS BALANCES	50
2.5.4 MEMBRANES PROPERTIES	52
2.5.5 POLARISATION COEFFICIENTS	52
2.5.6 PRESSURE DROPS, PUMPING POWER & NET POWER	54
2.5.7 NUMERICAL DETAILS	55
2.5.8 RED PROCESS MODEL VALIDATION	56
CONCLUSIONS	59
<u>3 PERFORMANCE ANALYSIS OF THE RED PROCESS.....</u>	<u>61</u>
ABSTRACT.....	63
3.1 EXERGY ANALYSIS OF RED	64
3.1.1 EXERGY ANALYSIS EQUATIONS	68
3.2 RESULTS AND DISCUSSION	70
3.2.1 EFFECT OF THE IRREVERSIBILITY SOURCE	71
3.2.2 EFFECT OF MEMBRANE PROPERTIES	74
3.2.3 EFFECT OF CONCENTRATE AND DILUTE CONCENTRATIONS	75
3.2.4 EFFECT OF FLOW ARRANGEMENT AND CELL PAIR LENGTH	77
3.2.5 EFFECT OF FEED VELOCITY	78
3.3 POTENTIAL APPLICATIONS OF RED IN REAL ENVIRONMENTS.....	80
3.3.1 RED UNIT POTENTIALS	82
3.4 CONCLUSIONS.....	87
<u>4 SELECTION OF SALT-SOLUTIONS FOR RED -HE.....</u>	<u>89</u>
ABSTRACT.....	91
4.1 INTRODUCTION	92
4.2 THERMODYNAMICS OF ELECTROLYTE SOLUTIONS	95
4.2.1 PITZER'S THERMODYNAMIC MODEL	97

4.2.2 BOILING POINT ELEVATION IN ELECTROLYTE SOLUTIONS	99
4.3 BPE, OSMOTIC AND ACTIVITY COEFFICIENTS OF SALT SOLUTIONS	99
4.3.1 EXPERIMENTAL	99
4.3.2 VALIDATION OF THE EXPERIMENTAL METHODOLOGY	101
4.4 KAC AND CSAC OSMOTIC AND ACTIVITY COEFFICIENTS.	104
4.5 GIBBS FREE ENERGY OF MIXING OF ARTIFICIAL SOLUTIONS	108
4.6 CONCLUSIONS	110

SECTION II: SOLVENT EXTRACTION RED WITH EVAPORATIVE REGENERATION STRATEGY..... 111

5 SOLVENT EXTRACTION RED HE: SIMPLIFIED ANALYSIS 113

ABSTRACT.....	115
5.1 INTRODUCTION	116
5.1.1 MED PROCESS	117
5.1.2 MD PROCESS	119
5.2 THEORETICAL ANALYSIS OF SGP-MED HE.....	121
5.2.1 THERMAL ENERGY CONSUMPTION (<i>TEC</i>)	121
5.2.2 THERMAL AND EXERGY EFFICIENCY OF THE IDEAL RED ENGINE	126
5.3 SIMPLIFIED RED-MED MODEL	129
5.3.1 CIEMAT-MED MODEL RESULTS	130
5.3.2 RED-MED COUPLED SYSTEM	132
5.3.3 RED MODEL RESULTS	137
5.3.4 RED-MED INTEGRATED SYSTEM RESULTS	140
5.4 SIMPLIFIED RED-MD MODEL.....	146
5.4.1 MATHEMATICAL MODELLING	146
5.4.2 RESULTS AND DISCUSSION	151
5.5 CONCLUSIONS	162

6 ADVANCED RED-MED MODEL..... 163

ABSTRACT.....	165
6.1 INTRODUCTION	166

6.2	EXERGY ANALYSIS	168
6.3	RESULTS	172
6.3.1	EFFECT OF IRREVERSIBILITY SOURCES	174
6.3.2	CURRENT MEMBRANE PROPERTIES	179
6.3.3	ANALYSIS WITH HIGH-PERFORMING MEMBRANE PROPERTIES	185
6.3.4	COMPARATIVE ANALYSIS	188
6.4	CONCLUSIONS.....	191

SECTION III: SALT EXTRACTION THERMOLYTIC SALTS 193

7 REGENERATION OF THERMOLYTIC SALTS SOLUTIONS..... 195

	ABSTRACT.....	197
7.1	THERMOLYTIC SALTS IN CLOSED-LOOP APPLICATIONS	198
7.1.1	THERMOLYTIC SALT SOLUTIONS FOR FO DESALINATION	200
7.1.2	STATE OF THE ART OF THERMOLYTIC SGP HEAT ENGINES	202
7.1.3	FINAL REMARKS AND CHAPTER OUTLINE	203
7.2	LABORATORY-SCALE REGENERATION UNITS	205
7.2.1	REGENERATION UNIT PROCESS SCHEMES	205
7.2.2	AIR STRIPPING: EXPERIMENTAL SYSTEM AND EQUIPMENT	206
7.2.3	VAPOUR STRIPPING: EXPERIMENTAL SYSTEM AND EQUIPMENT	209
7.3	MODELING OF THE STRIPPING PROCESSES.....	212
7.4	EXPERIMENTAL RESULTS AND MODEL VALIDATION.....	215
7.4.1	STRIPPING COLUMN PERFORMANCES	215
7.4.2	VAPOUR STRIPPING COLUMN PERFORMANCES	217
7.5	THEORETICAL ANALYSIS OF REGENERATION UNIT PERFORMANCE.....	219
7.6	CONCEPTUAL DESIGN OF THE WHOLE REGENERATION UNIT.....	226
7.7	CONCLUSIONS.....	230

8 THE FIRST OPERATING T-RED HE..... 231

	ABSTRACT.....	233
8.1	INTRODUCTION	234
8.2	THE FIRST OPERATING T-RED HE.....	236

8.2.1 PROCESS DESCRIPTION	236
8.2.2 PROTOTYPE DESCRIPTION	238
8.2.3 EXPERIMENTAL PROCEDURE	240
8.2.4 RESULTS AND DISCUSSIONS	244
8.3 THERMOLYTIC RED HEAT ENGINE (TRED-HE).....	251
8.3.1 INTEGRATED PROCESS MODEL DESCRIPTION	251
8.3.2 RESULTS	255
8.4 CONCLUSIONS.....	263
<u>FINAL REMARKS AND OUTLOOKS.....</u>	<u>265</u>
<u>NOMENCLATURE.....</u>	<u>271</u>
<u>REFERENCES.....</u>	<u>281</u>
<u>APPENDIX.....</u>	<u>295</u>
A.1. PHYSICAL PROPERTIES OF SALT-WATER SOLUTIONS.....	295
A.1.1. SOLUTION DENSITY	295
A.1.2. SOLUTION CONDUCTIVITY	296
A.1.3. SOLUTION VISCOSITY	297
A.1.4. SALT DIFFUSIVITY	298
A.2. CIEMAT MED MODEL	300

LIST OF DISSERTATION PUBLICATIONS

Published paper:

- F. Giacalone, P. Catrini, A. Tamburini, A. Cipollina, A. Piacentino, G. Micale, Exergy analysis of reverse electrodialysis, *Energy Conversion and Management* 2018, 164, 588-602, <https://doi.org/10.1016/j.enconman.2018.03.014>
- F. Giacalone, A. Tamburini, M. Papapetrou, A. Cipollina, G. Micale, “Reverse Electrodialysis: Applications to Different Case Studies”, *IEEE proceeding* 2018, 10.1109/EEEIC.2018.8493961.
- F. Giacalone, C. Olkis, G. Santori, A. Cipollina, S. Brandani, G. Micale, “Novel solutions for closed-loop Reverse Electrodialysis: thermodynamic characterisation and perspective analysis”, *Energy* Volume 166, 2019, Pages 674-689 <https://doi.org/10.1016/j.energy.2018.10.049>.
- M. Micari, A. Cipollina, F. Giacalone, G. Kosmadakis, M. Papapetrou, G. Zaragoza, G. Micale, A. Tamburini, “Towards the first proof of concept of a Reverse ElectroDialysis Membrane Distillation Heat Engine”, *Desalination*, Volume 453, 1 March 2019, Pages 77-88, <https://doi.org/10.1016/j.desal.2018.11.022>.
- P. Palenzuela, M. Micari, B. Ortega-Delgado, F. Giacalone, G. Zaragoza, D.C. Alarcon-Padilla, A. Cipollina, A. Tamburini, G. Micale, “Performance Analysis of a RED-MED Salinity Gradient Heat Engine”, *Energies* 2018, 11, 3385; <https://doi:10.3390/en11123385>.

Paper in-preparation:

- F. Giacalone, A. Tamburini, M. Papapetrou, A. Cipollina, G. Micale, “Techno-economic evaluation of reverse electrodialysis process in different real environments”.
- F. Giacalone, F. Vassallo, M. Bevacqua, F. Scargiali, Cipollina, A. Tamburini, G. Micale, “Regeneration Units for Thermolytic salts applications: Modelling and Experimental assessments”.
- B. Ortega-Delgado, F. Giacalone, P. Catrini, A. Cipollina, A. Tamburini, A. Piacentino, G. Micale, “Exergy Analysis of Reverse Electrodialysis Heat Engine with Multi-Effect Distillation Regeneration Stage”.

LIST OF DISSERTATION PUBLICATIONS

- F. Giacalone, F. Vassallo, F. Scargiali, Cipollina, A. Tamburini, G. Micale, “Modelling Analysis of a thermolytic Reverse Electrodialysis Heat Engine”.
- F. Giacalone, F. Vassallo, F. Scargiali, Cipollina, A. Tamburini, G. Micale, “The first operating Thermolytic Reverse Electrodialysis Heat Engine”.

I NTRODUCTION

Our society is undergoing a progressive change about the life style and habits. The world population is continuously increasing with 7.6 billion of human beings in 2018, resulting in an increasingly demand of resources in terms of food, water and energy. The exploitation of the planet resources since the first Industrial Revolution, results today in an unsustainable condition, which requires fundamental changes. In particular, in the energy sector the adoption of fossil fuels as the main energy source for human beings' activities resulted in a strong impact on our planet, leading to climate changes and environmental pollution. Nowadays these aspects have induced society to a substantial challenge to find new sustainable energy sources for the future of human civilization.

Low-grade thermal energy, derived from industrial or geothermal sources, represents an interesting resource for energy production. Indeed, huge amounts of low-grade thermal energy are available. Considering the industrial sector an amount ranging between 20-50% of the energetic input of industrial plants, are lost every day, in the form of hot gasses and liquid streams. However, the recovery and re-use of low-grade thermal energy or waste heat is limited due to the lack of efficient technologies for converting low-temperature heat sources into electrical power. Recently, Salinity Gradient Power Heat Engines (*SGP-HEs*) have been proposed as a viable process for the recovery of low-grade heat. In particular, this PhD thesis focuses on the analysis of Reverse Electrodialysis Heat Engines (*RED-HEs*), contributing to the activities of the European project "*RED-Heat-to-Power*" funded by the European Union's Horizon 2020 Research and Innovation Programme (www.red-heat-to-power.eu). The aim of the project is to study and develop the first prototypes for the conversion of low-grade heat into electricity through a reverse electrodialysis (*RED*) unit.

A reverse electrodialysis heat engine consists of two main units: (i) a *power generation* unit based on the reverse electrodialysis process, where the salinity gradient between two salt solutions is exploited to produce electricity, and (ii) a *regeneration unit* where low-grade heat

is used to restore the salinity gradient of the reverse electro dialysis solutions exiting from the power generation unit. The restoring of the two solutions can be achieved by means of different strategies, e.g. solvent extraction and salt extraction, as summarized in the following.

- (a) In *solvent extraction*, the salt exchanged within the reverse electro dialysis unit is integrated by adding a part of the exhausted dilute stream to the exhausted concentrate stream, then, the resulting solution is fed to the regenerative unit where solvent is recovered by a thermal separation process (e.g. multi-effect distillation, membrane distillation) and transferred to the dilute solution.
- (b) In *salt extraction*, the exhausted dilute solution is fed to the regenerative unit where the salt is recovered by using low-grade heat as an energy source and transferred again to the concentrate solution. Rebalancing of the solvent is eventually carried-out to restore the solvent amount in the two streams.

The main objective of this thesis is to provide a proof of the ground-breaking concept of a reverse electro dialysis heat engine, demonstrating the technological readiness level of such technology at a lab-scale prototype level. To this aim, both configuration, solvent and salt extraction reverse electro dialysis heat engines were investigated.

The first part of this PhD thesis was dedicated to the development of a mathematical model for the *RED* process, based on a multi-scale modelling approach, considering two different scales of description: (i) a lower-scale model, describing the main phenomena involved in a single repeating unit (cell pair) and (ii) a higher-scale model related to the whole system, including all cell pairs and the relevant interconnections. The mathematical model was validated against experimental results and integrated with exergy analysis tools useful to evaluate the main causes and location of irreversibility sources.

Ad hoc experimental campaigns were carried out in order to characterize the behaviour of different salt-water solutions, membrane properties and the operability of lab-scale units. In particular, a purposely-developed test rig was built in order to evaluate the osmotic and activity coefficients of salt-solutions from vapour pressure measurements, then used to determine novel data for caesium and potassium acetate salt solutions. This activity was performed at the University of Edinburgh, during a period abroad of six months. Furthermore, several experimental results on lab-scale reverse electro dialysis unit were carried out in order to provide membrane properties and experimental results for the mathematical model validation.

In the case of solvent extraction strategies, validated mathematical models were developed for a reverse electrodialysis heat engine implementing either membrane distillation or multi-effect distillation as regeneration unit. These activities were performed in collaboration with the “Centro de Investigaciones Energéticas, Medioambientales y Tecnológicas (CIEMAT)” of Almeria. Finally, an exergy analysis at component level was performed for the integrated *RED-MED HE*, analysing the impact of the main operating conditions and membranes properties on the exergy efficiency of the system and identifying the main irreversibility sources.

In the case of salt extraction strategies, thermolytic salts were selected and studied as working solutions of the *RED-HE*. Solutions of thermolytic salts have the peculiarity that their ions dissolved in water undergo a degradation process into gaseous species when the temperature is increased over a certain limit. Then, the dissolved thermolytic salt can be removed nearly completely from the solution by means of a thermal desorption process. The stripped gaseous species can be dissolved again in the aqueous solutions through an absorption step, resulting in an aqueous solution consisting of the very same ions of the thermolytic salt. Experimental test-rigs were designed, built and tested to investigate the stripping process of thermolytic salts. Mathematical models were developed in *ASPEN Plus*[®] and validated by comparison with experimental results. The model was also used to perform a sensitivity analysis and investigate the performance of the whole regeneration unit, including also the absorption process. Then, a mathematical model of a *RED-HE* fed by thermolytic salts was developed by coupling the *ASPEN Plus*[®] process model for the regeneration unit to the *RED* process model and used to perform sensitivity analyses.

Finally, all the knowledge gained by theoretical and experimental works have made possible the design, construction and operation of the first world prototype of the thermolytic *RED HE*, demonstrating for the first time the feasibility of the process.

The present thesis has been organised in order to cover the main aspects of the *RED* process and describe the aforementioned objectives.

Chapter 1 introduces the concept of salinity gradient power (*SGP*) and related *SGP-HEs*, describing the *SGP-HE* concept and analysing the state of the art of the technology.

Section I - Reverse Electrodialysis process

Chapter 2 presents an overview of the reverse electrodialysis process, describing the technological fundamentals, experimental tests and modelling.

Chapter 3 reports an original exergy analysis of the *RED* unit and the potential applications of the process in real environments.

Chapter 4 presents the analysis on the influence of salt-solution properties on the *RED-HE* performance, reporting novel osmotic and activity coefficients for potassium acetate and caesium acetate water solutions.

Section II - Solvent Extraction: RED with evaporative regeneration unit

Chapter 5 and *Chapter 6* are dedicated to the solvent extraction reverse electrodialysis heat engine. In particular, *Chapter 5* reports the simplified mathematical models used to evaluate preliminary performances of (i) theoretical *SGP* unit fed by different salt solutions, (ii) *RED-MED HE* and (iii) *RED-MD HE* fed by NaCl solutions. *Chapter 6* describes the advanced *RED-MED-HE* model developed to perform exergy analysis on the integrated system.

Section III - Salt Extraction: Thermolytic salts

Chapter 7 and *Chapter 8* reports the analysis on thermolytic salts. In particular, *Chapter 7* is focused on the regeneration unit of thermolytic salts presenting mathematical models and experimental assessments. *Chapter 8* presents the first operating thermolytic *RED* heat engine (*t-RED HE*) and a perspective analysis based a validated process model for the *t-RED HE*.

1

CONVERSION OF LOW GRADE HEAT INTO POWER

Chapter Outline

1.1	SALINITY GRADIENT POWER.....	7
1.1	LOW-GRADE HEAT INTO ELECTRICITY	8
1.2	SGP HEAT ENGINE: FUNDAMENTALS	12
1.3	STATE OF THE ART OF SGP ENGINES.....	15
1.4	MOTIVATION AND GOALS OF THIS WORK.....	17

1.1 Salinity Gradient Power

Salinity gradient power (*SGP*) or Salinity Gradient Energy (*SGE*) is a sustainable energy source identified for the first time in the 1950s by Pattle [1]. This energy source is based on harvesting the chemical energy released during the mixing process of salt solutions at different concentration. As an example, this process naturally occurs when a river flows in to the sea.

The world theoretical potential for recovering the energy dissipated when rivers flow into the seas by using of *SGP* technology has been estimated in the range 1.4 and 2.7TW [2,3]. The power generated from *SGP* processes clearly depends on the salinity gradient between the streams used for the mixing. When 1 m³ of saturated brine is mixed with 1 m³ of river water the Gibbs free energy of mixing released is equal to 15 MJ, which is 10 times larger than the energy released considering seawater as concentrated solution. Clearly, just a fraction of the theoretical potential may be recovered in real applications, depending on the conversion efficiency of the specific *SGP* process.

The main *SGP* technologies proposed so far for converting the salinity gradient into electricity through a “*controlled mixing process*” are: (i) Pressure Retarded Osmosis (*PRO*), and (ii) Reverse ElectroDialysis (*RED*).

PRO [4,5] uses osmotic membranes to separate a concentrate salt solution from a dilute one. The salinity gradient between the two solutions produces a water osmotic flux, from the dilute to the concentrate, “retarded” from the application of a hydraulic pressure in the concentrate side. Therefore, the permeate water flux stores pressure energy, which is converted into mechanical energy through hydraulic turbine.

In the *RED* process [6,7], Ionic Exchange Membranes (*IEMs*) are used to convert the concentration difference between two solutions into an electrical potential raise and an ionic flux. A *RED* unit consists of a stack in which cationic and anionic exchange membranes are alternatively piled. The compartments between two different membranes are consecutively fed with concentrate and dilute solutions. The chemical potential difference between the two solutions generates a selective transport of cations and anions through the membranes resulting in an ionic current and an electric potential difference over each membrane. Then, this ionic current is converted into electricity by redox reactions, which occur at two electrodes placed at the end of the cell-pairs pile.

Notwithstanding the large potential of salinity gradient technologies in natural environments, their applications are restricted by the localization and quality of the available salt solutions. However, an alternative application of SGP technologies has been recently proposed which aims to operate the system in closed-loop fashion as a heat engine, converting low grade heat into electricity and eventually, allowing the storage of electricity as salinity gradient or chemical energy. Closed-loop SGP or Salinity Gradient Power Heat Engine (*SGP-HE*) may be regarded as integrated process where one of the aforementioned *SGP* processes (i.e. *PRO* or *RED*) is coupled with a thermal regeneration process in which *Low Grade Heat* (LGH) is used to restore the initial condition of the saline solutions exiting from the *SGP* unit.

In the wide framework of the *SGP-HEs*, this thesis aims to analyse and develop *RED-HEs* able to convert low grade waste heat into electricity through a Reverse Electrodialysis Heat Engine in agreement with the goals of the European project *RED-heat-to-power* funded by the Horizon 2020 research and innovative programme under grant agreement No 640667. (www.red-heat-to-power.eu).

1.1 Low-grade heat into electricity

The recovery and re-use of waste heat is an interesting perspective aims to increase the efficiency of existing industrial plant and, at the same time, to reduce the energy costs and the CO₂ emissions. Waste heat is a massive available source of energy. Referring to the industrial sector, a huge amount of the energetic input, between 20-50% [8], is lost as waste heat contained in hot liquid and gaseous streams, but even if these streams are often considered a waste, they still have suitable amount of exergy, which can be reused or converted in other energy forms.

Several examples of waste heat availability are reported in the literature. In 2012 in the USA, 38 billions of GJ of carbon, natural gas and nuclear energy were converted in 12.3 billion GJ of electricity with an average efficiency of 32 %, releasing in the environment as waste heat about 18.9 billions of GJ [9]. Another study has evaluated the annual theoretical availability of waste heat in the UK industrial sector, which has been estimated around 14 TWh [10]. The recovery of such waste heat would results in an economic saving on the order of £ 200-300 million/year and in environmental benefits due to the reduction of thousands of tonnes of CO₂ emissions [11].

The yearly production of industrial waste heat in Europe, classified per industrial sector and waste temperature referring to the 2015, is reported in *Figure 1.1* [12]. According to Papapetrou et al. [12] a potential of 304.13 TWh/year of waste-heat from EU industrial sector was available in 2015, mainly represented by waste-heat at temperature lower than 200 °C (40% of the total).

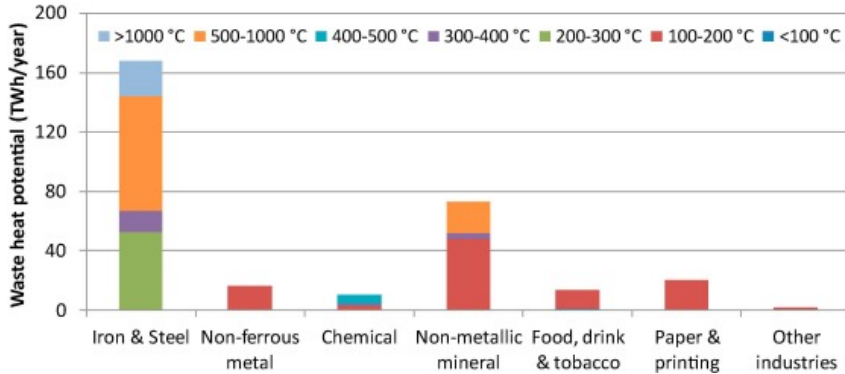


Figure 1.1 Yearly production of Waste heat per industrial sector and temperature level for EU industry in 2015 [12].

Waste heat sources are classified in three different levels according to the releasing temperature: (i) *high temperature waste heat* (HT, $T > 400\text{ }^{\circ}\text{C}$), (ii) *medium temperature waste heat* (MT, $100\text{ }^{\circ}\text{C} < T < 400\text{ }^{\circ}\text{C}$) and (iii) *low temperature waste heat* (LT, $T < 100\text{ }^{\circ}\text{C}$). A detailed classification of waste-heat sources based on industrial process and temperature is reported in Table 1.1[13]

Several strategies can be employed to recover and reuse the waste heat. The waste heat recovery technologies are classified in passives and actives. The passive technologies are based on re-using the waste-heat at the same or lower temperature level. Thermal integration heat exchangers and thermal energy storage are two examples. The active technologies are based on the conversion of heat into another form of energy or into heat at higher temperature level. The active technology can be classified in: (i) “*waste-heat to heat*”, (ii) “*waste-heat to cold*” and (iii) “*waste-heat to power*”.

Table 1.1 Waste heat sources per industrial process and exhausted gas temperature. Adapted from [13].

Temperature level	Industrial Process	Exhausted gas temp (°C)
HT	Iron- and steelmaking	1450–1550
HT	Nickel refining furnace	1370–1650
HT	Steel electric arc furnace	1370–1650
HT	Glass melting furnace	1300–1540
HT	Basic oxygen furnace	1200
HT	Aluminium reverberatory furnace	1100–1200
HT	Steel heating furnace	1450–1550
HT	Copper reverberatory furnace	900–1090
HT	Glass oven without regenerator	900–1300
HT	Iron cupola	820–980
HT	Cooper refining furnace	760–820
HT	Reheating furnace without regenerator	700–1200
HT	Hydrogen plants	650–980
HT	Fume incinerators	650–1430
HT	Coke oven	650–1000
HT	Glass oven with regenerator	600–800
HT	Cement kiln	450–620
HT	Heat treating furnace	430–650
HT, MT	Melting oven	400–700
HT, MT	Gas turbine exhaust	370–540
HT, MT	Reciprocating engine exhaust	320–590
HT, MT	Reheating furnace with regenerator	300–600
MT	Blast furnace stoves	250–300
HT, MT	Drying and baking ovens	230–590
HT, MT	Steam boiler exhaust	230–480
HT, MT	Finishing soaking pit reheat furnace	200–600
MT	Steam boiler	200–300
MT	Coke oven	190
MT	Stack gas	160–200
MT	Container glass melting	140–160
MT	Flat glass melting	160–200
HT, MT	Ceramic kiln	150–1000
LT, MT	Drying, baking, and curing ovens	90–230
LT, MT	Cooling water from annealing furnaces	70–230
LT, MT	Cooling water from internal combustion engines	70–120
LT, MT	Exhaust gases exiting recovery devices in gas-fired boilers, ethylene furnaces, etc	70–230
LT, MT	Conventional hot water boiler Process	60–230
LT	Process steam condensate	50–90
LT	Condensing hot water boiler	40–50
LT, MT	Hot processed liquids/solids	40–230
LT	Cooling water from air conditioning and refrigeration condensers	30–40
LT	Cooling water from air compressors	30–50
LT	Cooling water from furnace doors	30–50

Among “waste-heat to power” processes, both conventional and innovative technologies have been proposed so far. Examples of well-established technologies are Steam Rankine Cycle (*SR*), Organic Rankine Cycle (*ORC*) and Kalina Cycle (*KC*) [14–16]. Examples of innovative technologies, proposed in the literature, are ThermoElectric Generator (*TEG*) [17], Piezoelectric Generator Power (*PEPG*), Stirling Engine (*SE*), and Carbon Carrier (*CC*)

cycle[18]. Recently, Salinity Gradient Power Heat Engines (*SGP-HEs*) have been proposed among *waste-heat to power* applications, for converting low-grade heat into electricity.

The most relevant performance parameter of a heat engine is the thermal efficiency, defined as the ratio between the power generated (W) and the thermal power consumed (Q):

$$\eta_{th} = \frac{W}{Q} \quad (1.1)$$

However, the thermal efficiency is not an effective parameter to compare the performance of heat engines operating at different temperature ranges. In fact, given the cold sink temperature, the higher the temperature of the heat source, the higher the theoretical efficiency obtainable, i.e. the Carnot's efficiency of the system (η_C), defined as:

$$\eta_C = 1 - \frac{T_{cold}}{T_{hot}} \quad (1.2)$$

where T_{hot} is the temperature of the hot reservoir and T_{cold} is the temperature of the cold sink where the heat is discharged. Then, the heat engines operating at higher temperature levels could reach efficiencies higher than the ones operating at lower temperatures. With this respect, a more useful performance parameter is the exergy efficiency (η_{ex}) defined as the fraction of the thermal efficiency and the thermodynamic limit efficiency given by the Carnot's cycle:

$$\eta_{ex} = \frac{\eta}{\eta_C} \quad (1.3)$$

This parameter compares the efficiency of a given engine to the one of the corresponding ideal engine operating in the same temperature interval. *Figure 1.2* reports the operating performance parameters (i.e. heat temperature, energy and exergy efficiency of the most important “*heat to power*” technology proposed in the literature[19,20].

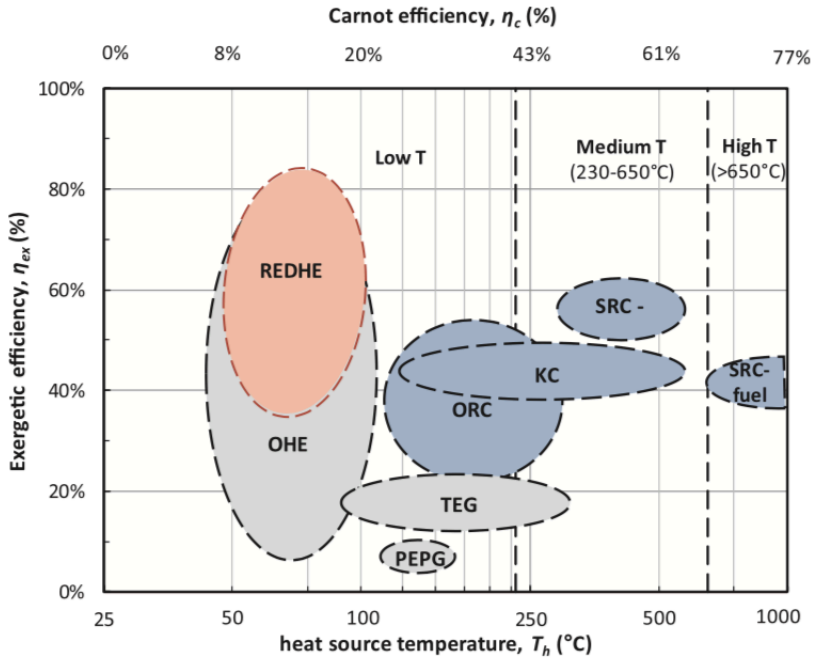


Figure 1.2 Performance parameters for the most important “waste-heat to power” technology. Cold sink temperature equal to 25 °C. Legend: SRC-hot gases: Steam Rankine Cycle integrated with gas turbine/other topping cycles; SRC-fuel: Steam Rankine Cycle directly fuelled by oil, coal or other fuels; KC: Kalina Cycle; ORC: Organic Rankine Cycle; TEG: Thermoelectric Generation; PEPG: Piezoelectric Power Generation with waste heat- powered expansion/compression cycle; OHE: Osmotic Heat Engine [19,20]. Worth noting that efficiency values of RED-HE and OHE refer to theoretical values, while experimental values are reported for all other cases.

As reported in *Figure 1.2*, the most consolidated technologies recover waste heat at temperature higher than 100°C, while, concerning very low-temperature heat ($T < 100^\circ\text{C}$), no-viable technologies have been proposed so far. The aims of this PhD work are the conceptual development, design, modelling and experimental proof of the concept of *RED-HE* for the recovery and conversion of low temperature heat, contributing to increase the understanding of such technology.

1.2 SGP Heat Engine: Fundamentals

A typical *SGP-HE* or *closed-loop SGP* consists of (i) a *power generation unit* based on one of the above-mentioned *SGP* technologies, (ii) a *regeneration unit* in which a thermally driven regeneration process is used to restore the initial conditions of the two solutions and (iii) eventual mixers for water/salt rebalancing in the concentrate and/or dilute solution loop.

Within the *SGP* unit, the salinity gradient between two solutions at different concentration is exploited to generate electricity. As result of the power generation process, the original concentration gradient of the two solutions is partially consumed and two exhausted solutions are obtained. In an open-loop configuration these “waste” solutions are released in the environment, conversely, in the case of closed-loop applications, the exhausted solutions are regenerated in order to restore same conditions owned at the inlet of the reverse electrodialysis unit. This is carried-out in the regeneration unit where thermally driven separation processes are used, using low temperature heat (i.e. $T < 100^{\circ}\text{C}$) as an energy source. The system requires also a cold sink where part of the heat provided in the regeneration unit is discharged. Generally, cold utility temperatures between 15°C and 25°C are enough to ensure the required cooling, thus the use of conventional cooling water can be the most suitable. However, the availability of the cold sink, in some cases, might represent a limitation of this technology, requiring additional costs. A schematic representation of the process is depicted in *Figure 1.3*.

The system can be used in both continuous and discontinuous conditions. During continuous operation, the heat engine converts constantly heat into electricity. In discontinuous operation, the heat is used whenever available to regenerate the two solutions. The accumulation of those regenerated solutions represents a chemical energy storage convertible into electricity by the *SGP* unit when required. This aspect represents a big advantage of this technology in comparison to other conventional renewable energy sources. Moreover, *SGP HE* generates electricity without any emissions, rather valorising the waste-heat produced from industrial plants, reducing their environmental impact and increasing the efficiency of the process.

Closed-loop SGP do not suffer of the typical restrictions of the conventional *open-loop SGP* process, having the following features:

- (i) Application can be made in any location where waste-heat is available, regardless to the local availability of natural salinity gradients;
- (ii) Use of unconventional saline solutions, which can be optimized to maximize heat to electricity conversion;
- (iii) No need of pre-treatment processes to prevent fouling/biofouling phenomena;
- (iv) Excellent potential for energy storage applications when using low-grade waste heat to restore the original salinity levels of feed solutions.

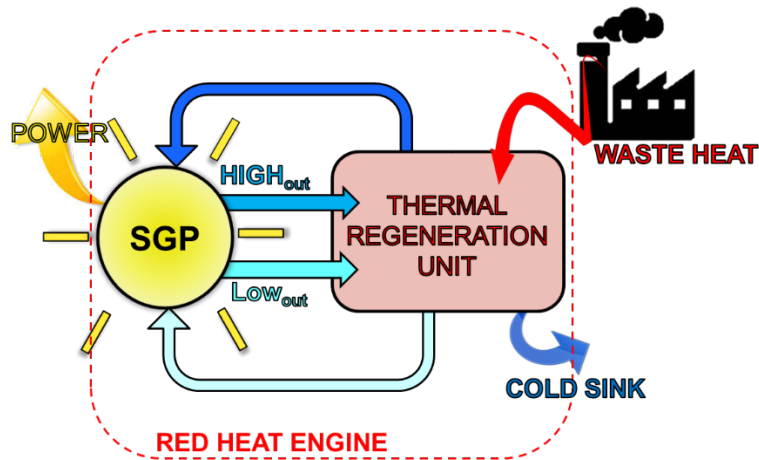


Figure 1.3 Schematic representation of the Salinity Gradient Power Heat Engine

One of most interesting aspect of closed-loop operation is the possibility to select an ad-hoc saline solution to enhance the overall performance of the integrated process. The careful choice of the artificial saline solution ensures (i) the availability of large amounts of Gibbs free energy of mixing, (ii) easy regeneration of the original concentration levels of feed solutions, (iii) use of low temperature waste heat (i.e. 40-100°C).

Depending on the choice of artificial saline solution, a variety of different processes can be adopted for the regeneration stage. These can be grouped in two main categories: (i) *solvent extraction processes* and (ii) *salt extraction processes*. A schematic representation of the two options is reported in Figure 1.4.

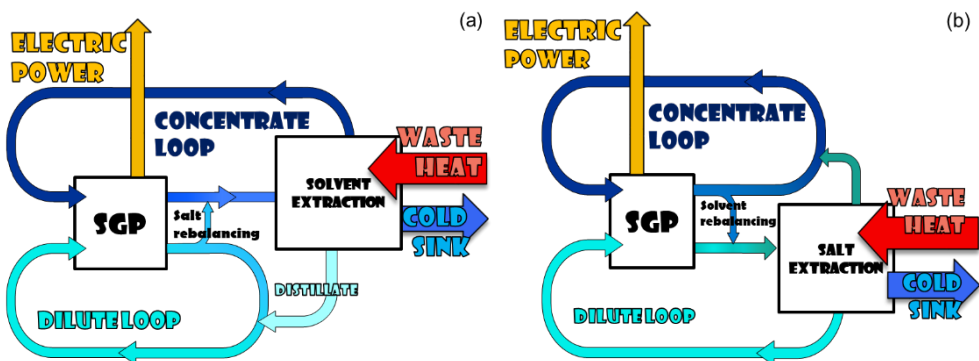


Figure 1.4 Schematic representation of the two regeneration processes: (a) solvent extraction and (b) salt extraction.

In *solvent extraction processes*, the regeneration of solutions is obtained by transferring the solvent from the exhausted concentrate stream to the exhausted dilute. In principle, no salt is transferred in the regeneration unit, then, a salt balance step is required to restore the original salt content of the concentrate loop. To this aim, part of the outlet dilute stream is mixed to the concentrate one. The main options proposed so far are: (i) *evaporative processes*, either conventional or unconventional, such as Multi Effects Distillation (*MED*) [21] and Membrane Distillation (*MD*) [22,23]; (ii) *adsorption/desorption process*, such as the Adsorption Desalination (*AD*) [24]; (iii) *liquid-liquid extraction* using organic solvent [19] and (iv) *forward osmosis process* using temperature sensitive draw agent followed by thermally regeneration step [25,26].

Conversely, in *salt extraction processes* the regeneration is performed transferring the salt from the exhausted dilute solution to the exhausted concentration solution. Then, also in this case a rebalancing process could be required for restoring the solvent eventually exchanged between the two streams. Suitable salt solutions or suitable mechanisms could be adopted in the regeneration unit. Among the proposed strategy, the use of thermolytic salts is the most promising thank to their properties. The ions of thermolytic salts dissolved in water undergo a degradation process in gaseous species if solution is heated above the salt decomposition temperature [27]. Other options poorly investigated are represented by salt precipitation process in which the separation of salt from the dilute stream is obtained by the addition of compounds with anti-solvent properties [28] or changing the temperature [29].

1.3 State of the art of SGP Engines

The idea to convert waste-heat into electricity through *SGP* technologies was proposed for the first time by S. Loeb in 1975 applied to the case of *PRO* process [30] and in 1979 for the case of *RED* process [31]. Notwithstanding *SGP-HE* is an old concept, only in recent years, thanks to the developments of suitable membranes, the idea of Loeb has shown first applications and deep-studies. In 2007 McGinnis et al. [32] proposed the “Osmotic Heat Engine (*OHE*)” consisting of a *PRO* unit coupled with a distillation column fed with ammonium bicarbonate solutions. The exiting solutions from *PRO* module are restored thanks to the distillation column in which the ammonium bicarbonate is firstly degraded in CO_2 and NH_3 from the dilute solution and then absorbed in the concentrate stream.

Similarly, Luo et al. [33] and Cusick et al. [34] in 2012 proposed respectively a *RED* unit and a microbial *RED* unit coupled with a distillation column fed with ammonium bicarbonate solution. In the same year, Logan and Elimelech [35] standardized the idea of *SGP-HEs*.

In 2015, Shaulsky et al [36], proposed an *OHE* fed by LiCl-methanol solutions. The use of an organic solvent may lead to high thermal efficiency of the regeneration unit due to the higher volatility and lower heat of vaporization of the organic solvent compared to water. Experimentally investigations were carried-out to evaluate the water permeability and salt flux in *PRO* process. Despite the lower solvent permeability, the theoretical calculation on the *OHE* energy efficiency have shown, in some conditions, higher efficiencies using LiCl-methanol than the one obtainable with LiCl-water.

In the same year, Kwon et al. [37] presented experimental characterization of the *RED* unit fed by aqueous solutions of ammonium bicarbonate (NH_4HCO_3) for waste-heat recovery applications. The authors found a maximum power density (0.77 W/m^2 of membrane area) doubled than the one achieved by Luo et al. [21].

In 2016, also Bevacqua et al. [38] presented an experimental investigation on a *RED* system fed with NH_4HCO_3 solutions showing the highest net power density so far achieved using such solutions, i.e. equal to $2.42 \text{ W/m}^2_{\text{cp}}$. In 2016, Long et al. [39] performed a parametric study on a hybrid *RED-MD HE* fed by NaCl solutions. The results have shown, in best conditions, maximum electric efficiency of 1.15% operating *MD* unit between 20 and 60 °C and NaCl solution concentration of 5 mole/kg. In the same year, Hickenbottom et al. [40] experimentally investigated the impact of using different salt solutions as possible working fluid of a *PRO-MD HE*. Their findings indicate CaCl_2 as a promising salt for the both *PRO* and *MD* process.

In 2017 Kim et al. [41] also proposed a validated mathematical model to access the performance of a *RED* unit fed by ammonium bicarbonate solutions for low-grade waste heat recovery. In the same year, Tamburini et al.[19], analysed the efficiency of a (i) NaCl *RED-MED HE* and of a (ii) NH_4HCO_3 *RED-HE* adopting a simplified model approach. In the first case, two different scenarios were analysed: a) current state of the art, where the *RED* unit adopts commercial membranes and the energy consumption was fixed at 40 kWth/m^3 for *MED* unit (b) future state of the art, where the *RED* unit adopts future membranes and *MED* energy consumption is set at 25 kWth/m^3 . In the second case, the energy consumption for regenerating thermolytic salts solutions was fixed at 100 kJ/mol. In the current state scenario, a maximum energetic efficiency of 5% (27.9% exergy efficiency) was reported for *RED-MED*

HE, while in the future state scenario the maximum energetic efficiency reported is around 15.4% (86% exergy efficiency) for *RED-MED HE*. An efficiency 10.5% (51.4% exergy efficiency) is resulted for the NH_4HCO_3 *RED-HE* case. A more accurate analysis was performed by Bevacqua et al. [42], who carried out a modelling analysis on *RED-HE* system operating with NH_4HCO_3 . The *HE* proposed is constituted by a *RED* unit and thermal regeneration unit including an air-stripping column to restore the initial salinity gradient. The highest exergy efficiency is found equal to 22%. In the same year, Hickenbottom et al. [43] performed an interesting techno-economic assessment of a closed-loop osmotic heat engine based on experimentally validated technical model. Results have shown that the current state of the technology provides a levelized cost of electricity (*LCOE*) of 0.48\$/kWh which is not competitive with the actual grid electricity price, however future processes improvements and large installation may lead to a large reduction of the *LCOE* up to value near to 0.10\$/kWh making the process competitive.

In 2018, Hu et al. [44] performed a detailed theoretical analysis on the performance of a hybrid *MED-RED* heat engine. A maximum electrical generation efficiency of 1% was found coupling a *RED* unit with a 10 effects *MED* unit powered by low-grade heat at 95 °C.

1.4 Motivation and goals of this work

In the last decade, *SGP* heat engines gained growing interest within the scientific community due to the ever increasing research of novel technology for the production of electricity from waste resources. Among the different *SGP-HEs*, this thesis focuses on the analysis of *RED-HEs*. Different theoretical studies have been carried so far on the, highlighting the interesting performance of *SGP-HE* technology in the recovery of low-grade heat. However, most of the works reported in the literature focused on modelling analysis, often based on simplified assumptions. Furthermore, no real demonstration of the process feasibility has been reported in the literature so far due to the significant efforts required to design, construct and operate a fully integrated *SGP-HE* system.

The activities of this PhD thesis are carried out within the framework of the European project “*RED-Heat-to-Power*” funded from the European Union’s Horizon 2020 research and innovation programme (www.red-heat-to-power.eu), which aims to study and develop the first prototypes for the conversion low-grade waste heat into electricity through a closed-loop reverse electrodialysis.

The main objective of this thesis is to provide a proof of the ground-breaking concept of a reverse electro dialysis heat engine, demonstrating the technological readiness level of such technology at a lab-scale prototype level. To this aim, both modelling and experimental activities have been carried-out. In particular:

- (i) Modelling activities focused on the development of advanced modelling tools validated against experimental results, in order to predict the performance of different *RED-HEs* and provide realistic perspective performances for such technologies.
- (ii) Ad hoc experimental campaigns were carried out to characterize the behaviour of different salt-water solutions, membrane properties but also the operability of lab-scale units.
- (iii) All the knowledge gained, have made possible the design, construction and testing of the first thermolytic *RED-HE* prototype, demonstrating for the first time the feasibility of the process.

S SECTION I:

Reverse ElectroDialysis Process



REVERSE ELECTRODIALYSIS

Chapter Outline

ABSTRACT	23
2.1 INTRODUCTION	24
2.2 GIBBS FREE ENERGY OF MIXING	26
2.3 RED PROCESS: FUNDAMENTALS	28
2.3.1 ION EXCHANGE MEMBRANES	30
2.3.2 MEMBRANES PROPERTIES	32
2.4 EXPERIMENTAL	38
2.4.1 CORRECTED POWER DENSITY	40
2.4.2 AVERAGE MEMBRANE PERMSELECTIVITY AND RESISTANCES.....	42
2.5 MODELLING REVERSE ELECTRODIALYSIS	46
2.5.1 EQUIVALENT CIRCUIT SCHEME AND ELECTRICAL EQUATIONS	46
2.5.2 WATER AND SALT FLUX THROUGH THE IEMS	49
2.5.3 SALT AND GLOBAL MASS BALANCES	50
2.5.4 MEMBRANES PROPERTIES	52
2.5.5 POLARISATION COEFFICIENTS.....	52
2.5.6 PRESSURE DROPS, PUMPING POWER & NET POWER	53
2.5.7 NUMERICAL DETAILS	54
2.5.8 RED PROCESS MODEL VALIDATION	55
CONCLUSIONS	59

Part of this chapter has been published in:

F Giacalone, P Catrini, A Tamburini, A Cipollina, A Piacentino, G Micale, Exergy analysis of reverse electrodialysis, Energy Conversion and Management 2018, 164, 588-602,

<https://doi.org/10.1016/j.enconman.2018.03.014>

Abstract

Reverse electrodialysis (RED) is a relevant salinity gradient power (SGP) technology for harvesting the energy released during the mixing of salt-water solutions at different concentration.

This chapter presents the RED technology, providing an overview of the process: the main phenomena involved in the process and the role of ionic exchange membranes in the power generation unit are thoroughly described and discussed.

Experimental apparatus and typical tests are presented together with the procedure to obtain average permselectivities and resistances of membranes implemented in the mathematical model of the RED process. Fujifilm type 10 Membrane properties using NaCl and NH_4HCO_3 are reported as a function of the concentration of the feed solutions.

A mathematical model for the RED process was developed adopting a multi-scale modelling approach, considering two different scales of description: (i) a lower-scale model, describing the main phenomena involved in a single repeating unit (cell pair) and (ii) a higher-scale model related to the whole system, including all cell pairs and the relevant interconnections. The model was validated against experimental results, considering different stack lengths and operating conditions, such as solution concentrations and velocities, for two different salts, i.e. NaCl and NH_4HCO_3 .

2.1 Introduction

Reverse ElectroDialysis (*RED*) is a membrane process for the direct conversion of salinity gradients into electricity. In reverse electro dialysis, a “controlled mixing” process allows the harvesting of part of the Gibbs free energy of mixing dissipated when solutions at different concentrations are mixed.

Applications of the *RED* process started for the case of open-loop configuration systems, where natural salinity gradients (i.e. generated by mixing river water, seawater, brine, or brackish water) are exploited to produce electricity and are subsequently released into the environment. In particular, the first studies about *RED* units were focused on the recovery of the Gibbs free energy released from the mixing of seawater and river water, a natural process very common in nature occurring at the mouth of a river.

Several laboratory investigations have been performed and presented in literature, all focusing on how operating conditions and membrane properties can affect the main process performance parameters such as the power density (i.e. the power generated per m^2 of membrane area) and the process yield (i.e. energy generated per cubic meter of feed solutions). The first experiments related to the *RED* process were carried-out by Pattle in 1954, who reported a power density of 0.05 W/m^2 [1]. Several years later, higher power density values (i.e. 0.17 W/m^2) were found by Weinstein and Leitz [45] in 1976, by Audinos [46] (i.e. 0.4 W/m^2) and by Jagur-Grodzinski and Kramer [47] in 1986 (i.e. 0.41 W/m^2). A further doubling (about 0.93 W/m^2) was reported in 2008 by Veerman et al. [48].

During the last years, the process performance has been enhanced thanks to the developments of the technology leading to a further increase in power density up to values around 2.2 W/m^2 [49]. Scientific efforts were focused on the overall system design [50,51], the fluid-dynamics within the channels [52] or the electrode material investigation [53]. Several studies are also focused on the development of Ionic Exchange Membranes (*IEMs*) with low electrical resistance and high perm-selectivity [54], the investigation of membrane materials [55,56] and the specific interactions between membrane and ions in the solution [57,58].

A further development of the *RED* process is related to the exploitation of high salinity streams, as in the case of brines. Laboratory investigations performed with artificial brackish water and brine have shown the possibility to reach a power density up to 6.7 W/m^2 [59]. Furthermore, in 2014, the first demonstration plant operating with real brines and saline waters was built in Trapani (Italy) [51,60].

However, the applications for the case of natural high salinity gradients are very limited in the areas where these sources are available. A possibility to overcome this natural limit is the use of artificial salinity gradients within a *RED* Heat Engine (*RED-HE*). The *RED-HE* can be in fact implemented in principle anywhere, thanks to the use of a limited quantity of artificial saline solutions suitably-selected for optimal process performance in *RED* unit operated in closed loop [19,42].

Another interesting application of closed-loop reverse electro dialysis systems is the development of a “*salinity-gradient flow battery*”. Some examples of this application have been proposed so far both in scientific papers [61,62] and high-risk cooperation projects [63]. The enhancement of the energy performance of *RED* units is a matter of crucial importance both in open- and closed-loop configurations. Further investigations are needed in order to make this sustainable power production system competitive with the most common power generation processes.

The goal of this chapter is to provide an overview of the *RED* technology, presenting the main phenomena involved in the process and some theoretical background. Furthermore, experimental apparatus and tests are presented. The last part of the chapter is devoted to the description of the mathematical model of the *RED* process developed during this PhD work. The model is based on the conventional equations adopted in other models presented in the literature [64,65], but it considers a different equivalent electrical circuit of the *RED* unit, making predictions more accurate.

2.2 Gibbs free energy of mixing

The Gibbs free energy of mixing gives the maximum amount of work obtainable from any *SGP* technology. When a solution at high concentration (C_H) is mixed with a solution at low concentration (C_L), the resulting effect is a variation of the Gibbs free energy of the system, i.e. the Gibbs free energy of mixing, which may be in principle totally be converted in electricity when no dissipative phenomena are involved in the recovery process. These chemical potential variation is associated to an increase of the total entropy of the system when independent solutions at different composition are mixed together [6].

The Gibbs free energy of a generic salt aqueous solution is defined as:

$$G_i = n_{MX,i}\mu_{MX,i} + n_{s,i}\mu_{s,i} \quad (2.1)$$

where, $n_{MX,i}\mu_{MX,i}$ are the product of the salt moles (mol) and the salt chemical potential (J/mol) and $n_{s,i}\mu_{s,i}$ are the product of the water moles (mol) and the water chemical potential (J/mol). The chemical potentials of salt and solvent are evaluated through the Pitzer's model (presented in *Chapter 4*).

The Gibbs free energy of mixing is evaluated as the difference between the Gibbs free energy of the solutions resulting from the mixing (G_{mix}) and the Gibbs free energy of the two original solutions (i.e. G_L and G_H):

$$\Delta G_{mix} = (G_{mix} - G_L - G_H) \quad (2.2)$$

The Gibbs free energy of mixing (ΔG_{mix}) is evaluated considering both salt and solvent influence on the chemical potential. However, when streams at low concentration are considered (as in the case of natural streams like seawater and river water) the contribution of water can be neglected, thus simplifying *eq. 2.2* by deleting the last term [66]. Conversely, when streams have high salt concentration (as in the case of saturated brines or closed loop applications) the effect of water can be significant in the determination of the free energy of mixing and all terms have to be considered. This is highlighted in *Figure 2.1* for NaCl solutions at a fixed dilute concentration of 10^{-6} mol/kg_s by referring to the same amount of solutions (1 m³ o 1 kg of diluted solution and 1 m³ or 1 kg of concentrate solution).

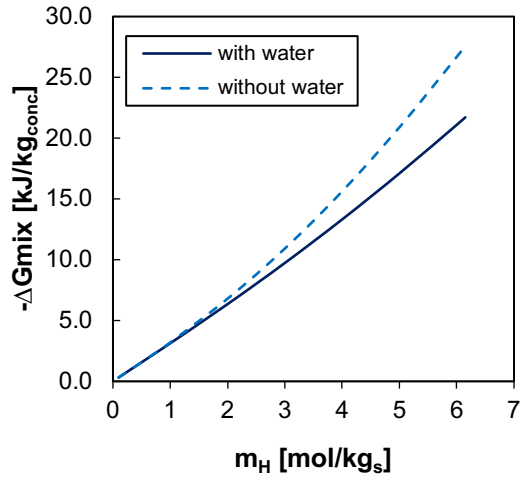


Figure 2.1. Gibbs free energy of mixing as a function of concentrate NaCl solutions molarity at 25°C calculated neglecting the effect of water on the chemical potential (without water, blue dashed-line) and including it (with water, blue line). Dilute molality set at 10^{-6} mol/kg_s and equal amount of solutions (1 kg) mixed.

The Gibbs free power of mixing ($\Delta\dot{G}_{mix}$) can be evaluated substituting the moles of species with the molar flowrates (mol/s) in eq.s 2.1 and 2.2. Then, the specific Gibbs free energy of mixing (*SME*), expressed in kJ/m³ or kWh/m³, is defined as the ratio of the ΔG_{mix} (or $\Delta\dot{G}_{mix}$) to the lower available solution volume (or flowrate (m³/s)):

$$SME = \frac{\Delta G_{mix}}{V_{lim}} = \frac{\Delta\dot{G}_{mix}}{\dot{V}_{lim}} \quad (2.3)$$

where V_{lim} and \dot{V}_{lim} are the limiting volume and flow rate, respectively.

2.3 RED process: fundamentals

Reverse electrodialysis is an *Ionic Exchange Membrane (IEM)* process driven by the chemical potential difference between two salt solutions. A reverse electrodialysis unit consists of repetitive units called *cell pairs*. Each cell pair consists of two membranes, i.e. a cation exchange membrane (*CEM*) and an anion exchange membrane (*AEM*) and two compartments, i.e. a dilute (*LOW*) and a concentrate (*HIGH*) compartment.

All the compartments are alternately fed with the two feed streams, thus generating a concentration gradient across all the membranes. Once the *RED* system is connected to an external load, an ionic current is produced in the unit. This current is converted into an electronic current in the electrode compartments where an electrodic solution containing a suitable redox couple (e.g. $\text{K}_3\text{Fe}(\text{CN})_6 / \text{K}_4\text{Fe}(\text{CN})_6 \cdot 3\text{H}_2\text{O}$) is recirculated. A schematic representation of the *RED* unit is reported in *Figure 2.2*.

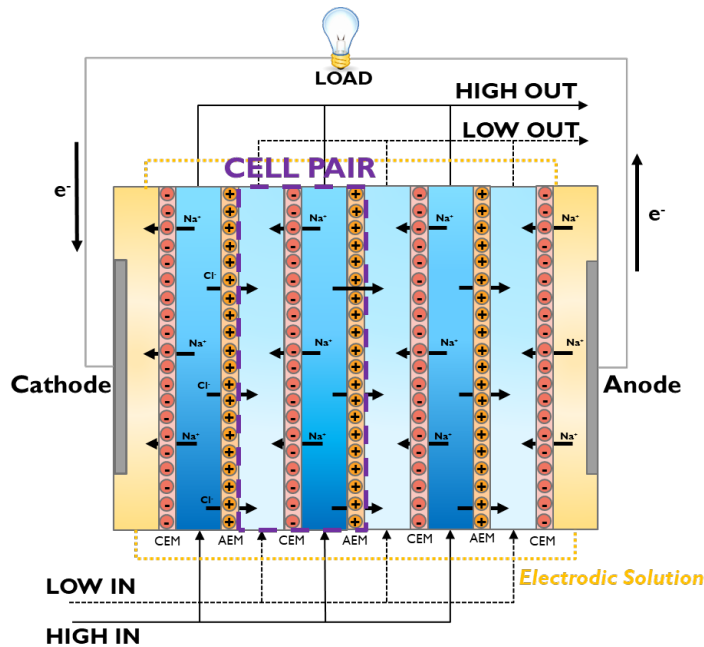


Figure 2.2. Schematic representation of a RED unit.

Conventional *RED* unit configuration consists of net spacers interposed between the membranes to generate the feed channels, maintaining fixed channel dimensions and promoting fluid dynamics enhancing the mass transfer. Common spacers are made by two arrays of polymeric wires either extruded (overlapped) or woven, with circular cross section,

though other geometries have been devised too [67–70]. Novel stack configurations adopt profiled membrane without the use of any spacer. In fact, in the case of profiled membrane, the surface contains “*membrane’s reliefs*” acting as the traditional spacers.

The standard geometry adopted in *RED* unit is plate-and-frame. A schematic representation of the unit is reported in *Figure 2.3*. Membranes and spacers or profiled membranes are piled up between two end plates. The sealing between each compartment is provided by the use of rubbery gaskets. The electrodic compartments, including electrodes and electrodic channels, are generally located in the end plates.

Co-current, counter-current and cross-flow arrangements can be used in *RED* units. In general, the counter-current arrangement gives higher driving force and thermodynamic yield (the ratio between the power generated and the maximum theoretical Gibbs power) than co-current but it might cause larger pressure difference between the two feed solutions, which may result in leakages and membrane deformations. In the case of the cross-flow arrangement, if the stack is symmetric, it performs in between co- and counter-current. However, a cross-flow stack allows for channel optimization as the channel length and width can be different.

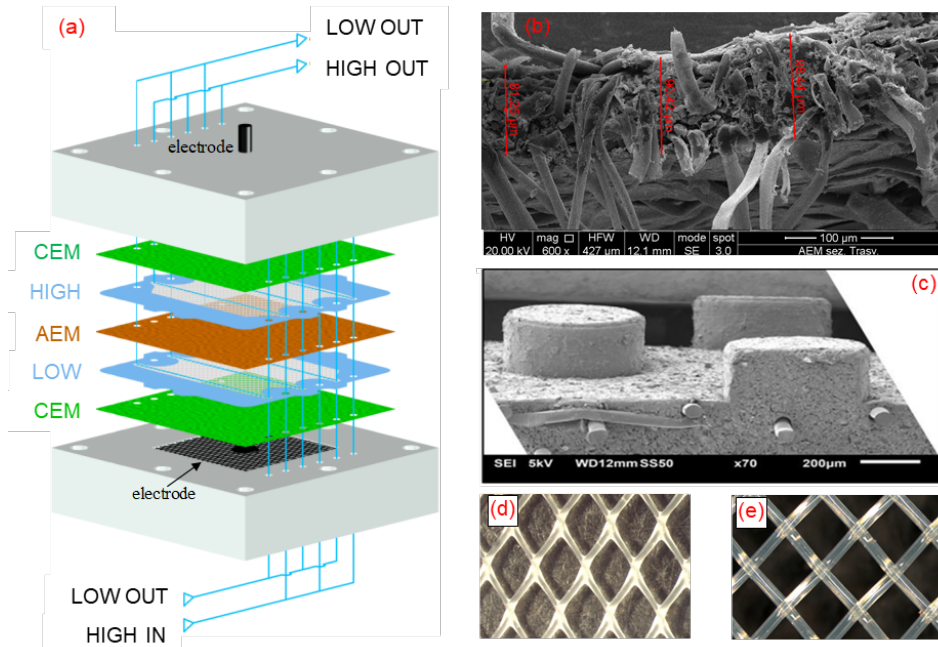


Figure 2.3 Schematic representation of a RED stack elements (a); Standard IEM membrane (Fujifilm® type III) (b) profiled membrane (c) Overlapped spacers (d); Woven (e)[71].

2.3.1 Ion exchange membranes

In the *RED* process, ionic exchange membranes play the key role. In general, a membrane is a selective barrier, which allows the passage of some components of a mixture and retains others. Ionic exchange membranes are a particular case of membranes, consisting in polymeric films where charged groups are attached. Based on the functionality of these charged groups (i.e. fixed basic or acidic dissociating groups), the membrane may result positively or negatively charged when it is immersed in water.

A cation exchange membrane contains negative fixed charges, thus allowing positive ions to pass through it and rejecting negative ions. Conversely, anion exchange membrane allows the passage of anions and rejects cations. The ions with same electrical charge of the IEM are called co-ions, while the ions with opposite electrical charge to the IEM are called counter-ions.

When an *IEM* permeable to a given ionic component is in contact with an electrolyte solution, an electrochemical equilibrium between the membrane and the adjacent solution is established, resulting in an electrical potential difference, i.e. the so-called *Donnan Potential* [72] given by:

$$\Delta\varphi_{Don} = \varphi^{IEM} - \varphi^{SOL} = \frac{1}{z_i F} \left[RT \ln \frac{a_i^{SOL}}{a_i^{IEM}} + \bar{V}_i \Delta\pi \right] \quad (2.4)$$

where φ^{IEM} is the electrical potential on the IEM side, φ^{SOL} is the electrical potential on the solution side, F is the Faraday constant, z is the charge number, R is the universal gas constant, T is the temperature, a is the activity of the ion, \bar{V} is the partial molar volume, $\Delta\pi$ is the osmotic pressure difference between the two phases. The subscript i refers to the salt ion i and the superscripts *IEM* and *SOL* represent the membrane and the solution respectively. The Donnan potential can be computed either from cations or anions according to [72]:

$$\Delta\varphi_{Don} = \frac{1}{z_i F} \left[RT \ln \frac{a_c^{SOL}}{a_c^{IEM}} + \bar{V}_i \Delta\pi \right] = \frac{1}{z_i F} \left[RT \ln \frac{a_a^{SOL}}{a_a^{IEM}} + \bar{V}_i \Delta\pi \right] \quad (2.5)$$

An ideal membrane completely excludes the co-ions in the membrane phase (*Donnan exclusion*), instead a real membrane has a certain co-ions concentration. At nanoscale level, the repulsion and attraction force between ions and ionic exchange membrane results in an electric double layer (*EDL*) at the solution-membrane interphase [73]. In fact, the

concentration of the counter-ions in the solution layer in contact to the membrane is larger than the co-ions one, while in the bulk of the solutions the co- and counter-ions concentrations is the same (electro-neutrality condition). The typical thickness of the *EDL* is in the order of Debye-length, i.e. few tens of nanometres.

A schematic representation of the ion concentration of a binary monovalent electrolyte and of the electrical potential within a membrane and two solution at different concentration are reported in *Figure 2.4*. The electrical potential consists of three terms, i.e. the two interphase potentials ($\Delta\varphi_{Don}^L$ on the left side and $\Delta\varphi_{Don}^R$ on the right side in *Figure 2.4*) and the *diffusion potential* arising from the concentration gradient within the membrane and from the different diffusivity of the two ions ($\Delta\varphi_{diff}$):

$$\Delta\varphi^{IEM} = \Delta\varphi_{Don}^L - \Delta\varphi_{Don}^R + \Delta\varphi_{diff} \quad (2.6)$$

The simplest expression of the membrane potential for a monovalent salt is given by [72]:

$$\Delta\varphi_{Don} = (2 t_{counter}^{IEM} - 1) \frac{RT}{F} \ln \frac{a^{SOL,R}}{a^{SOL,L}} \quad (2.7)$$

where $t_{counter}^{IEM}$ is the transport number of the counter-ion in the membrane, $a^{SOL,R}$ and $a^{SOL,L}$ are the activities in the right and left solutions, respectively .

As depicted in *Figure 2.4*, the transport of ions from the high-concentration (HIGH) solution to the low-concentration (LOW) solution generates a diffusion boundary layer (*DBL*). The thickness of the *DBL* depends on the channel thickness and on the mass transfer coefficient (or Sh number). Typical values are in the order of tens of micron. As a result, the solution concentrations at the membrane interphase ($C_{H,m}$ and $C_{L,m}$) are different from the bulk concentrations of the solution (i.e., $C_{H,b}$ and $C_{L,b}$) producing a reduction of the driving force (i.e. the concentration difference) of the process. These phenomena are often defined as *concentration polarisation*.

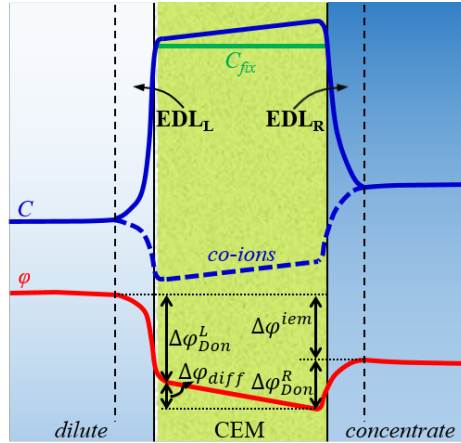


Figure 2.4. Schematic representation of the ion concentration of a binary monovalent electrolyte and of the electrical potential within a membrane and two solutions. The example in the picture shows a CEM immersed between a dilute solution and a concentrate solution. [71].

2.3.2 Membranes properties

The behaviour of *IEMs* is characterized by several properties related to physical and chemical aspects. The main properties that characterize the performances of *IEMs* are the (i) permselectivity, (ii) membrane resistance, (iii) water permeability and (iv) salt permeability.

2.3.2.1 Membrane permselectivity

The permselectivity is an important property that quantifies the *IEMs* selectivity towards the passage of either cations or anions, representing a measure of the *Donnan's* exclusion phenomena. In order to explain the permselectivity, it is appropriate to define the ion transport number, which gives the fraction of the total current transported by a certain ion, in formula:

$$T_i = \frac{z_i J_i}{\sum z_i J_i} \quad (2.8)$$

where z_i and J_i represent the valence and the molar flux of the generic i -th ion.

The permselectivity relates the difference between the transport number of the counter-ion in the membrane and in the solution to the transport number of the co-ion in the solution.

$$\alpha_{CEM} = \frac{T_c^{CEM} - T_c}{T_a} \quad (2.9)$$

$$\alpha_{AEM} = \frac{T_a^{AEM} - T_a}{T_c} \quad (2.10)$$

where T_i^{IEM} and T_i are the transport number of counter-ion inside the membrane phase and in the bulk of solution, respectively, while the subscript c and a refer to cations and anions.

The permselectivity tends to zero if the counter-ions have similar transport numbers into the membrane and solution. Generally, in the *IEMs*, the transport number of counter-ions into the membrane is larger than the one in solution, resulting in high permselectivity values.

The membrane permselectivity depends on the concentration of the fixed ions but also on the concentration of the high solution in contact to the membranes. When the concentration of the high solution is around 0.5M NaCl, typical α_{IEM} values of commercial membrane range between 80-99% [74]. Conversely, in applications with larger high solution concentrations permselectivity values decrease significantly, reaching values between 50-70% [59,64]. The permselectivity reduction due to the increase of the solution concentration can be explained by the increase of the co-ions concentration within the membrane required to guarantee the electro-neutrality condition, which reduces the transport number of counter-ions in the membrane.

Commonly, *IEM* permselectivity is evaluated through static membrane potential measurement [75]. This methodology is based on the measurement of the electrical potential arising at the two sides of an *IEM* placed between a concentrate and a dilute solution, (typical solution concentrations equal to 0.5 M and 0.05M, respectively). The permselectivity is evaluated as the ratio of the measured potential (ΔE_{exp}) and the theoretical value (ΔE_{theo}).

$$\Delta E_{theo} = \frac{RT}{z_i F} \ln \left(\frac{a_H}{a_L} \right) \quad (2.11)$$

2.3.2.2 Membrane electrical resistance

The electrical membrane resistance represents the opposition given by the membrane to the flowing of ions across it. It is usually expressed in the form of areal resistance ($\Omega \cdot \text{cm}^2$) referring to the active membrane area surface.

The membrane resistance strongly affects the performance (i.e. power output and efficiency) of the *RED* unit. In applications where low solution concentrations are considered (i.e. $C_H=0.6\text{M}$ and $C_L=0.02\text{M}$) the membrane resistance accounted for as much as 30% of the total

stack resistance while it is the dominant contribution in applications where high solution concentrations are considered (i.e. $C_H=4-5M$) [76].

The membrane resistance is influenced by a number of factors related to the membrane structure and solutions properties, mainly represented by: (i) charge density and cross-linking, (ii) ions mobility, (iii) solution concentrations, composition and temperature. Concerning membrane properties, high charge density and small cross-linking result in lower resistance. Lower *IEM* resistance is also given by solutions containing small hydrated ions, low ion valence and high ion concentration. According to [77] the conductance of *CEMs* decreases as function of cation type along the sequence $Li^+ < Na^+ < K^+ < H^+$.

The behaviour of membrane resistance with ions concentration can be explained according to the analysis proposed by [76,78–80]. The membrane resistance could be modelled as the sum of the resistance of two different contributions, representing two different domains: (1) membrane permeation regions with attached fixed charge and (ii) permeation regions without fixed charges (*Figure 2.5*). In domain 1, the membrane resistance is independent by the ionic concentration which is given by *Donnan*' equilibrium and electro-neutrality condition. While, in domain 2, membrane resistance is a function of the ion concentration, which is related to the bulk solution concentration. The membrane resistance is strongly increased when the solution concentration is decreased from concentration of 0.1-0.3M (i.e. the contribution of domain 2 prevails), while remain approximatively constant at higher concentration (i.e. the contribution of domain 1 on the membrane resistance prevails) [76,80].

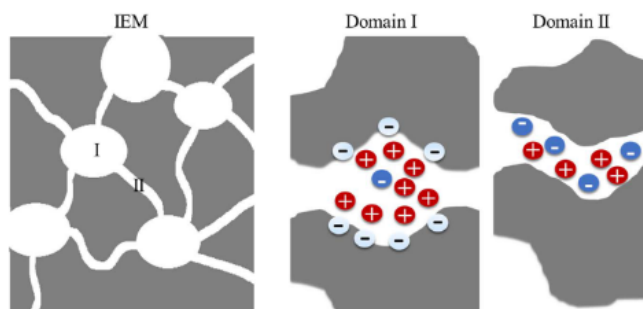


Figure 2.5. Schematic representation of the two domains in IEMs contributing to the resistance: the concentration- independent domain I and the concentration-dependent domain II [76].

Temperature has also a large influence on the membrane resistance value. In particular, an increase in operating temperature lead to large decreases on the membrane resistance as demonstrated by Benneker et al. [81].

The electric resistance of *IEMs* can be determined by direct current (*DC*) measurements or by applying alternating current (*AC*) conditions in a standard six-compartments cells [79] or using electrochemical impedance spectroscopy method [54] Typical values of *IEMs* electric resistance in standard conditions (i.e. 0.5M NaCl and 0.5M of Na₂SO₄ as electrodic solution, T=25°C) range between 0.5 and 4Ω cm². Some relevant data for *IEMs* commercially available are reported in ref. [74].

2.3.2.3 *Diffusive salt and water flux*

Ideal *IEMs* have a permselectivity equal to 100%. In this case, only counter-ions can move through it, while co-ions are rejected. In real *IEMs*, a small flux of co-ions is existing, reducing the permselectivity of the membrane and at the same time, resulting in an electroneutral diffusive flux of salt, given by the sum of a co- and a counter-ion, from the concentrate to the dilute solution across the membranes. This effect is more evident when highly concentrated solutions are considered.

A schematic representation of the fluxes involved in the *RED* process is reported in *Figure 2.6*. The dominant flux across each *IEM* is the flux of counter ions, while the flux of co-ions represents a small flux. This latter flux does not generate any ionic current, conversely is responsible of a loss of salinity gradient between the two solutions, reducing the efficiency of the process. The electroneutral diffusive salt flux represents a source of irreversibility and one of the “*uncontrolled mixing processes*” which consumes the salinity gradient without producing any beneficial effects (see *Chapter 3*).

The diffusive salt flux across each membrane can be calculated using an equation formally equal to the Fick’s law:

$$J_{diff} = \frac{P_{salt}}{\delta_m} [C_H - C_L] \quad (2.12)$$

where C_H and C_L are the concentrations of the two solutions at the membrane interface, δ_m is membrane thickness and P_{salt} is the salt permeability. Using the same approach adopted in [82], the permeability (P_{salt}) is the product of salt diffusion and sorption coefficient in membrane. The salt diffusion coefficient (or diffusivity) in the membrane accounts for the diffusion of the specie within the membrane, while the sorption coefficient describes the equilibrium of the specie concentration in the solution and in the membrane at the interphase.

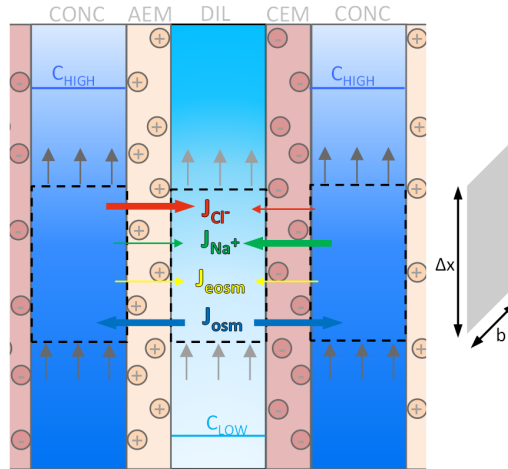


Figure 2.6. Schematic representation of the modelled fluxes across the IEMs

The other “*uncontrolled mixing process*” is the water flux across the membranes. The water flux is due to two different contributions: (i) the osmotic flux and (ii) the electro-osmotic flux.

The osmotic flux is produced from an osmotic pressure difference across the IEMs. The concentration difference between the membrane results in a difference of chemical potential of the water molecules in the two solutions, generating a flux of water from the dilute (higher water activity) to the concentrate (lower water activity), given by:

$$J_w = -vRTP_w(\phi_H m_H - \phi_L m_L) \quad (2.13)$$

where P_w is the average water permeability of the IEMs, ϕ the osmotic coefficient (*Chapter 4*), m the molal concentration, and v is the number of ions generated by the complete dissociation of the salt.

The electro-osmotic flux is due to the water molecules transported by the ions as first hydration shell. Assuming a certain number of water molecules in the first hydration shell (n_{hy}) of the ions, the electro-osmotic flux (J_{eosm}) is given by the product of the total salt flux (J_{salt}), i.e. the sum of diffusive and migrative fluxes (more details in section 2.5.2), by n_{hy} :

$$J_{eosm} = n_{hy} \cdot J_{salt} \quad (2.14)$$

2.4 Experimental

The main performance parameters in the reverse electro dialysis process are (i) the open circuit voltage (OCV) and (ii) the power density (P_d), this last defined as the power produced by the unit divided by the total membrane area (W/m^2_m) or by the cell pair area (W/m^2_{cp}). Both values can be measured from a *standard test*.

A typical experimental test rig consists of:

- two inlet and outlet tanks for each feed solutions;
- a tank for the electrodic solution (if normal electrodes are used);
- pumps for feeding the solutions in the *RED* unit (i.e. two feed solutions and eventually the electrolyte rinse solution);
- a variable external load;
- multimeters to measure electrical current and electrical potential generated by the *RED* unit;
- conductivity meters to measure the conductivity of inlet and outlet solutions;
- thermal bath to maintain a desired temperature within the unit.

The salt solutions are prepared dissolving fixed amounts of the salt into deionizer water. The electrodic solution is commonly prepared by dissolving in deionized water suitable salts containing redox couples, e.g. $K_3Fe(CN)_6$ and $K_4Fe(CN)_6 \cdot 3H_2O$, and adding a support salt.

In a standard test, the *RED* unit is powered by the feed solutions at fixed flow rates and connected to a variable external load. Starting from open circuit condition (*O.C.* or external resistance $\rightarrow\infty$), the resistance of the external load is gradually decreased until short-circuit condition (*S.C.* or resistance $\rightarrow 0$) is reached. As shown in *Figure 2.7-a* and *b*, when the stack operates in *O.C.* condition the maximum electrical potential is generated by the unit, the electrical current is zero and no electrical power is produced. Conversely, when the stack operates in *S.C.* the electrical current reaches the maximum value while the electrical potential is zero. The power output of the *RED* unit is again zero because it is consumed in the internal resistances. As shown in *Figure 2.7-a* and *b* the maximum power density is obtained when the external resistance is approximatively equal to the internal resistance of the *RED* unit, or when the electrical current equals half of the short-cut current (I_{sc}).

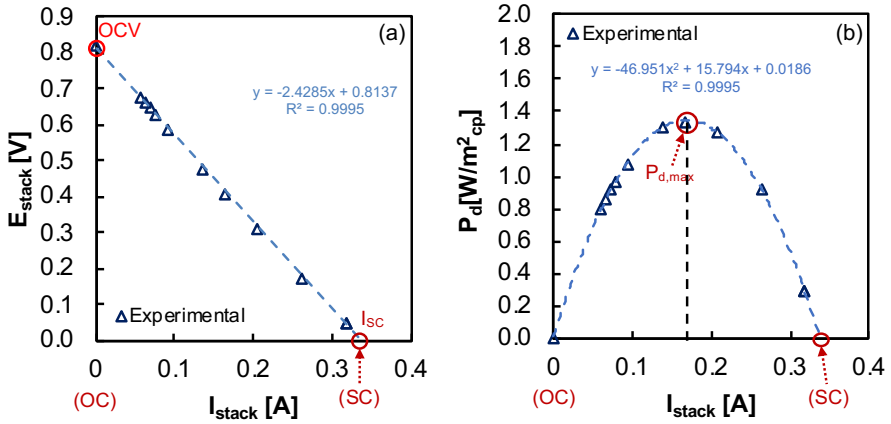


Figure 2.7. Electrical potential vs electrical current (A) and power density vs electrical current diagrams for a RED unit consists of 5 cps 0.1×0.1 m² fed by 2 M and 0.02 M Ammonium Bicarbonate solutions, channel flow velocities 3 cm/s. Fujifilm type 10 membranes

The electrical current and the electrical potential produced by the RED unit are related by Ohm's law:

$$I_{stack} = \frac{E_{stack}}{R_{ext}} \quad (2.15)$$

where E_{stack} is the electrical potential measured on the electrodes of the RED unit, I_{stack} is the electrical current generated by the RED unit and R_{ext} is the external resistance of the load connected to the RED electrodes.

The electrical potential of the RED unit may be evaluated as:

$$E_{stack} = OCV - R_{stack} \cdot I_{stack} \quad (2.16)$$

where OCV is the electrical voltage in open circuit condition and R_{stack} is the internal resistance of the stack, which accounts for the resistance of channels, membranes and electrodic compartments. The stack resistance is the slope of the curve electrical potential vs current. For small residence times (i.e. high solution flow rates), the relation between voltage and current is represented by a straight line, meaning that the resistance is approximatively constant in the unit, varying R_{ext} . In the case of large residence times, the concentration of the inlet/outlet solutions varies with R_{ext} producing a variation of the solution and membrane

resistances, and then of R_{stack} . Therefore, the relationship voltage/current deviated from the linear behaviour.

The electrical power generated by the RED unit (P_{RED}) is given by:

$$P_{RED} = E_{stack} \cdot I_{stack} \quad (2.17)$$

while the power density for unit of membrane area ($P_{d,m}$) and cell pair area ($P_{d,cp}$) are equal to:

$$P_{d,m} = \frac{P_{RED}}{2N_{cp} \cdot A_{cp}} \quad (2.18)$$

$$P_{d,cp} = \frac{P_{RED}}{N_{cp} \cdot A_{cp}} \quad (2.19)$$

where N_{cp} and A_{cp} are the number of cell pairs and the active area of one cell pair respectively. The factor 2 in the denominator of the $P_{d,m}$ denotes that each cell pair consists of two membranes.

2.4.1 Corrected Power density

The power output values evaluated using small laboratory-scale *RED* units, constituted by few cell pairs, are affected by the electrical resistance due to the electrodic compartments, the so-called blank resistance (R_{blank}). The influence of blank resistance is reduced increasing the number of cell pair and becomes negligible when N_{cp} is higher than 100 cps. In order to predict the power density of larger unit it is useful to define the so-called *corrected power density*.

The blank resistance can be evaluated using galvano-static measurements. A purposely-assembled *RED* unit with only one *CEM* plus the electrodic compartments is connected to a galvanostat, which provides a constant current and measures the corresponding electrical potential of the stack. The blank resistance is the slope of the curve electrical potential vs electrical current, as shown in *Figure 2.8*.

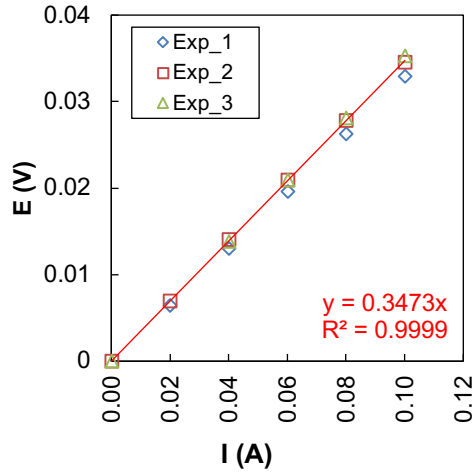


Figure 2.8. Blank resistance test using a galvanostatic measurement.

Therefore, the resistance associated to the cell pairs (R_{cells}) may be evaluated as:

$$R_{cells} = R_{stack} - R_{blank} \quad (2.20)$$

Then, the corrected stack voltage ($E_{stack,corr}$) is estimated removing the drop due to the blank resistance:

$$E_{stack,corr} = OCV - R_{cells} \cdot I_{stack,corr} \quad (2.21)$$

where $I_{stack,corr}$ is the corresponding corrected electrical current, computed as:

$$I_{stack,corr} = \frac{E_{stack,corr}}{R_{ext}} \quad (2.22)$$

Finally, the corrected power density ($P_{d,corr}$) is evaluated as:

$$P_{d,corr} = \frac{OCV^2}{N_{cp}A \cdot R_{ext} \left(1 + \frac{R_{cells}}{R_{ext}}\right)^2} \quad (2.23)$$

A comparison between actual and corrected results is reported in *Figure 2.9*.

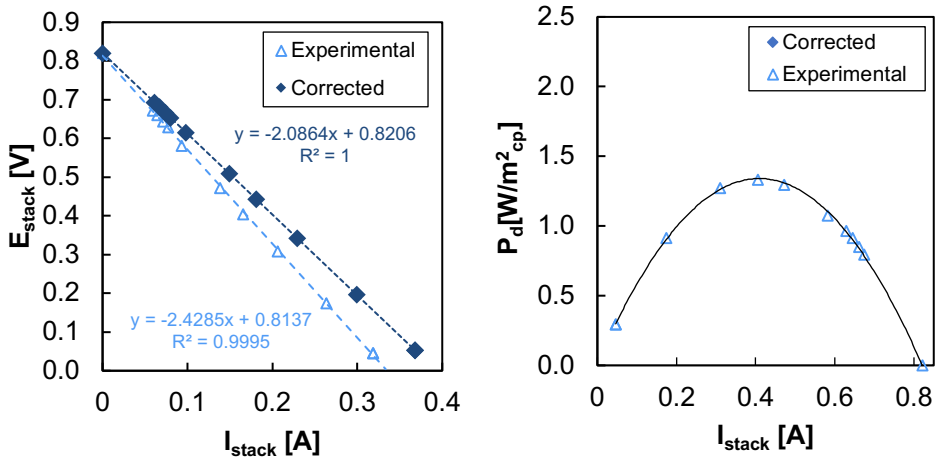


Figure 2.9. Comparison of actual values and corrected values for a RED unit consists of 5 cps $0.1 \times 0.1 \text{ m}^2$ fed by 2 M and 0.02 M Ammonium Bicarbonate solutions; channel flow velocities 3 cm/s. Fujifilm type 10 membranes

2.4.2 Average membrane permselectivity and resistances

The standard test can be used also to evaluate average membrane permselectivity and resistance. The term average refers to the fact that it is not possible to evaluate the contribution of each membrane, i.e. *CEM* and *AEM*, as in the methods reported in section 2.3.2.1 and 2.3.2.2 but an average value of the two membranes. The main advantage of this method in comparison is that the evaluated membrane properties refer to the real operating conditions in a *RED* unit, i.e. the membranes are in contact with two solutions at different concentration and in between spacers.

In particular, from the *OCV* value it is possible to evaluate the average membrane permselectivity (α_{av}), by comparing the experimental open circuit voltage (OCV_{exp}) with the one theoretically calculated (OCV_{theo}) considering $\alpha=1$, in formula:

$$\alpha_{av} = \frac{OCV_{exp}}{OCV_{theo}} \quad (2.24)$$

where the theoretical *OCV* is evaluated from Nernst's equation:

$$OCV_{th} = \frac{RT}{zF} \ln \left(\frac{m_{HYH}}{m_{LYL}} \right) \quad (2.25)$$

where m_H , m_L , γ_H and γ_L are the average molality and activity coefficients of the two solutions, R is the universal gas constant, T the absolute temperature ($T=298K$) and F the Faraday's constant.

Average membranes resistance can be also evaluated from the standard test. The cell pairs' resistance included (i) the channel resistance (R_{sol}) related to the spacers and solutions and (ii) the resistance of membranes (R_{IEM}).

The channel resistance (R_{sol}) depends on the geometrical features of spacers and the solution conductivity according to:

$$R_{sol} = f \frac{\delta_{sol}}{\Lambda_{sol} \cdot C_{sol}} \quad (2.26)$$

where δ is the spacer thickness, Λ and C are the average equivalent conductivity (see *Appendix A.1.2*) and molarity of the solution flowing in the channel, respectively, and f is the so-called obstruction factor representing a correction term which considers the increase of electrical resistance caused by the presence of the spacer (e.g. due to tortuosity of ion path or shadow effect on membranes). The subscript *sol* either indicates the concentrate (subscript *H*) or dilute (subscript *L*) compartment. The concentration in the above equation refer to the average concentration, inlet-outlet, in the *RED* unit.

The contribution of membranes on stack resistance is obtained, subtracting to the resistance of the cell pairs the channel resistance. Then, the average membrane resistance ($R_{IEM,av}$) is obtained dividing the global membrane resistance by the number of membranes involved in the *RED* unit (accounting both *AEM* and *CEM*), in formula:

$$R_{IEM,av} = \frac{R_{cps} - N_{cp}R_L - N_{cp}R_H}{2 N_{cp}} \quad (2.27)$$

The proposed methodology is affected by the influence of the polarisation phenomena involved in the process. In order to reduce their contribution, high channel velocities are adopted during the test.

The average permselectivity and membrane resistance of Fujifilm® type 10 membranes as a function of solution concentration in the case of NaCl (results provided by Fujifilm®) are reported in *Figure 2.10*, while the corresponding equations are reported in *eq.s 2.28-2.29*:

$$\alpha_{av}(x) = 0.987 - 0.0441 C_H(x) - 0.183 C_L(x) \quad (2.28)$$

$$R_{IEM,av}(x) = 0.487 C_H^2(x) - 2.81 C_H(x) + 7.21 - 0.14 C_L(x) \quad (2.29)$$

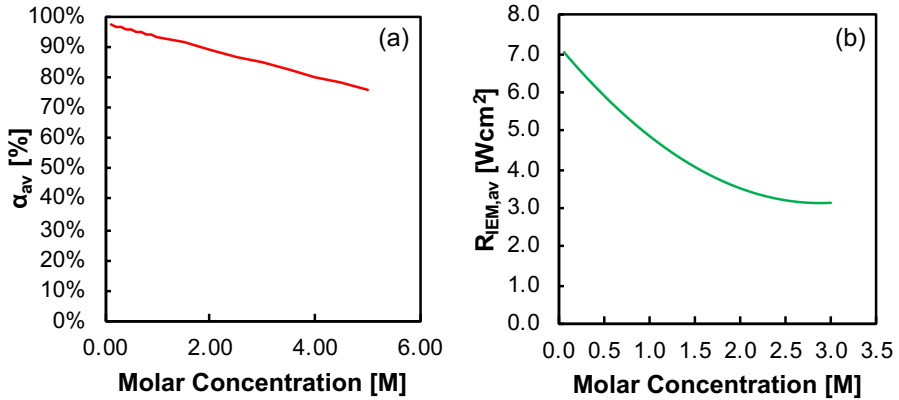


Figure 2.10. Average permselectivity (a) and IEM resistance (b) of type 10 Fujifilm[®] membranes as a function of the solution concentration for NaCl solutions

Figure 2.11 reports the average permselectivity and resistance of Fujifilm Type 10 membranes operating with ammonium bicarbonate solutions at different concentrations, obtained from experimental tests performed during an internship at Fujifilm (in September 2017). The permselectivity is a function of the concentration of the concentrate solution while it is practically independent by the dilute concentration. Conversely, average membrane resistance is heavily affected by the dilute solution concentration while it is not affected by the concentration of the concentrate.

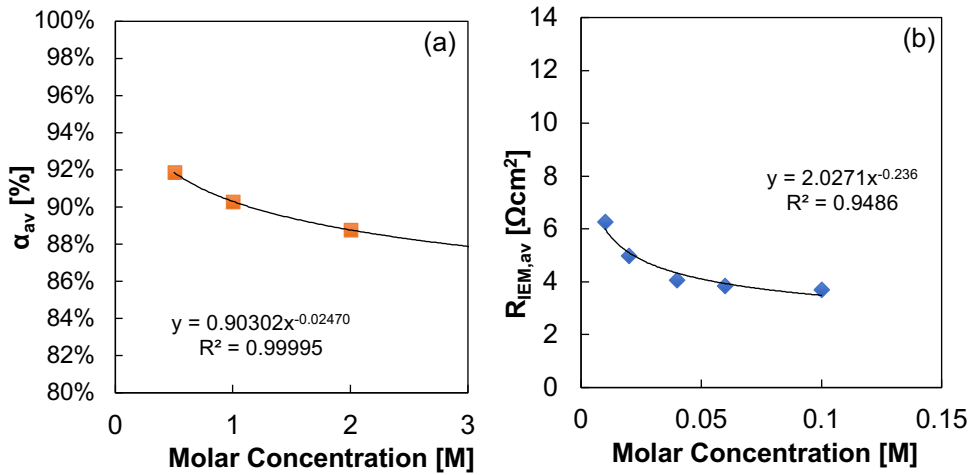


Figure 2.11. Average membrane permselectivity as function of the high solution concentration (a) and average membrane resistance as function of the low solution concentration (b). Results obtained using ammonium bicarbonate solution, channel velocities of 3 cm/s and average working temperature 20°C.

The average membrane resistance and permselectivity together with water and salt permeability, provided by *Fujifilm*, are used in the RED process model to predict the behaviour of real RED unit as explained in the following section.

2.5 Modelling Reverse Electrodialysis

This section describes the monodimensional semi-empirical mathematical model for the *RED* process developed, validated and used in this PhD thesis. The model is a steady-state model, which adopts a multi-scale modelling approach, considering two different scales of description: (a) a lower-scale model, describing the main phenomena involved in a single repeating unit (cell pair) and (b) a higher-scale model related to the whole system, including all cell pairs and the relevant interconnections. The RED process model, implemented in both Engineer Equation Solver[®] and Excel[®] describes all the main phenomena involved in the process, considering:

- (i) thermodynamic and electrical equations ;
- (ii) equations describing the transport phenomena through *IEMs*;
- (iii) differential mass balances discretized along the solution flow path, to take into account the concentration and flowrate variations along the channels;
- (iv) computational fluid dynamics correlations [52,83–87] to evaluate concentration polarisation and pressure drops;
- (v) experimental correlations to evaluate the properties of the *IEMs* as a function of the concentrations of the solutions as already discussed in the previous section;

In agreement with previous studies available in the literature [64,65], the present model is based on a few simplifying assumptions:

- a mono-dimensional approach was used to describe the system, considering the variation of the main variables (concentrations, electrical current, fluxes, resistances etc.) along the channel length (L) coinciding with the flow direction (both in co- and counter-current arrangement);
- all cell pairs operate in the same way, assuming an ideal flow distribution with no parasitic currents [64].

2.5.1 Equivalent circuit scheme and electrical equations

The equivalent circuit scheme of the *RED* unit is showed in *Figure 2.12-a*. The stack can be considered as consisting of N_k parallel branches where N_k is the number of intervals adopted for the numerical discretization of the domain along the flow direction (channel length). Each of them supplies part of the global current (I) circulating in the external circuit and consists

of N_{cp} (cell pair number) identical repetitive units connected in series. As shown *Figure 2.12-a*, each cell pair is divided in N_k elements of length Δx along the main flow direction ($\Delta x=L/N_k$). The generic k -th element is constituted of two electric voltage generators, one for each *IEM* (E_{CEM} and E_{AEM}), and four resistances, relevant to the solutions (R_H and R_L) and the *IEMs* (R_{CEM} and R_{AEM}) resistances. It is worth noting that the sketch in *Figure 2.12-b* is only a schematic representation of the phenomena involved in the cell pair.

Finally, *RED* equivalent is connected in series to an external branch, which indicates the resistance of the electrodic compartments R_{blank} and, eventually, closed by the external load resistance R_{ext} .

All the variables presented in this scheme will be described in details in the following paragraphs.

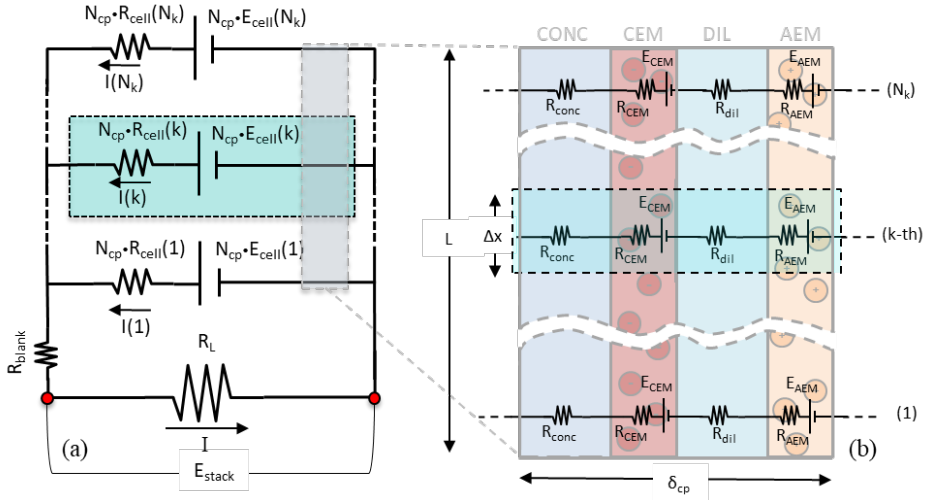


Figure 2.12. Equivalent electrical circuit scheme of the RED unit (a) and of an individual cell pair (b).

The voltage generated from each k^{th} element of cell pair (E_{cell}), is calculated by an equation formally similar to the *Nernst's* equation (eq. 2.30).

$$E_{cell}(k) = E_{CEM}(k) + E_{AEM}(k) = 2\alpha_{av}(k) \frac{RT}{zF} \ln \left(\theta_H(k) \theta_L(k) \frac{m_H(k) \cdot \gamma_H(k)}{m_L(k) \cdot \gamma_L(k)} \right) \quad (2.30)$$

which m_H , m_L , γ_H and γ_L are the molality and activity coefficients of the two solutions (i.e. concentrate and dilute) and α_{av} is the average permselectivity of the two *IEMs*, θ_H and θ_L are the polarisation coefficients which account for the concentration variation between the

channel bulk and the membrane surface (see *section 2.5.5*), R is the universal gas constant, T the absolute temperature ($T=298$ K) and F the Faraday's constant. The k^{th} internal resistance is made of 4 series resistances as reported in *eq. 2.31*.

$$R_{cell}(k) = [R_H(k) + R_L(k) + R_{CEM}(k) + R_{AEM}(k)] \cdot \frac{1}{\Delta x \cdot b} \quad (2.31)$$

where b is the width of the channel, $R_H(k)$ and $R_L(k)$ are the electrical resistances of feed compartments, while $R_{CEM}(k)$ and $R_{AEM}(k)$ are the *IEMs* resistances. The feed compartments resistance is calculated according to the discretized form of *eq. 2.26*:

$$R_{sol}(k) = f \frac{\delta_{sol}}{\Lambda_{sol}(i) \cdot C_{sol}(k)} \quad (2.32)$$

The solution specific conductivity is evaluated according to equation reported in *Appendix A.1.2*). The value of the obstruction factor of Deukum® spacers is reported in *Table 2.1*.

The electric current ($i(k)$) generated in each k^{th} branch of the circuit is calculated from *eq. 2.33*:

$$N_{cp} E_{cell}(k) = N_{cp} i(k) R_{cell}(k) + E_{stack} + R_{blank} I_{stack} \quad (2.33)$$

which can be rearranged into *eq. 2.34*:

$$i(k) = \frac{N_{cp} E_{cell}(k) - (E_{stack} + R_{blank} I_{stack})}{N_{cp} R_{cell}(k)} \quad (2.34)$$

where E_{stack} is the stack voltage, the electric potential measurable from the outside of the *RED* unit and R_{blank} is the resistance of the electrodic compartments. The electric current circulating on the external load is the sum of each one produced in the k^{th} branch (*Kirchhoff's junction rule*).

$$I_{stack} = \sum_k i(k) \quad (2.35)$$

The closing equation is obtained by the ohm-law on the external load (*eq. 2.35*).

$$E_{stack} = R_{ext} \cdot I_{stack} \quad (2.36)$$

The Gross power (P_{RED}) and gross power density (P_d) of the *RED* unit are calculated according to eq.s 2.37 and 2.38.

$$P_{RED} = E_{stack} \cdot I_{stack} \quad (2.37)$$

$$P_d = \frac{P_{RED}}{N_{cp} \cdot A_{cp}} \quad (2.38)$$

where A_{cp} is the membrane area of a cell pair. The maximum power density ($P_{d,max}$) is the power density of a *RED* unit connected to an external load which maximize the power generation.

The ohmic loss due to the internal resistance of the *RED* unit is calculated according to eq. 2.39

$$P_{loss} = \sum_k R_{cell}(k) \cdot i(k)^2 + r_{blank} I_{stack}^2 \quad (2.39)$$

The net specific energy (SE) for unit of limiting stream obtained from the *RED* unit is defined as the ratio of the *RED* power (gross or net) divided by the limiting flow rate:

$$SE = \frac{P_{RED}}{\dot{V}_{lim}} \quad (2.40)$$

Finally, the ratio between SE and the SME is the thermodynamic yield of the process:

$$Y = \frac{SE}{SME} \quad (2.41)$$

2.5.2 Water and salt flux through the IEMs

The salinity gradient across each membrane is responsible also of some detrimental effects producing *uncontrolled mixing phenomena*, which reduce the driving force of the process, generally identified with water flux (J_w) and salt flux (J_{sali}). In *Figure 2.6* a schematic representation of fluxes across the *IEMs* was already provided.

Due to non-ideality of the membranes ($\alpha_{av} \neq 1$), few co-ions pass through the *IEMs* resulting in a diffusive flux of salt. The total salt flux from the two contiguous concentrate channels to the dilute one is described by eq. 2.42.

$$J_{salt}(k) = J_{mig}(k) + J_{diff}(k) = \frac{i(k)}{zF} + 2 \frac{P_{salt}}{\delta_m} [C_H(k) - C_L(k)] \quad (2.42)$$

where i is the current density or the current for unit of membrane area, δ_m is membrane thickness (assumed equal for both *IEMs* and value reported in *Table 2.1*) and P_s is the salt permeability (assumed equal for both *IEMs* membranes see *section 2.4.2*). Using the same approach adopted in [82], the permeability (P_{salt}) is the product of salt diffusion and sorption coefficient in membrane.

In eq. 2.42, the first term, the *migrative flux* (J_{mig}), gives the salt transferred with the counter-ions migration through the *AEM* and the *CEM*, while, the second term, the *diffusive flux* (J_{salt}), refers to the salt flux due to the diffusion of co-ions. Factor 2 multiplying the second term considers the presence of two *IEMs* in contact with the dilute channel.

As already explained in *section 2.3.2.3*, also the water flux consists of two terms (eq. 2.43). The first named (i) *osmotic flux* is generated by the osmotic pressure difference between the two solutions and directed from the dilute to the concentrate chamber. The second named (ii) *electro-osmotic flux* is due to the water molecules transported in the solvation shell of the ions and directed in opposite direction. In formula:

$$\begin{aligned} J_w(k) &= J_{osm}(k) + J_{osm}(k) = \\ &= -2 \nu RTP_w [m_H(k)\phi_H(k) - m_L(k)\phi_L(k)] + n \cdot J_s(k) \end{aligned} \quad (2.43)$$

where P_w is the average water permeability of the *IEMs* (value reported in *Table 2.1* for *Fujifilm type 10* membranes), ϕ the osmotic coefficient and n the hydration number for Na^+ and Cl^- . The hydration number was fixed equal to 7 according to [64]. From eq. 2.43 a volumetric water flux is calculated (m/s).

2.5.3 Salt and Global Mass Balances

For each computational domain element, considering a co-current flow arrangement, salt mass balance and global mass balance equations in each compartment (dilute and concentrate)

are applied to calculate the exiting concentration and flow rate. These are adopted as inlet conditions of the following element, thus solving the system of equations and characterizing concentration and flow-rate profiles along the entire channel length.

In particular, for the concentrate channel, the salt mass balance and the global mass balance can be written as in *eq.s 2.44 and 2.45*:

$$C_H(k+1) \cdot \dot{V}_H(k+1) = C_H(k) \cdot \dot{V}_H(k) - J_{salt}(k) b \Delta x \quad (2.44)$$

$$\begin{aligned} \rho_H(k+1) \cdot \dot{V}_H(k+1) &= \\ &= \rho_H(k) \cdot \dot{V}_H(k) - J_w(k) \cdot b \Delta x \frac{\rho_w}{M_w} - J_{salt}(k) \cdot b \Delta x M_{salt} \end{aligned} \quad (2.45)$$

where ρ_H is the high solution density (see *Appendix A.1.1*), and ρ_w the density of pure water equal to 997 kg/m³ at 298.15 K, $C_H(k+1) \cdot \dot{V}_H(k+1) = C_{H,out}(k) \cdot \dot{V}_{H,out}(k)$ is the product of outlet concentration and flow-rate of the exiting concentrate solution (i.e. the salt molar flow rate), while $C_H(k) \cdot \dot{V}_H(k) = C_{H,in}(k) \cdot \dot{V}_{H,in}(k)$ is the product of concentration and flow-rate of the concentrate inlet solution.

In a similar way, for the dilute channel, *eq.s 2.46 and 2.47* are obtained:

$$C_L(k+1) \cdot \dot{V}_L(k+1) = C_L(k) \cdot \dot{V}_L(k) + J_{salt}(k) b \Delta x \quad (2.46)$$

$$\begin{aligned} \rho_L(k+1) \cdot \dot{V}_L(k+1) &= \\ &= \rho_L(k) \cdot \dot{V}_L(k) + J_w(k) \cdot b \Delta x \rho_w + J_{salt}(k) \cdot b \Delta x M_{salt} \end{aligned} \quad (2.47)$$

When a counter-current arrangement is considered, the mass balances are formally the same, though the inlet-outlet flow-rate terms in the dilute channel mass balance have the opposite sign:

$$C_L(k) \cdot \dot{V}_L(k) = C_L(k+1) \cdot \dot{V}_L(k+1) + J_{salt}(k) b \Delta x \quad (2.48)$$

$$\begin{aligned} \rho_L(k) \cdot \dot{V}_L(k) &= \\ &= \rho_L(k+1) \cdot \dot{V}_L(k+1) + J_w(k) \cdot b\Delta x \rho_w + J_{salt}(k) \cdot b\Delta x M_{salt} \end{aligned} \quad (2.49)$$

where ρ_L is the low solution density, $C_L(k+1) \cdot \dot{V}_L(k+1) = C_{L,in}(k) \cdot \dot{V}_{L,in}(k)$ is the product of dilute inlet concentration and dilute inlet flow-rate, while $C_L(k) \cdot \dot{V}_L(k) = C_{L,out}(k) \cdot \dot{V}_{L,out}(k)$, is the product of dilute outlet concentration and flow-rate.

The solution flow-rates feed to the pile were selected imposing an inlet velocity of 1 cm/s within the channel, typical values adopted in *RED* systems [88].

2.5.4 Membranes properties

The *IEMs* behaviour is characterized by means of several properties already presented in the previous sections. The most relevant properties are the *permselectivity* (α_{AEM} or α_{CEM}), which identifies the selectivity of membrane to the passage of counter ions and rejections of co-ions, and *electrical resistance* (R_{AEM} or R_{CEM}). Other important features are the *water* and *salt permeability* (P_w and P_s), which generate the osmotic water flux and diffusive salt flux, respectively. Manufacturers usually provide the values of these properties in reference conditions. Average membrane properties can be evaluated as already explained in *section 2.4.2*.

In this work, Fujifilm type 10 membranes were considered. Constant values of water and salt permeability, were considered (value reported in *Table 2.1*), while concentration dependent correlations were experimental obtained and implemented in the model in order to describe the membrane resistance and permselectivity for each specific salt solution (see *section 2.4.2*)

2.5.5 Polarisation coefficients

The transport of ions through the membrane causes alterations of concentration at the membrane-solution interface with respect to the bulk of the solution, leading to a concentration difference between bulk and interface, resulting in the so called “*polarisation phenomena*”. In particular, in the case of the *RED* process, the transport of ions from the concentrate channel to the dilute channel leads to a reduction of the salt concentration at the membrane interface on the *HIGH*-side and an increase of the salt concentration at the

membrane interphase on the LOW-side of each membrane . The overall effect is a reduction of the available driving force across the IEMs, which can be quantified introducing “polarisation coefficients”, which are defined as in the following [89]:

$$\theta_H(k) = \frac{C_{H,m}(k)}{C_{H,b}(k)} = 1 - \frac{2J_{tot}(k)\delta_H}{C_H(k)D_H(k)Sh_H(k)} \quad (2.50)$$

$$\theta_L(k) = \frac{C_{L,b}(k)}{C_{L,m}(k)} = \left(1 + \frac{2J_{tot}(k)\delta_L}{C_L(k)D_L(k)Sh_L(k)} \right)^{-1} \quad (2.51)$$

where D_H and D_L are the Diffusivity of dilute and concentrate (see *Appendix A.1.4*); J_{tot} is the global salt flux across the *IEMs* membrane, δ_L and δ_H the spacers thickness, Sh_H and Sh_L are the numbers of *Sherwood* of concentrate and dilute in the k^{th} element. The equations 2.50 and 2.51 are derived by applying the film theory in the diffusion boundary layer, as reported in references [89–92].

The *Sh* number is evaluated using dimensionless correlations obtained from Computational Fluid Dynamics (*CFD*) simulations as function of *Re*, *Sc* and spacer type [84,86]. For *Deukum*[®] spacer *Sh* numbers are evaluated as:

$$\begin{aligned} Sh(k) = & \\ & (-1.481 \cdot 10^{-7} Re(k)^5 + 3.739 \cdot 10^{-5} Re(k)^4 - 3.253 \cdot 10^{-3} Re(k)^3 + \\ & + 1.117 \cdot 10^{-1} Re(k)^2 + 1.34 \cdot 10^{-1} Re(k) + 6.954) \left(\frac{Sc(k)}{Sc_{ref}(k)} \right)^{0.5} \end{aligned} \quad (2.52)$$

where Sc_{ref} is the *Schmidt* number of the reference solution, i.e., NaCl solution at 25°C, 1 atm and 0.017 M.

From *eq.s 2.50* and *2.51*, the actual concentrations of dilute and concentrate at membrane interface for each calculation element are evaluated. These concentrations are used in the Nernst’s equation and in the equations of water and salt fluxes to evaluate the real stack performance, considering the effect of polarisation phenomena.

2.5.6 Pressure drops, Pumping power & Net Power

The pressure drops in each k^{th} calculation element are evaluated according to the following equation:

$$\Delta p(k) = \frac{1}{2} \frac{\Delta x}{D_{eq}} f_{Darcy}(k) \rho_{av}(k) v_{av}(k)^2 \quad (2.53)$$

where D_{eq} is equivalent diameter (i.e. 2 times the spacer thickness δ), ρ_{av} and u_{av} are the average velocity and density of the solution in the generic k^{th} calculation element, Δx the length of the discretization element, f_{Darcy} is the friction factor. The friction factor values for a specific spacer is obtained from *CFD* simulations as function of the *Re* number as reported in [84,86]. Fitting the *CFD* results suitable correlations of f_{Darcy} as function of the *Re* number is obtained.

$$f_{Darcy}(k) = (5.711 \cdot 10^{-5} \text{Re}(k)^2 + 2.640 \cdot 10^{-2} \text{Re}(k) + 6.600) \cdot \frac{96}{\text{Re}(k)} \quad (2.54)$$

The global pumping power ($P_{pumping}$) within the stack is obtained as sum of the product of the element pressure drop for the element flow rate for dilute and concentrate, divided by the pump efficiency ($\eta_p=0.8$). In formula:

$$P_{pumping} = \frac{1}{\eta_p} \sum_k^{N_k} \Delta p(k)_H \dot{V}_H(k) + \sum_k^{N_k} \Delta p(k)_L \dot{V}_L(k) \quad (2.55)$$

Then, the net power ($P_{RED,net}$) and net power density ($P_{d,net}$) of the *RED* unit are calculated according to eq.s 2.56 and 2.57

$$P_{RED,net} = P_{RED} - P_{pumping} \quad (2.56)$$

$$P_{d,net} = \frac{P_{RED,net}}{N_{cp} \cdot A_{cp}} \quad (2.57)$$

2.5.7 Numerical details

The RED process model was implemented in both *Engineer Equation Solver*[®] (EES) and *Excel*[®], using the Euler's method to solve the mass balance equations. In this method, the numerical accuracy of the solution depends on the discretization length (Δx), which is a function of N_k and L . In order to identify the N_k value that gives a good compromise in accuracy and time calculation, a grid dependence analysis was performed, considering a RED unit with a length of 1 meter (longer RED unit considered in this thesis). As shown in *Figure 2.13*, the grid dependence analysis indicates that a discretization length of 2.5 cm (i.e. 40 elements) is small enough to get stable and accurate solutions. Further, passing from 40 to 50 discretization intervals the power output varies less than 1% and concentration profiles are practically overlapped.

Table 2.1 Physical and geometrical parameters assigned for simulations

Parameter	Value
$P_w^{(1)}$ [m/(Pa·s)]	$2.22 \cdot 10^{-14}$
δ_m [m]	$1.25 \cdot 10^{-4}$
P_{salt} [m ² /s]	$1.4 \cdot 52 \cdot 10^{-12}$
f [-]	1.5625

⁽¹⁾experimental values measured @ ref. conditions: $T=25^\circ\text{C}$, $C_{conc}=3\text{ M}$, $C_{dil}=0.05\text{ M}$ NaCl solution (Fujifilm).

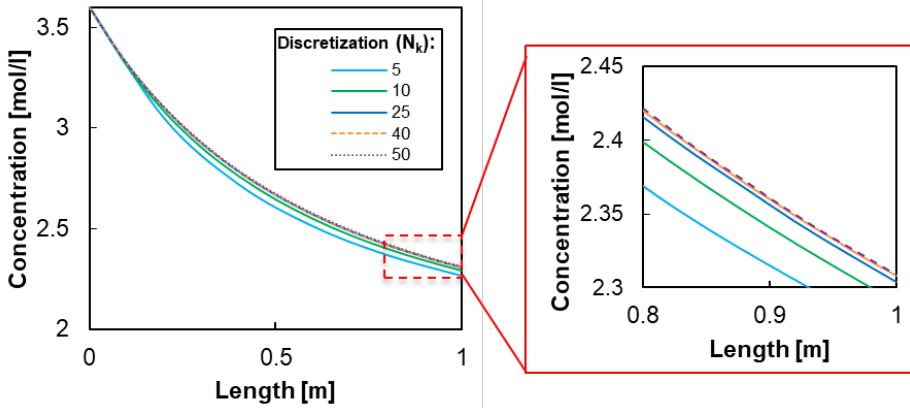


Figure 2.13. Grid dependence analysis: concentration profiles along the channel varying the number of grid elements (N_k). RED stack of 1000 cell pairs $0.1\text{ m} \times 1.0\text{ m}$, $v_H=v_L=1\text{ cm}\cdot\text{s}^{-1}$, $C_H=3.6\text{ M}$, $C_L=0.05\text{ M}$.

2.5.8 RED process model validation

The mono-dimensional *RED* model was validated by comparison with experimental results reported in the literature [93] but also novel experimental results. *Figure 2.14.a* and *b* show the trend of experimental stack voltages and power densities for three different concentrate concentrations (i.e. 0.5, 2 and 5M) as a function of the current and the stack voltage for a small-size *RED* unit (5 cell pairs $0.1 \times 0.1 \text{ m}^2$).

The model predictions fit very well experimental trends, thus indicating the reliability of the model in the investigated concentration range. The maximum deviation between predicted power density and the experimental results is around 15%.

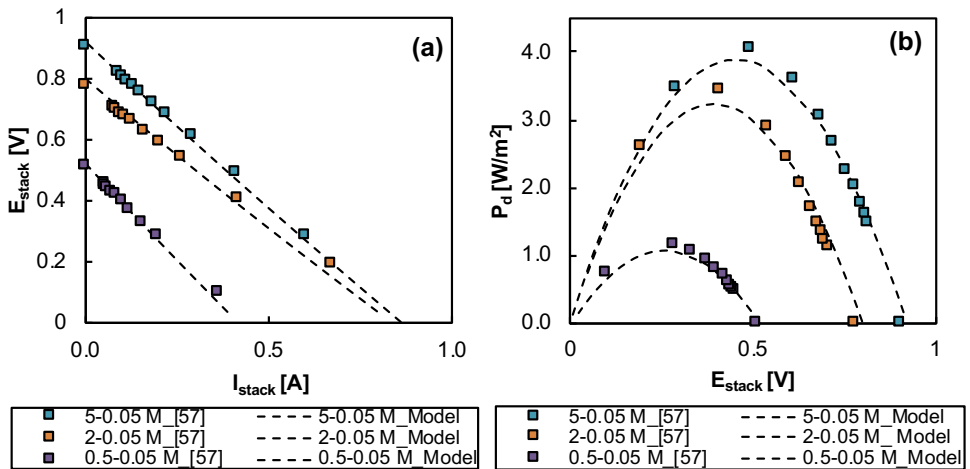


Figure 2.14. Comparison between experimental trends and model predictions for (a) stack potential and (b) power density [93]. Operating conditions: 5 cell pairs-stack, $A=0.1 \times 0.1 \text{ m}^2$; $C_L=0.05 \text{ M}$; $C_H=0.5 \text{ M}, 2 \text{ M}, 5 \text{ M}$; $v_L=v_H=2 \text{ cm/s}$, $T=25^\circ\text{C}$.

Model was further validated with different flow velocities and stack dimensions, resulting always in a good agreement between predictions and experiments.

A comparison of experimental and simulation results obtained using longer *RED* unit (50 cell pair $0.1 \times 0.44 \text{ m}^2$ equipped with Fujifilm® type 10 membranes) is reported in *Figure 2.15* for the case of NaCl solutions and in *Figure 2.16* for the case of ammonium bicarbonate solutions. In particular *Figure 2.15 a-d* shows the comparison of experimental result and model predictions of NaCl solutions 3M-0.05M for two different velocity 0.5 cm/s and 1 cm/s, while *Figure 2.16* report the same comparison for ammonium bicarbonate-water solutions considering a velocity of 0.5 cm/s and two different solution concentrations 0.5M-0.05M and 1.0M-0.05M. The membrane properties adopted in the RED process models are reported

Figure 2.15. In all the investigated conditions, always a good agreement between model predictions and experimental results was found, validating the model. The deviation between calculated power density and experimental value is lower than 10%.

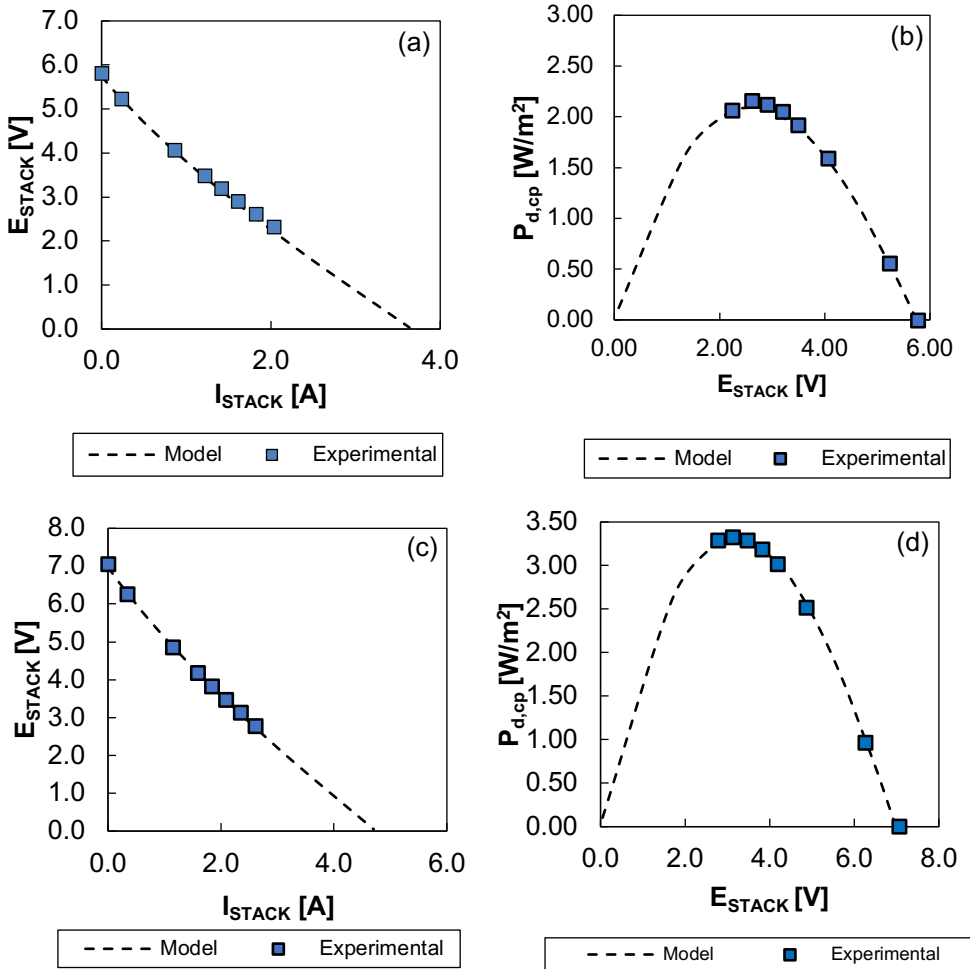


Figure 2.15. Power density and Electrical potential from RED unit fed by 3M and 0.05 NaCl solutions at 0.5 cm/s (a-b) and 1 cm/s (c-d). RED unit 50 cell pairs 0.1×0.44 m².

Table 2.2 Average Fujifilm type 10 membrane properties used in the simulation for NaCl solutions at 3 M -0.05 M.

α_{av}	$R_{IEM,av}$	P_{salt}	P_w
[%]	[Ωm^2]	[m/s]	[ml/(h bar m ²)]
88	$3 \cdot 10^{-4}$	$4.5 \cdot 10^{-12}$	8

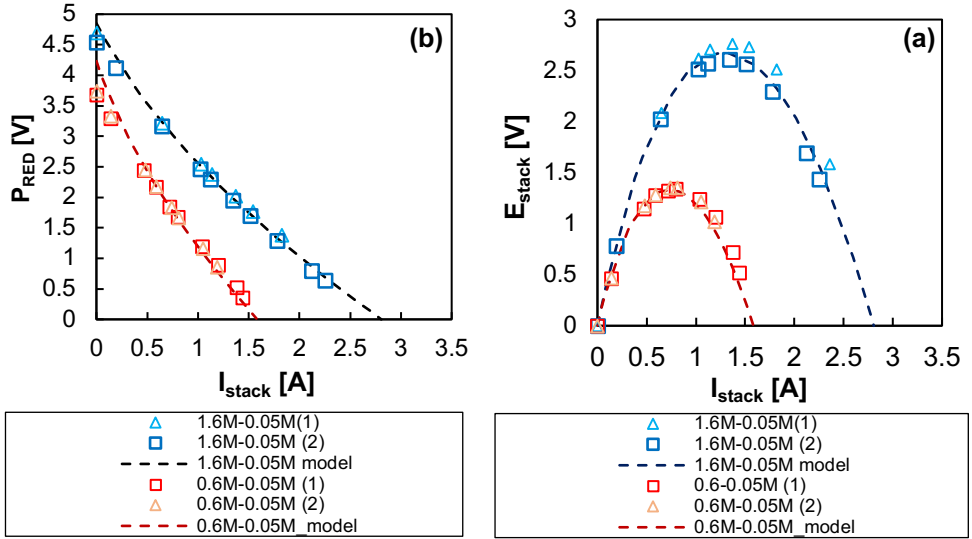


Figure 2.16 Power density and Electrical potential from RED unit fed by ammonium bicarbonate solutions at 0.5 cm/s, concentrations: (a-b) 0.6 M -0.05 M and (c-d) 1.6 M-0.05M. RED unit 50 cell pairs 0.1x0.44 m². (UNIPA)

Table 2.3 E1 membrane properties using NH₄HCO₃ at 0.6M-0.05 M.

α_{av}	$R_{IEM,av}$	P_{salt}	P_w
[%]	[Ωm^2]	[m/s]	[ml/(h bar m ²)]
91	$3.5 \cdot 10^{-4}$	$4.5 \cdot 10^{-12}$	6

Conclusions

In this chapter, an overview of the *RED* process was presented, including the description of the experimental lab-scale unit with typical experimental tests. Results from experimental campaigns were used as reference data for model validation and to obtain average permselectivities and resistances of Fujifilm *IEMs*, for two different salts, i.e. NaCl and NH_4HCO_3 .

A multi-scale *RED* process model was developed, using a mono-dimensional approach to take in to account the variation of solution properties along the flow-directions. All the main phenomena involved in the process were considered, including salt and water flux, pressure drops and polarisation phenomena. The mathematical model was extendedly validated by comparison with experimental results in different operating conditions and using different stack configurations.

3

PERFORMANCE ANALYSIS OF THE RED PROCESS

Chapter Outline

ABSTRACT	63
3.1 EXERGY ANALYSIS OF RED.....	64
3.1.1 EXERGY ANALYSIS EQUATIONS	68
3.2 RESULTS AND DISCUSSION	70
3.2.1 EFFECT OF THE IRREVERSIBILITY SOURCE.....	71
3.2.2 EFFECT OF MEMBRANE PROPERTIES.....	74
3.2.3 EFFECT OF CONCENTRATE AND DILUTE CONCENTRATIONS	75
3.2.4 EFFECT OF FLOW ARRANGEMENT AND CELL PAIR LENGTH.....	77
3.2.5 EFFECT OF FEED VELOCITY	78
3.3 POTENTIAL APPLICATIONS OF RED IN REAL ENVIRONMENTS.....	80
3.3.1 RED UNIT POTENTIALS	82
3.4 CONCLUSIONS.....	87

Part of this chapter has been published as:

F. Giacalone, P. Catrini, A. Tamburini, A. Cipollina, A. Piacentino, G. Micale, Exergy analysis of reverse electrodialysis, Energy Conversion and Management 164, 588-602.

F. Giacalone, A. Tamburini, M. Papapetrou, A. Cipollina, G. Micale, "Reverse Electrodialysis: Applications to Different Case Studies", IEEE proceeding 2018, 10.1109/EEEIC.2018.8493961.

Paper in-preparation:

F. Giacalone, A. Tamburini, M. Papapetrou, A. Cipollina, G. Micale, "Techno-economic evaluation of reverse electrodialysis process in different real environments".

Abstract

The RED process model presented in the previous chapter is here used to carry out performance analyses on the RED process.

An original exergy analysis of the RED process fed by NaCl solutions is illustrated. In particular, a rigorous exergy model is introduced in order to highlight the effect of non-ideal behaviour of the IEMs on the performance of the RED process. All the irreversibility sources are investigated considering real membrane properties provided by Fujifilm®. In addition, the effect of the main operating conditions, i.e. solution concentrations and residence times are analysed.

For the first time, results have highlighted that water and salt fluxes strongly reduce the exergy efficiency of the unit.

Furthermore, potential applications of open-loop RED units in real environments are also investigated. The validated RED model presented in the previous chapter is used to estimate the amount of electric energy that can be harvested from real salinity gradients. Different scenarios existing in different parts of the world are investigated. For each scenario, the potentials in terms of Gibbs free energy of mixing, power density and yield are evaluated considering the real availability of each stream.

3.1 Exergy analysis of RED

Salinity gradients are available from (i) natural resources or industrial/human activities worldwide distributed or (ii) artificial solutions ad-hoc prepared. The first category is more suitable in *open-loop* applications, where the available salinity gradient from salt-water solutions is used to produce electricity and subsequently the “exhausted solutions” are released again in the environments. Conversely, in *closed-loop* applications, the possibility to select an artificial ad-hoc saline solution to enhance the overall performance of the integrated process represented one of the big advantages of such technology.

While in open-loop *RED* applications the process yield (i.e. how much energy is generated from the available salinity gradient) is the most important parameter, in closed-loop applications the efficiency of salinity gradient conversion dominates the overall process efficiency. In fact, only a part of the available salinity gradient is reversibly converted into electricity, while the remaining is dissipated without producing energy, yet requiring additional effort in the regeneration stage. With this respect, exergy analysis can be very useful to drive stack design and identify optimal operating conditions.

Exergy analysis represents a powerful method to identify the main sources of energy loss and quantify how much energy is effectively converted within a process.

Kotas in 1985 [94] defined the exergy of a system as “*the maximum amount of work obtainable when it evolves from its thermodynamic state to the thermomechanical and chemical equilibrium with the environment through reversible processes involving mass and heat transfer between the system and the environment*”. Differently from energy, exergy is destroyed in real systems operation due to irreversible phenomena like heat exchange, uncontrolled mixing, friction or chemical reactions [94]. The assessment of exergy destruction due to irreversibility occurring within each component of a cycle provides fundamental information on the main limiting factors of the entire cycle, identifying possible design and operative improvements, in order to achieve profitable energy conversion and/or savings [95].

In scientific literature, exergy analysis has been extensively applied to the study of several “energy systems” performance. Sun et al. [15] carried out an exergy analysis to support Organic Rankine Cycle (ORC) systems design. Ranjbar applied the energy and exergy analysis (method) to the design of a novel trigeneration system based on a solid oxide fuel cell [96]. Other researches have been focused on cryogenic process as natural gas liquefaction [97], energy recovery in natural gas compressor station [98] and steam power plant [99], air

treatment for heating, ventilation, air conditioning systems [100] and the design of controllers in refrigeration system [101]. Exergy analysis has been also applied to membrane [102,103] and thermal [104,105] desalination processes. Conventional exergy analysis identifies and quantifies irreversibility sources, though it does not allow to evaluate the economic and environmental benefits that may arise by their reductions [106]. To this aim, more complex and refined exergy-based approaches have been proposed during these years. For instance, thermo-economics [107] combines exergy analysis with economic principles to provide criteria for costs allocation in energy system [108] or for optimization of the design and operation of energy systems [109] and to support diagnosis malfunction in thermal energy systems [110]. Exergy can also be used to assess the quality and the consumption of natural resources burdening a given product [111]. To this aim, Cornelissen et al. [112] combine exergy analysis with Life Cycle Assessment framework, i.e. Exergy Life Cycle Assessment (*ELCA*), to evaluate the usage of non-renewable exergy occurring along the entire life of a product. A further evolution of the ELCA approach was presented in [113] and integrates the well-known Input-Output analysis into ELCA, through the use of the Monetary Input Output Tables of national economies. An example of application of this alternative approach is presented in 2016 by Rocco et al. [114], who assessed the primary non-renewable exergy embodied in electricity produced by a Waste-to-Energy power plant operating in the Italian context.

In a *RED* process, exergy variations of the feed streams occur due to the variation in solutions composition within the unit. Only if the process is operated reversibly, exergy would be entirely converted into electric power. In real cases, some detrimental phenomena inevitably occur there by contributing to reduce the exergy performance of *RED* units. Irreversibility sources involved in the *RED* process are summarized in *Table 3.1*.

The non-ideal behaviour of *IEMs* is responsible for *uncontrolled mixing effects* (i.e. water and salt diffusion), which reduce part of the available driving force, consuming part of the exergy content of the inlet streams without producing electrical power. Non-ideal *IEMs* permselectivity also affects the generated electromotive force, which is reduced with non-unitary permselectivity. Furthermore, membrane and solution resistances are also significant causes of exergy destruction (i.e. internal ohmic losses). Other sources of irreversibility are the friction losses inside the channels, the activation losses in the electrodic compartments and the parasitic currents in the distribution manifolds. However, friction losses are dramatically dependent on channels configuration (not considered in this study) and the latter

two losses have a minor role in the overall process exergy performance and have been thus neglected in the present work.

Table 3.1 Description of the irreversibility sources involved in the RED process.

Irreversibility source	Description
Permselectivity	Exergy destruction due to the non-ideality of the IEMs, which affects interface equilibria, thus also reducing the electro-motive force and the overall generated stack voltage.
Ohmic losses	Exergy destruction due to the power dissipated due to the internal stack resistance.
Water flux	Exergy destruction associated to the water flux across the IEMs which reduces the available salinity gradient for power production.
Salt flux	Exergy destruction associated to the salt flux across the IEMs which reduces the available salinity gradient for power production.
Friction losses & pumping power	Exergy dissipated for flowing of the solutions within the channels.
Parasitic currents	Exergy destruction due to the generation of parasitic currents through the stack which dissipating part of the electrical energy generated inside the system.
Activation losses	Exergy destruction due to the electrical potential drops often related to redox reactions in the electrodic compartments (smaller with reversible redox couples, as in the present case).

Few research efforts have been devoted so far to thermodynamic analysis of the RED units. Veerman et al. [115] pointed out the crucial role played by membrane properties on energy performance. Based on an ideal model for thermodynamic properties estimation, they experimentally analysed the thermodynamic efficiency and power densities of a RED unit equipped with six commercial membranes, reporting thermodynamic efficiency between 14% and 35%. They also demonstrate that the non-ideal behaviour of the membranes is due to osmosis and co-ion transport and that loss in efficiency due to osmosis is small compared to co-ion. The same authors in [65] developed a 1-D mathematical model for the RED unit, which introduced the exergy concept. The model was calibrated with experimental data and used to study response parameters, suitable for optimization purposes. It was found that

performance of co-current and counter-current operation is almost identical and that segmentation of the electrodes can increase the power density with about 15%. Yip et al. [116] proposed a mathematical model to assess the production of work in a reversible and real *RED* process. The model defines suitable dimensionless parameters, which have to be properly assessed according to the type of membrane and operating conditions considered. By thoughtful selection of the operating parameters they achieved a thermodynamic efficiency of 37% and an overall gross power density of 3.5 W/m² with seawater-river water *RED* system with low-resistance ion exchange membranes (0.5 Ωcm²) at very small channels thickness (50 μm). Vermaas et al. [117] investigated the effects of different flow arrangements, single and multi-electrodes configurations on the energy efficiency of *RED* unit equipped with perfect membranes. They reported a maximum energy efficiency of 95% when using seawater and river water flowing in counter-current arrangement.

Most of the works reported in literature limited their investigation to the case of seawater and river water as it is the most common natural salinity gradient. Conversely, a variety of artificial solutions could be in principle used in closed-loop applications, leaving large room for further studies. Moreover, literature works typically refer to thermodynamic efficiency (or energy efficiency) as performance indicator, while exergy efficiency is not mentioned or not properly quantified in any study.

For the first time, exergy analysis is extensively applied to a *RED* process to identify the main sources of irreversibility and quantifying their detrimental effect on process performance. The analysis was supported by a robust 1-D model for the description of all the transport phenomena within the *RED* unit assuming real membrane properties. The effect of each *IEM* properties (i.e., permselectivity, water and salt permeability, and resistance) are quantitatively identified, providing relevant information for orienting future development of better performing *IEMs*. As a matter of fact, some detrimental effects as the water flux, usually neglected for the case of low salinity gradients, considerably reduce the *RED* unit exergy performance when high salinity gradients are applied.

The effect of varying saline solution concentrations (0.5-5 M for concentrate and 0.01-1 M for dilute) were investigated including high concentrated cases which required a more complex formulation of the mathematical model than those reported so far in the literature [66]. Also, the effect of operating conditions (e.g. external load, residence time and flow-arrangements) on exergy efficiency was investigated. Optimal operating conditions in order to achieve minimum exergy consumption and maximum process efficiency were identified

for *RED* process in closed loop applications. In fact, in closed-loop applications exergy consumption related to the *RED* unit has to be restored by a thermal regeneration unit using low-grade waste heat. The higher the exergy destruction in the *RED* unit, the higher the thermal power required in the regeneration unit.

3.1.1 Exergy Analysis equations

Eq. 3.1 presents the general formula used for calculating the exergy of a stream (*B*) flow at pressure *p*, temperature *T* and composition *x_i* (where the subscript “*i*” refers to species “*i*th” compounding the mixture)[118].

$$\dot{B} = \sum_{i=1}^n \left[\left(\tilde{h}_i(T, p, x_i) - T_0 \tilde{s}_i(T, p, x_i) \right) - \left(\tilde{h}_i(T_0, p_0, x_{i,0}) - T_0 \tilde{s}_i(T_0, p_0, x_{i,0}) \right) \right] \dot{N}_{i,in} \quad (3.1)$$

where, *x_i* the mole fraction of the *i*th-component, \tilde{h}_i and \tilde{s}_i are respectively the partial molar enthalpy and entropy of the “*i*th” species compounding the mixture function of *T*, *p*, *x_i*, while $\dot{N}_{i,in}$ the molar flow rate of the “*i*th” species compounding the mixture. The subscript “*0*” refers to equilibrium conditions with the environment.

1. According to the well-known approach proposed by Szargut [119], in order to assess whether (and how much) work is produced by a change in chemical composition or by changes in temperature and pressure of the stream, exergy is commonly split into two fractions:

- *Physical exergy*: this fraction is the amount of work obtained when the stream reaches reversibly thermal and mechanical equilibrium with the environment, while not changing its chemical composition. The thermodynamic state reached by the system is characterized by the same temperature and pressure of the environment, and it is commonly named “*restricted dead state*”;
- *Chemical exergy*: this fraction indicates the amount of work obtained when the stream reaches chemical equilibrium with the environment, while keeping its temperature and pressure equal to T_0 and p_0 . The thermodynamic state of the system in equilibrium with the environment is commonly indicated as “*dead state*”.

Eq.s 3.2 and 3.3 express physical and chemical exergy respectively.

$$\dot{B}_{ph} = \sum_{i=1}^n \left[\left(\tilde{h}_i(T, p, x_i) - T_0 \tilde{s}_i(T, p, x_i) \right) - \left(\tilde{h}_i(T_0, p_0, x_i) - T_0 \tilde{s}_i(T_0, p_0, x_i) \right) \right] \cdot \dot{N}_{i,in} \quad (3.2)$$

$$\begin{aligned} \dot{B}_{ch} &= \sum_{i=1}^n \left[\left(\tilde{h}_i(T_0, p_0, x_i) - T_0 \tilde{s}_i(T_0, p_0, x_i) \right) - \left(\tilde{h}_i(T_0, p_0, x_{i,0}) - T_0 \tilde{s}_i(T_0, p_0, x_{i,0}) \right) \right] \cdot \dot{N}_{i,in} = \\ &= \sum_{i=1}^n \left[\mu_i(T_0, p_0, x_i) - \mu_i(T_0, p_0, x_{i,0}) \right] \cdot \dot{N}_{i,in} \end{aligned} \quad (3.3)$$

where μ_i is the chemical potential of a component i in a solution, evaluated using the Pitzer's model [120], see Chapter 4 for more details.

Differently from energy that can be neither created nor destroyed, exergy is always consumed due to irreversible phenomena, which naturally occur in real processes. Some example of sources of irreversibility are flow friction, uncontrolled mixing phenomena and heat transfer through finite temperature difference. By applying an exergy balance, it is possible to assess the amount of exergy destroyed ($\dot{I}r$) due to irreversibility.

$$\sum_{j \in \text{Input}} \dot{B}_j - \sum_{h \in \text{Output}} \dot{B}_h = \dot{I}r \quad (3.4)$$

As previously explained, in *RED* process, electric power is generated by ions transfer between two solutions at different concentration. Since chemical composition of both streams changes when passing through a *RED* unit, part of their chemical exergy is used to generate electricity. Only in the case of reversible operation of a *RED* unit, the overall exergy variation would be entirely converted into electrical power.

In order to assess the magnitude of exergy destruction occurring within *RED* unit, an exergy balance is set out as shown in eq. 3. 5. The variation of the chemical exergy of dilute and concentrate solutions is described on the *LHS*, while the electrical power produced P_{RED} and the exergy destroyed due to irreversibility Ir_{RED} appear on the *RHS*.

$$\left(\dot{B}_{H,in} - \dot{B}_{H,out} \right) + \left(\dot{B}_{L,in} - \dot{B}_{L,out} \right) = \dot{P}_{RED} + \dot{I}r_{RED} \quad (3.5)$$

Since a *RED* unit often operates at environmental temperature (i.e. approximately $T_0=298$ K) and pressure (i.e. approximately $p_0=100$ kPa), only chemical exergy was considered throughout the analysis, neglecting physical exergy variations within the unit. As already mentioned, no pressure drops were considered in the *RED* model, thus pressure was

considered constant along the channels. Seawater composition of 38000 ppm NaCl was considered as reference state to evaluate the chemical exergy of each stream.

Eq.s 3.6 and 3.7 provide the chemical exergy variation of concentrate and dilute solutions respectively. Both equations are derived from eq. 3.3 where chemical potential are explicitly expressed in terms of activities of salt and water, calculated by means of Eqs 1-6.

$$\begin{aligned} \dot{B}_{H,in} - \dot{B}_{H,out} = RT_0 \left[\dot{N}_{H,in} \left(x_{salt,H}^{in} \nu \ln \left(\frac{a_{salt,H}^{in}}{a_{salt,0}} \right) + x_{w,H}^{in} \ln \left(\frac{a_{w,H}^{in}}{a_{w,0}} \right) \right) + \right. \\ \left. - \dot{N}_{H,out} \left(x_{salt,H}^{out} \nu \ln \left(\frac{a_{salt,H}^{out}}{a_{salt,0}} \right) + x_{w,H}^{out} \ln \left(\frac{a_{w,H}^{out}}{a_{w,0}} \right) \right) \right] \end{aligned} \quad (3.6)$$

$$\begin{aligned} \dot{B}_{L,in} - \dot{B}_{L,out} = RT_0 \left[\dot{N}_{L,in} \left(x_{salt,L}^{in} \nu \ln \left(\frac{a_{salt,L}^{in}}{a_{salt,0}} \right) + x_{w,dil}^{in} \ln \left(\frac{a_{w,L}^{in}}{a_{w,0}} \right) \right) + \right. \\ \left. - \dot{N}_{L,out} \left(x_{salt,L}^{out} \nu \ln \left(\frac{a_{salt,L}^{out}}{a_{salt,0}} \right) + x_{w,dil}^{out} \ln \left(\frac{a_{w,L}^{out}}{a_{w,0}} \right) \right) \right] \end{aligned} \quad (3.7)$$

Exergy efficiency can be defined as the ratio of electric power produced to the variation of chemical exergy of dilute and concentrate solutions.

$$\eta_{ex} = \frac{\dot{P}_{RED}}{(\dot{B}_{H,in} - \dot{B}_{H,out}) + (\dot{B}_{L,in} - \dot{B}_{L,out})} \quad (3.8)$$

Exergy efficiency indicates the fraction of the chemical exergy consumed within *RED* stack which is usefully converted into electrical power. As it will be shown in the next section, it represents a useful thermodynamic indicator whose numerical values provide insights on the effect of irreversibility for alternative design and operating scenarios of *RED* process.

3.2 Results and Discussion

The integrated model consists of the *RED* process model and the exergy model, was used to perform several sensitivity analyses in order to investigate the effects of irreversibility sources (permselectivity, water and salt fluxes, all linked to the membrane properties), flow arrangements (co and counter current) and residence times on the exergy efficiency of the

process. A stack of 1000 cell pairs was considered in order to neglect the effect of the electrodic compartment resistance (R_{blank}) on RED performance.

3.2.1 Effect of the irreversibility source

The following exergy analysis is carried out considering a stack equipped with square membranes of 0.1m x 0.1m. As regards concentrate and dilute feeds, NaCl solutions with a concentration respectively of 3.6 M and 0.05 M are supplied to the RED unit. The inlet velocity of both streams is set equal to 1 cm/s. The main sources of irreversibility involved in RED process are: (i) *internal ohmic losses* (P_{loss}), which identify the power dissipated by the internal resistances (eq. 2.39); (ii) *membrane permselectivity* (α), which affects the electromotive force of the pile (eq. 2.30); (iii) *diffusive salt flux* (J_{salt}), which identifies the co-ions transport across the IEM (eq. 2.42); *water flux* (J_w), which identifies the flux of water across the IEM (eq. 2.43).

In order to assess at which extent each irreversibility source affects the exergy performance of the unit, four different scenarios were considered:

- Scenario A: the pile is equipped with ideal membranes ($P_w=0$ m/(Pa·s), $P_{salt}=0$ m²/s and $\alpha=1$) and internal resistance of the pile is considered as unique source of irreversibility;
- Scenario B: the effect of non-ideal permselectivity on the Donnan's potential generation at the IEMs-solutions interface (and consequentially, on the electromotive force) is considered still neglecting diffusive water and salt fluxes in the transport equations ($P_w=0$ m/(Pa·s), $P_{salt}=0$ m²/s and $\alpha \neq 1$). This is still an ideal scenario where the effect of co-ions diffusion is neglected ($P_{salt}=0$);
- Scenario C: non-ideal permselectivity and diffusive salt flux ($P_{salt}=10^{-12}$ m²/s and $\alpha \neq 1$), conversely, water flux is neglected ($P_w=0$ m/(Pa·s));
- Scenario D: the pile is equipped with real membranes all the irreversibility sources are considered ($P_w=2.22 \cdot 10^{-14}$ m/(Pa·s), $P_{salt}=10^{-12}$ m²/s and $\alpha \neq 1$).

In Figure 3.1-a and b, the exergy efficiency and power density are shown for each simulated scenario as a function of the ratio between external load and internal stack resistance (R_{ext}/R_{int}). More specifically, when considering R_{ext}/R_{int} equal to 0, the stack operates in short-circuit condition (S.C.): in this case the maximum electrical current through the pile is observed and no electrical power is produced. Conversely, when R_{ext}/R_{int} tend to ∞ , the pile

works in open circuit condition (*O.C.*): in this case, the stack voltage is equal to the electro-motive force and no electric current circulates in the system. As shown *Figure 3.1-b*, the maximum power density is obtained when the ratio R_{ext}/R_{int} is approximately 1, with stack voltage equal to half of the Open Circuit Voltage [73].

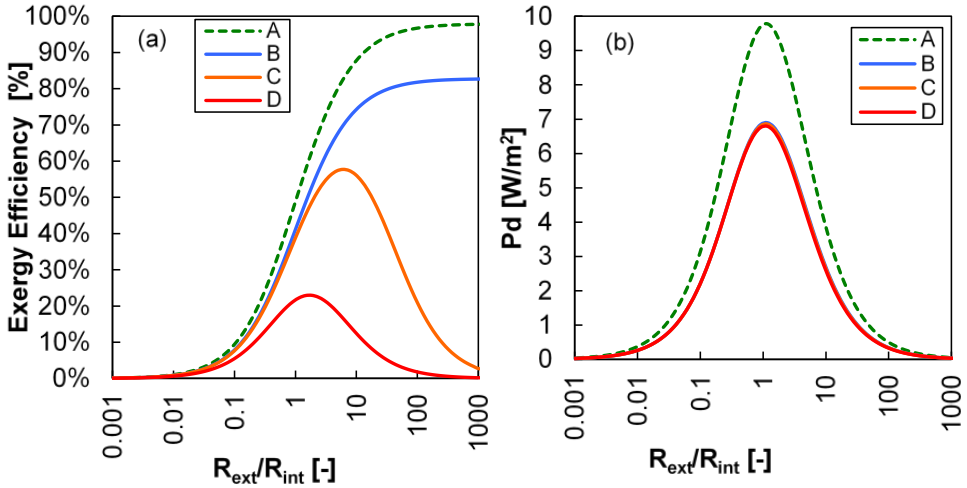


Figure 3.1 Exergy Efficiency (a) and Power density (b) as a function of external/internal resistance ratio for each examined scenario. RED stack $0.1m \times 0.1m$, $v_H=v_L=1cm \cdot s^{-1}$, $C_H=3.6M$, $C_L=0.05M$.

As shown in *Figure 3.1-a*, when considering *S.C.* condition in all simulated scenarios, exergy efficiency is equal to zero, indicating that the exergy consumed is entirely destroyed by the pile internal resistance without producing electric power.

In *Scenario A*, RED exergy efficiency increases with the R_{ext}/R_{int} ratio. It is worth noting that exergy efficiency is nearly equal to unity when approaching *O.C.* condition. This result indicates that under this circumstance, reversible transformation occurs within the pile, all the irreversibility approach to zero. When $R_{ext}/R_{int}=1$, the exergy efficiency is equal to 0.5: half of the exergy consumption is converted into electric power by the pile, being the other fraction dissipated due to internal stack resistance (average membrane resistance is equal to $3 \Omega \cdot cm^2$).

In *Scenario B* the effect of non-ideal membrane permselectivity on the electrical voltage is considered. Comparing to *case A*, a similar trend for exergy efficiency is observed but lower values are obtained due to the decrease in the electro-motive force and power output (eq. 2.30).

In both *A* and *B* scenarios maximum exergy efficiency is obtained in *O.C.* condition though the power output from the stack tends to zero. In this ideal condition, solutions are virtually mixed through reversible steps with an infinitesimal current thus reducing to zero ohmic dissipations.

As previously mentioned, in *case C* salt diffusion and permselectivity were considered as sources of irreversibility, conversely, for *case D*, also osmosis was included. In these scenarios the exergy efficiency curve increases with the R_{ext}/R_{int} ratio up to reach the maximum value slightly after the maximum power density (R_{ext}/R_{int} between 1 and 10), while decreasing for higher values of R_{ext}/R_{int} . In fact, a larger external load lowers the current (and the power output), while uncontrolled mixing phenomena keep the same absolute influence on mixing dissipation (as shown in *Figure 3.2-a*) as they only depend on salinity gradient and salt/water permeability of *IEMs*. This leads to a dramatic increase of the relative effect of irreversible phenomena on exergy efficiency, so that, in *O.C.* conditions, exergy efficiency approaches zero: even with zero electric current exergy can be destroyed within the stack due to uncontrolled mixing phenomena.

For the case of a pile equipped with real membranes *Figure 3.2-b* a breakdown of the exergy consumption (Ex_{cons}) into exergy destruction due to uncontrolled mixing phenomena (E_{mix}), exergy destruction due to ohmic dissipation (P_{cons}), and electric power produced. It is interesting to observe how irreversibility magnitude due to uncontrolled mixing phenomena is almost equal for all operating conditions. Under these conditions, E_{mix} is dominated by the osmotic water transport, with migrative salt flux playing only a minor role in enhancing it when current is increased, contrarily to the effect of electro-osmosis (directly promoted by the current increase). Indeed, osmosis and salt diffusion phenomena themselves are indirectly reduced when current increase due to the reduction of concentration gradients. All these complex and counteracting phenomena lead to only a slight reduction (less than 5%) of E_{mix} , observed when increasing stack current. Conversely, exergy destruction due to internal ohmic resistance strongly affects exergy performance when load resistance lower than internal stack resistance is considered, whereas being negligible when approaching *O.C.* condition.

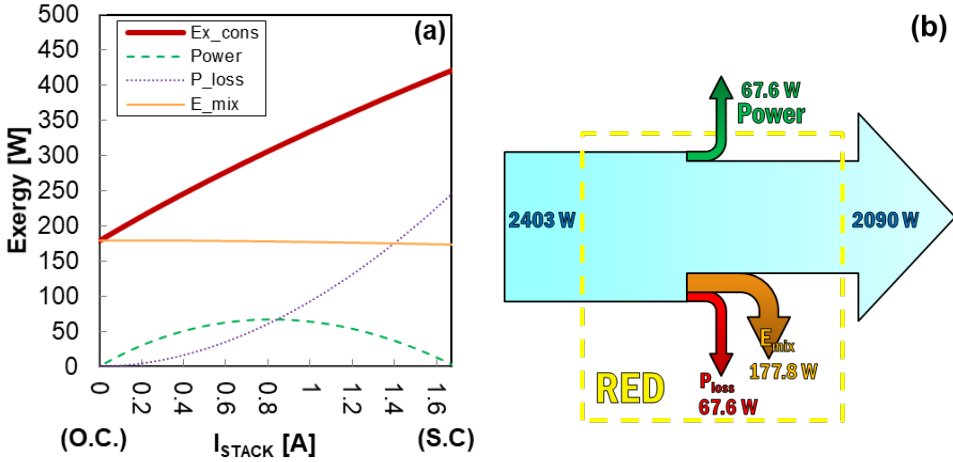


Figure 3.2 (a) Variation of exergy consumption/conversion terms as a function of the electrical current (I) showing total consumed exergy (Ex_{cons}), power output ($Power$), ohmic losses (P_{loss}) and uncontrolled mixing phenomena (E_{mix}); (b) Graphical breakdown of exergy consumption/conversion terms for a real RED process in maximum power conditions. RED stack $0.1\text{ m} \times 0.1\text{ m}$, $v_H=v_L=1\text{ cm}\cdot\text{s}^{-1}$, $C_H=3.6\text{ M}$ $C_L=0.05\text{ M}$, scenario D.

3.2.2 Effect of membrane properties

In the previous analysis, fixed values of membrane salt and water permeability were considered. It is worth assessing how the RED exergy performance may change when equipping this membrane parameters change. To this aim, a sensitivity analysis changing salt and water permeability was carried out. Results are shown *Figure 3.3*. In particular:

- In *Figure 3.3-a*, salt permeability was fixed equal to $P_{salt}=10^{-12}\text{ m}^2/\text{s}$, while water permeability P_w was varied in the range of $2.22\cdot 10^{-14}$ to $0\text{ m}/(\text{Pa}\cdot\text{s})$. It can be observed how exergy efficiency improves from 23% to 58%, when water flux is null: this proves a strong impact of water flux on the unit performance.
- In *Figure 3.3-b*, a similar analysis was carried out by considering a reduced salt permeability from $10^{-12}\text{ m}^2/\text{s}$ to $10^{-11}\text{ m}^2/\text{s}$. Results show a strong reduction of exergy efficiency due to the increase of salt flux effect. In particular, when no osmosis is considered (i.e. $P_w = 0$), the exergy efficiency is reduced from 58% to 27%.

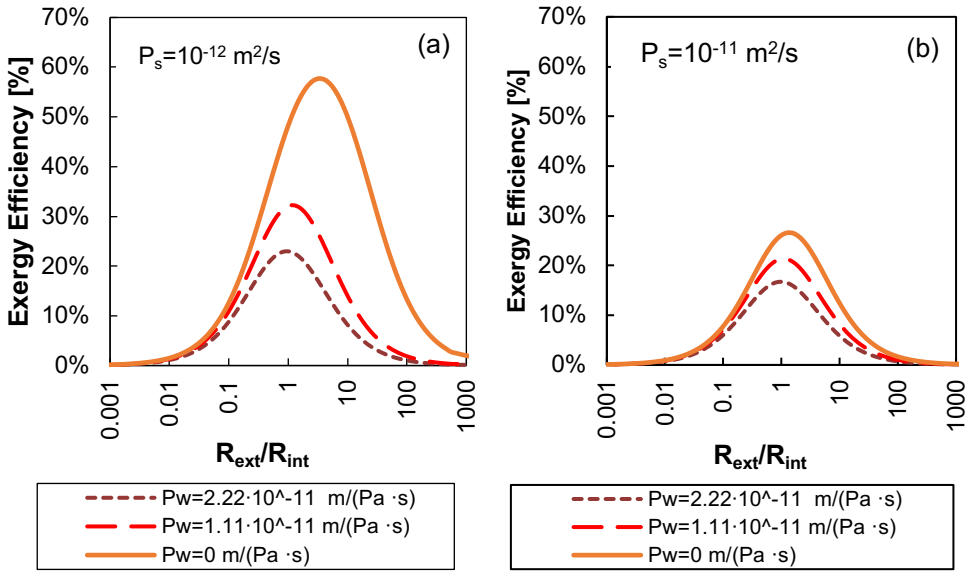


Figure 3.3 Effect of diffusive water and salt flux on RED exergy efficiency varying the resistance ratio and assuming three different values for P_w ($2.22 \cdot 10^{-14}$, $1.11 \cdot 10^{-14}$ and $0 \text{ m}/(\text{Pa} \cdot \text{s})$) fixing P_s equal to $10^{-11} \text{ m}^2/\text{s}$ in fig. (a) and $10^{-12} \text{ m}^2/\text{s}$ in fig. (b). RED stack $0.1 \text{ m} \times 0.1 \text{ m}$, $v_{conc} = v_{dil} = 1 \text{ cm} \cdot \text{s}^{-1}$, $C_{conc} = 3.6 \text{ M}$, $C_{dil} = 0.05 \text{ M}$.

3.2.3 Effect of concentrate and dilute concentrations

In this section, the influence of inlet concentrations on the exergy efficiency and power density is analysed. As already mentioned, one of the main advantages of RED-HE is the possibility of selecting suitable feed concentrations which could lead to a more performing process.

For the analysis, the same stack configuration previously proposed was considered.

First, the effect of the concentrate was evaluated by gradually decreasing its concentration from 5.0M to 0.5M while keeping a dilute fixed to 0.05M. Conversely, in the second analysis, the dilute concentration was increased from 0.05M to 1M while keeping a concentrate at 3.6M.

Exergy efficiency and Power densities for all simulated cases are shown in *Figure 3.4-a* and *b* and *Figure 3.5-a* and *b*.

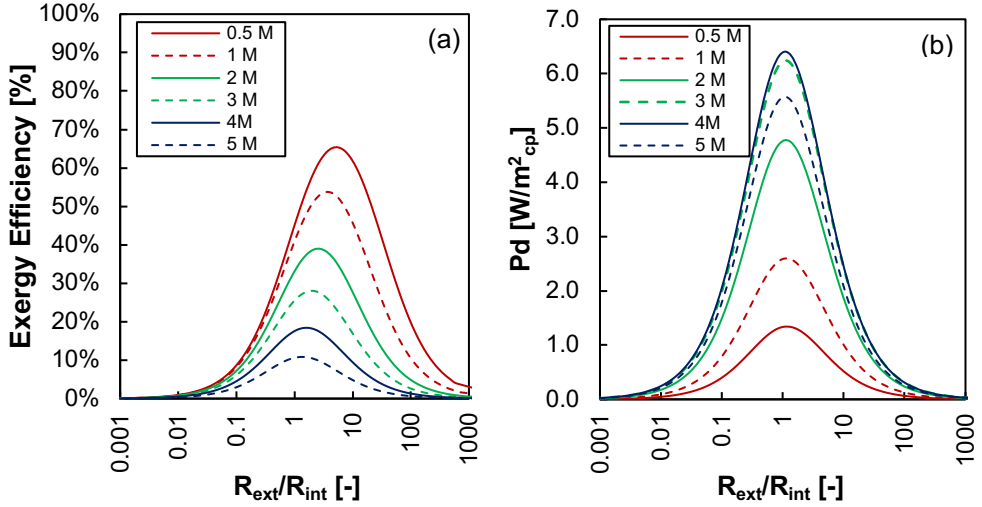


Figure 3.4 Exergy efficiency (a) and Power density (b) as function of the R_{ext}/R_{int} ratio and the concentrate solution concentration (C_H), setting the dilute concentration $C_L=0.05M$. RED stack $0.1 m \times 0.1 m$, $v_H=v_L=1 cm \cdot s^{-1}$, scenario D.

Results shown in *Figure 3.5-a* and *b* indicate that a decrease in concentrate from 5.0M to 0.5 M produces a substantial improvement of exergy efficiency from 11% at 5.0 M to 65% for 0.05 M. Conversely, as regards power density, results show a decrease from 5.6 W/m^2 at 5M to 1.3 W/m^2 at 0.5M. The highest power density, equal to 6.4 W/m^2 , is observed for 3.6 M. This result is related to the membranes resistance, which approaches a minimum value near 3.6 M. As reported in Micari et al. [93], the resistance of IEMs tends to increase at high value of the concentration. In particular in this case, the membrane average resistance is around 3 Ωcm^2 at 3 M while it increases up to 5 Ωcm^2 at 5 M.

According to *eq.s 2.42* and *2.43*, a reduction of salinity gradient reduces both electrical power and osmosis and salt diffusion across the membranes.

The improvements of exergy efficiency when reducing concentrated solution indicate that even though less electrical power is produced, a better exploitation of exergy occurs due to a reduction of the exergy destroyed by uncontrolled mixing phenomena.

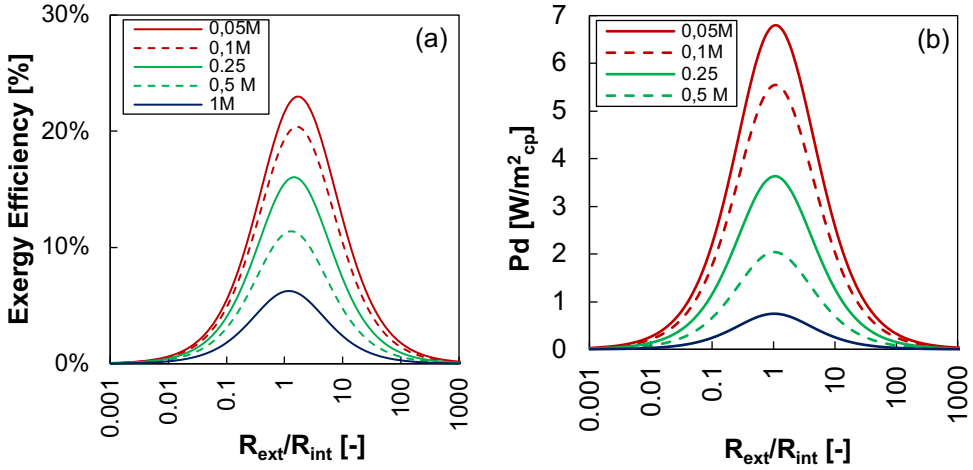


Figure 3.5 Exergy efficiency (a) and Power density (b) as function of the R_{ext}/R_{int} ratio and the dilute solution concentration, setting the concentrate concentration $C_H=3.6$ M. RED stack 0.1 m x 0.1 m, $v_H=v_L=1$ cm·s⁻¹, scenario D.

As shown in *Figure 3.5*, different results were obtained when the dilute concentration was increased from 0.05M to 1.00M, while keeping the concentrate solution at 3.6M (value maximizing the power). Also, in this case, the reduction in concentration difference produces a decrease of the uncontrolled mixing phenomena, however, the increase of the dilute solution concentration strongly affects *OCV* values. Indeed, as shown in *eq. 2.30*, *OCV* is dependent from the logarithm of the ratio between concentrate and dilute solution. Thus, an increase of dilute solution concentration while keeping constant the concentrate solution, affect *OCV* much more than a decrease in concentrate while keeping constant the dilute concentration. Therefore, the heavy reduction in *OCV* drastically reduces the electric power produced by the unit which is not compensated by the decrease of irreversibility generated by osmosis and salt diffusion.

3.2.4 Effect of flow arrangement and cell pair length

This section presents a sensitivity analysis to highlight the influence of flow arrangement and cell pair length (L) on RED performance.

The analysis was performed considering counter-current and co-current flow arrangement, varying stack length from 0.1m to 1.0m and fixing inlet velocity equal to 1cm·s⁻¹. Concentration values equal to 3.6M and 0.05M were considered for concentrate and dilute, respectively.

When changing channel length from 0.1m to 1.0m, residence time of solutions within the stack increases. Then, more electrical power is produced by the pile as well more water and salt are exchanged between solutions due to osmosis and salt fluxes.

Considering a stack length less or equal to 0.4m (i.e. short stack), though for the two flow arrangements a different profile concentration is observed, the values of electrical outputs are practically the same due to low residence time of both stream within the stack. In these cases, flow arrangement does not influence RED exergy performance, which equals to 23 % for both cases. Conversely, when channel length is greater than 0.5 m, concentration profiles along stack length differ for the two cases. In both configurations, the exergy efficiency decreases when increasing the channel length. This trend can be easily explained by means of the following consideration: due to higher residence time within the stack, more electric power is produced as well more irreversibility is generated by uncontrolled mixing phenomena. In these cases, the exergy destruction occurring due to osmosis and salt diffusion is not offset by the increase in electric power generation, thus a decrease of RED performance occurs.

Still, it is possible to observe how the counter-current stack is more performing than the co-current when increasing stack length. As shown in Figure 3.6-a and b moving from 0.1m to 1m, exergy destruction is nearly equal for both cases, conversely, power production is greater in counter-current arrangement.

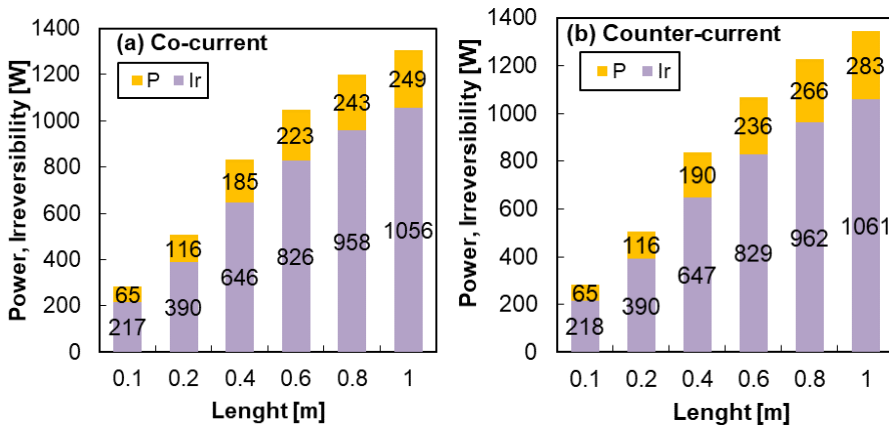


Figure 3.6 Power generation and Irreversibility losses in Co-current (a) and Counter-current (b) arrangements. RED stack $L \text{ m} \times 0.1 \text{ m}$, $C_H=3.6 \text{ M}$ $C_L=0.05 \text{ M}$, $v_H=v_L=1 \text{ cm}\cdot\text{s}^{-1}$

3.2.5 Effect of feed velocity

In this section, the effect of the different residence times on exergy efficiency and gross power is analysed. In the first scenario, the dilute velocity is set at 2cm/s, while the concentrate

velocity is increased from 0.4cm/s to 2cm/s. Conversely, in the second scenario, the concentrate velocity is set at 2cm/s while dilute velocity is varied from 0.4cm/s to 2cm/s.

As shown in *Figure 3.7-a*, when increasing dilute velocity from 0.4 to 2.0cm/s, an increase of both power and exergy efficiency is observed. In particular, the exergy efficiency improves from 8.6 % to 22%, while the power increases from 76W to 440W. The low residence time of dilute solution within the stack results in a low average dilute concentration. Thus, according to *eq. 2.30*, a significant increase of the electric voltage is observed, with negligible variation of the uncontrolled mixing phenomena.

Conversely, the increase of the concentrate velocity results in a slight increase of power output and a decrease of the exergy efficiency as shown in *Figure 3.7-b*. In particular, increasing concentrate velocity from 0.4 to 2 cm/s, the exergy efficiency decreases from 31% to 22%, while the power increases from 360 W to 440 W. In this case, the higher average concentration of concentrate along the channels results, in a slight increase in pile electric voltage according to *Eq. 9*. However, exergy destruction due to uncontrolled mixing phenomena is not balanced by the increase of electric power, leading to a less performing unit results. Interestingly, at very low v_H , η_{ex} reaches the highest value indicating that the reduction of uncontrolled mixing phenomena (due to the much lower average concentration in the channel) dominates the overall efficiency being more important than the reduction of power output also caused by the lower average concentration. Worth noting that results reported in *Figure 3.7* do not consider the effect of polarisation phenomena and pressure drop.

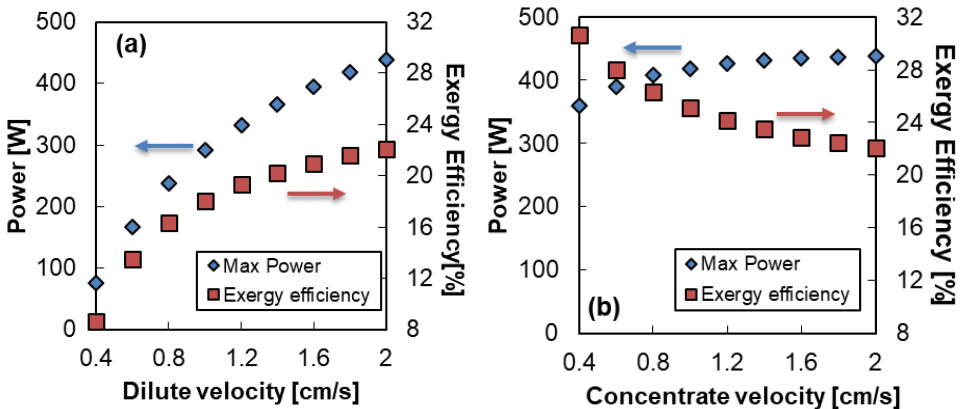


Figure 3.7 Maximum power and corresponding exergy efficiency as function of (a) dilute velocity, (setting concentrate velocity at $2\text{ cm}\cdot\text{s}^{-1}$) and (b) concentrate velocity (setting dilute velocity at $2\text{ cm}\cdot\text{s}^{-1}$). RED stack $1\text{ m} \times 0.1\text{ m}$ Counter-Current arrangement, $C_H=3.6\text{ M}$ $C_L=0.05\text{ M}$, scenario D.

3.3 Potential applications of RED in real environments

In the case of open loop applications, salinity gradients available in natural resources (*e.g.* river water, seawater or brines) or from industrial/human activities, *e.g.* seawater reverse osmosis (*SWRO*) brines or treated wastewater (*TWW*), are used as working solutions for the *RED* process.

The most abundant naturally resource is seawater with an average salinity of 35 g/l, while river water, salty-lakes and brine represent minor sources. Generally, NaCl represents the main component in natural salt solutions, then, NaCl molar composition is often adopted to simulate the behaviour of the total salt content of such natural solutions.

The theoretical amount of work obtained from the mixing of 1 m³ of river water (1 g/l) with unlimited amount of seawater (35 g/l), *i.e.* a common situation on the rivers' mouths, is equal to 0.66 kWh/m³ of river water. Part of this energy may be theoretical converted into electricity by using an *SGP* technology. Larger amounts of chemical exergy are released by the mixing of 1 m³ concentrated brine and 1 m³ seawater (1.5-4 kWh/m³ of concentrated solution) or 1 m³ concentrated brine and 1 m³ river water (2.5-6 kWh/m³).

In order to investigate the performance of *RED* unit in open loop applications different real existing scenarios were investigated, as shown in Table 1. The first three scenarios (*A-C*) refer to Italian country, while the others (*D-J*) refer to salinity gradients existing in non-European countries.

Apart from the concentration difference (*i.e.* salinity gradient), the resource availability (*A*) (also reported in *Table 3.3*) is an important parameter to evaluate the potentialities of the *RED* technology. It represents the maximum available flow rate for each considered stream.

The less available flow rate between the two is the limiting one (\dot{V}_{lim}).

The availability affects the amount of power obtainable from the different resources and the plant size. In the case of salty lakes, the maximum allowable flow rate was assumed equal to an annual volume of 0.1% of the total salty lake, in order to limit the impact of the *RED* system on the lake ecosystem. In the case of saltworks brines the availability refers to 5 months per year, according to the saltworks cycle. In the case of river, the availability was fixed equal to 10% of the river flowrate

Table 3.2 Investigated scenarios

Case	Solutions involved (region)	C_H [g/l]	C_L [g/l]	A_H [m ³ /s]	A_L [m ³ /s]
A	Adriatic Sea [121] -Po river (Italy)[122]	38	0.25	unlimited	1600
B	Trapani saltworks brine ⁽¹⁾ – Mediterranean Sea (Italy)	234	38	0.023	unlimited
C	Trapani saltworks brine ⁽¹⁾ - Brackish water (Italy)	234	5.8	0.023	unlimited
D	Atlantic sea [123] - Amazon river (Brazil)[124]	35	0.04	unlimited	155 000
E	Dead Sea ⁽²⁾ – Red Sea [125] (Jordan-Israel)	310	41	3.96	unlimited
F	Great Salt Lake ⁽³⁾ - TWW (Utah-US) ⁽⁴⁾	260	1	0.656	3.3
G	Great Salt Lake ⁽³⁾ - Jordan River (Utah US)	260	0.5	0.656	14.4
H	Sorek SWRO plant ⁽⁵⁾ - TWW Tel Aviv (Israel) ⁽⁶⁾	70	1	2.8	4.28
I	Dead Sea[126,127] – Sorek SWRO plant (Israel) ⁽⁵⁾	310	70	3.96	2.8
J	Kara-Bogaz-Gol Bay ⁽⁷⁾ - Caspian Sea (Türkmenistan) ⁽⁸⁾	300	13.5	4.51	2708

⁽¹⁾Total capacity 120 10³ m³ for 5 months/y. ⁽²⁾Total capacity 114 km³[126,127]. ⁽³⁾Total capacity 18.9 km³[126,128]. ⁽⁴⁾Total capacity 75 MGD (<https://www.cwwrf.org/brief-history>). ⁽⁵⁾Total capacity 411 10³ m³/day [129], inlet flowrate evaluated assuming a recovery of 40%. ⁽⁶⁾Total capacity 10³ m³/day (www.igudan.org.il/home-en/about-us/). ⁽⁷⁾Total capacity 130 km³ [130]. ⁽⁸⁾Total capacity 78200 km³[126,131].

The validated RED model presented in Chapter 2 was used to evaluate the performance of the process in different natural environments. Simulations are performed for each scenario by referring to a stack constituted by 1000 cell pairs fed by solutions flowing at 1cm/s in spacer-filled channels (*Deukum*[®] 155 μm) in a counter-current arrangement. The influence of three different stack dimensions (i.e. 0.1x0.1 m², 0.5x0.5 m² and 1.0x1.0 m²) are investigated. Then, the limiting flowrate of each scenario limits the number of RED units that can be used in that particular case. In fact, the number of RED piles is obtained as the ratio of the limiting flow rate to the feed flow rate in each stack considering for each different RED unit dimension a fixed velocity of 1cm/s.

Concentration dependent correlations were used to evaluate the membrane electrical resistance and permselectivity (see section 2.4.2 -NaCl solutions), while constant values were used for water and salt permeability. Reference values for membranes properties are reported in Table 3.3. Two different set of membranes properties were considered in the calculations, i.e. base case membranes (BC), i.e. Fujifilm type 10 IEMs, and high performing (HP) membranes. Basis on the results obtained from the exergy analysis, the properties of HP membranes are assumed by improving the BC membranes. In particular, the HP membranes permselectivity was set equal to 95% while the other properties were set equal to ¼ of the BC

ones. In the seawater-river water scenario, a further increasing of permselectivity at 98% was considered because *BC* membranes have already permselectivity of about 95-96%. It is worth noting that current commercial membranes have already reached the singular target, i.e. one or two properties of such membranes are similar to the one assumed as high performing membranes [74].

Table 3.3 Base case and high performing membrane properties adopted in the analysis.

Properties	Base case (BC)	High performing (HP)
Water Permeability [ml/(bar·h·m ²)]	8 ⁽²⁾	2 ⁽²⁾
Permselectivity [%]	89 ⁽¹⁾	95 ⁽²⁾⁽³⁾
Salt permeability [m ² /s]	4.5 10 ⁻¹²⁽²⁾	1.1 10 ⁻¹²⁽²⁾
Resistance [Ω·m ²]	3.53 10 ⁻⁰⁴⁽¹⁾	8.82 10 ⁻⁰⁵⁽¹⁾

⁽¹⁾reference concentration of 2 M-0.05M NaCl water solutions. Property functions of the solution concentrations.

⁽²⁾assumed constant in the whole range of concentrations and equal to 98% in the case of river water-seawater.

Given the variety of the streams considered (each one has a different ionic composition), each of them was assumed as composed by NaCl only. Effect of other ions on power production in *RED* is still an open issue in the literature. Some studies report a performance reduction for solutions containing multi-valent ions (as Mg²⁺) [16]. However, since the effect of each single ion has not been quantified yet, it was chosen to neglect it in the present analysis.

3.3.1 RED unit potentials

A comparison between the specific Gibbs free energy of mixing (*SME*) for each scenario is reported in *Figure 3.8*. As expected the higher the salinity gradient between the two solutions, the higher the mixing free energy released from the mixing process. The highest *SMEs* around 17 MJ/m³ are observed in the cases F, G, and J.

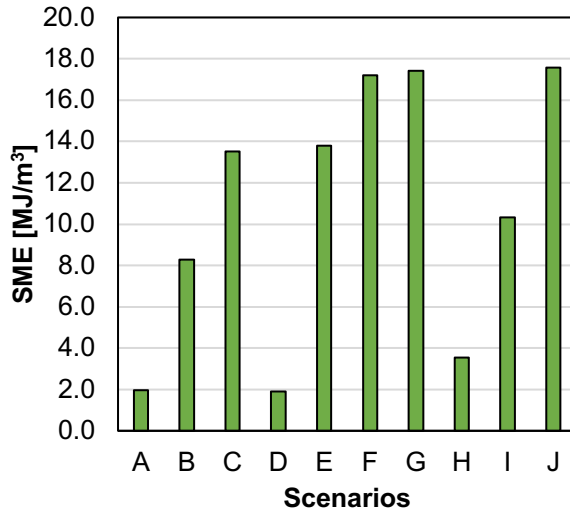


Figure 3.8 Specific Gibbs free energy of mixing for the different investigated scenario. Mixing same volume of solutions (1 m^3).

Considering the theoretical power (or Gibbs free power of mixing) obtainable from each different scenario as the product of the SME for \dot{V}_{lim} , the sources availability plays a predominant role. The highest theoretical power equal to 0.03 TW is obtained for the D case.

Of course, only a part of this potential can be recovered using real RED unit due to non-ideal and detrimental phenomena. Considering RED units consist of $1.0 \times 1.0 \text{ m}^2$ of membrane area the power generated in the D case, is equal to 0.012 TW and 0.017 TW adopting BC and HP membranes, respectively (Figure 3.9). Notwithstanding the low power density, the large sources availability leads to reach in theory very large values of power.

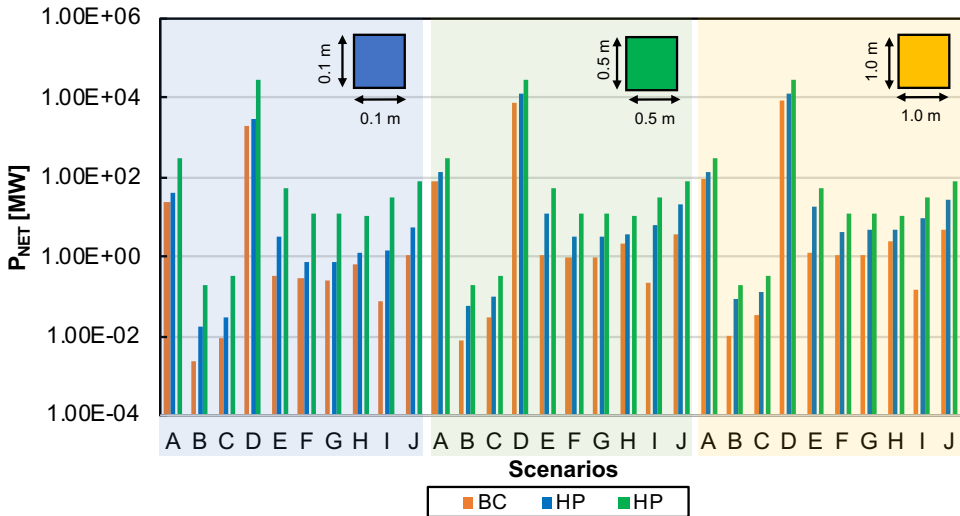


Figure 3.9 Net power of the RED unit for the different investigated scenarios as function of different stack sizes (0.1×0.1 m², 0.5×0.5 m² and 1.0×1.0 m²) and membranes properties (BC: base case membranes, HP: high performing membranes). Solutions velocity fixed equal to 1 cm/s in all cases. For each different stack size, the number of stacks (each stack consists of 1000 cell pairs) is calculated in order to use the available flowrate, considering the limitations (see Table 3.3).

The BC and HP membranes power density of the RED unit in each scenario is reported in Figure 3.10. The P_d values depend significantly on the residence time of the two solutions within the unit. For constant velocities (i.e. 1 cm/s in both channels), the longer the stack the lower the power density due to the drop of driving force along the channels and the effect of uncontrolled mixing phenomena (i.e. water and salt flux). When stack sizes of 0.1×0.1 m² are considered the net power density in the case of river water –seawater is around 2 W/m^2_{cp} for BC membranes and 3.4 W/m^2_{cp} for HP membranes. The highest power densities equal to 5.3 W/m^2_{cp} in BC membranes and 15.7 W/m^2_{cp} in HP membranes are obtained in the F and D scenarios, respectively.

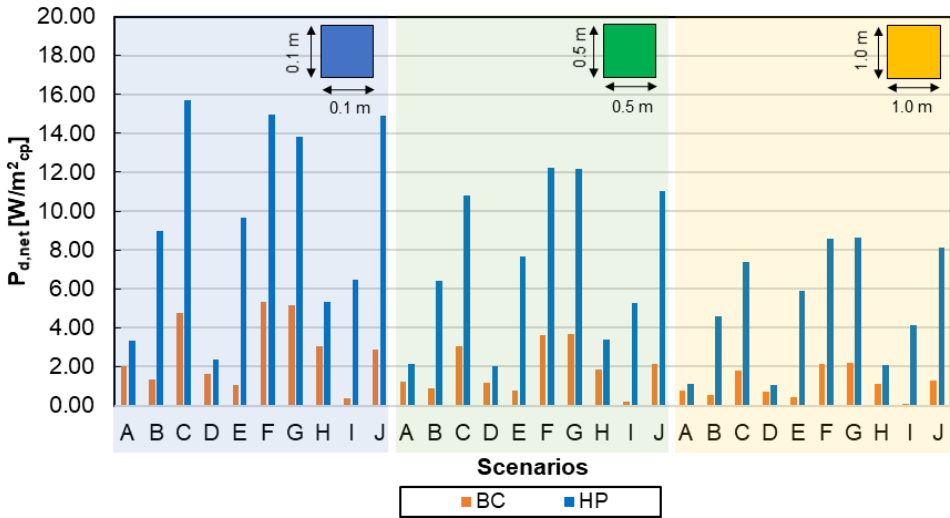


Figure 3.10 $P_{d,net}$ of the RED unit for the different investigated scenarios as function of different stack sizes ($0.1 \times 0.1 \text{ m}^2$, $0.5 \times 0.5 \text{ m}^2$ and $1.0 \times 1.0 \text{ m}^2$) and membranes properties (BC: base case membranes, HP: high performing membranes). Solutions velocity fixed equal to 1 cm/s in all cases.

The $P_{d,net}$ of BC membranes is strongly affected by irreversible phenomena (mainly water and salt flux) involved in the process which reduce the available salinity gradient for power production. The reduction is particularly evident at higher C_H where both high driving force and fewer performing membranes are involved. Furthermore, it is important to observe that some cases with low $P_{d,net}$ (i.e. cases B, E and I) become attractive if HP membranes are considered.

In the case of BC membranes, increasing the stack sizes from $0.1 \times 0.1 \text{ m}^2$ to $0.5 \times 0.5 \text{ m}^2$ the power density is reduced of $\sim 30\%$ on average. A further decrease of $\sim 43\%$ is obtained when the stack sizes are increased from $0.5 \times 0.5 \text{ m}^2$ to $1.0 \times 1.0 \text{ m}^2$. In the case of HP lower average reductions is observed, $\sim 25\%$ and $\sim 32\%$ respectively.

Figure 3.11 shows the yield of the RED process for each case, considering both BC and HP membranes. The yield represents the fraction of energy recovered with respect to the maximum amount available. Conversely from the $P_{d,net}$, the Y is a growing function of solution residence time. Then, the higher the stack sizes the higher the Y . For BC membranes, increasing the stack sizes from $0.1 \times 0.1 \text{ m}^2$ to $0.5 \times 0.5 \text{ m}^2$ doubles the Y . A further increasing from $0.5 \times 0.5 \text{ m}^2$ to $1.0 \times 1.0 \text{ m}^2$ produces only a slight increase of Y (i.e $\sim 15\%$).

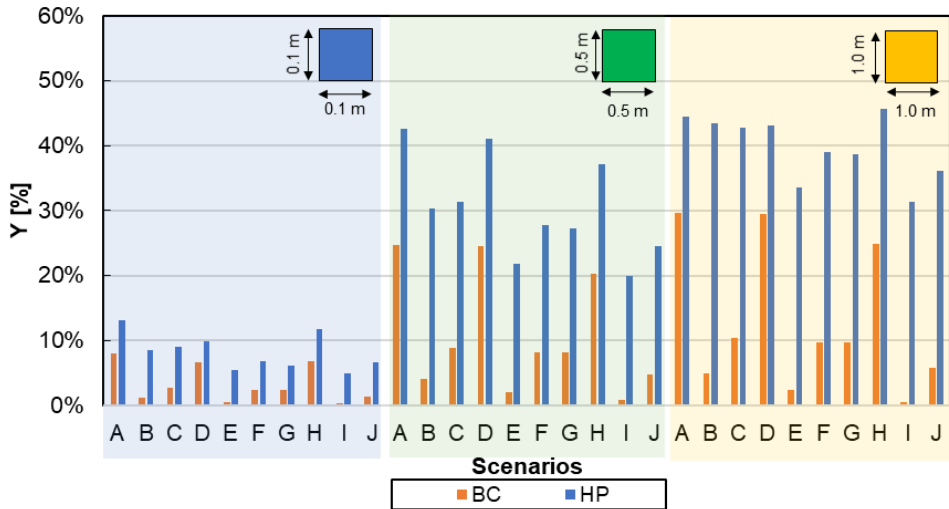


Figure 3.11 Yield of the RED process for the different investigated scenarios as function of different stack sizes ($0.1 \times 0.1 \text{ m}^2$, $0.5 \times 0.5 \text{ m}^2$ and $1.0 \times 1.0 \text{ m}^2$) and membranes properties (BC base case membranes, HP high performing membranes). Solutions velocity equal to 1 cm/s in all cases.

The yield is also largely affected by the irreversibility phenomena involved in the process. For this reason, adopting BC membranes, the highest yields, ranging between 25-30%, are obtained when the lowest salinity gradients are considered (cases A, D and H). The highest increments of Y , due to the adoption of HP membranes in the stack, are observed in scenarios where the highest C_H or C_L are considered.

3.4 Conclusions

In the present chapter, an original exergy analysis of the *RED* process was carried out in order to investigate the performance of *RED* units in terms of exergy efficiency and power yield in a wide range of system operations. To this aim, the *RED* process model presented in *Chapter 2*, was integrated with the exergy analysis tools.

A sensitivity analysis was carried-out in order to assess the influence of the irreversibility source caused by the average membrane properties on the process performance. In particular, water flux due to osmosis has been found to have the most detrimental effect on exergy efficiency when salinity gradient above 2M was adopted, with exergy losses (at maximum Power output conditions) accounting for 60-80% of total losses in the worst scenarios. A less dramatic, yet important effect is associated with diffusive salt flux.

A sensitivity analysis was also carried out in order to assess the influence of operating parameters on process performance. The analysis showed the exergy efficiency heavily increasing when decreasing dilute concentration. Conversely, the exergy efficiency increases when decreasing the salinity of concentrate feed reaching values up to 25% and 60% in the two cases, respectively. In both cases, power density decreases from values around 7 W/m^2_{cp} to slightly above 1 W/m^2_{cp} due to the salinity gradient reduction across the membranes.

The effect of counter-current and co-current flow arrangement was also assessed, indicating how the former leads to better performance only for long-length pile design.

The influence of different residence times for dilute and concentrate were considered in each simulated scenario, showing that exergy efficiency improves when increasing residence time in the concentrate channel or decreasing it in the dilute.

Finally, reverse electro dialysis potentials by referring to specific real case studies were investigated. The cases with the highest driven forces (i.e. C, E, F, G and J) were found to provide the highest specific mixing free energies and the highest power densities p in the *RED* unit. Present *RED* unit power outputs are largely limited by the current *IEMs* properties, particularly when high salinity gradients are fed to the unit. In particular employing current membranes, the maximum calculated *SE* is equal to 1.7 MJ/m^3 while values around 6.8 MJ/m^3 could be obtained using in the future *IEMs* with optimized properties. As it concerns the yield, the couple river water – seawater exhibits the highest yield for current *RED* units, while for future scenarios, case H appears as the most promising. Larger power outputs may be achieved considering river water and seawater due to the wide availability. In the case of the couple

Amazon river – Atlantic sea a potential near to 30 GW is available, however the power density in this scenario is the lowest, which could result in a high levelized cost of electricity (*LCOE*), near to 0.3 €/kWh [132]. Conversely, scenarios with a lower availability but large power density, as in the case of large salinity gradient difference (salt lake or saltworks brine), would result in values of the *LCOE* near to 0.10 €/kWh.

4

SELECTION OF SALT-SOLUTIONS FOR RED -HE

Chapter Outline

ABSTRACT	91
4.1 INTRODUCTION	92
4.2 THERMODYNAMICS OF ELECTROLYTE SOLUTIONS	95
4.2.1 PITZER'S THERMODYNAMIC MODEL	97
4.2.2 BOILING POINT ELEVATION IN ELECTROLYTE SOLUTIONS	99
4.3 BPE, OSMOTIC AND ACTIVITY COEFFICIENTS OF SALT SOLUTIONS..	99
4.3.1 EXPERIMENTAL.....	99
4.3.2 VALIDATION OF THE EXPERIMENTAL METHODOLOGY	101
4.4 KAC AND CSAC OSMOTIC AND ACTIVITY COEFFICIENTS.	104
4.5 GIBBS FREE ENERGY OF MIXING OF ARTIFICIAL SOLUTIONS.....	108
4.6 CONCLUSIONS.....	110

Part of this chapter has been published in:

F. Giacalone, C. Olkis, G. Santori, A. Cipollina, S. Brandani, G. Micale, "Novel solutions for closed-loop Reverse Electrodialysis: thermodynamic characterisation and perspective analysis", Energy Volume 166, 2019, Pages 674-689 <https://doi.org/10.1016/j.energy.2018.10.049>

Abstract

Closed-loop Reverse Electrodialysis is a novel technology to convert low-grade heat directly into electricity. One of the most important advantages of closed-loop systems compared to the open systems is the possibility to select ad-hoc salt solutions to achieve high efficiencies. Therefore, the properties of the salt solution are essential to assess the performance of the energy generation and solution regeneration processes. The aim of this chapter is to analyse the influence of thermodynamic properties of non-conventional salt solutions and their influence on the operation of the closed-loop RED and provide. In particular, osmotic and activity coefficients of salt solution determine the thermodynamic performance of the two unit. For non-conventional salt-solutions, as in the case of caesium and potassium acetate salts, osmotic and activity coefficients are available just in limited concentration ranges and at 25°C. A specific test rig has been designed and built in order to evaluate osmotic and activity coefficients from vapour pressure measurements. New data for caesium and potassium acetate salts, in terms of osmotic and activity coefficients, in aqueous solutions at temperature between 20 and 90°C have been collected and presented as a function of molality.

4.1 Introduction

Salt-water solutions and membranes are the main factors determining the performance of the *RED-HE* unit. Then, the characterization of membrane properties and salt-water solutions are fundamental for the process understanding. The membrane properties and their effect on the performance of *RED* process were already discussed in *Chapter 2 and 3*. The focus of this chapter is on the salt-water solutions characterization.

In the case of closed loop applications, artificial solutions are used in the reverse electrodialysis unit to generate electricity, and the exhausted solutions are subsequently regenerated in a thermally driven regeneration unit using low-grade heat.

The selection of the most suitable salt solution must consider a number of factors, which characterize the whole closed-loop system.

The optimal salt for *RED* should have (i) high solubility in water, (ii) high salt activity coefficients at high concentrations and (iii) high conductivity.

The solubility and the activity coefficients strongly influence the *RED* process performance in terms of electro-motive force (e.m.f.) and consequently the power density, but also the energy density (or Gibbs free energy of mixing, kWh/m³). As an example, the solubility of sodium chloride (NaCl) in water is 6.15 molar (26.45 gr. salt/100 gr. solution) at 25 °C [133], while the e.m.f. is around 0.2 V per cell-pair when a saturated NaCl solution is mixed to a dilute stream of NaCl (0.05M) [19]. Other inorganic salts, such as lithium chloride (LiCl), lithium bromide (LiBr), caesium acetate (CsAc), potassium acetate (KAc), have a remarkably high solubility (*Figure 4.1-a*) [133,134], allowing, in principle, to obtain much larger values of Gibbs free energy of mixing. *Figure 4.1-b* reports the salt-activity coefficients for some selected salt as a function of molality at 298.15 K [135–137]. For some salts, e.g. KAc and CsAc, literature information about activity and osmotic coefficients are available in a limited range of concentration and temperature.

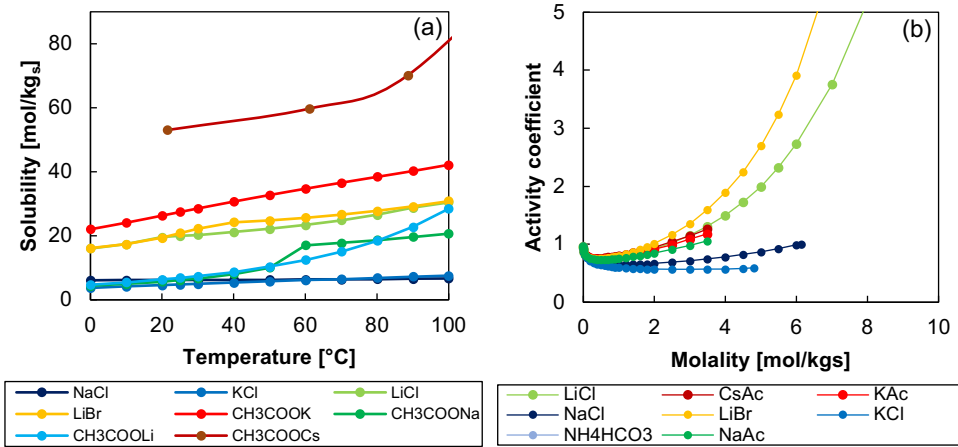


Figure 4.1 Salt-water solution solubility as a function of temperature [133,134] (a), salt-activity coefficients as a function of the molality at 25°C (b) [135–137].

Solution conductivity is another important property, as it affects the electrical resistance of the two solutions. In particular, the dilute channel electrical resistance represents the most important contribution to the overall stack internal electrical resistance [48], when small solutions residence time and low dilute solutions are considered. Electrical conductivities of some common salt solutions are reported in Figure 4.2.

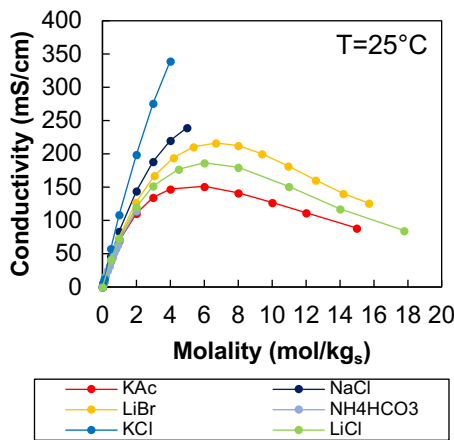


Figure 4.2 Conductivity of different salt-water solutions at 25°C [138–140]

As reported by Tamburini et al. [19] the use of non-conventional salt solutions can result in values of e.m.f. and power density significantly higher than conventional NaCl solutions. In particular, the use of the above mentioned salts (LiCl, LiBr, KAc and CsAc) can lead to values up to 6 times higher [19].

Depending on the choice of the artificial saline solution, a variety of different processes can be developed for the regeneration stage (Figure 4.3). These can be grouped in two main categories: (i) *solvent extraction processes* and (ii) *salt extraction processes*.

As already mentioned, in *solvent extraction processes* the regeneration of the original concentration of the two streams exiting from the RED unit occurs by removing solvent from the exhausted concentrate stream, which is after transferred to the exhausted dilute stream. Then, low grade heat is used to vaporize the solvent from the exhausted concentration stream, like in a thermal desalination process. In this context, Multi Effects Distillation (MED) and Membrane Distillation (MD) represent the most interesting options.

Conversely, in *salt extraction processes* the regeneration of the initial salt concentration is performed by removing the salt from the exhausted dilute solution, which is subsequently solubilized again into the exhausted concentration solution. Specific thermochemical properties of salt solutions or specific removal mechanisms are required to remove the salt from the solution. Among the proposed strategy, the use of thermolytic salts solutions and in particular ammonium bicarbonate is the most promising.

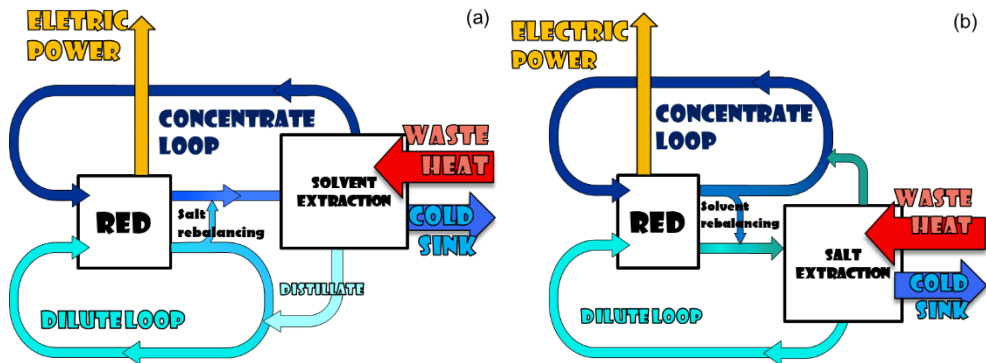


Figure 4.3. Schematic representation of the two regeneration processes: solvent extraction (a) and salt extraction (b).

In the case of evaporative regeneration processes, in principle any salt-water solution can be used. In such application, an optimal salt solution must have (i) low Boiling Point Elevation (BPE) and (ii) low enthalpy of vaporization. The enthalpy of vaporization influences the heat consumption of the evaporative unit, while the BPE affects the temperature of the heat source required and can limit the number of stages of a multi-stage evaporative process [21]. The latent heat depends mainly on the solvent nature. Water is the most widely used solvent, while organic solvents provide a lower latent heat. Therefore, the use of organic solvents can

theoretically reduce the specific energy consumption but, due to low salt solubility, low solution conductivity and reduced membrane compatibility, the power production unit is negatively affected so that the choice of such solvents is not viable. The *BPE* depends on the nature of the salt and its concentration. An accurate investigation about its effect in the evaporative regeneration unit is reported in *Chapter 5*.

The characterization of salt aqueous solutions requires the calculation of thermodynamic properties such as osmotic and activity coefficients in solution but also the identification of physical properties such as solubility, density, conductivity and viscosity. All this information is useful for theoretical calculations and for the development of advanced models.

In general, these solution properties depend on the concentration and operating conditions such as temperature and pressure. Then, a fully characterization is required in a wide range of conditions.

Most of the properties are in general available in the literature, but sometimes, for unconventional salts and/or in some specific conditions some data are missing. As already observed in *Figure 4.1*, activity and osmotic coefficients for KAc and CsAc water solutions are not fully available but just in a limited range of concentrations (i.e. from 0.1 to 3.5 mol/kg_{solv}) [135,141,142] and only at temperature of 25 °C. Then, further investigation is needed to extend this range. To this aim, a specific measurement cell was developed to assess the solution vapour pressure and regress the parameters of the Pitzer's model which allows to describe the osmotic and activity coefficients of potassium and caesium acetates in a wide range of temperature (20-90 °C) and molality (up to 9 molal). This activity was carried-out in collaboration with the University of Edinburgh during the PhD period abroad (February-July 2016, supervisor prof. S. Brandani).

4.2 Thermodynamics of electrolyte solutions

When an electrolyte is in contact with a polar solvent (e.g. water), a solvation process occurs: the solvent molecules (dipoles) interact with the ions, orienting themselves in the direction of the electric field and reducing the electrostatic force of the electrolyte lattice. As result of the solvation process, the electrolyte is separated into cations and anions uniformly disperse in the solvent. Due to the ion-ion and ion-solvent interactions, the behaviour of the solvent and solute in an electrolyte solution deviates from the ideal case when solute

concentration increases. These deviations are thermodynamically accounted by means of *activity coefficients* for ions and solvent.

The chemical potential of individual ionic species can be written as:

$$\mu_i = \mu_i^0 + RT \ln(a_i) \quad (4.1)$$

in which a_i is the activity of the i^{th} ion in the solution and μ_i^0 is the chemical potential of the i^{th} ions in the standard state (J/mol), T is the absolute temperature (K) and $R=8.3144$ J/(mol K) is the universal gas constant. Thermodynamic measurements yield properties of the solute and not of individual ionic species. Thus, the chemical potential for a generic electrolyte (MX) is given by:

$$\mu_{MX} = \mu_{MX}^0 + \nu RT \ln(m_{\pm} \gamma_{\pm}) \quad (4.2)$$

The μ_{MX}^0 term is a combination of the chemical potentials of the two ions in the standard (J/mol) state, $\nu = \nu_+ + \nu_-$ is the number of ions generated on complete dissociation, m_{\pm} (mol/kg_{solv}) and γ_{\pm} are the geometrical average of molality and activity coefficient of the two ions (coinciding with salt's ones for the case of monovalent salts). It is worth mentioning that the reference state for the solute is that of infinite dilution in the solvent, i.e. $\gamma_{\pm} \rightarrow 1$ as $m_{\pm} \rightarrow 0$.

For the generic solvent, the chemical potential is defined as:

$$\mu_s = \mu_s^0 + RT \ln(a_s) \quad (4.3)$$

in which a_s is the solvent activity and μ_s^0 is the solvent chemical potential in the standard state (J/mol). For the solvent the normal reference state is used, i.e. that of the pure liquid at the same temperature and pressure of the mixture. Pressure effects are negligible and therefore no pointing correction factors are needed.

The solvent activity in electrolyte solutions is given by the ratio of the solution fugacity (f_s) (bar) and pure solvent fugacity (f_s^0) (bar) at the saturation temperature:

$$a_s = \frac{f_s}{f_s^0} \quad (4.4)$$

If ideal behaviour in gas phase is assumed, *eq. 4.4* simplifies to:

$$a_s = \frac{p_s}{p_s^0} \quad (4.5)$$

where p_s and p_s^0 are the solution vapour pressure and the pure water vapour pressure (bar), respectively. *Eq 4.6* links measurable properties (i.e. vapour pressure measurements) to the activity of the solvent and the osmotic coefficient ϕ , which characterise the deviation of a solvent from ideal behaviour. The osmotic coefficient is related to the activity coefficient according to:

$$\phi = \frac{-1000 \ln a_s}{MW_s \sum_k \nu_k m_k} \quad (4.6)$$

where MW_s is the molar mass of the solvent (g/mol), m_k is the electrolyte molality in the solution (mol/kg), ν_k is the number of ions generated on complete dissociation, equal to 2 in the case of uni-univalent electrolytes.

The osmotic coefficient and the activity coefficient are related by the Gibbs-Duhem equation [1,13], which eventually leads to the following relationship:

$$-\ln \gamma_{\pm} = \int_{m=0}^m (1 - \phi) d \ln m \quad (4.7)$$

4.2.1 Pitzer's thermodynamic model

The most accurate approach to describe osmotic and activity coefficients of salt-water solutions is the ion interaction model of Pitzer [120], where the model parameters describing the interaction of ions in solution have to be determined from experimental data. In the Pitzer's model the long-range interactions between the charges are described using the Debye-Huckel term, while the short-range interactions are modelled using an empirical virial expansion. The coefficients of this expansion are the virial coefficients. The second virial coefficient is expressed in terms of the parameters $\beta_{MX}^{(0)}$, $\beta_{MX}^{(1)}$, while the third virial coefficient is C_{MX}^{ϕ} . The osmotic and salt activity coefficients can be calculated from the following equations, which are consistent with the Gibbs-Duhem relationship, *eq. 4.7*:

$$\phi - 1 = |z_+z_-|f^\phi + \frac{m}{m_0} \left(\frac{2\nu_+\nu_-}{\nu} \right) B_{MX}^\phi + \frac{m^2}{m_0^2} \frac{2(\nu_+\nu_-)^{1.5}}{\nu} C_{MX}^\phi \quad (4.8)$$

$$\ln \gamma_\pm = |z_+z_-|f^\gamma + \frac{m}{m_0} \left(\frac{2\nu_+\nu_-}{\nu} \right) B_{MX}^\gamma + \frac{3m^2}{2m_0^2} \frac{2(\nu_+\nu_-)^{1.5}}{\nu} C_{MX}^\phi \quad (4.9)$$

with

$$f^\phi = -A_\phi \frac{I_s^{0.5}}{1+b_P I_s^{0.5}} \quad (4.10)$$

$$f^\gamma = -A_\phi \left[\frac{I_s^{0.5}}{1+b_P I_s^{0.5}} + \frac{2}{b_P} \ln(1 + b_P I_s^{0.5}) \right] \quad (4.11)$$

$$B_{MX}^\phi = [\beta_{MX}^{(0)} + \beta_{MX}^{(1)} \exp(-\alpha_P I_s^{0.5})] \quad (4.12)$$

$$B_{MX}^\gamma = 2\beta_{MX}^{(0)} + \frac{2\beta_{MX}^{(1)}}{\alpha_P^2 I_s} \left[1 - \left(1 + \alpha_P I_s^{0.5} - \frac{\alpha^2 I_s}{2} \right) \cdot \exp(-\alpha_P I_s^{0.5}) \right] \quad (4.13)$$

in which ν_+ , ν_- , z_+ and z_- are the number and the charge of positive and negative ions, respectively, $m_0 = 1 \text{ mol} \cdot \text{kg}^{-1}$ is the standard molality, $b_P = 1.2 \text{ kg}^{1/2} \cdot \text{mol}^{-1/2}$ is a universal parameter; α_P is a numerical constant equal to 2 for univalent ions; I_s is the ionic strength and A_ϕ is the Debye-Huckel parameter for the osmotic coefficient. This is related to the long-range forces and depends on solvent type, temperature and pressure, according to *eq. 4.14*.

$$A_\phi = \frac{1}{3} \left(\frac{2\pi N_0 \rho_w}{1000} \right)^{\frac{1}{2}} \left(\frac{e^2}{4\pi\epsilon_0 \epsilon kT} \right)^{\frac{3}{2}} \quad (4.14)$$

with N_0 Avogadro's number (kmol^{-1}), ρ_w the density of the water (kg/m^3), e the electron charge (C), k Boltzmann's constant (J/K), and ϵ is the relative permittivity of water [120,143], and T is the absolute temperature (K), $\epsilon_0 = 8.854187817 \times 10^{-12} \text{ F} \cdot \text{m}^{-1}$ the permittivity of free space.

$\beta_{MX}^{(0)}$, $\beta_{MX}^{(1)}$ and C_{MX}^ϕ are salt specific parameters and can be obtained regressing experimental data of osmotic coefficients or from vapour pressure measurements. . For common salts like NaCl [144], LiCl [145,146], KCl [147], LiBr [146] several data are published in the literature but only few thermodynamic data are available for less common salts such as the acetate salts.

4.2.2 Boiling point elevation in electrolyte solutions

The thermal energy consumption (*TEC*) of the regeneration unit, defined as the thermal energy required to restore the concentration of the two solutions exiting from the *RED* unit, depends on heat of vaporization and boiling point elevation (*BPE*) (especially when multi-stage approaches are used). In particular, assuming similar heat of vaporization for salt solutions with the same solvent (e.g. water), the main effect of the salt consists of an increase (at fixed pressure) of the boiling temperature of the solution compared with the pure solvent (*BPE*). Experimental values of BPEs may be evaluated from vapour pressure measurements of salt solutions at different concentrations and temperatures.

In fact, *BPE* is related to the activity of the solvent in the solution and thus to the osmotic coefficient. The relevant equations used to evaluate the *BPE* via Pitzer's model are reported below.

$$BPE = T_{sol}^{eb}(p_s, m) - T_{pure}^{eb}(p_s) \quad (4.15)$$

where p_s is derived from eq.s 4.5, 4.6 and 4.8:

$$p_s = p_s(m, T_{sol}^{eb}) = \exp \left[-\frac{\phi(m, T_{sol}^{eb})}{1000} MW_s m v \right] \cdot p_w^0(T_{sol}^{eb}) \quad (4.16)$$

For a given p_s the boiling temperature of pure water (T_{pure}^{eb}) or its vapour pressure (p_w) can be evaluated using the Saul and Wagner Equation [148]. The actual calculation procedure for BPE starts from fixing a value of T_{sol}^{eb} , from which determining p_s (eq. 4. 15, after fixing a value for m) and, eventually, T_{pure}^{eb} (at p_s), thus obtaining the value of BPE from eq.(17).

4.3 BPE, osmotic and activity coefficients of salt solutions

4.3.1 Experimental

A schematic representation of the test-rig used to evaluate the partial pressure of salt solutions is shown in *Figure 4.4*. The main element of the system is a static cell consisting of a glass flask equipped with a thermal jacket, fed with water from a thermal bath in order to maintain the solution at a controlled temperature measured with a T-Type thermocouple.

The cell is provided with a glass arm, where the vacuum line and the pressure transducer are connected. The vacuum line is equipped with (i) a regulating valve, (ii) a cold trap, and

(iii) a vacuum pump. The glass tube connecting the sample flask to the pressure gauge was insulated and maintained at $T = 90\text{ }^{\circ}\text{C}$ with a heating tape to avoid vapour condensation. The solution in the sample flask was agitated during the measurement with a magnetic stirrer. Details of the experimental apparatus components are reported *Table 4.1*.

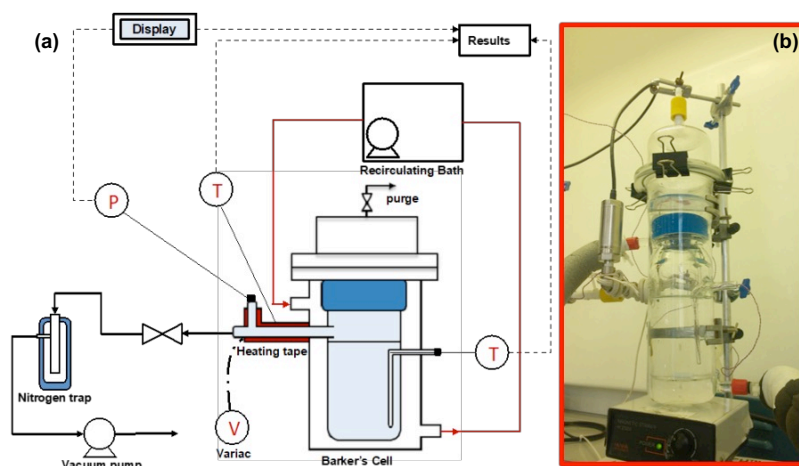


Figure 4.4 Schematic representation of the test-rig (a) and picture of the static cell (b)

Calibration of the system was carried out using pure de-ionized water to determine the temperature offset between the measured temperature and the temperature in the liquid phase. See appendix for details.

Table 4.1 Specification of the experimental apparatus equipment and reagents.

Components	Specifications
Pressure Transducer	General Electric UNIK5000, accuracy: $\pm 0.165\text{ kPa}$
Thermal bath	Julabo Corio CD-300F, temperature stability: $\pm 0.03\text{ }^{\circ}\text{C}$, resolution: $\pm 0.1\text{ }^{\circ}\text{C}$
Thermocouples	RS Pro Type T Thermocouple Copper probe 814-0153, accuracy: $\pm 0.1\text{ }^{\circ}\text{C}$
Heating tape	Electrothermal MC5
Vacuum pump	Edwards nXDS 6i
Magnetic stirrer	Hanna Instruments HI 200M
Balance	Mettler Toledo XS205 Dual Range, accuracy: $\pm 0.01\text{ mg}$
Sodium Acetate (NaAc)	Sigma Aldrich, purity $\geq 99.0\%$
Potassium Acetate (KAc)	Sigma Aldrich, purity $\geq 99.0\%$
Caesium Acetate (CsAc)	Sigma Aldrich, purity $> 99.9\%$
Lithium Chloride (LiCl)	Sigma Aldrich, purity 99.0%
Sodium Chloride (NaCl)	Sigma Aldrich, purity $\geq 99.0\%$
De-ionised water	Elga Centra R200

4.3.1.1 Test preparation

Solutions were prepared using anhydrous salt (analytical grade, purity > 0.99, Sigma-Aldrich) and de-ionised water was obtained from a (Elga Centra R200). The salt was dried at $T = 393 \text{ K}$ for 1 week until no mass variation was detected. The solution was prepared weighing separately the salt (scale accuracy $\pm 0.01 \text{ mg}$) and the water. For each test, the salt was dissolved in 250 g of water at room temperature and the solution was then loaded in the cell for the test.

Before cell loading, the sample solution is degassed with a sonic bath to remove air bubbles, then the solution was loaded inside the cell, making sure that its level is under the glass arm.

All the dissolved and gaseous air present in the cell was evacuated before running the experiment. Vacuum was obtained in two steps: the measurement cell (step 1) was cooled to 10°C in order to pull the vacuum at a temperature in which the solvent vapour pressure is reasonably low. Opening the vacuum valve, the pressure of the cell decreased until a constant value. Then, the valve was closed, the pressure inside the cell increased due to the degassing of the dissolved air present in the solution and some evaporation of the solvent. The cell (step 2) was heated to 50°C to facilitate the degassing process. When this condition was achieved the valve was opened briefly to evacuate the gas. After this, step 1 was repeated to achieve a good vacuum level. Any solvent evaporated during these steps was condensed in the liquid nitrogen trap and this amount of liquid was measured and the concentration of the solution corrected accordingly.

4.3.1.2 Test procedure

Starting from a temperature of 293.15 K , a stepwise increase of 10 K was adopted to reach a final temperature of 363.15 K , always ensuring the attainment of vapour-liquid equilibrium.

To test the experimental apparatus and procedure, experimental measurements of vapour pressures for three different salt-water solutions (NaCl, LiCl and NaAc). The resulting activities were converted to osmotic coefficients and compared with literature data.

4.3.2 Validation of the experimental methodology

The thermocouple used to evaluate the solution temperature is in a glass branch not directly in contact with the liquid. Therefore, in order to overcome the uncertainty of the sensor, the cell was first calibrated against water vapour pressures [148]. *Figure 4.5* shows the comparison of the temperature measured using the thermocouple and the actual boiling temperature of the solution. The equation used to correct the measured values is also reported in the same figure.

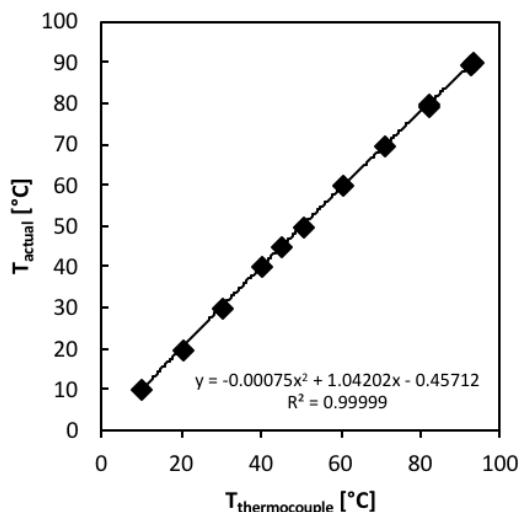


Figure 4.5 Temperature calibration curve of the thermocouple

In order to validate the overall methodology of extracting the Pitzer's model parameters from the vapour pressure data, the derived osmotic coefficients for three different salts are compared with Pitzer's model predictions and data reported in the literature. The salt analysed for the validation are (i) Sodium Chloride, (ii) Lithium Chloride and (ii) Sodium Acetate, within a wide range of compositions.

A comparison of osmotic coefficients obtained from experimental measurements of solution vapour pressure and the ones obtained using literature thermodynamic models is reported *Figure 4.6*. The model osmotic coefficients refer to calculated values obtained using literature virial coefficients, as in the case of NaCl [144] and KAc, or fitting [149] available literature model for osmotic coefficients, as in the case of LiCl [145]. For each salt, several molalities and solution temperatures were analysed.

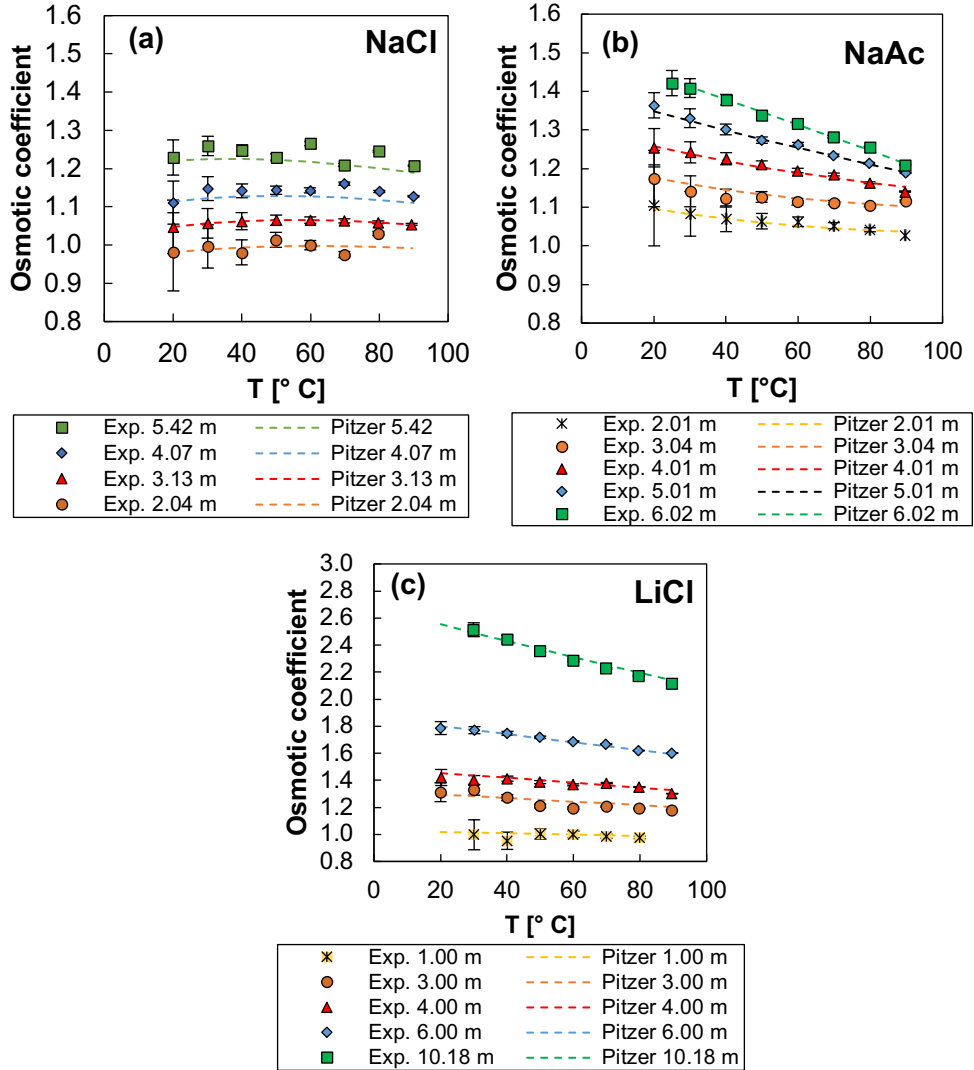


Figure 4.6 Comparison between experimental and Pitzer's model predictions of osmotic coefficient for NaCl (a), NaAc (b) and LiCl (c) as a function of molality and solution temperature. Pitzer's coefficients from literature date [144–146,149].

At low concentration and temperature (or vapour pressure) the relative experimental error increases. The error bars in the figures are evaluated according to the expression:

$$\Delta\phi = \frac{-1000}{2MW_s m} \frac{\Delta p}{p} \quad (4.17)$$

A very small deviation in vapour pressure can lead to an important deviation in ϕ , when the molality m tends to zero [150]. This means that the evaluation of experimental virial

coefficients through experimental osmotic coefficients with the proposed test rig can be done with a low error at concentrations above 2 molal and temperatures higher than 20°C, which are the conditions of interest in this study.

4.4 KAc and CsAc osmotic and activity coefficients.

Vapour pressure measurements for KAc- and CsAc-water solutions were used to evaluate the corresponding solution osmotic coefficients (*eq.s 4.5-4.6*), which are reported in *Figure 4.7* as a function of molality and temperature. For all the investigated salt-water solutions, the osmotic coefficients increase with the molality of the solution. The temperature dependence of the osmotic coefficient changes a significantly with salt type and molality.

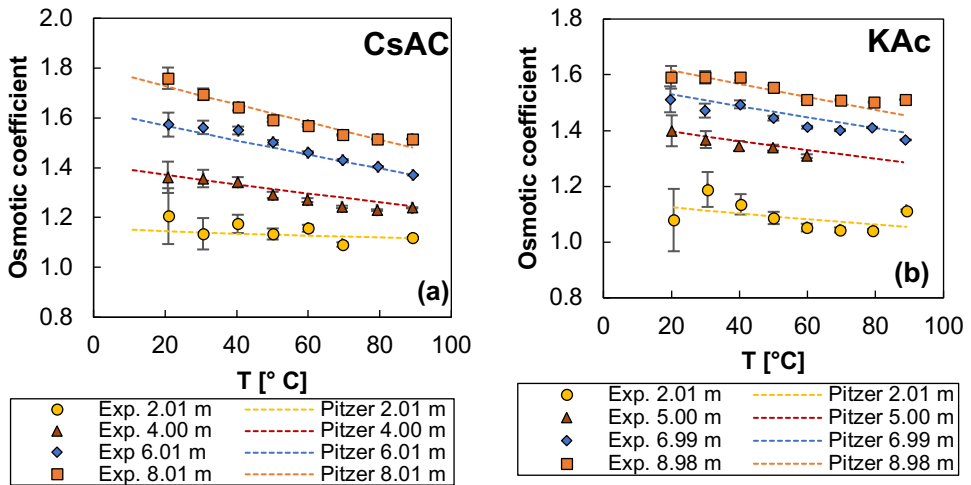


Figure 4.7 Comparison between calculated and experimental osmotic coefficient for caesium acetate (a) and potassium acetate (b) as function of temperature and solution molality.

In order to fit the experimentally evaluated osmotic coefficients reported in *Figure 4.7* using Pitzer's model (*eq.s 4.8, 4.10 and 4.12*), the virial coefficients were evaluated using the following correlations:

$$\beta_{MX}^{(0)} = b_{01} + b_{02}T \quad (4.18)$$

$$\beta_{MX}^{(1)} = b_{11} + b_{12}T \quad (4.19)$$

$$C_{MX}^{\phi} = 2(c_1 + c_2T) \quad (4.20)$$

where b_{0i} , b_{1i} and c_i are fitting parameters. The simple linear temperature dependence of the parameters is used here since it provides a fit that is within the experimental uncertainty and also because it allows for moderate extrapolation beyond the range of measurements.

A comparison of osmotic coefficient obtained from experimental measurements of vapour pressure (eq.s 4.5 and 4.6) and calculated ones (eq. 4.8), is depicted in *Figure 4.7*. The fitting parameters adopted in eq.s 4.20-4.22 are summarized in *Table 4.2*. In the same table, the root-mean-square error (*RMSE*), which is the difference between predicted values and actual values of ϕ is reported.

Table 4.2 Fitting parameters adopted to calculate the virial coefficients for CsAc and KAc.

	CsAc	KAc
b01	$3.292 \cdot 10^{-1}$	0.2044
b02	$-5.523 \cdot 10^{-4}$	$-1.662 \cdot 10^{-4}$
b21	-2.924	0.3611
b22	$1.101 \cdot 10^{-2}$	-
c1	$-6.088 \cdot 10^{-3}$	-0.0033
c2	$1.088 \cdot 10^{-5}$	-
RMSE	0.0237	0.0084

Previous studies [142] on Potassium and Caesium acetate aqueous solutions are available only at 298.15 K and limited to a maximum molality of 3.5 mol/kg_{solv}. The parameters presented in this work extend the range of applicability of the Pitzer's equations for both temperature, i.e. between 20 and 90°C, and molality, i.e. 8 mol/kg in the case of CsAc and 9 mol/kg in the case of KAc. A validation with literature data is reported in *Figure 4.8* at 25°C, as function of molality.

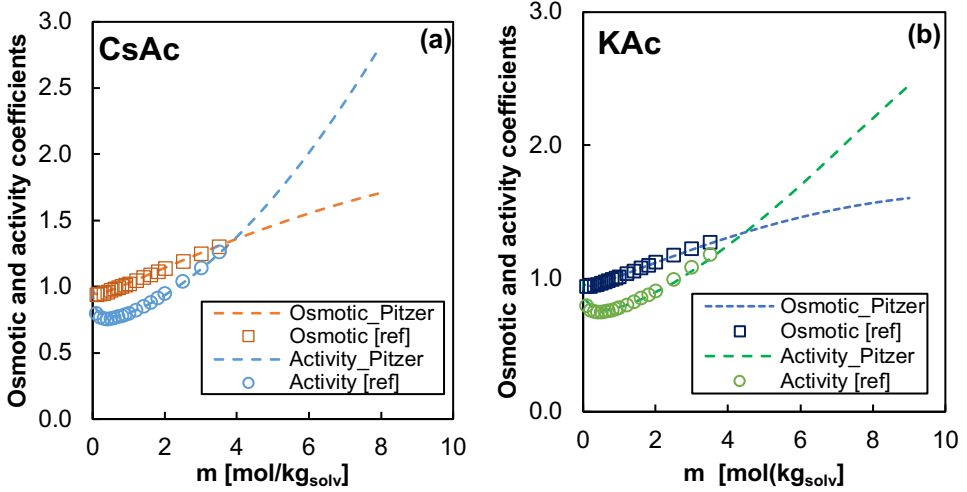


Figure 4.8 Comparison of calculated salt activity and osmotic coefficient for CsAc (a) and KAc (b) and literature information [141,142] as function of solution molality at 25°C.

A comparison of experimental *BPEs* and the ones calculated via Pitzer's model (see eq.s. 4.17 and 4.18) as a function of the solution boiling temperature and salt solution molality, is reported in Figure 4.9, for CsAc, KAc, NaCl, NaAc and LiCl water solutions. For all salts, experimental and calculation *BPE* are in excellent agreement.

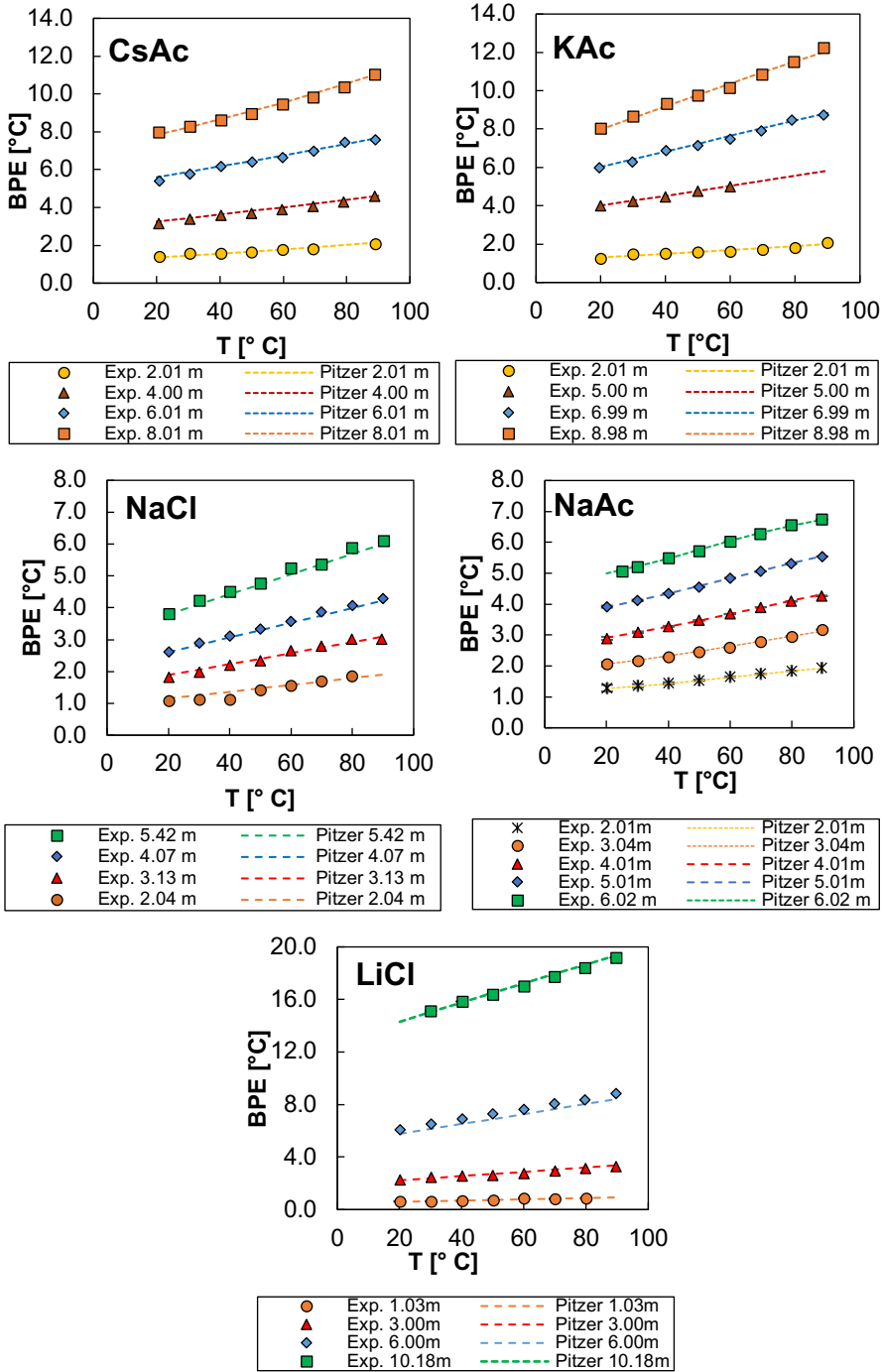


Figure 4.9 Calculated and experimental BPEs as function of molality and temperature for CsAc, KAc, NaCl, NaAc and LiCl. The square markers represent the experimental values while dashed curves refer to model predictions.

4.5 Gibbs free energy of mixing of artificial solutions

The Gibbs free energy of mixing of different artificial salt solutions was evaluated by using eq.s 2.1-2.2 and the osmotic and activity coefficients obtained from Pitzer's model using the experimental evaluated parameters. Only salts-water solutions of monovalent ions were considered in the analysis due to the fact that divalent ions produce lower *RED* performance due to lower OCV values and higher membrane resistances than monovalent ions [151]. Then, the salts considered in the analysis are Ammonium Bicarbonate (NH_4HCO_3), Lithium Chloride (LiCl), Lithium Bromide (LiBr), Sodium Chloride (NaCl), Potassium Chloride (KCl), Sodium Acetate (KAc), Caesium Acetate (KAc) and Potassium Acetate (KAc).

A comparison of the different Gibbs free energy of mixing resulting from the mixing of different salt-water solutions as a function of the high solution concentration ($\text{mol}/\text{kg}_{\text{solv}}$) at temperature of 25°C and fixing the dilute solution concentration equal to $10^{-6} \text{ mol}/\text{kg}_{\text{solv}}$ is reported in *Figure 4.10*.

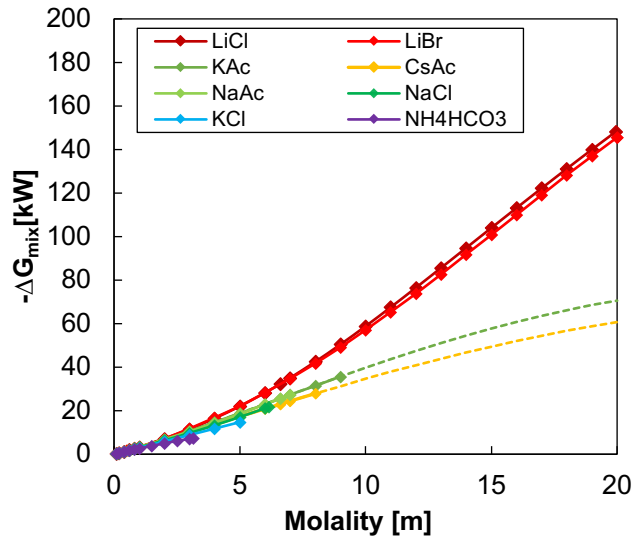


Figure 4.10 Comparison of Gibbs free energy of mixing for NH_4HCO_3 , NaCl , LiCl , NaAc , KAc and CsAc at 25°C , considering a dilute solution molality equal to $10^{-6} \text{ mol}/\text{kg}_{\text{solv}}$. The concentration intervals, where the Gibbs free energy is calculated using extrapolated activity coefficients are indicated using dashed lines.

Among the considered salts, the most promising salt in terms of Gibbs free energy of mixing are LiCl and LiBr which give the highest potential, i.e. $-148 \text{ kJ}/\text{kg}_{\text{high}}$ and $-140 \text{ kJ}/\text{kg}_{\text{high}}$ at their solubility. Thanks to their remarkable solubility and activity coefficients, also KAc

and CsAc have relevant Gibbs free energy, $-70 \text{ kJ/ kg}_{\text{high}}$ and $-60.7 \text{ kJ/ kg}_{\text{high}}$, respectively, which makes them interesting salts for the power generation in closed loop applications using solvent extraction regeneration unit. It is worth to noting that in comparison with saturated NaCl solutions the Gibbs free energy of mixing of LiCl and LiBr is seven times larger, while the one for KAC and CsAc is 3 times larger, highlighting the larger potential of closed loop applications with respect to open loop applications. The use of these salts in solvent extraction *RED-HE* is further investigated in Chapter 5.

Ammonium bicarbonate water solution, which is the only thermolytic salt-solution considered, has the lower potential in terms of power generation unit. However, this salt should give an easily regeneration process thanks to its thermal degradation properties, making ammonium bicarbonate salt one of the most promising for closed-loop application using salt extraction scheme and very low-grade heat ($40\text{-}100^{\circ}\text{C}$). A complete analysis of the use of ammonium bicarbonate solutions within a *RED-HE* is presented in *Chapter 5* and *6*.

4.6 Conclusions

Reverse electrodialysis in a closed-loop system is a promising technology for converting low-grade waste-heat into electricity. The adoption of a closed-loop arrangement allows the selection of different salt solutions. In particular, in this work, the possibility of using different salts from NaCl has been investigated

An experimental campaign has been carried out in a purposely-built laboratory set-up in order to characterise the thermodynamic properties of several salt solutions (LiCl, NaCl, NaAc, CsAc and KAc) through vapour pressure measurements in a constant volume cell. Experimental data were used to determine the virial coefficients in Pitzer's model, which allows evaluating activity and osmotic coefficients, as well as *BPE*, of all salt aqueous solutions. Compared to literature information, the novel data here obtained allowed to extend the range of applicability of Pitzer's model in terms of temperature and molality for the case of CsAc and KAc water solutions.

S **SECTION II:**
SOLVENT EXTRACTION
RED with Evaporative regeneration
strategy



SOLVENT EXTRACTION RED HE: Simplified analysis

Chapter Outline

ABSTRACT	115
5.1 INTRODUCTION	116
5.1.1 MED PROCES	117
5.1.2 MD PROCESS	119
5.2 THEORETICAL ANALYSIS OF SGP-MED HE	121
5.2.1 THERMAL ENERGY CONSUMPTION (TEC)	121
5.2.2 THERMAL AND EXERGY EFFICIENCY OF THE IDEAL RED ENGINE.....	126
5.3 SIMPLIFIED RED-MED MODEL	129
5.3.1 CIEMAT-MED MODEL RESULTS	130
5.3.2 RED-MED COUPLED SYSTEM.....	132
5.3.3 RED MODEL RESULTS.....	137
5.3.4 RED-MED INTEGRATED SYSTEM RESULTS	140
5.4 SIMPLIFIED RED-MD MODEL.....	146
5.4.1 MATHEMATICAL MODELLING.....	146
5.4.2 RESULTS AND DISCUSSION	151
5.5 CONCLUSIONS.....	162

Part of this chapter has been published in:

F. Giacalone, C. Olkis, G. Santori, A. Cipollina, S. Brandani, G. Micale, "Novel solutions for closed-loop Reverse Electrodialysis: thermodynamic characterisation and perspective analysis", Energy Volume 166, 2019, Pages 674-689 <https://doi.org/10.1016/j.energy.2018.10.049>

M. Micari, A. Cipollina, F. Giacalone, G. Kosmadakis, M. Papapetrou, G. Zaragoza, G. Micale, A. Tamburini, "Towards the first proof of concept of a Reverse ElectroDialysis Membrane Distillation Heat Engine", Desalination, Volume 453, 1 March 2019, Pages 77-88, <https://doi.org/10.1016/j.desal.2018.11.022>

P. Palenzuela, M. Micari, B. Ortega-Delgado, F. Giacalone, G. Zaragoza, D.C. Alarcon-Padilla, A. Cipollina, A. Tamburini, G. Micale, "Performance Analysis of a RED-MED Salinity Gradient Heat Engine", Energies 2018, 11, 3385; <https://doi:10.3390/en1123385>

Abstract

Reverse electrodialysis heat engines with solvent extraction regeneration units adopt thermal evaporative processes to restore the concentration of the two original solutions. To this aim, the main technologies proposed in the literature are membrane distillation (MD) and multi-effect distillation (MED).

In this chapter the influence of different salts on the performance of a theoretical SGP unit couple with a single stage and multi-stage evaporative regeneration unit are evaluated by considering the properties estimated in Chapter 4. Among the screened salts, from a thermodynamic point of view, LiCl, KAc and CsAc seem the most promising, thanks to their remarkable solubility.

Furthermore, simplified mathematical models were developed in order to predict the performance of a RED-MED HE and RED-MD HE fed by NaCl solutions, considering current state of the art units and future improved units. Results indicated that membrane properties improvements can lead the technology to reach interesting values of efficiency.

5.1 Introduction

A reverse electro dialysis heat engine with solvent extraction regeneration unit is a system where the restoration of the original conditions of the two streams occur by partial removal of the solvent from the exhausted concentrated solution, which is transferred to the exhausted dilute solution (see *Figure 5.1*). In principle in solvent extraction processes, free salt solvent is separated from the exhausted concentrate stream, then, before entering the regeneration unit a salt re-balancing process occurs, where part of the exhausted dilute stream (F_2) is mixed to the concentrate one ($F_{H,out}$). Then, the resulting stream (F_3) is fed to the solvent extraction regeneration unit, where low-grade heat is used to restore the original condition of the concentrate stream ($F_{H,in}$), while the vapour is condensed (F_4) and added to the remaining outlet dilute stream (F_1).

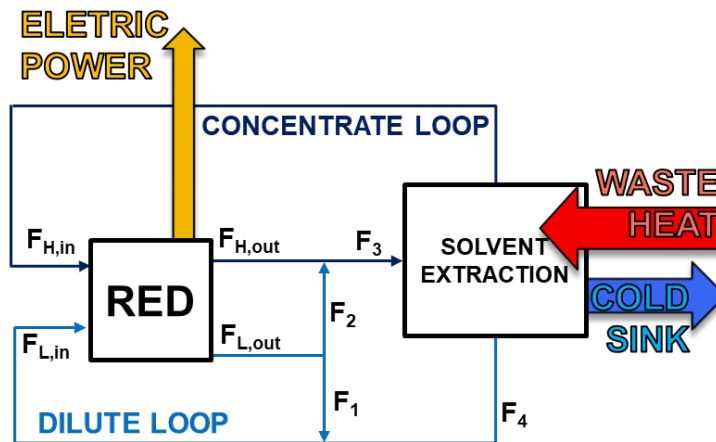


Figure 5.1. Process scheme of a solvent extraction RED-HE.

The main solvent extraction regeneration units proposed in the literature are based on thermally-driven evaporative processes such as multi-effect distillation (*MED*) and membrane distillation (*MD*).

The *MED* process is a thermal separation process based on multi-stage evaporation/condensation units or effects [21]. The main application of *MED* technology is for the case of thermal desalination processes of seawater using low grade heat, among which, *MED* represents the process with the highest thermal efficiency [152]. In fact, in a *MED* process the thermal energy is used multiple times in the form of latent heat to partially vaporize the solvent from a salt-solutions. In this way, it is possible to reach values of specific

energy consumption as low as 50-70 kWh/m³ of distillate produced [22]. The *MED* is intrinsically a large-scale technology which cannot be scaled-down to less than several hundreds of m³/day, which is a scale much larger than the laboratory one [153].

MD is an emerging membrane technology in the field of solvent separation based on thermally-driven separation process where microporous hydrophobic membranes are used [23]. Membrane Distillation is particularly advantageous for its modularity and operational simplicity, which makes it suitable for being operated at any scale, from the lab-scale up to the industrial level [154]. However, the energy consumption of the *MD* process is higher than the one of *MED*, i.e. around 100-200 kWh/m³_{distillate} [155].

Differently from salt extraction processes where specific thermochemical properties of solutions or mechanisms are involved in the regeneration unit, in principle any stable salt-water solutions at the operating conditions of the system is suitable for the operation. Then, a careful selection of the best salt-water coupled is required (see *Chapter 4*).

Only few works reported in the literature are focused on the case of *RED-HE* with solvent extraction regeneration unit. In particular, in 2017, Long et al. [39] performed a parametric study on a hybrid *MD-RED* system powered by NaCl solutions. The results indicated a maximum electric efficiency of 1.15%. In the same year, Tamburini et al. [19] analysed the performance of a *RED-MED HE* adopting a very simplified mathematical model approach for two different scenarios: i) current state of the art, where the *RED* unit adopts current membranes and *MED* energy consumption is 40 kW_{th}/m³; (ii) future state of the art, where the *RED* unit adopts future membranes and *MED* energy consumption is 25 kW_{th}/m³. In the current state scenario, a maximum energetic efficiency of 5% (27.9% exergy efficiency) was reported, while in the future state scenario the maximum efficiency reported is around 15.4% (86% exergy efficiency). In 2018, Hu et al. [44] performed a detailed theoretical analysis on the performance of a hybrid *MED-RED* heat engine. A maximum electrical generation efficiency of 1% was found coupling a *RED* unit with a 10 effects *MED* unit powered by low grade heat at 95 °C.

5.1.1 MED process

In a multi-effect distillation unit, the vaporization of the solvent is achieved by dividing the process in sub sequential steps. Indeed, in each effect, part of the feed solution is evaporated and the rest is concentrated in salts (brine). Only the heat powering in the first stage is

provided by an external energy source, while the other stages are powered by the vapour produced in the previous stage. It is worth noting that low-grade heat produced in any industrial process can be used as the external energy source.

The heat transfer from the condensing vapour to the evaporating brine is controlled by reducing the pressure along the stages, so that in each evaporative stage, the solvent reaches the boiling point at lower temperatures. In this way, the thermal efficiency of the process is increased almost proportionally to the number of stages.

In some configurations, part of the vapour produced in each effect is used to preheat the feed solution in the preheater, where part of it condenses. All the condensates, from the preheaters and evaporators, are collected in the flash boxes, where a small part of vapour is produced and introduced in the correspondent effect. The condensation of vapour produced in the last effect takes place in an external tube bundle called end condenser, using cooling water from a cold source. A schematic representation of the process is reported *Figure 5.2*.

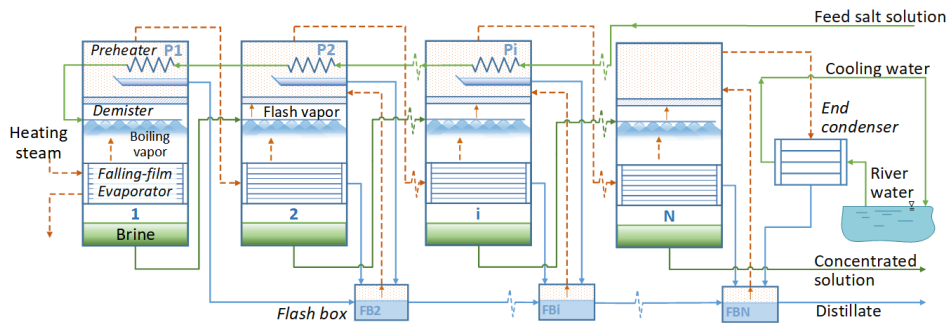


Figure 5.2. Scheme of the FF-MED selected regeneration unit.

The thermal energy efficiency of desalination MED plants is mainly limited by the top brine temperature, i.e. the maximum temperature that can be achieved in the first effect. When a natural solution is used, (e.g. seawater), scaling and strong corrosion problems [156] occur if temperatures are higher than 70°C. This temperature limit is overcome if artificial salt-water solutions different from seawater (e.g. without bivalent ions) are used, as in the case of MED unit for *RED-HE* regeneration unit. Then, the top brine temperature can be increased above 70°C and the potential for improving the energy efficiency becomes larger, thanks to the increase of the number of effects, which leads to a potential reduction in the specific thermal consumption of the separation process.

MED plants can be classified based on the direction of the heat and feed flows in: (i) *forward feed*, (ii) *parallel feed* and (iii) *backward feed* [22,157]. (i) In *forward feed* the feed is

introduced in the first effect and goes through the plant from the first to the last effect. Both feed and vapour flow in the same direction (ii). In *parallel feed*, the global feed flow rate is split and fed in each effect. Even in this case, feed and vapour flow in the same direction. Conversely, in *backward feed* (iii) vapour and feed flow in opposite direction, the feed solution enters the last effect and goes through the plant reaching the first effect.

In the case of a *MED* system as regeneration unit, the best configuration is forward feed. This configuration reduces the average thermal losses due to the Boiling Point Elevation (*BPE*) as the maximum feed concentration is reached only in the last stages operating at lower temperatures (see Chapter 4). The *BPE* often results as a limiting factor for a multi-stage regeneration unit of a *RED* closed loop system. In fact, the higher the *BPE*, the higher the temperature (i.e. pressure) drop required from one stage to the following. Thus, the number of stages is reduced.

5.1.2 MD process

In membrane distillation, a microporous hydrophobic membrane is used. The membrane is interposed between two channels, i.e. (i) the feed channel where a heated water solution is fed and (ii) the cold channel for the permeate. The hydrophobic nature of the membrane allows the passage of vapour only, avoiding the liquid transfer. Then volatile species in the feed solution evaporate from the hot solution and diffuse through the membrane under a temperature/partial pressure driving force, reaching the permeate channel where are condensed or removed [22,23]. A schematic representation of the process is reported in *Figure 5.3*.

In comparison to normal distillation technology, in *MD* process low temperature (typically ranging between 40-80°C) and pressure are enough to generate acceptable transmembrane fluxes (1-40 kg/m² h).

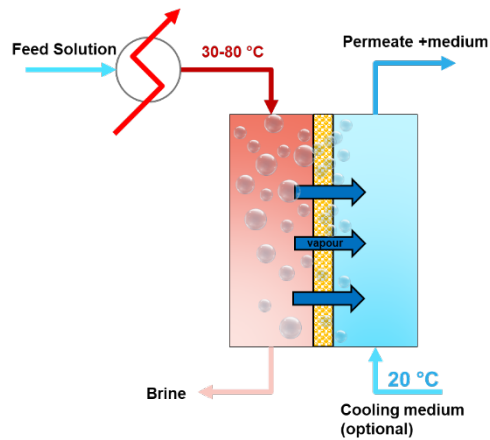


Figure 5.3. Schematic representation of the MD process.

Four different types of MD membrane modules were proposed so far, as described in the following:

- (i) *Direct contact membrane distillation (DC-MD)*, where the cooling solution flows in the permeate channel in direct contact with the membrane;
- (ii) *Air-gap membrane distillation (AG-MD)* where an air gap is interposed between the membrane and a condensation surface where the permeated vapour is condensed;
- (iii) *Sweeping gas membrane distillation (SG-MD)* where the permeate is driven out from the membrane module using a sweeping gas and then it is condensed outside;
- (iv) *Vacuum membrane distillation (V-MD)* where vacuum is applied in the permeate channel allowing the extraction of the permeated vapour which is condensed outside.

5.2 Theoretical analysis of SGP-MED HE

In this section, the influence of salt-water solution on the performance of *SGP* closed loop system using single and multi-stage evaporative regeneration units is investigated. In particular, the thermodynamic properties of salt solutions reported in *Chapter 4* are here used to perform estimation on the thermal energy required by single and multi-stage evaporative regeneration units for selected salts. Finally, the Gibbs free energies of mixing evaluated in *Chapter 4* are here combined to the thermal energy consumptions in order to evaluate the theoretical thermal and exergy efficiency of a closed-loop *SGP* engine operating with different salt-solutions.

5.2.1 Thermal Energy Consumption (*TEC*)

The energy consumption of an evaporative regeneration unit can be approximately evaluated considering only the contribution of the energy required to evaporate the solvent, neglecting the sensible heat needed to heat up the solutions. Therefore, in a single-stage evaporative regeneration unit the thermal energy consumption per unit of kg of solvent is equal to the solvent's latent heat of evaporation (for water $\lambda_{ev}=2260$ kJ/kg at 100°C). In a multi-stage regeneration unit, the thermal energy consumption depends on the number of stages adopted. The larger the number of effects, the larger the thermal integration of the process which requires less external energy to produce the same amount of distillate. The number of effects depends on the temperature of the heat used in the first effect and on the *BPE* of the specific salt-water solution considered.

In order to quantify the effect of using different type and concentration of salt-water solution in a multi-stage regeneration unit, a simple mathematical model was developed to evaluate the minimum thermal power consumption, maximizing the number of stages. A schematic representation of the *MED* plant configuration considered is reported in *Figure 5.4*.

The calculation starts from the assumption of a fixed driving force (ΔT_{exch}) equal to 2°C, required in the heat exchanger to transfer the heat from the steam to the brine. The temperature of the solution in the k^{th} stage ($T_{sol,k}^{eb}$) is calculated subtracting ΔT_{exch} to the temperature of the condensing vapour obtained in the previous stage ($T_{vap,k-1}^{cond}$):

$$T_{sol,k}^{eb} = T_{vap,k-1}^{cond} - \Delta T_{exch} \quad (5.1)$$

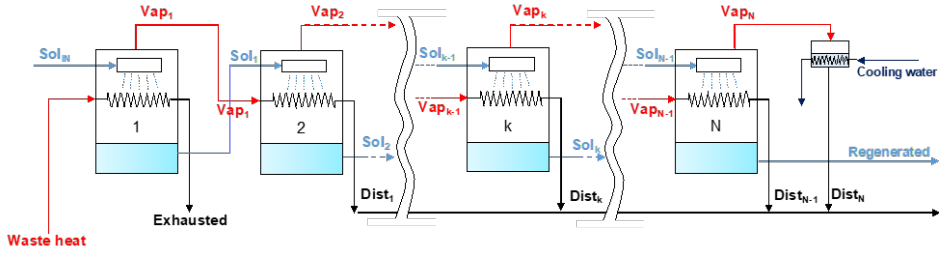


Figure 5.4. Schematic representation of a multi-stage regeneration unit

In the first stage, $T_{vap,k-1}^{cond}$ is the temperature of the external waste heat, fixed at 100°C for the present analysis. In each k^{th} stage the salt solution and the generated vapour are in equilibrium ($T_{sol,k}^{eb} = T_{vap,k}^{eb}$), but due to the *BPE*, a superheated vapour is produced. When reaching the following stage, the super-heated vapour cools down to the condensing temperature and, eventually, condensates by transferring the latent heat of condensation to the boiling brine. As an example, the temperature profiles (along the stages) of generated vapour, evaporating brine and condensing vapour in the subsequent stage is reported in *Figure 5.5* for the case of a regeneration unit consisting of 4 stages and fed by a 4.6 mol/kg_s solution of KAc. Then, the condensation temperature of the vapour in the k^{th} stage is calculated as:

$$T_{vap,k-1}^{cond} = T_{sol,k-1}^{eb} - BPE \quad (5.2)$$

where *BPE* is evaluated at the stage outlet brine molality.

The solvent enthalpy of vaporization ($\lambda_{ev,i}$) in kJ/kg is a function of the boiling temperature of the solution according to the Watson's equation [158]:

$$\lambda_{ev,k} = \lambda_{ev,n} \left[\frac{T_c - T_{sol,k}^{eb}}{T_c - T_n^{eb}} \right]^{0.38} \quad (5.3)$$

where $\lambda_{ev,n} = 2260 \text{ kJ/kg}$, $T_{ev,n} = 373 \text{ K}$ are the normal latent heat and boiling temperature of pure water, while $T_c = 647.3 \text{ K}$ is the critical temperature of water.

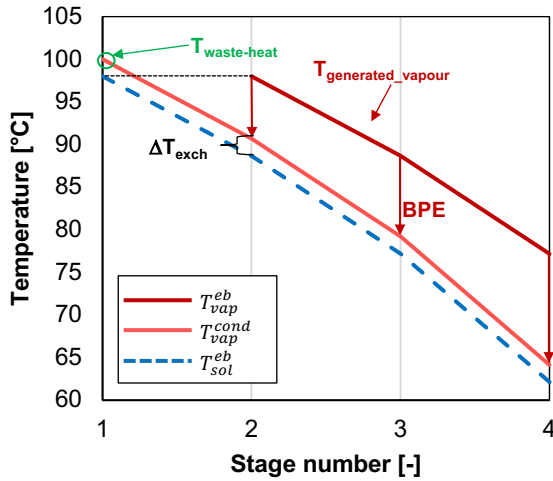


Figure 5.5. Example of temperature profile of generated vapour in the previous stage ($T_{v,eb}$), condensing vapour ($T_{v,cond}$) and boiling solution ($T_{sol,eb}$) along the stages. *KAc* solution, inlet molality 4.63 mol/kg_s, outlet molality 17 mol/kg_s.

The mass of solution exiting from the k^{th} stage ($w_{sol,k}^{out}$) is calculated as:

$$w_{sol,k}^{out} = w_{sol,k}^{in} - \frac{Q_k}{\lambda_{ev,k}} \quad (5.4)$$

Where $w_{in,i}^{sol}$ is the inlet mass of solution and Q_i the heat provided by the condensation of the vapour produced in the previous stage (w_{i-1}^{vap}) computed according to:

$$Q_k = w_{vap,k-1} \cdot \lambda_{ev,k-1} \quad (5.5)$$

For the first stage Q_1 is the heat provided as low-grade heat and represents the *TEC* of the multi-stage regeneration unit.

The molality of the solution feeds in the first stage was evaluated considering the equilibrium concentration given by the mixing of 1 kg of concentrate solution (variable concentration from 0.1 to 17 mol/kg_s, or up to the solubility limit for less soluble salts) to 1 kg of dilute solution ($m_{dil}=10^{-6}$ mol/kg_s), according to the conditions fixed in the theoretical calculation of the Gibbs free energy (see section 4.5).

Fixing a feed solution molality, the *TEC* in the regeneration unit is evaluated by maximizing the number of stages to obtain the vaporization of 1 kg of solvent limiting the pressure of the solution in the last stage to a minimum of 0.05 bar.

A comparison of calculated *BPEs* of different salt aqueous solutions is reported in *Figure 5.6*. In particular *Figure 5.6-a*, shows *BPEs* as a function of the boiling solution temperature, fixing the solutions concentrations at 5 mol/kg. A linear dependence of *BPEs* from boiling temperature is observed for all the salts considered. In *Figure 5.6-b*, *BPEs* are plotted as a function of solution molality, fixing the boiling temperature at 90°C. For NaAc and NaCl, *BPE* was calculated up to saturation molality, referring to the data reported in [133]. In the case of LiCl, KAc and CsAc, *BPE* was calculated up to a maximum molality of 17 mol/kg_s.

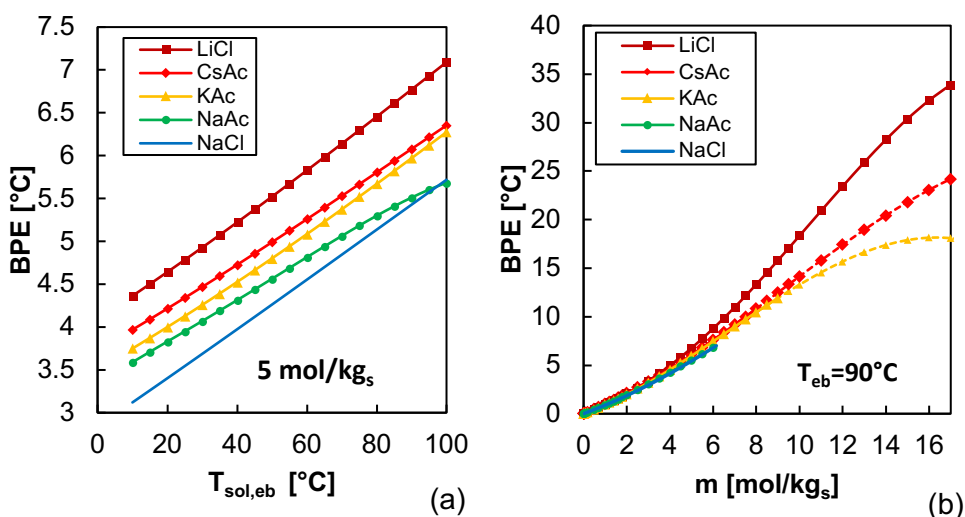


Figure 5.6. Comparison of computed Boiling Point Elevation (*BPE*) for NaCl, LiCl, NaAc, KAc and CsAc water solutions as function of solution boiling temperature (a) at 5 mol/kg, and as function of solution molality (b) at 90°C. The concentration intervals, where the *BPE* is calculated using extrapolated osmotic coefficients are indicated using dashed lines.

Referring to LiCl, CsAc and KAc, for concentrations higher than 5 molal, the *BPE* increases rapidly with the salt concentration. In the case of LiCl, at 90°C the *BPE* reaches values of about 18°C at 10 mol/kg_s and of 34°C at 17 mol/kg_s. Relatively lower *BPE* values are observed for the two acetates (i.e. CsAc and KAc) ranging between 13-14°C at 10 mol/kg_s and between 19-25 °C at 17 mol/kg_s. For these salts at high concentration, the ion-water and ion-ion interactions are so important that they largely affect the solution vapour pressure. In these conditions, a thermally driven regeneration unit would require more thermal energy. In fact, the possibility to adopt a multi-stage configuration to increase the thermal efficiency of the regeneration unit is limited to few stages.

Whit this respect, *Figure 5.7-a* reports the maximum number of stages for a multi-stage distillation unit used to restore the original molality by evaporating 1 kg of water. When an outlet solution molality of 17 mol/kg_s is considered, the maximum number of stages is equal to 5 in the case of CsAc, 4 in the case of KAc while it is reduced to 2 in the case of LiCl. The lower the number of stages, the higher the thermal power required, which is equal to 1150 kJ in the case of LiCl, 585 kJ in the case of KAc and 480 kJ in the case of CsAc (*Figure 5.7-b*).

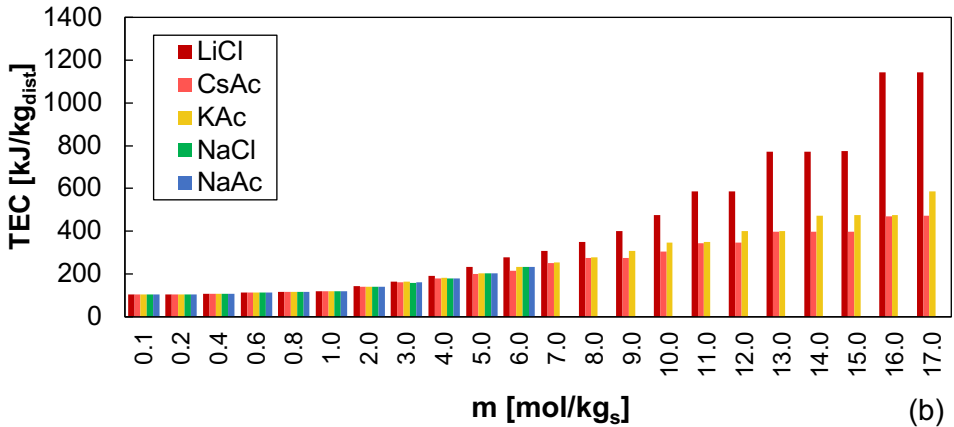
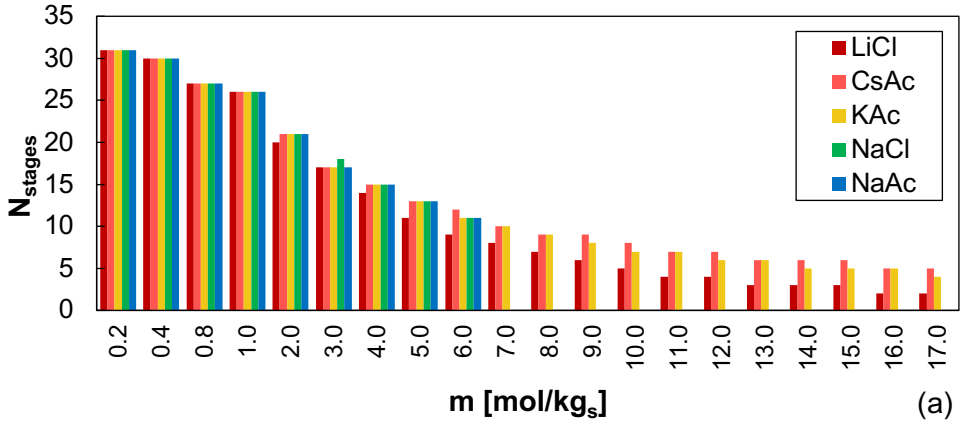


Figure 5.7. Maximum number of stages (a) and TEC (b) of the MED unit as function of the regenerated solution. $T_{waste-heat}=100^{\circ}\text{C}$, $T_{last}=30^{\circ}\text{C}$ $\Delta T_{exch}=2^{\circ}\text{C}$. Dilute molality= 10^{-6} mol/kg_{solv}.

At lower molality values (i.e. 6 mol/kg_s) close to the saturation molality for NaCl and NaAc, the *BPE* reaches maximum values around 6-9 °C for all salts. In this case, a thermally driven regeneration unit can work at lower temperature compared to the previous case and if a multi-stage configuration is considered, more stages can be adopted (i.e. 9-12), with a corresponding *TECs* ranging between 200-280 kJ. In all cases, a *TEC* around 100 kJ is

obtained when very low outlet molality is considered, i.e. 0.2 mol/kg_s, thanks to the adoption of 32 stages (maximum value considering $\Delta T_{exch} = 2^\circ\text{C}$).

Reducing the ΔT_{exch} , results in an increase of the maximum number of stages and a decrease of thermal energy consumption in the regeneration unit, but on the other hand produces a dramatic increase of the heat transfer area required, thus making the scenarios technically and economically infeasible.

5.2.2 Thermal and Exergy Efficiency of the ideal RED engine

The effect of using different salt-solutions within a *RED* heat engine can be analysed looking at the global thermal efficiency for both single and multi-stage regeneration unit. The theoretical thermal efficiency of the global system using a single evaporative regeneration unit ($\eta_{th,single}$) is evaluated as:

$$\eta_{th,single} = \frac{-\Delta G_{mix}}{TEC} = \frac{-\Delta G_{mix}}{2260 \text{ kJ}} \quad (5.6)$$

where ΔG_{mix} is the mixing free energy due to the mixing of 1kg of concentrate solution (variable concentration from 0.1 to 17 mol/kg_s, or up to the solubility limit for less soluble salts) and 1 kg of dilute solution ($m_{dil} = 10^{-6}$ mol/kg_s). Results for the salt-solution screened in this study are reported in *Figure 4.10*.

In the case of a multi-stage distillation process ($\eta_{th,multi}$), the thermal efficiency becomes:

$$\eta_{th,multi} = \frac{-\Delta G_{mix}}{TEC} = \frac{-\Delta G_{mix}}{Q_1} \quad (5.7)$$

The ratio of the thermal efficiency by the Carnot efficiency (η_C) gives the exergy efficiency:

$$\eta_{ex,i} = \frac{\eta_{th,i}}{\eta_C} \quad (5.8)$$

where η_C is evaluated between the lowest (298.15 K) and the highest (373.15 K) temperatures of the cycle.

It is worth to noting that the maximum achievable energy of mixing has been assumed to compute the power output (as in [159]), though in practical applications such conditions might be not realizable as discussed in *Section 3.1*.

The effect of using a different type of salt and solution molality on the theoretical thermal and exergy efficiency of the *RED* heat engine are reported in *Figure 5.8-a* for a single stage

evaporative regeneration unit and in *Figure 5.8-b* in the case of a multi-stage distillation process. The thermal efficiency of the single stage system is a monotonic function of the solution molality. A similar results was obtained by Carati et al. [159], who performed a theoretical analysis of a *SGP* engine based on the use of $MgCl_2$, $NaCl$ or $NaOH$ solutions and adopting a single distillation unit for the regeneration. Also in that case, the highest efficiency was achieved for salts with the highest *BPE*, thanks to their highest Gibbs free energy of mixing.

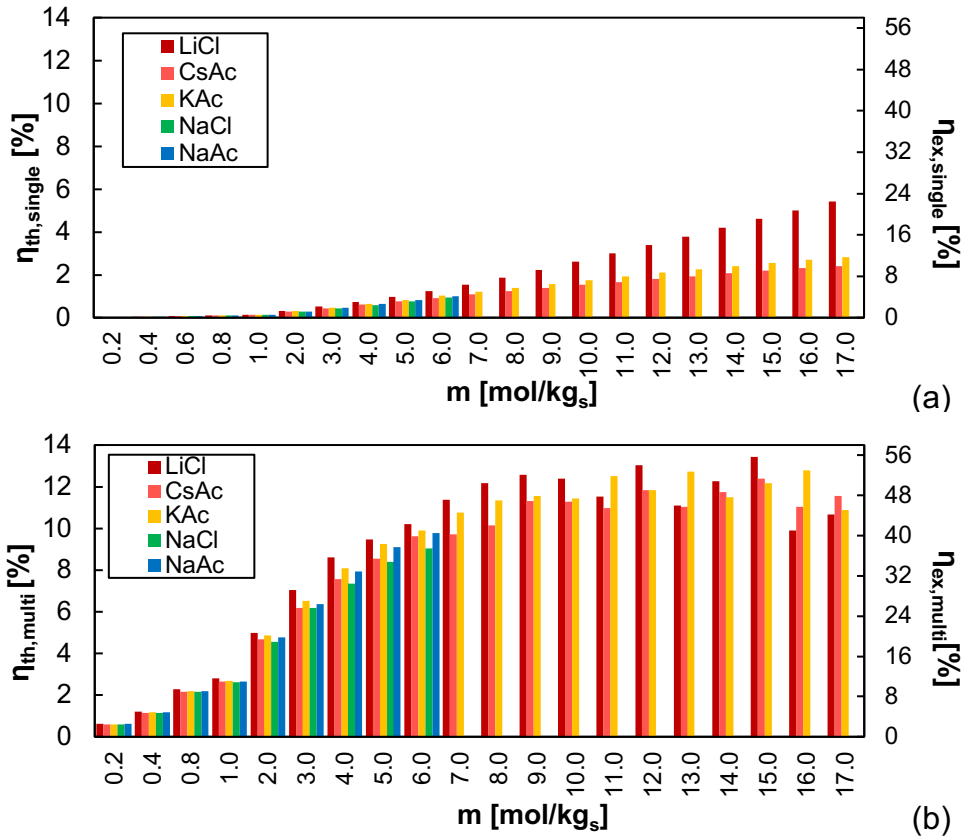


Figure 5.8. Thermal and exergy efficiency for an ideal RED heat engine using a single stage (a) and in a multi stage regeneration unit. $T_{waste\ heat}=100^{\circ}C$, $T_{last}=35^{\circ}C$ $\Delta T_{exch}=2^{\circ}C$. Dilute molality= 10^{-6} mol/kg_{solv}.

In the case of less soluble salts, i.e. $NaCl$ and $NaAc$, thermal and exergy efficiency maintain a monotonic behaviour also when a multi stage process is considered, because the increase in the Gibbs free energy with the solution molality prevails on the increase of the thermal energy consumption. For both salts ($NaCl$ and $NaAc$) a maximum thermal efficiency

around 10% is observed at 6 mol/kg_s using 11 effects. The thermal efficiency of the multi stage regeneration unit is ~10 times higher than the one of the single stage when 6 mol/kg_s concentrate solutions are regenerated.

Conversely, the efficiency of the multi stage system is not a monotonic function of the molality due to the balance of the two different contributions: (i) the increase of the Gibbs free energy of mixing and (ii) the decrease of the number of effects (or the increase of the *TEC*). As a result, the highest thermal efficiencies around 13% are achieved for LiCl at 15 mol/kg_s and 2 stages while for KAc at 17 mol/kg_s and 4 stages. Slightly lower thermal efficiency of about 12.5% is obtained for CsAc at 15 mol/kg_s. Notwithstanding the Gibbs free energy of mixing of KAc and CsAc are remarkably lower than the one of LiCl, similar overall performance can be obtained from the three salts thanks to the adoption of a suitable multi-stage evaporative regeneration unit.

Solubility, activity and *BPE* are the three thermodynamic features mostly affecting the performance of a *RED*-heat engine. The higher the salt solubility, the higher the *BPE*, but the lower the partial pressure of water in equilibrium with the solution. Thus, an optimal trade-off has to be identified between large chemical energy stored in the solution (depending on salt activity), which is released by the mixing process, and low energy requirements for the separation of the solvent for regeneration. The latter can be dramatically affected by high *BPE* where multiple-stage evaporation systems are adopted.

The use of acetate salts can lead to enhanced performances with respect to NaCl solutions, thanks to higher free energy of mixing and higher solubility. At the same time, multi-stage regeneration units lead to a remarkable reduction of the thermal energy consumption, thus enhancing the process overall efficiency, though reducing the available driving force increasing the heat transfer area requirements.

The highest thermal efficiency around 13%, corresponding to an exergy conversion efficiency of about 50%, was observed for KAc and LiCl at molalities between 15 and 17 mol/kg_s, though the effect of molality becomes almost negligible above 10 mol/kg_s.

With this respect, operating at lower concentrations might lead to advantages in terms of better performance of the actual ion exchange membranes, which are known to lose significantly permselectivity when solute concentration increases above 5-10 M. This points to the fact that specific interactions between salt solutions-membranes can be the real controlling aspects in the performance enhancement of this technology, thus requiring a closer consideration of the most recent advances in *IEMs* technology and their future perspectives.

5.3 Simplified RED-MED model

This section is devoted to the performance analysis of a simplified *RED-MED HE* fed by NaCl-water solution. To this aim, the mono-dimensional *RED* model validated and presented in *Chapter 2* is coupled to mathematical correlations, which evaluate the performance of the *MED* process as function of inlet-outlet concentrations in the unit. This activity was carried-out in collaboration with the Centro de Investigaciones Energéticas, Medioambientales y Tecnológicas (*CIEMAT -Almeria*), which provided *MED* simulation results in different operating conditions useful to obtain the performance correlations for the *MED* unit.

The mathematical model developed by CIEMAT, it is based on the mass and energy balances applied to the different elements of the plant, along with the heat transfer equations for heat exchangers. The model has been implemented in the *Engineering Equation Solver* software environment [160], which contains libraries for the thermo-physical properties of pure water and steam according to the *IAPWS* Formulation 1995 [161]. For the cooling flow required in the condenser, river water has been considered [162,163]. The model is a steady-state model for a *Forward feed-MED* plant thoroughly described in [164], including purposely developed correlations for the physical-chemical properties of the saline solution (BPE, latent heat of vaporization, enthalpy, density, specific heat, etc.). Also, the working range for several parameters has been enlarged, e.g. the heating steam temperature, can range between 60 °C and 100 °C and the recovery ratio between 10 and 70%. Finally, a proper initialization and bound of the variables is needed for the convergence of the *MED* model. A brief resume of the most significant equations of the cited model is presented in the Appendix (A.2).

The performance of the *MED* unit was identified by (i) the specific thermal consumption (*STC*) defined as the ratio between the thermal power supplied in the first effect and the distillate flow rate, and (ii) the corresponding number of effects (N_{stage}).

The *MED* model simulation results were carried-out in order to minimize the thermal power consumption of the system, considering the following assumptions:

1. The theoretical number of effects has been set in order to maximise the thermal efficiency of the system, yet guaranteeing a minimum effective driving force in each effect of at least 1°C. The total number of effects is significantly limited in the cases of high values of concentration due to high values of *BPE* reached in the last effects.
2. In all cases, the temperature of the cooling water at the inlet of the condenser has been set at 20°C.

3. The temperature of the feed salt solution at the inlet of the first preheater of the *MED* plant has been set as 25°C (this is the operating temperature assumed for the *RED* process).
4. In all cases, the temperature of the concentrated solution in the last effect was assumed equal to 35°C and the total distillate production equal to 100 m³/day, respectively.
5. The temperature of the external heating steam was set equal to 100°C

The operating conditions for the simulations are shown in *Table 5.1* considering a matrix of tests in which the inlet concentration of the salt solution ($C_{MED,in}$) and the recovery ratio (*RR*), defined as the ratio of the distillate flowrate to the inlet feed flow-rate are varied. The *RR* has been fixed in order to cover a wide range of *MED* outlet concentrations, up to a maximum of 5M. For each value of $C_{MED,in}$, the higher the *RR* the sooner the limit value of 5M is achieved. Therefore, at high values of $M_{MED,in}$ a finer discretization of *RR* values is adopted. For each inlet condition ($C_{MED,in}$ and *RR*), the number of effects (N_{stage}) minimizing the *STC* has been determined. The results of these simulations have been used to obtain two correlations (*STC* and N_{stage}) to be used in the integrated system.

Table 5.1 Matrix of simulations performed to investigate *MED* process performance

$C_{MED,in}$ (mol/l)	Recovery Ratio (%)									
0.5	10	15	20	25	30	40	50	60	70	80
1	10	15	20	25	30	40	50	60	70	80
1.5	10	15	20	25	30	40	50	60	70	
2	10	15	20	25	30	40	50	60		
2.5	10	15	20	25	30	40	50			
3	10	15	20	25	30	40				
3.5	10	15	20	25	30					
4	10	15	20							

5.3.1 CIEMAT-MED model results

Part of the results provided by *CIEMAT* for the minimum *STC* and corresponding N_{stage} is reported in *Figure 5.9* as a function of the inlet solution and recovery ratio. It is worth to

noting how the initial concentration significantly limits the number of effects allowed (especially for values above 1.5-2 M, where the effect on *BPE* raise becomes important) and also has a direct influence on the specific thermal consumption achieved. When the number of effects can be kept constant (e.g. with inlet salt concentration from 0.5 to 1.5 or 2 M), the *STC* only slightly decreases with the *RR*. In fact, the temperature difference between vapour generation and subsequent condensation is increased by the higher values of *BPE*. This leads to a reduced latent heat of evaporation (at higher temperature due to the *BPE*) compared to the latent heat of condensation of the vapour in the subsequent tube bundle, thus improving the thermal integration of the multi-stage system. However, this is visible only at very high *RR*, where an increase in *STC* is observed when increasing the inlet concentration.

The major influence of inlet concentration, however, is due to the lower number of effects, which dramatically reduce the thermal efficiency of the multi-effect distillation process. On the other hand, the higher the *RR* the lower the flow rate of the feed salt solution through the preheaters. This reduces the amount of vapour consumed and enhances the overall efficiency of the system. *STC* also significantly decreases with the operating temperature, as the number of effects can be increased by increasing the temperature of the energy source provided to the *MED* plant. A minimum value of 23 kWh/m³ at 100 °C and inlet concentration of 1.5 M is achieved.

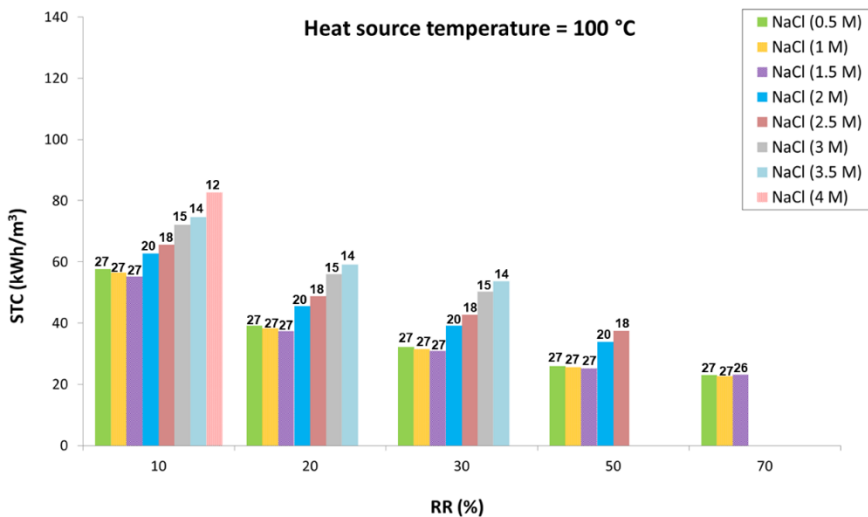


Figure 5.9. Variation of the specific thermal consumption with the recovery ratio at different inlet concentrations with a heat source at 100 °C.

5.3.2 RED-MED coupled system

A scheme of the coupled *RED-MED* system is shown in *Figure 5.10*. Here the *RED* stack converts an initial artificial salinity gradient into power, while the *MED* unit acts as a regeneration process, re-establishing the initial conditions of the two solutions exiting from the *RED* unit. The distillate produced in the *MED* unit is theoretically free of salts, then two mixers are used to restore in the two loops the mass of salt exchanged in the *RED* stack.

In particular, a fraction of the outlet dilute solution from the *RED* unit is mixed with the outlet concentrate (*Mixer 1*), restoring the salt content of the feed solution in the concentrate loop. Thus, the flow rate of the bypass solution (\dot{V}_{bypass}) is calculated by the following equation:

$$C_{H,out} \dot{V}_{H,out} + C_{L,out} \dot{V}_{bypass} = C_{H,in} \dot{V}_{H,in} \quad (5.9)$$

where $C_{H,in}$, $C_{H,out}$, $\dot{V}_{H,in}$, and $\dot{V}_{H,out}$ are the inlet and outlet concentrations and flow rates of the concentrate solution in the *RED* unit, while $C_{L,out}$ is the outlet concentration of the dilute solution from the *RED* unit.

The flow rate and the concentration of the solution fed to the *MED* plant ($\dot{V}_{MED,in}$ and $C_{MED,in}$, respectively) are determined according to the following equations:

$$\dot{V}_{H,out} + \dot{V}_{bypass} = \dot{V}_{MED,in} \quad (5.10)$$

$$C_{MED,in} \dot{V}_{MED,in} = C_{H,in} \dot{V}_{H,in} \quad (5.11)$$

The feed salt solution ($\dot{V}_{MED,in}$) enters in the *MED* unit in order to produce a concentrated and a distillate stream using low-grade heat (i.e. 100°C) as thermal energy source (see *Figure 5.10*) in the first effect. The concentrated solution is the sum of all the concentrates resulting from the evaporation process in each effect, conversely the distillate is the sum of all the solute free streams produced from the condensation process in each stage. The distillate output from the *MED* is then mixed with the rest of the dilute stream exiting from the *RED* unit (*Mixer 2*).

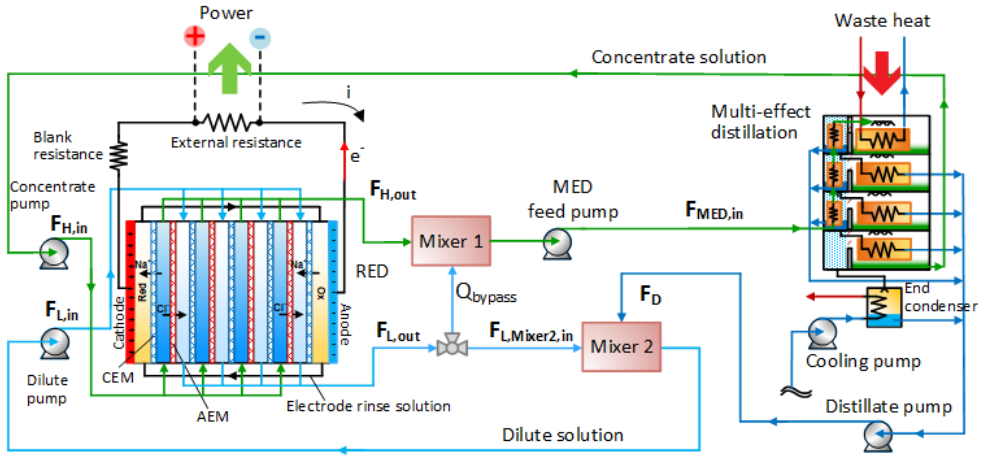


Figure 5.10. Process flow diagram of the RED-MED coupled system.

The distillate flow rate (\dot{V}_D), which is needed to restore the flow rate and concentration of the RED inlet dilute solution ($\dot{V}_{L,in}$), is determined through the following mass balance in the second mixer (*Mixer 2*):

$$\dot{V}_{L,out} + \dot{V}_D = \dot{V}_{L,in} \quad (5.12)$$

The performance of the MED unit was evaluated using simple correlations relating the specific thermal consumption and the optimised number of effects (N_{stage}) to the inlet MED concentration ($C_{MED,in}$) and the inlet-outlet concentration difference (ΔC_{MED}):

$$STC = A + B \cdot C_{MED,in} + \frac{C}{\Delta C_{MED}} + D \cdot C_{MED,in}^2 + \frac{E}{\Delta C_{MED}^2} \quad (5.13)$$

$$STC = A + B \cdot C_{MED,in} + \frac{C}{\Delta C_{MED}} + D \cdot C_{MED,in}^2 + \frac{E}{\Delta C_{MED}^2} \quad (5.14)$$

where A, B, C, D and E are constants derived by fitting model predictions reported in Table 5.2.

Table 5.2 Parameters of the fitting equations for the specific thermal consumption and number of effects of the MED unit (referring to waste-heat temperature of 100 °C, giving the lowest STC).

performance	A	B	C	D	E
STC [kWh/m ³]	11.84178	2.74172	8.22469	2.62355	0.36123
N_{stage}	37.50022	9.79094	0.15176		

A comparison of STC and N_{stage} evaluated using the correlations and the $CIEMAT$ simulation results is reported in Table 5.2. A maximum percentage deviation of 10 % was observed for the STC , while 8% for the N_{stage} .

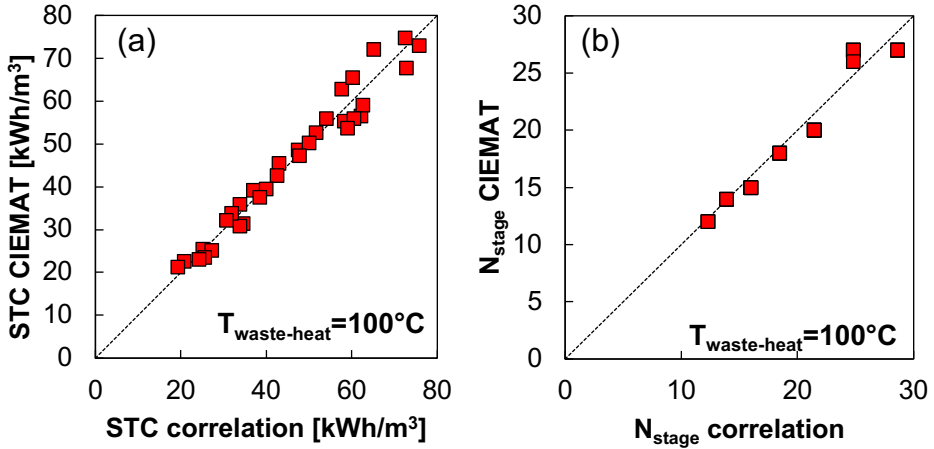


Figure 5.11. Comparison of MED model predictions and correlation results for STC (a) and N_{stage} (b) for the case of waste heat available at 100°C.

The product of the specific thermal consumption and the distillate flow rate gives the total Thermal Power Consumption of the MED plant (TPC):

$$TPC = STC \cdot \dot{V}_D \tag{5.15}$$

Therefore, the thermal or energy efficiency (η_{th}) of the $RED-MED$ integrated system is defined as:

$$\eta_{th} = \frac{P_{RED,net} - P_{MED,tot}}{TPC} \tag{5.16}$$

The pumping power consumption ($P_{MED,tot}$) of the *MED* unit is evaluated considering three different contributions:

- a) The electric power required to pump the inlet solution into the first effect ($P_{MED,in}$).
- b) The power requirement to pump the distillate and the concentrated solutions from the *MED* unit to the *RED* stack ($P_{MED,out}$).
- c) The pumping power of cooling water required in the final condenser ($P_{condenser}$).

The *MED* plant is assumed as a vertical plant and each effect is supposed to have a height of 1 m. The $P_{MED,in}$ is given by the product of the solution flow rate ($\dot{V}_{MED,in}$) by the hydraulic head (ΔP_{MED}), which depends on the number of effects.

$$P_{MED,in} = \frac{\dot{V}_{MED,in} \cdot \Delta P_{MED}}{\eta_P} = \dot{V}_{MED,in} \frac{N \cdot \rho_{MED,in} \cdot g \cdot h_{stage}}{\eta_P} \quad (5.17)$$

Concerning ($P_{MED,out}$); pressure increase ($\Delta P_{MED-RED}$) of 1 bar has been assumed, as the last effect of the *MED* unit operates at low vacuum conditions (about 50 mbar).

$$P_{MED,out} = \frac{\dot{V}_{MED,out} \cdot \Delta P_{MED-RED}}{\eta_P} = \dot{V}_{MED,out} \frac{N \cdot \rho_{MED,out} \cdot g \cdot h_{stage}}{\eta_P} \quad (5.18)$$

The pressure drops inside the condenser ($\Delta P_{condenser}$) are assumed equal to 0.5 bar while the cooling water flow rate (\dot{V}_{cw}), available at 20 °C, is evaluated according to eq. 5.19, assuming that in the last effect the distillate is equal to $1/N_{stage}$ of the global distillate flow rate (\dot{V}_D). An increase of the temperature of the cooling water (T_{cw}) of 10 °C in the condenser is assumed.

$$P_{condenser} = \frac{\dot{V}_{cond} \cdot \Delta p_{condenser}}{\eta_{pump}} \quad (5.19)$$

$$\dot{V}_{cw} = \frac{\lambda_w \dot{V}_D}{N_{stage}} \cdot \frac{1}{\bar{c}_p (T_{cw,out} - T_{cw,in})} \quad (5.20)$$

The total pumping power consumption of the *MED* unit is evaluated according to:

$$P_{MED} = P_{MED,in} + P_{MED,out} + P_{condenser} \quad (5.21)$$

Finally, the exergy efficiency (η_{ex}), is given by the ratio between the thermal efficiency (η_{th}) and the Carnot efficiency (η_C):

$$\eta_{ex} = \frac{\eta_{th}}{\eta_C} \quad (5.22)$$

$$\eta_C = 1 - \frac{T_{cold} [K]}{T_{hot} [K]} \quad (5.23)$$

The *RED-MED* model was used to perform a sensitivity analysis in order to identify the exergy efficiency of the global system varying inlet concentrations and velocities of the two solutions entering to the *RED* unit. In particular, the concentration $C_{H,in}$ was varied from 2M to 5M and $C_{L,in}$ from 0.01M to 0.2M, while the velocities in both channels were varied from 0.5 to 2cm/s. These simulations have been performed for a stack of 50 cell pairs with membrane areas of $0.1 \times 0.88 \text{m}^2$ and spacer thickness of 155 μm , in counter-current flow arrangement. In order to assess the effect of improving *IEMs* properties for a perspective analysis of potential, all simulations were first performed assuming typical properties of current state of the art membrane (Fujifilm type 10 membranes) and then assuming future perspective *IEMs* with ideal selectivity and reduced electrical resistance. All the simulations were done by assuming both current membrane properties and ideal membranes properties, whose features are reported in *Table 5.3*.

Table 5.3 Membrane properties adopted in the two scenarios current and ideal membranes [165].

Scenario	$R_{IEM,av}$ [$\Omega \cdot \text{cm}^2$]	P_w [m/(Pa·s)]	P_{salt} [m ² /s]	α_{av} [%]
<i>Current membrane</i>	1.5 ^(c)	$2.22 \cdot 10^{-14(a,d)}$	$10^{-12(d)}$	95-98 ^(b)
<i>Ideal membrane</i>	$\frac{1}{4} \cdot R_{IEM,current}$	0 ^(d)	0 ^(d)	100 ^(d)

^(a)experimental values measured @ ref. conditions: $T=25^\circ\text{C}$, $C_{H,in}=3 \text{ M}$ $C_{L,in}=0.05\text{M}$ -variable with concentration;

^(b)experimental values measured-constant value @ ref. conditions: $T=25^\circ\text{C}$, $C_{H,in}=0.5\text{M}$ $C_{L,in}=0.05\text{M}$ - variable with concentration; ^(c)experimental values measured @ ref. conditions: $T=25^\circ\text{C}$, $C_{sol}=2 \text{ M}$; ^(d)assumed constant in the whole range of concentration.

5.3.3 RED model results

The aim of this section is to characterise the *RED* unit performance when varying concentrations or velocities, considering a short and a long stack. The analysis has been performed considering *IEMs* properties typical of currently available membranes and assuming ideal membranes.

5.3.3.1 RED performance with current IEMs

The first analysis investigates the effect of the feed inlet concentration and feed inlet velocity on the cell pair power density (P_d) of the *RED* unit. As shown in *Figure 5.12-a*, the P_d obtainable in the shorter stack is much higher than that achievable in the longer stack (*Figure 5.12-b*), as expected, because of the evident decrease of the average driving force across the *IEMs* with the increase of length. In the case of stack length equal to 0.1 m, $P_{d,max}$ was found equal to 5.4W/m², when solution concentrations equal to $C_{H,in}=3.75M$ and $C_{L,in}=0.02M$ are considered. Conversely, in the case of stack length equal to 0.88 m, assuming the same inlet conditions (i.e. velocity and concentration), $P_{d,max}$ was found equal to 2.8W/m² that does not correspond to the maximum value. A maximum value equal to 2.9W/m² was found at $C_{H,in}=4.5M$ and $C_{L,in}=0.01M$. Such values are considerably lower than the case of short stack due to the large change in concentration of the two streams (i.e. short stack: $C_{H,out}=3.5M$ $C_{L,out}=0.08M$; long stack: $C_{H,out}=3 M$ $C_{L,out}=0.6M$).

Interestingly, the maximum values of $P_{d,max}$ are not found in correspondence with the maximum inlet concentration difference, i.e. $C_{H,in}=5M$ and $C_{L,in}=0.01M$. This is due to the variation of *IEMs* and stack properties with concentration. In fact, the higher the $C_{L,in}$ the lower the driving force and the electrical potential generated by the *RED* unit but, at the same time, the lower the electrical resistance of *IEMs* and dilute channels. On the other side, the higher the $C_{H,in}$ the lower the *IEMs* permselectivity. Then, the $P_{d,max}$ value is given by a trade-off between the behaviour of electrical potential, membrane and solution resistances and permselectivity.

The effect of fluid velocity on $P_{d,max}$ is shown in *Figure 5.12-c* for the case of the longer stack at the inlet concentration conditions $C_{H,in}=4.5 M$ and $C_{L,in}=0.01 M$ identified for $P_{d,max}$. The effects of the variation of $v_{L,in}$ and $v_{H,in}$ on $P_{d,max}$ are quite different. When v_L increases, for every $v_{H,in}$, $P_{d,max}$ increases since the higher the velocity of the dilute stream,

the higher the driving force along the entire channel. Conversely, a variation of $v_{H,in}$ for every $v_{L,in}$, does not result in a significant variation of $P_{d,max}$.

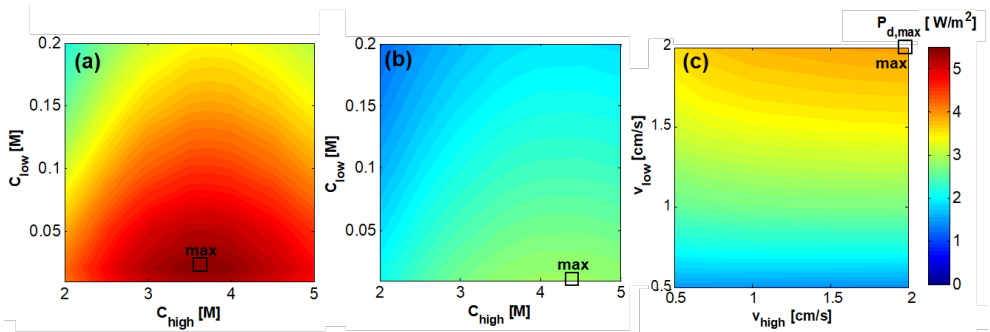


Figure 5.12. Effect of the feeds inlet concentration on the power density $P_{d,max}$ [W/m^2] for the case of RED stack with 50 cell pairs, $v_L = v_H = 1$ cm/s, counter-current arrangement, and membrane area of 0.1×0.1 m² (a) and 0.1×0.88 m² (b). Effect of the feeds inlet velocity for the case of RED stack with 50 cell pairs, $C_L = 4.5$ M and $C_H = 0.01$ M, counter-current arrangement, and membrane area of 0.1×0.88 m² (c).

Notwithstanding the higher values of power density are obtained using the shorter stack, the yields of the process resulted in very low values. Increase the stack length has a beneficial effect on the yield as shown in *Figure 5.13-a* and *Figure 5.13-b*. The larger the yield, the larger the exploitation of the solutions in the RED unit, resulting in a higher power production. For this reason, in the next sections just a stack length of 0.88 m has been considered *Figure 5.13-a* and *Figure 5.13-b* show the influence of the inlet solution concentration on the yield. The high values of yield are observed for the case of low inlet salinity gradient due to the reduction of the uncontrolled-mixing phenomena, which consume part of the available salinity gradient, without contributing to the power generation.

In *Figure 5.13-c* the effect of variation of $v_{L,in}$ and $v_{H,in}$ on yield is shown for the case of $C_{H,in} = 4.5$ M and $C_{L,in} = 0.01$ M, which was found to maximize the $P_{d,max}$ (*Figure 5.12-b*). It was found that the yield largely depends on the value of v_H , which determines the residence time in the concentrate channel. Conversely, the effect of $v_{L,in}$ is significant in the range 0.5 - 1 cm/s while for values higher than 1 cm/s the effect is negligible.

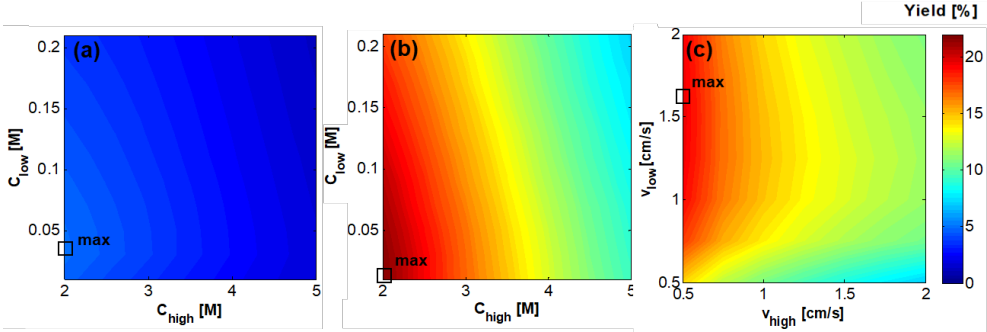


Figure 5.13. Effect of the feeds inlet concentration on Yield [%] for the case of RED stack with 50 cell pairs, $v_{H,in} = v_{L,in} = 1$ cm/s, counter-current arrangement, and membrane area of 0.1×0.1 m² (a) and 0.1×0.88 m² (b). Effect of feeds inlet velocity for the case of RED stack with 50 cell pairs, $C_{H,in} = 4.5$ M and $C_{L,in} = 0.01$ M, counter-current arrangement, and membrane area of 0.1×0.88 m² (c).

5.3.3.2 RED performance with ideal IEMs

The RED performance is dramatically affected by the properties of the membranes as the “non-ideal” behaviour of IEMs determines several exergy losses (see Chapter 3), e.g. due to the diffusive flux of the neutral salt and water through the membranes. Thus, it is interesting to investigate the behaviour of a RED stack equipped with ideal IEMs.

As shown in Figure 5.14-a, the maximum power density is produced at the highest concentration in the concentrate compartment and at the lowest concentration in the dilute compartment, since the prominent term, in this case, is the driving force, while the effect of concentration on IEMs permselectivity is not considered and the values of IEMs resistance are low for ideal IEMs.

A maximum power density equal to 9.8 W/m² is reached (Figure 5.14-a), which is more than three times higher than the maximum power density achieved with current membranes (2.9 W/m²).

As for the simulations carried out for the current membranes, a set of concentration has been selected and fixed (i.e. 5M and 0.01M for the concentrate and the dilute solution respectively, since these concentrations maximize $P_{d,max}$), in order to investigate the influence of the fluid velocity on the power produced in the RED stack. Also in this case, $P_{d,max}$ increases as the two fluid velocities increase, reaching its maximum value at the highest velocity in both channels (Figure 5.14-b).

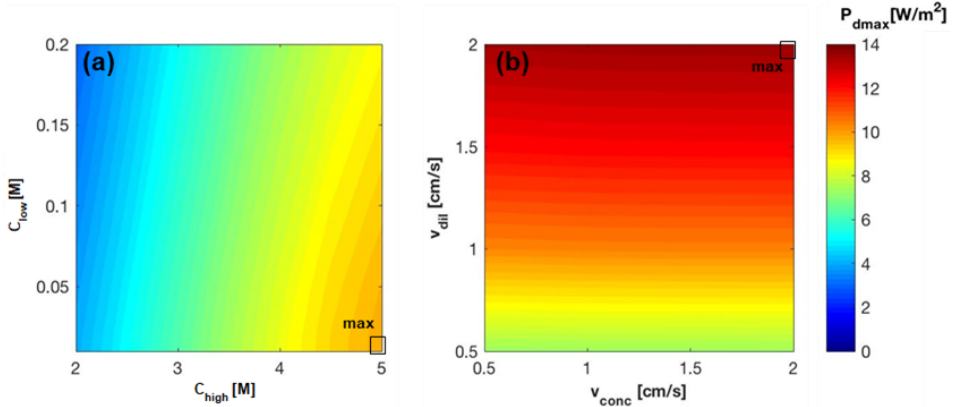


Figure 5.14. Dependence of $P_{d,max}$ on a) feeds inlet concentration with fixed inlet solution velocities ($v_L = v_H = 1$ cm/s); b) feeds inlet velocity with fixed inlet solution concentrations ($C_L = 0.05$ M and $C_H = 4.5$ M). RED stack of 50 cp, with a membrane area of 0.1×0.88 m², counter-current arrangement, ideal membranes.

5.3.4 RED-MED integrated system results

5.3.4.1 Analysis of the integrated RED-MED system performance with current IEMs

The analysis of the integrated *RED-MED* system has been performed varying the *RED* inlet concentration and velocity as these determine the concentration of the solution fed to the *MED* unit, as well as the required distillate flow rate \dot{V}_D . These two parameters have a prominent role in the definition of the thermal energy consumption of the *MED* process, since the *STC* depends on the inlet *MED* concentration and the relevant ΔC_{MED} , while the total energy consumption is given by the product of the *STC* by \dot{V}_D (see eq. 5.15). In particular, $C_{MED,in}$ increases as $C_{H,in}$ and $C_{L,in}$ increase (eq. 5.9-5.11). As a consequence, the higher the two concentrations, the higher the specific thermal consumption. On the other side, \dot{V}_D largely depends on the value of $C_{L,in}$, while the effect of $C_{H,in}$ is negligible. An increase of $C_{L,in}$ reduces the \dot{V}_D . As global results, the product of the two terms, i.e. *STC* and \dot{V}_D , gives rise to the map of the thermal power consumption, reported in Figure 5.15-a. The influence of $C_{H,in}$ and $C_{L,in}$ on the thermal power consumption is reported in Figure 5.15-a. Concerning the effect of $C_{H,in}$, since the *STC* increases as $C_{H,in}$ increases, the thermal power consumption is expected to increase with $C_{H,in}$. An increase $C_{L,in}$ has a double effect: a higher specific energy

consumption but also a lower \dot{V}_D . This last effect prevails determining a decrease of the thermal power consumption when an increase of $C_{L,in}$ is considered.

The ratio between the net power generated in the RED unit and the thermal power consumption by the MED defines the thermal efficiency of the closed-loop, while the ratio between thermal and Carnot efficiency gives the exergy efficiency, reported in

Figure 5.15-b. In the current scenario, the highest exergy efficiency equal to 4.5% is obtained at the lowest concentration for the dilute solution, which maximizes in all the cases the driving force, and at $C_{H,in}$ equal to 3.5 M, as higher values negatively affect both permselectivity, membrane properties and the energy consumption in the MED plant.

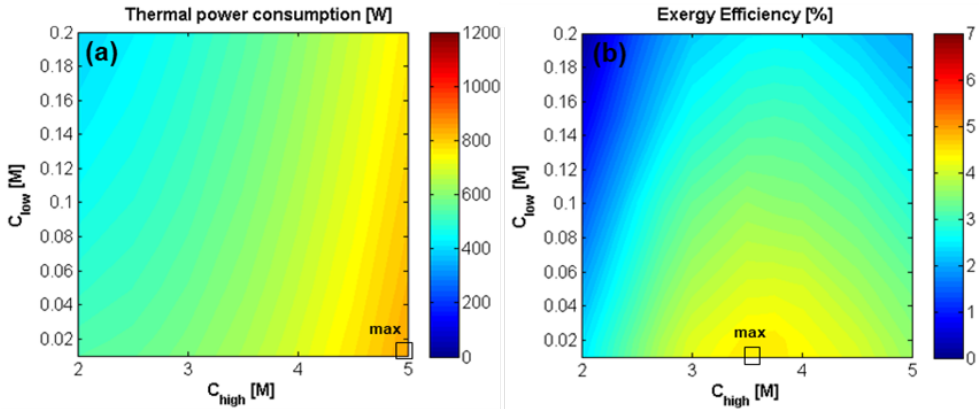


Figure 5.15. Effect of $C_{H,in}$ and $C_{L,in}$ on the thermal power consumption [W] of the MED unit (a) and on exergy efficiency of RED-MED Closed loop (b). RED stack: 50 cell pairs, membrane area of $0.1 \times 0.88 \text{ m}^2$, counter-current arrangement, $v_{H,in} = v_{L,in} = 1 \text{ cm/s}$. MED: $T_{hot} = 100^\circ\text{C}$, $T_{cold} = 20^\circ\text{C}$, optimized number and area of the effects.

The effect of velocity in the two channels has been also analysed in terms of thermal power consumption and exergy efficiency (Figure 5.16). As it has already mentioned, STC is a growing function of $C_{MED,in}$, which increases as $v_{H,in}$ increases and $v_{L,in}$ decreases (due to the decrease of \dot{V}_{bypass}). \dot{V}_D is almost independent on $v_{H,in}$ and, conversely, dramatically increases with $v_{L,in}$. On overall, the TPC increases both with $v_{L,in}$ and $v_{H,in}$, as shown in Figure 5.16-a.

Finally, the exergy efficiency is reported as a function of the two velocities (Figure 5.16-b). The maximum exergy efficiency (6.7%) is reached when $v_{L,in}$ is equal to 1 cm/s and $v_{H,in}$ to 0.5 cm/s. As observed in Figure 5.12-c, this is due to the fact that the higher the velocity

of the dilute solution with respect to the concentrate one, the higher driving force is maintained along the entire channel. This effect is particularly evident when long *RED* stacks are used, which are much more affected by the drop of driving force along the channel length.

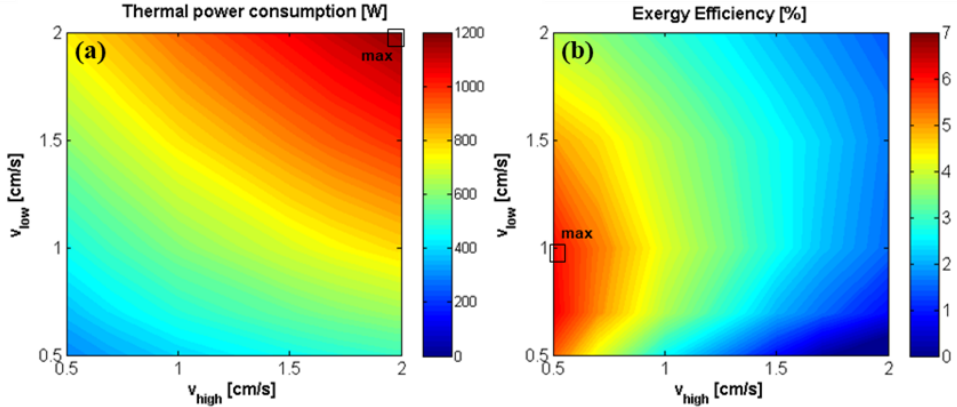


Figure 5.16. Effect of $v_{H,in}$ and $v_{L,in}$ on the total thermal power consumption [W] of the MED unit (a) and on exergy efficiency of the RED-MED system (b). RED stack: 50 cell pairs, membrane area of $0.1 \times 0.88 \text{ m}^2$, counter-current arrangement, $C_{H,in} = 3.5 \text{ M}$ and $C_{L,in} = 0.01 \text{ M}$. MED: $T_{hot} = 100^\circ\text{C}$, $T_{cold} = 20^\circ\text{C}$, optimized number and area of the effects.

5.3.4.2 Analysis of the integrated RED-MED system performance with ideal IEMs

The performance of the *RED-MED* integrated system has been investigated also considering a future *RED* stack, equipped with ideal membranes. As observed in *Figure 5.14*, the power density produced is more than three times higher than the one in a current stack, due to the fact that the exchange of counter-ions is maximized and non-ideal dissipative. This has two direct consequences on the system operation: 1) higher electrical currents, leading to larger power generation and closer outlet concentrations of the two streams exiting the *RED* unit; 2) null diffusive salt and water flux, which significantly reduce the concentration drops along the channel, thus preserving the salinity gradient at the *RED* unit outlet. The two phenomena affect the overall performance of the system in different ways, depending on the operating conditions. In particular, at low flow velocity similar thermal power consumptions are registered with respect to the reference membrane case, as shown in *Figure 5.17-a*, which also highlights how thermal power requirements increase as $C_{H,in}$ increases and decrease as $C_{L,in}$ increases.

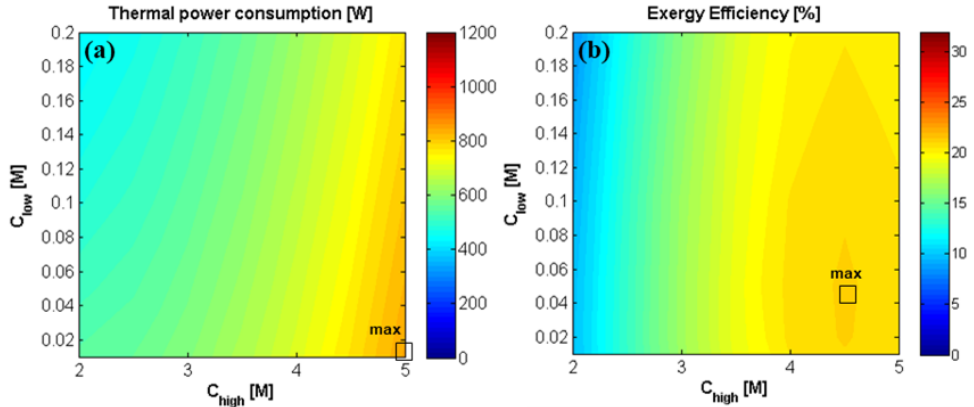


Figure 5.17. Effect of $C_{H,in}$ and $C_{L,in}$ on thermal power consumption [W] of the MED unit (a) and on exergy efficiency of the RED-MED system (b). RED stack: 50 cell pairs, ideal membranes, membrane area of $0.1 \times 0.88 \text{ m}^2$, counter-current arrangement, $v_{H,in} = v_{L,in} = 1 \text{ cm/s}$. MED: $T_{hot} = 100^\circ\text{C}$, $T_{cold} = 20^\circ\text{C}$, optimized number and area of the effects.

Concerning the exergy efficiency (Figure 5.17-b), a maximum for $C_{H,in}$ equal to 4.5 M and $C_{L,in}$ equal to 0.05 M is observed. With regards to the effect of $C_{H,in}$, the maximum efficiency is identified at a higher concentration than the case of current RED stack (3.5 M). In fact, here, the net power increases as $C_{H,in}$ increases in the whole range of concentration. Thus, the increase in thermal power consumption prevails only at higher concentrations, determining a decrease of the overall efficiency above 4.5 M. Regarding the influence of $C_{L,in}$, while the system with a current RED stack reached the maximum efficiency at the lowest $C_{L,in}$ investigated (0.01 M), in this case the efficiency slightly decreases at concentrations below 0.05 M, indicating that the increase of thermal energy consumption (due to the higher \dot{V}_D) prevails on the increase of generated power, which determine a decrease in the overall efficiency.

In the case of ideal membranes, the effect of the fluid velocity on the performances of the coupled system has been also investigated (see Figure 5.18), adopting the concentration that corresponds to the maximum exergy efficiency, i.e. 4.5 M and 0.05 M for the concentrate and the dilute solution, respectively. The trends of STC , \dot{V}_D and thermal power consumption are analogous to the ones already described for the coupled system with the current RED stack: the specific energy consumption increases with the increase of $v_{H,in}$ and the decrease of $v_{L,in}$ while the thermal power consumption rises with both $v_{H,in}$ and $v_{L,in}$.

Finally, the exergy efficiency is reported as a function of the two velocities (*Figure 5.18-b*), for the case of optimal $C_{H,in} = 4.5$ M and $C_{L,in} = 0.05$ M (*Figure 5.18-b*). The maximum exergy efficiency (31%) is reached when $v_{L,in}$ is equal to 0.7 cm/s and $v_{H,in}$ to 0.5 cm/s, combining high net power output in the *RED* unit and low thermal energy consumption in the *MED* unit.

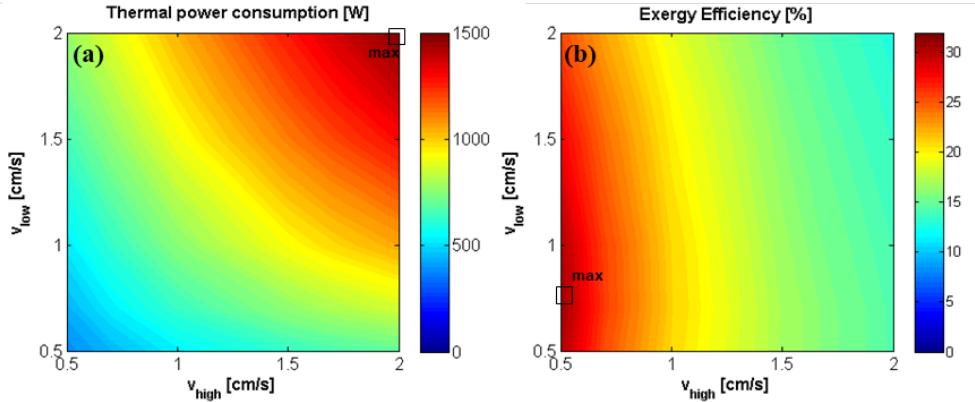


Figure 5.18. Effect of $v_{H,in}$ and $v_{L,in}$ on thermal power consumption [W] of the *MED* unit (a) and on exergy efficiency of the *RED-MED* system (b). *RED* stack: 50 cell pairs, ideal membranes, membrane area of 0.1×0.88 m², counter-current arrangement, $C_{H,in} = 4.5$ M and $C_{L,in} = 0.05$ M. *MED*: $T_{hot} = 100^\circ\text{C}$, $T_{cold} = 20^\circ\text{C}$, optimized number and area of the effects.

5.3.4.3 Overview of the effects of ideal membranes on the system performance

To summarise the qualitative effects of changing the membrane properties on the performance of *RED*, *MED* and integrated *RED-MED HE*, reader can refer to *Table 5.4*. In particular, the *RED* unit performance is largely enhanced by decreasing the membrane resistance and increasing permselectivity, while a smaller improvement is observed by the reduction of the water flux and salt diffusivity. A reduction of these latter terms affects the outlet solution concentrations by lowering the salinity gradient consumption in the *RED* unit. Thus, in this case, also the *MED* consumption is marginally reduced. At the contrary, the reduction of resistance and the increase of permselectivity increase the electrical current and salt flux in the *RED* unit, thus leading to a small increase of the *MED* consumption. However, on overall, the increase of permselectivity and the reduction of the resistance significantly enhance the global efficiency, while water permeation and salt diffusion have a smaller detrimental effect on the process. It is worth noting that the membrane properties weakly

affect the *MED* performance due to the presence of mixer 1, which practically equalizes the *MED* inlet concentration.

Table 5.4 Qualitative effect of membrane properties on the performance of RED, MED and RED-MED-HE.

IEM properties	RED	$C_{RED,H,out}$	$C_{RED,L,out}$	MED	Global
	Power			STC	Efficiency
<i>Resistance</i> ($R_{IEM,av}$)	↓	↑↑↑	↓	↑↑	↑↑↑
<i>Permselectivity</i> (α_{av})	↑	↑↑↑	↓	↑	↑↑↑
<i>Water permeability</i> (P_w)	↓	↑↑	↑↑↑	↓	↑↑
<i>Salt diffusivity</i> (P_{salt})	↓	↑	↑	↓	↑

5.4 Simplified RED-MD model

The present section reports a simplified modelling analysis on a reverse electro dialysis-membrane distillation heat engine (*RED-MD HE*) fed by NaCl-water solutions. Modelling was based on real existing units in order to develop the first proof of concept of the *RED-MD HE*. Both Reverse Electro dialysis and Membrane Distillation are described combining theoretical validated models and data from commercial *MD* units provided by *Aquastill*[®]. In particular, the validated mono-dimensional *RED* model reported in *Chapter 3* was here used to evaluate the performance of the *RED* unit. The performances of the *MD* unit are evaluated by means of correlations derived from a validated mathematical model developed by *Aquastill*[®]. They refer to the real *MD* working range of operating concentrations, limited by the decrease of the driving force, especially for long *MD* units. On overall, the aim of this section is to highlight the potential of the integrated *RED-MD* system, accounting for real equipment. Furthermore, a perspective analysis is carried-out in order to investigate the performance of future *RED-MD HE*, considering improvements in both units.

5.4.1 Mathematical modelling

The layout of the coupled *RED-MD* system is sketched in *Figure 5.19*. The integrated system was designed considering the two processes as connected in a discontinuous way, due to the different scale (or working times) of the two units employed, a commercial *RED* stack and commercial *MD* module.

More precisely, the whole system operates cyclically. In each working cycle, the *RED* unit is supposed to work in continuous for 5 h, during that a dilute and concentrate solutions are fed in the unit with fixed flow rates ranging from 10 to 50 l/h. The outlet concentrate solution ($\dot{V}_{H,out}$) is mixed with a fraction of the outlet dilute solution (\dot{V}_{bypass}), in order to restore the initial content of salt (see *Figure 5.19*). The resulting solution volume is accumulated in the *MIX* tank during the *RED* working time. This volume is recirculated within the *MD* unit up to the achievement of the desired concentration ($C_{H,in}$) with a fixed flow rate of 600 l/h (typical of commercial *MD* modules). Then, the *MD* working time (t_{MD}) depends on the *RED* outlet concentrations. This working time, typically in the range of 1-10 hours, is defined as the ratio between the volume of distillate that is required to re-establish the inlet concentration of the dilute solution and the distillate flow rate produced by the *MD* module. Notably, $t_{RED} = 5h$ was arbitrarily set in order to have also reasonable operation times on the *MD* sides: in some

conditions high t_{RED} may lead to t_{MD} larger than 12h, thus requiring operator shift during the monitoring of the future proof of concept.

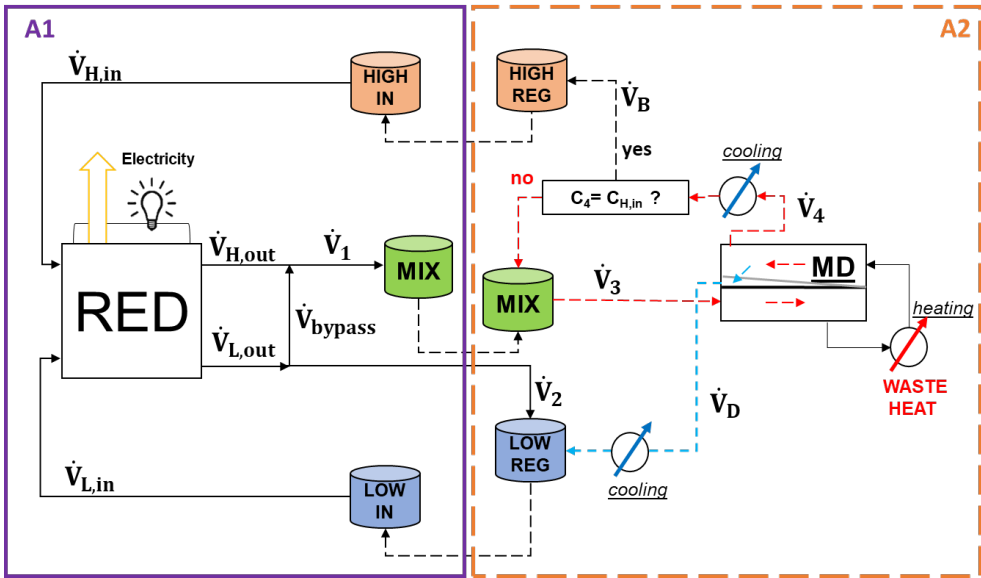


Figure 5.19. RED-MD integrated system. The area inside the purple-solid rectangle (A1) works in continuous while the area inside the orange-broken rectangle (A2) works in batch conditions. Dashed lines refer to batch operations while continuous lines refer to continuous operations.

The distillate produced in the MD unit is continuously cooled and accumulated in the *LOW REG* tank where also the RED outlet dilute solution is stored. Conversely, once the MD concentrate reaches the desired concentration, it is discharged in the *HIGH IN* and a new cycle starts.

A lab scale RED unit consists of 50 cell pairs $0.1 \times 0.88 \text{ m}^2$ equipped with Fujifilm type 10 membranes and 0.155 mm spacer was considered for the analysis.

5.4.1.1 Membrane Distillation (MD): correlations from a validated literature model

Among the different configuration proposed for MD units, a vacuum-assisted air gap module configuration developed by Aquastill® was selected for the analysis.

The MD process is described through some correlations, derived from the simulation results kindly supplied by Aquastill® for current commercial modules with channel lengths of 1.5 m and 5 m. These data are collected employing the mathematical model described

extensively in ref. [166] and validated from experimental analysis carried-out at *CIEMAT* [167].

Starting from these data, some simple correlations were built in order to simulate the behaviour of real *vacuum assisted AG-MD* units (see *Figure 5.20*). *Figure 5.20-a* reports the trends of the distillate flow rate value (\dot{V}_D) produced by the *MD* unit for two different *MD* module length of 1.5 m and 5 m as a function of the solution concentration. In *Figure 5.20-b*, the trends of the *STC* as a function of the distillate flow rate for the same two module lengths are shown.

The module length has a strong impact on the specific thermal consumption, since the feed is firstly sent to the cold compartment, where it is preheated by the fluid flowing in the hot compartment, then it is heated up to T_{hot} (i.e. 80°C) through an external source. Thus, the longer the *MD* unit, the higher the heat recovery from the hot compartment.

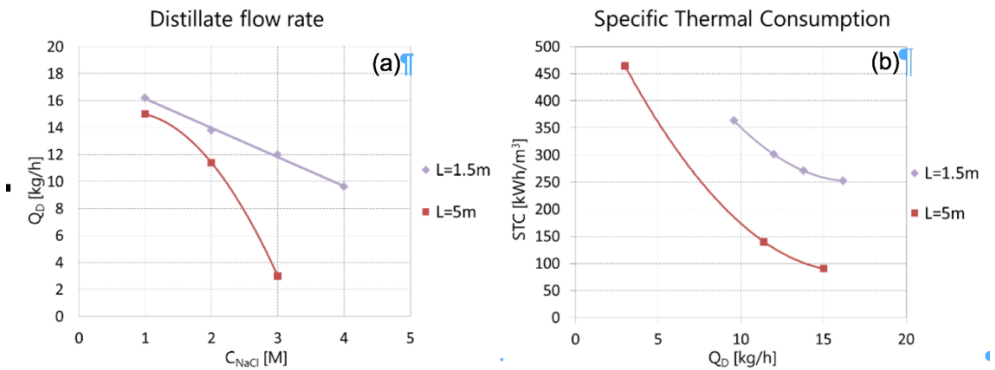


Figure 5.20 Distillate flow rate \dot{V}_D as function of the concentration (a) and *STC* as function of the distillate flow rate (b) at two different *MD* unit lengths (1.5 m and 5 m) for an existing *MD* unit.

The trends of \dot{V}_D vs. C_{NaCl} and *STC* vs. \dot{V}_D can be reliably fitted by a 2nd grade polynomial function:

$$f_u = a x^2 + b x + c \quad (5.24)$$

where fitting coefficients are reported in *Table 5.5*.

Table 5.5 Fitting coefficients for the correlations of \dot{V}_D vs. C_{NaCl} and STC vs. \dot{V}_D for real MD unit, according to the polynomial function in (S.27).

	Module length[m]	a	b	c
\dot{V}_D vs C_{NaCl}	1.5	0	-2.16	18.3
	5	-2.4	3.6	13.8
STC vs \dot{V}_D	1.5	2.13	-71.84	856.03
	5	2.06	-68.29	650.3

For each case, given a certain feed flow rate and concentration in the MD unit, distillate flow rate (\dot{V}_D) and the Specific Thermal Consumption (STC) are evaluated. The flow rate of the solution fed to the MD unit was set equal to 600 l/h (i.e. typical flow rate for commercial units), while the feed concentration varies depending on the RED inlet concentrations and operating conditions. The simulation results refer to real commercial units, considering the strong influence of the solution concentration on the driving force of the MD process. The higher the solution concentration, the higher the depletion in the vapour pressure difference across the membrane and the lower the water flux, leading to a limitation in the maximum concentration of 3M in the longer unit and 4M for the smaller one.

Moreover, the performance of future MD modules was evaluated using simulation results provided by Aquastill® considering enhanced MD units able (i) to operate in a larger range of concentrations (from 1 to 5M) and (ii) to provide higher water flux.

The results of the model simulations accounting for improved MD modules were also kindly provided by Aquastill®. As in the case before, the results were employed to derive correlations, which were used to simulate the highly performing RED-MD cycle. *Figure 5.21-a* shows the trends of the distillate flow rate as a function of the solution concentration, while *Figure 5.21-b* reports the trends of the STC as a function of the distillate flow rate for two different module lengths.

Also in this case, the trends of \dot{V}_D vs. C_{NaCl} and STC vs. \dot{V}_D can be reliably fitted by a 2nd grade polynomial function, as in eq. 5.24, and the fitting coefficients for this case are reported in *Table 5.6*.

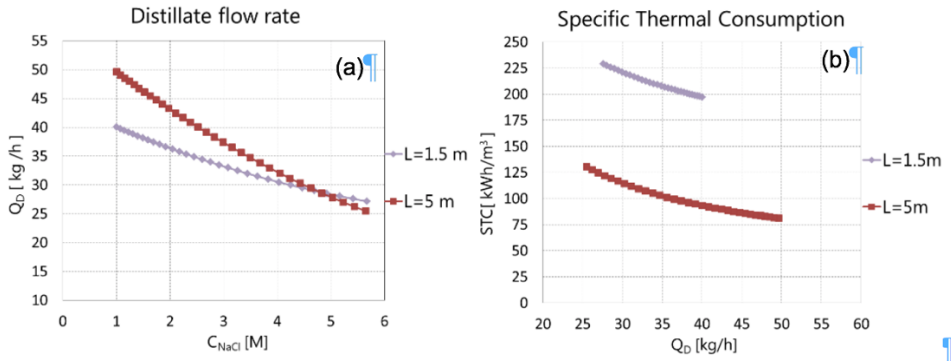


Figure 5.21 Distillate flow rate \dot{V}_D as function of the concentration (left) and STC as function of the distillate flow rate (right) at two different MD unit lengths (1.5 m and 5 m) for a future MD module.

Table 5.6 Fitting coefficients for the correlations of \dot{V}_D vs. C_{NaCl} and STC vs. \dot{V}_D for highly performing MD unit, according to the polynomial function in (S.27).

	Module length [m]	a	b	c
\dot{V}_D vs C_{NaCl}	1.5	0.24	-4.35	44.1
	5	0.35	-7.55	56.77
STC vs \dot{V}_D	1.5	0.068	-7.15	374.17
	5	0.056	-6.21	250.96

The calculation of \dot{V}_D and STC is performed using the above-mentioned correlations. The values of STC and \dot{V}_D were evaluated dividing the concentration range from the MD feed concentration up to the desired outlet concentration into four intervals. Since \dot{V}_D and STC are expressed as functions of the concentration in the feed compartment, it is possible to calculate \dot{V}_D and STC for each concentration interval. Finally, the sum of the products of \dot{V}_D and STC for any interval gives the total thermal energy requirement of the MD module.

5.4.1.2 RED-MD integration

In order to simulate the performances of the whole system, the RED model was integrated with the MD correlations, according to the system layout shown in Figure 5.19. Once RED feeding solutions features have been chosen ($C_{H,in}$, $C_{L,in}$, $\dot{V}_{H,in}$ and $\dot{V}_{L,in}$), RED model is used

to calculate $C_{H,out}$, $C_{L,out}$, $\dot{V}_{H,out}$ and $\dot{V}_{L,out}$. The bypass flow rate s , (i.e. the fraction of the outlet dilute solution to be mixed with the outlet concentrate one, is evaluated through a mass balance on the solute:

$$C_{H,out}\dot{V}_{H,out} + C_{L,out}\dot{V}_{bypass} = C_{H,in}\dot{V}_{H,in} \quad (5.25)$$

Thus, the feed solution of the regeneration unit results from the mixing of the outlet concentrate solution and the bypass solution. This solution is accumulated for 5 hours of continuous operation of the *RED* unit, before being fed to the *MD* unit: the *MD* feed solution volume and concentration are indicated hereafter as V_{mix} and C_{mix} . In order to close the loop, the remaining part of the outlet dilute solution has to be mixed with the distillate produced by the *MD* as indicated by the following balance, which is used to calculate the amount of distillate (V_D):

$$(\dot{V}_{L,out} - \dot{V}_{bypass}) * 5h + V_D = \dot{V}_{L,in} * 5h \quad (5.26)$$

The *MD* distillate flow rate is computed using the specific correlation (eq. 5.24), then the ratio between the required distillate volume (V_D) and the distillate flow rate \dot{V}_D corresponds to the working hours of the *MD* unit. The product of the *STC* times V_D gives the total thermal energy consumption, required by the regeneration process. Therefore, the thermal efficiency of the cycle (η_{th}) is given by the ratio between the total net energy generated by the *RED* stack in 5 hours, and the total thermal energy consumption of the *MD* unit. Finally, exergy efficiency (η_{ex}) is given by the ratio between the thermal efficiency of the cycle (η_{th}) and the thermal efficiency of a Carnot cycle (η_c) operating at the same hot and cold temperature sinks. The Carnot efficiency is equal to 17%, considering $T_{cold}=20^\circ\text{C}$ and $T_{hot}=80^\circ\text{C}$.

5.4.2 Results and discussion

The results section consists of two main parts:

- (i) *current performance* where the performances of an integrated system composed of a real *RED* and a real *MD* unit, considering current Fujifilm type 10 membrane properties (see current scenario in Table 5.3) and existing *MD* units (Figure 5.20) are considered;

- (ii) *future performance* where a combination of high performing equipment. In particular, in this case future membrane properties (*Table 5.7*) and improved *MD* performance (see *Figure 5.21*) were considered.

All the simulations were performed fixing the geometrical features of the *RED* stack corresponding to real pilot scale *RED* unit. In particular, the number of cell pairs was fixed equal to 50, *RED* membrane area of $0.1 \times 0.88 \text{ m}^2$ and 0.155mm spacers were considered.

In all the cases, the *RED* unit is fed by NaCl-water solutions in counter current arrangement.

Concerning the *MD* unit, the nominal feed flow rate was set equal to 600l/h in all the cases. In the real case, the maximum concentration that can be reach in the *MD* unit depends on the system length, according to the diving force depletion. In particular, a maximum concentration of 4M is fixed for the smaller *MD* unit (1.5m) and of 3M for the longer one (5 m). Conversely, in the second case (i.e. enhanced MD units), no limitations were imposed in terms of reachable concentration and a wider range of concentration, up to 5M, was investigated.

5.4.2.1 *Current performance*

A parametric analysis was performed in order to investigate the influence of *MD* length (i.e. 1.5m and 5m), *RED* inlet concentrations and fluid velocities on the *RED-MD HE*. In particular, the inlet solution concentrations in the *RED* stack were varied from 1M up to 4M for the concentrate while for the dilute solution values of 0.01M, 0.05M and 0.1M were considered. While varying the concentrations, the fluid velocities were kept fixed and equal to the typical value of 1 cm/s in both compartments. Thus, the most performing set of inlet concentrations and *MD* unit length was fixed and the fluid velocities were varied from 0.5 cm/s to 2 cm/s for both the dilute and the concentrate compartment.

Effect of solution concentrations

The trends of the power density as a function of the two inlet concentrations in reported in *Figure 5.22*. As expected, the power density generated by the *RED* unit increases when the concentration of the concentrate solution increases and when the concentration of the dilute

solution decreases, due the enhancement of the available driving force. Therefore, the maximum $P_{d,net}$ equal to 2.2 W/m^2_{cp} is reached at $C_{H,in} = 4\text{M}$ and $C_{L,in} = 0.01\text{M}$.

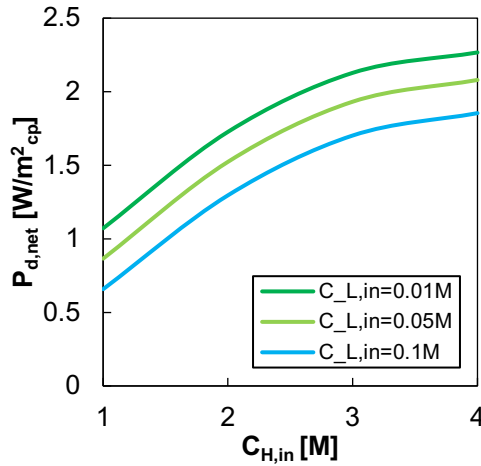


Figure 5.22. $P_{d,net}$ trend varying the concentrations in the concentrate and in the dilute compartment and the MD unit length. (RED stack features: membrane length=0.88 m, $N_{cell}=50$, counter-current arrangement, $t_{RED}=5\text{h}$, $v_H=v_L=1 \text{ cm/s}$. MD unit features: $T_{hot}=80^\circ\text{C}$ and $T_{cold}=20^\circ\text{C}$).

The STCs as a function of the RED inlet concentration and MD length are reported in Figure 5.23-a. It is possible to observe that the concentration of the dilute solution has a negligible role. Indeed, the trends at $C_{L,in}=0.01\text{M}$, 0.05M and 0.1M are almost overlapped. This is not surprising because the role of $C_{H,in}$ in the definition of the MD feed concentration is much more significant. With this respect, it is noticeable that the higher the $C_{H,in}$, the higher the STC, since the increase of the concentration corresponds to a reduction of the partial vapour pressure of water at the membrane interface and consequently a depletion of the driving force. This is particularly evident in the trend of the STC relevant to the long module. In this case, a much deeper increase of the thermal consumption takes place, because the longer module is more affected by the fall of the driving force, since it works at a higher average concentration. For this reason, the longer module cannot operate at concentration higher than 3M.

The global exergy efficiency of the RED-MD HE as a function of the solution concentrations and the two MD unit lengths is reported in Figure 5.23-b. For the whole range of concentrations, the exergy efficiencies achievable with the longer MD unit are higher than the ones relevant to the shorter unit, due to the different thermal consumption. It is remarkable that both trends relevant to the two MD unit lengths encounters a maximum: in the case of

short MD unit ($L_{MD}=1.5m$) the highest exergy efficiency is observed at $C_{H,in}=3M$ while in the case of long MD unit ($L_{MD}=5m$) at $C_{H,in}=2M$. This behaviour is also due to the different STC trends, since the $P_{d,net}$ is the same in the two cases and it increases with $C_{H,in}$. In fact, for the case of the longer MD unit, the net increase of the STC becomes prominent at $C_{H,in}>2M$, thus causing a decreasing trend of the exergy efficiency. Conversely, the flatter trend of the STC relevant to the shorter MD unit ensures an increasing trend of the exergy efficiency up to $C_{H,in}=3M$ and also the efficiency reduction after the maximum is much less enhanced than in the case of $L_{MD}=5m$. Finally, the role of $C_{L,in}$ is more evident for the longer MD unit where the STC is lower. In general, $C_{L,in}$ reduction is beneficial for the engine as the lower the $C_{L,in}$, the higher the $P_{d,net}$ and the exergy efficiency. On overall, the highest exergy efficiency equal to 2.2% is reached at $C_{L,in}=0.01M$, $C_{H,in}=2M$ and $L_{MD}=5m$.

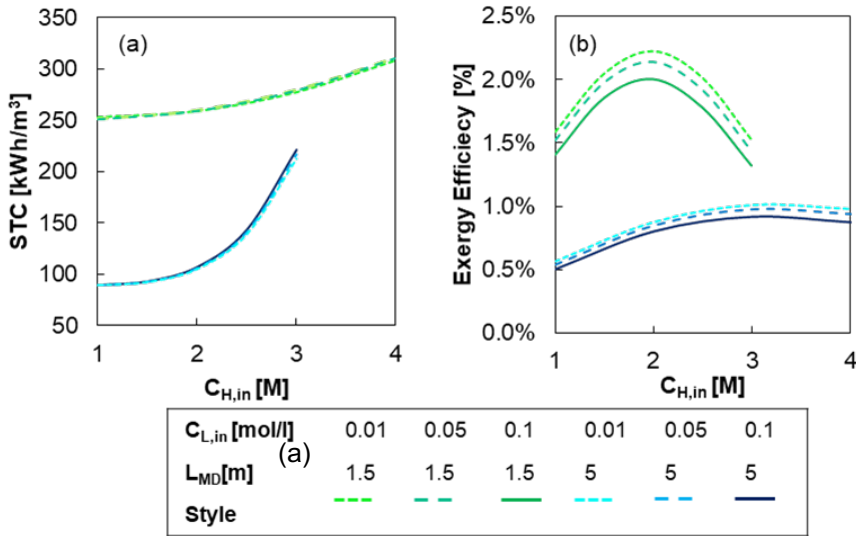


Figure 5.23 STC (a) and exergy efficiency (b) varying the concentrations in the concentrate and in the dilute compartment and the MD unit length. (RED stack features: membrane length=0.88 m, $N_{cell}=50$, counter-current arrangement, $t_{RED}=5h$, $v_H=v_L=1$ cm/s. MD unit features: $T_{hot}=80^\circ C$ and $T_{cold}=20^\circ C$).

Effect of solution velocities

Selecting the set of RED inlet solution concentrations corresponding to the maximum exergy efficiency, the following analysis regards the effects of RED inlet solution velocities on the RED - MD HE performance was carried-out. In particular, Figure 5.24 shows the trends of $P_{d,net}$ as a function of $v_{L,in}$ and $v_{H,in}$. As it is shown in Figure 5.24 the role of $v_{L,in}$ is more

significant than the one of $v_{H,in}$. since a higher dilute inlet velocity (i.e. a lower residence time) leads to a lower dilute concentration variation along the channel (i.e. an almost constant driving force along the RED stack).

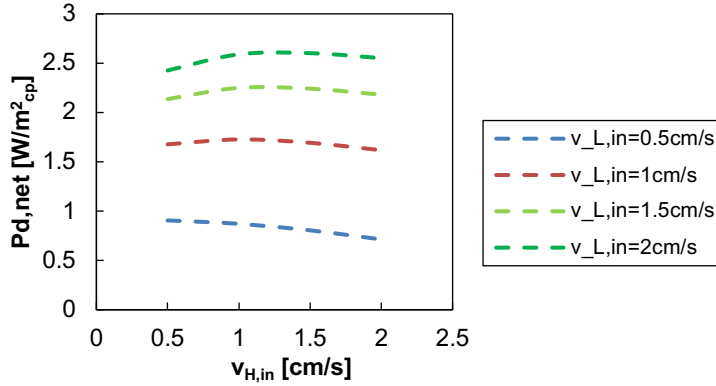


Figure 5.24 $P_{d,net}$ varying the velocities in the concentrate and in the dilute compartment. (RED stack features: membrane length=0.88 m, $N_{cell}=50$, counter-current arrangement, $t_{work}=5h$, $C_{high}=3M$ and $C_{low}=0.01M$. MD unit features: length=5 m, $T_{hot}=80^{\circ}C$ and $T_{cold}=20^{\circ}C$).

The *STCs* of MD unit as a function of the velocity of the solutions fed to the RED stack are reported in Figure 5.25-a. The *STC* increases with $v_{H,in}$ at any $v_{L,in}$ and it decreases with the increase of $v_{L,in}$. The *STC* value depends on the distillate flow rate produced in the MD unit, which is estimated on the basis of the concentration of the MD feed solution. The higher $v_{H,in}$, the higher the outlet concentration of the concentrate solution, which leads to a higher concentration of the MD feed and a lower distillate flow rate. Conversely, the concentration of the MD feed decreases when $v_{L,in}$ increases.

Overall, combining the $P_{d,net}$ and *STC* results gives rise to the exergy efficiency Figure 5.25-b. The exergy efficiency decreases when $v_{H,in}$ is increased at any $v_{L,in}$, due to the *STC* increase. Remarkably, at any $v_{H,in}$ a $v_{L,in} = 1$ cm/s seems to maximize the $P_{d,net}$. The highest exergy efficiency, equal to 2.31%, is achieved in the case of $v_{H,in}=0.5$ cm/s and $v_{L,in}=1$ cm/s or 0.5cm/s.

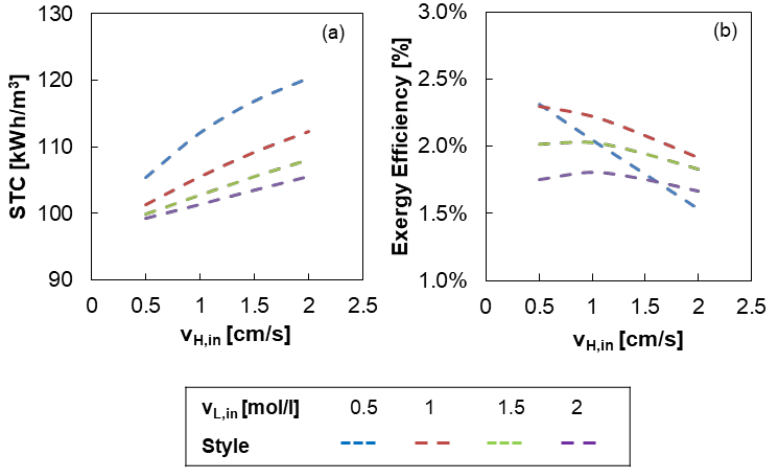


Figure 5.25 STC (a) and exergy efficiency (b) varying the velocities in the concentrate and in the dilute compartment. (RED stack features: membrane length=0.88 m, $N_{cell}=50$, counter-current arrangement, $t_{work}=5h$, $C_{high}=3M$ and $C_{low}=0.01M$. MD unit features: length=5 m, $T_{hot}=80^{\circ}C$ and $T_{cold}=20^{\circ}C$).

5.4.2.2 Future performance

A perspective analysis was carried out analysing the effect of using high performing *IEMs* in the *RED* unit (see *Table 5.7*) and future *MD* on the efficiency of the cycle. Notably, the input of this scenario should not be considered as far from reality, rather, these can be reasonably considered as achievable technological targets in the foreseen future.

Table 5.7 Properties used to simulate highly performing membranes.

Membrane properties	Value
Electrical resistance	Current value*/8
Permselectivity	0.98
Salt diffusivity	Current value*/4
Water permeability	Current value*/4

* See chapter 2; ** 10^{-12} m²/s [64]; *** 8 ml / (bar h m²);

As a matter of fact, the *RED* membrane properties of this scenario were selected by referring to the best values among those already achieved and reported in literature [74]. This can be easily inferred from *Figure 5.26*, where the resistance and permselectivity values for both current and highly-performing membranes are shown to be comparable with literature values

[74]. Similarly, water permeability and salt diffusivity values are in the range of typical literature values: 10^{-11} - 10^{-14} m²/s for salt diffusivity and 1-20 ml/(bar h m²) for water permeability (see Figure 4 in [168]).

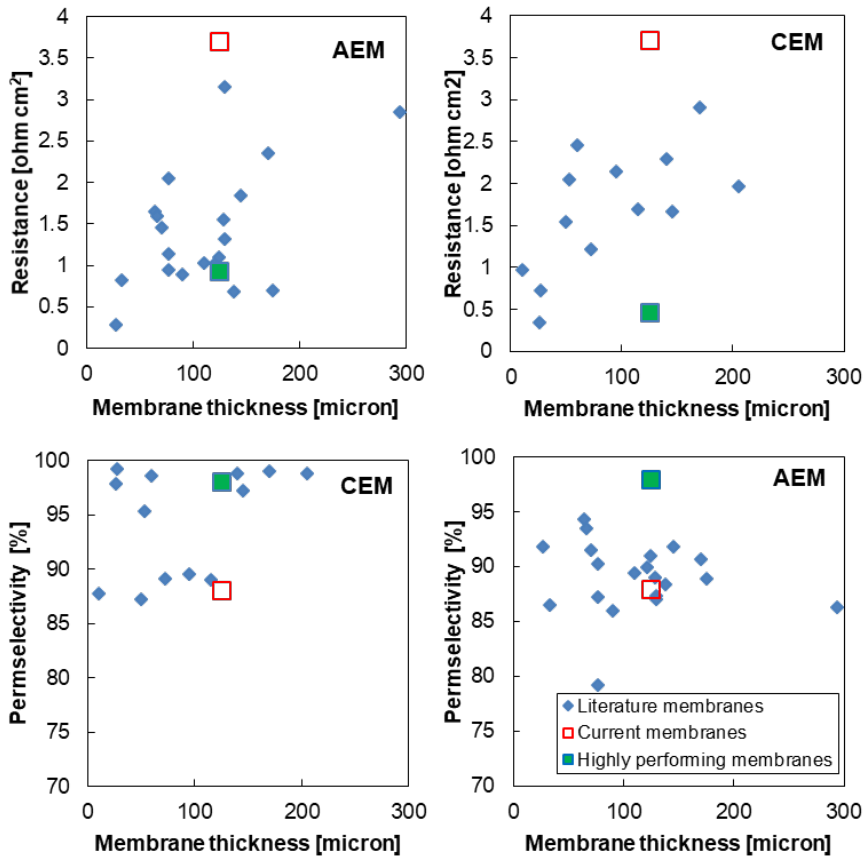


Figure 5.26 Membrane resistance (up) and permselectivity (down) as a function of membrane thickness for current, literature [74] and highly performing membranes. Left: anionic exchange membranes. Right: cationic exchange membranes. Properties are relevant to measurements at 0.5M for the resistance and 0.5M-0.05M for the permselectivity.

Regarding the MD module, the perspective performances of the units were kindly provided by Aquastill[®], based on future improvements of current module. In particular, these improvements include the heat recovery and the design of innovative modules, which are already under development by Aquastill[®]. Experimental results from Aquastill[®] v-AGMD modules at high salinity feeds, obtained at CIEMAT are consistent with Aquastill[®] calculations [167]. There is certainly room for improvement in Aquastill[®] modules. For instance, the membranes currently used by the company are not designed specifically for the

MD process [169]. It has been sufficiently discussed in the literature that optimization of the heat and mass transfer properties of the *MD* membrane can raise water flux and reduce unit energy consumption [170]. Using a membrane specifically designed for *MD*, as those currently used in laboratory experiments [171], can give a significant increase in performance, especially for higher salinity. As a matter of fact, the future *MD* results projected here are similar to current ones at low concentration, and the enhancement is mostly in the high concentration range. Another potential improvement is at the level of module design, for instance using novel spacers for improving heat and mass transfer and reducing the polarisation effects between the bulk stream and the membrane surface, which are also more important for high salinity feeds [172–174].

Another possible enhancement of the *RED-MD* heat engine performance may come from operating the *RED* unit at higher temperatures, as it is well known that *RED* unit work well at larger temperatures. However, analysing temperature influence on the cycle performance would require the knowledge of temperature effect on each membrane property and was, thus, not investigated in the present work.

Also in this case, the performance of the system was investigated through sensitivity analyses varying the solutions concentration and velocity. While varying the inlet concentrations, the fluid velocities are kept constant and equal to 0.5 cm/s in both compartments, since this was the most performing set of fluid velocities in the real case.

Effect of solution concentrations

Figure 5.27 reports the colour-maps relevant to the $P_{d,net}$ and the *STC* of the heat engine as a function of $C_{H,in}$ and $C_{L,in}$. Again, as expected, $P_{d,net}$ increases with $C_{H,in}$ in the whole range of investigated concentrations, because of the increase of the available driving force in the *RED* stack. Conversely, $C_{L,in}$ has a minor role in the definition of $P_{d,net}$. This is explicable because a significant variation in the concentration of the fed solutions occurs when long residence times are considered (i.e. long channels and/or low flow rates). In particular, the stream-wise increase of C_L along the dilute channel of the *RED* stack (e.g. from 0.01 M → 0.3 M) leads to a reduction of its influence on the produced $P_{d,net}$. Regarding the *STC* colour-map, as already observed in the previous analysis, the concentration of the *MD* feed depends much more heavily on $C_{H,in}$ and, as a consequence, the variation of the *STC* with $C_{L,in}$ is almost negligible.

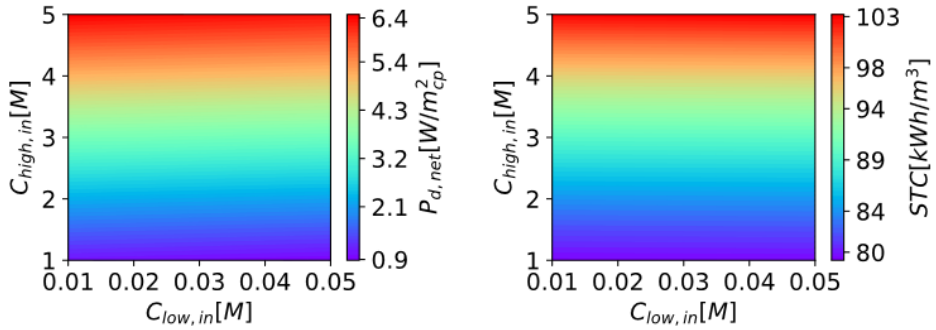


Figure 5.27 Maps showing the $P_{d,net}$ (left) and the STC (right) varying the concentrations in the concentrate and in the dilute compartment for highly-performing RED membranes. (RED stack features: membrane length=0.88 m, $N_{cell}=50$, counter-current arrangement, $t_{work}=5h$, $v_{H,in}=v_{L,in}=0.5$ cm/s. MD unit features: length=5 m, $T_{hot}=80^{\circ}C$ and $T_{cold}=20^{\circ}C$).

On overall, using high-performing *IEMs* the effect of the uncontrolled mixing process is reduced, while the migrative flux increases, resulting in a net increase of the power produced (see *Chapter 4*). On the other hand, future *MD* modules require lower *STC* than current modules and are able to operate with a wider range of feed concentrations (i.e. up to 5M). The corresponding exergy efficiency map is reported *Figure 5.28*, showing much higher values, with a maximum of 16.5% at $C_{H,in}=5M$ and $C_{L,in}=0.01M$.

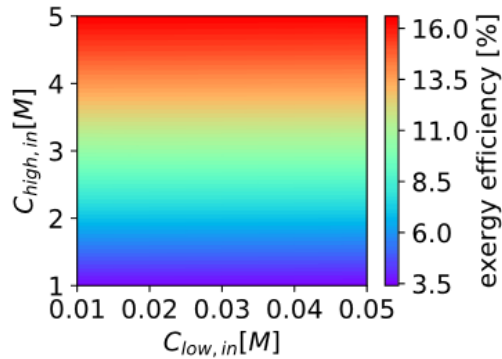


Figure 5.28 Map showing the exergy efficiency varying the concentrations in the concentrate and in the dilute compartment for highly-performing RED membranes. (RED stack features: membrane length=0.88 m, $N_{cell}=50$, counter-current arrangement, $t_{work}=5h$, $v_{H,in}=v_{L,in}=0.5$ cm/s. MD unit features: length=5 m, $T_{hot}=80^{\circ}C$ and $T_{cold}=20^{\circ}C$).

Effect of solution velocities

Also in this case the impact of the RED inlet solution velocities was investigated considering the values of concentrations, which maximized the exergy efficiency of the previous analysis (i.e. 5M for the concentrate and 0.01M for the dilute). In Figure 5.29 the colour-maps relevant to the $P_{d,net}$ and the STC versus the fluid velocities are reported. Differently from what observed varying the solutions concentration, both solution velocities have an appreciable influence on the system performance. Regarding the $P_{d,net}$, a considerable increase of the generated power density is observed when both velocities are maximized. Therefore, in the case of $v_{H,in}=v_{L,in}=1.5$ cm/s the $P_{d,net}$ value is doubled with respect to the maximum value observed in the previous analysis. Conversely, in order to minimize the STC , the most suitable velocity set presents the minimum investigated $v_{H,in}$ (i.e. 0.25cm/s) and the maximum investigated $v_{L,in}$ (i.e. 1.5cm/s). This is due to the fact that, in this condition, the concentration change in the concentrate solution is maximized, which leads to a lower concentration in the MD feed.

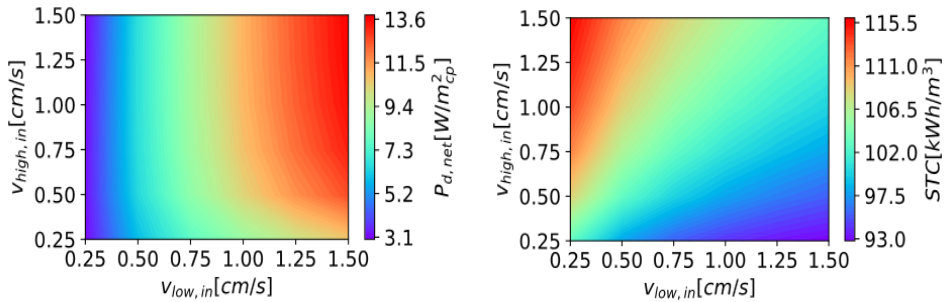


Figure 5.29 Maps showing the $P_{d,net}$ (left) and STC (right) varying the velocities in the concentrate and in the dilute compartment with highly-performing RED membranes. (RED stack features: membrane length=0.88 m, $N_{cell}=50$, counter-current arrangement, $t_{work}=5h$, $C_H=5M$ and $C_L=0.01M$. MD unit features: length=5 m, $T_{hot}=80^\circ C$ and $T_{cold}=20^\circ C$).

Finally, the map reporting the exergy efficiency values varying the fluid velocities is shown in Figure 5.30. The combination of the producible power and the thermal consumption gives rise to a maximum of exergy efficiency which is located at $v_{H,in}=v_{L,in}=0.5$ cm/s, i.e. the same set of velocities employed for the solution concentration analysis. Then, the maximum exergy efficiency achievable with highly performing RED and MD equipment is equal to 16.5%, as already stated.

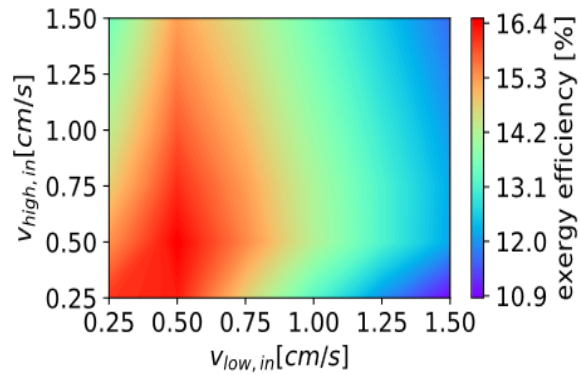


Figure 5.30 Map showing the exergy efficiency varying the velocities in the concentrate and in the dilute compartment with highly-performing RED membranes. (RED stack features: membrane length=0.88 m, $N_{cell}=50$, counter-current arrangement, $t_{work}=5h$, $C_H=5M$ and $C_L=0.01M$. MD unit features: length=5 m, $T_{hot}=80^{\circ}C$ and $T_{cold}=20^{\circ}C$).

5.5 Conclusions

In this chapter, simplified mathematical models were presented to describe the performance of solvent extraction regeneration units.

A theoretical analysis of the performance of an ideal *RED-HE* was presented, in which a regeneration with a single stage or multi stage evaporative process was considered. Results indicated how the use of acetate salts can lead to enhanced performances with respect to NaCl solutions, thanks to higher free energy of mixing and higher solubility. At the same time, multi-stage regeneration units led to a remarkable reduction of the thermal energy consumption, thus enhancing the process overall efficiency. However, the reduction of the available driving force resulted in an increase of the heat transfer area requirements. The highest thermal efficiency around 13% was observed for KAc and LiCl at molalities between 15 and 17 mol/kg, though the effect of molality becomes almost negligible above 10 mol/kg.

Furthermore, performance analyses of *RED-MED HE* and *RED-MD-HE* fed by NaCl solution were performed, considering the influence of membrane properties and operating conditions. In the case of *RED-MED HE* with current state of the art membrane properties the higher thermal efficiency obtained is equal to 1.4%. Assuming the adoption of membranes with ideal properties, the exergy and thermal efficiencies can reach values up to 31% and 6.6%, respectively.

In the case of *RED-MD HE*, the performances of a lab-scale prototype were evaluated investigating different operating conditions and process configurations. As a result an optimal configuration which maximizes the cycle efficiency was identified to support the design of the first *RED-MD HE* prototype within the EU project RED-Heat-to-Power. Moreover, perspective analyses were carried out by accounting for highly performing equipment. As concerns the current system, an exergy efficiency equal to 2.3% was achieved. Higher values can be obtained by considering improved *IEMs* and *MD* units, resulting into an exergy efficiency of about 16.5%, which is much higher than the values reported in literature until now.



ADVANCED RED-MED MODEL

Chapter Outline

ABSTRACT	165
6.1 INTRODUCTION	166
6.2 EXERGY ANALYSIS	168
6.3 RESULTS	172
6.3.1 EFFECT OF IRREVERSIBILITY SOURCES	174
6.3.2 CURRENT MEMBRANE PROPERTIES.....	179
6.3.3 ANALYSIS WITH HIGH-PERFORMING MEMBRANE PROPERTIES.....	185
6.3.4 COMPARATIVE ANALYSIS	188
6.4 CONCLUSIONS.....	191

Paper in-preparation:

B. Ortega-Delgado, F. Giacalone, P. Catrini, A. Cipollina, A. Tamburini, A. Piacentino, G. Micale, "Exergy Analysis of Reverse Electrodialysis Heat Engine with Multi-Effect Distillation Regeneration Stage".

Abstract

This chapter is devoted to the analysis of a Reverse Electrodialysis heat engine which adopts a thermal evaporative process for the solvent extraction regeneration step in order to restore the concentration of the two original solutions. Among the available technologies, multi-effect distillation appears as the most suitable process due to its higher thermal efficiency in comparison to the other processes. An advanced mathematical model, developed in collaboration with CIEMAT, is here used to carry out a rigorous exergy analysis of the whole RED-MED HE fed by NaCl. To this aim, sensitivity analyses were performed to investigate the effect of the irreversibility sources, operating conditions and design parameters on the exergy efficiency of each component of the RED-MED HE. Further, a perspective analysis was carried out considering the improvements obtainable by using enhanced IEMs in the RED unit.

Results indicates that the main limiting factor on the exergy efficiency (ranging between 2 and 5 %) of the current technology is given by the membrane properties. The adoption of future enhanced membranes with higher permselectivity and reduced resistance, water and salt permeability, could lead to a huge increase on the heat engine efficiency, reaching value up to 25%

6.1 Introduction

In this chapter, an exergy analysis at component level is applied to the integrated *RED-MED* heat engine to provide insight into the performance potential of this technology, using advanced mathematical modelling.

Starting from the existing simplified *RED-MED HE* model presented in *Chapter 5*, an *advanced RED-MED HE* model was developed in collaboration with *CIEMAT* by coupling the 1-*RED* model to the *CIEMAT MED* model. The whole model has been implemented in Engineering Equation Solver (EES) [160] software and it consists of four sections:

- (i) Reverse Electrodialysis Process model, which is the mono-dimensional model describing all the main phenomena involved in the power generation process described in *Chapter 2*;
- (ii) Multi Effect Distillation Process model based on the resolution of mass and energy balances described in *Section 5.3* and *Appendix 2*;
- (iii) Model integration, where the *RED* model and the *MED* model are coupled together including the two mixing stages described in *Section 5.3.4*
- (iv) Exergy analysis, which provides the equations to evaluate the exergy fluxes and the exergy efficiency definition in each component of the system.

In addition to integrating mass and enthalpy balance equations, it is worth mentioning that a number of auxiliary equations have been used to estimate all thermodynamic properties of artificial NaCl-water solutions being the working fluids of the *RED-MED HE*. With this respect, the activity and osmotic coefficients of aqueous sodium chloride solution are estimated using the Pitzer's thermodynamic model (as described in *Section 4*), which is recommended for the chemical exergy calculation using electrolytic solutions such as NaCl-water [175]. The specific enthalpy and entropy of the sodium chloride aqueous solution are tabulated in [144] as function of the temperature (0–300 °C), pressure (1–1000 bar) and molality (0.1–6.0 mol/kg) and correlations have been derived from these values and used in the present model formulation. Other physical properties, namely density, conductivity and viscosity have been also calculated by means of empirical correlations as a function of molar concentration and temperature.

The resulting advanced integrated model was used to carry out a rigorous exergy analysis on the *RED-MED HE* system fed by NaCl-water solutions. As a first step, a base case scenario

has been selected, and the main performance indicators (exergy and thermal efficiency, power density, specific thermal energy consumption, etc.) have been determined. Later, the main sources of irreversibility have been analysed as function of the external to internal electrical resistance ratio in the *RED* unit. Also, sensitivity analyses of the exergy efficiency, at global and component level, have been carried out. Particularly, the inlet concentration and velocity of the concentrate and dilute solutions to the *RED* stack have been considered, along with the stack geometry (length, width and thickness of the membranes). Finally, the evaluation of the exergy efficiency with high-performing membranes is presented and comparatively analysed.

6.2 Exergy analysis

The exergy flux for each stream of matter is evaluated by considering both physical and chemical exergy content. For the *RED-MED* heat engine, which main objective is to generate power using low-grade heat as fuel, the evaluation of the exergy destroyed and lost in each sub-system can help to improve the performance of the whole system.

For a system consisting of a mixture of n species with n_1, n_2, \dots, n_n moles, in general at different temperature, pressure, and composition from the environment (and with the same velocity and elevation), the maximum theoretical work obtainable when the system reaches thermal, mechanical and chemical equilibrium with the environment is defined as exergy [176]. In these conditions, the total exergy is the sum of the physical and the chemical terms, neglecting the nuclear, magnetic, electrical, kinetic and surface tension effects.

The physical exergy is identified as the maximum useful work attainable by the system when undergoes a process from a generic thermodynamic state at a pressure p temperature T to the *restricted dead state* (*RDS*), denoted with an asterisk (*). In the *RDS* the system is in thermal and mechanical equilibrium with the environment at T_0 and p_0 but with the original composition x . The chemical exergy relates the concentration difference between the *RDS* and the *dead state* (T_0, p_0, x_0). It represents the maximum work obtainable when the system changes from its concentration to the one of the environment (at the environment pressure and temperature (p_0, T_0)).

Therefore, if steady-state flow is considered, the total specific molar flow exergy (\bar{e}_t) is given by the sum of the thermomechanical (\bar{e}_{ph}) and chemical (\bar{e}_{ch}) contributions:

$$\bar{e}_t = \bar{e}_{ph} + \bar{e}_{ch} \quad (6.1)$$

$$\bar{e}_{ph} = \bar{h} - \bar{h}^* - T_0(\bar{s} - \bar{s}^*) \quad (6.2)$$

$$\bar{e}_{ch} = \sum_{i=1}^n (\mu_i^* - \mu_{0,i}) x_i \quad (6.3)$$

where \bar{h} and \bar{s} the molar enthalpy and entropy of the inlet mixture, x_i the mole fraction of the i^{th} -component and μ_i the chemical potential of a component i in a solution, as already reported in *Chapter 4*. The total molar exergy of the stream (B_i) is given by the product of the

total specific exergy for the total molar flow rate. In the exergy analysis the following assumptions have been made:

- Steady-state operation of the system.
- The kinetic and potential terms in the exergy calculation were neglected
- In the flow exergy calculation, the physical part of the specific exergy of the solution has been neglected as all the NaCl-water streams entering and exiting each component are assumed to be at 25 °C, which is the dead state temperature, and the influence of the pressure variation is much lower than that of the temperature variation [105,144].
- The following dead state has been considered: $x_0=38,000$ ppm of NaCl, $p_0=101,325$ Pa, and $T_0=25$ °C.

The exergy efficiency definition of each component of the system follows the guidelines presented by Tsatsaronis [177], where exergy efficiency is defined as the ratio of a *product* and a *fuel*. The *product* is considered as the stream of interest, material or energy, simple or compound, for which the system has been designed and conceived. Conversely, the *fuel* is defined as every resource used to generate the desired product, simple or compound stream of matter or energy. Therefore, the exergetic efficiency is calculated as the ratio of the exergy rate of the product ($\dot{B}_{Product}$) and the exergy rate of the fuel (\dot{B}_{Fuel}):

$$\eta_{ex} = \frac{\dot{B}_{Product}}{\dot{B}_{Fuel}} = 1 - \frac{\dot{B}_{Loss} + \dot{I}r}{\dot{B}_{Fuel}} \quad (6.4)$$

where \dot{B}_{Loss} represents the exergy of the loss streams (rejected to the environment without further use) and $\dot{I}r$ is the exergy destruction due to the irreversibility sources of the system. The exergy efficiency definition is applied to all the components (i.e. *RED* unit, *Mixer 1*, *Mixer 2* and *MED* unit), of the system depicted in *Figure 6.1*.

In the *RED* process, as already presented in in *chapter 3*, the product is the net electrical power produced in the system ($P_{RED,net}$), while the fuel is the chemical power or the rate of exergy consumed in the *RED* unit from the inlet solutions ($\dot{B}_{H,in} - \dot{B}_{H,out}$) + ($\dot{B}_{L,in} - \dot{B}_{L,out}$):

$$\eta_{ex,RED} = \frac{P_{RED,net}}{(\dot{B}_{H,in} - \dot{B}_{H,out}) + (\dot{B}_{L,in} - \dot{B}_{L,out})} \quad (6.5)$$

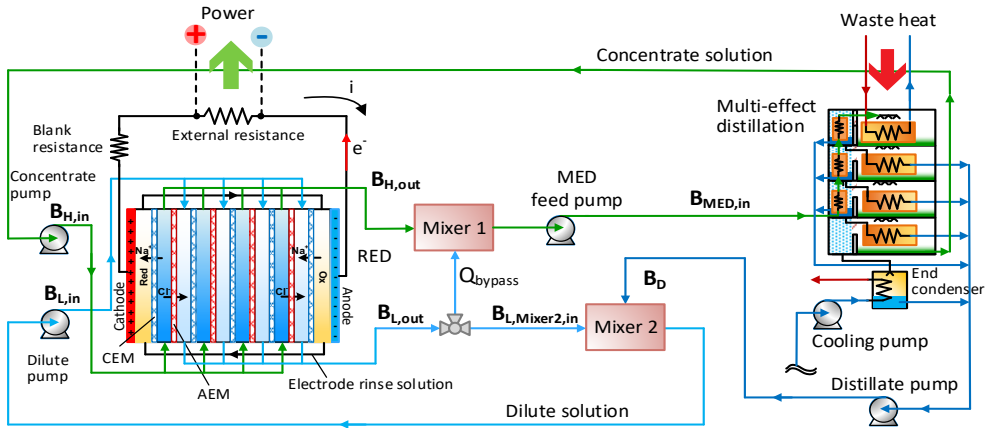


Figure 6.1. Process flow diagram of the RED-MED coupled system.

Within the *RED* unit part of the salt content in the concentrate stream is transferred to the dilute stream due to the migrative ion flux (product) and diffusive salt flux (irreversibility source). In the *MED* process, only water is extracted from the concentrate stream, then *Mixer 1* is used to re-establish the original salt content in the concentrate stream by mixing part of the dilute stream to the concentrate one. As a result, the concentration of the resulting stream is decreased. The mixing process is purely a dissipative process, that only add irreversibility to the process, then, no product is obtained. In order to maintain the same definition of the exergy efficiency also for the mixers, the exergy rate of the outlet solution from the mixing ($\dot{B}_{MED,in}$) is considered as product while the two inlet streams ($\dot{B}_{H,mixer1,in} + \dot{B}_{L,mixer1,in}$) are considered as fuel. Due to this definition the exergy efficiency will be 100% when no exergy variation of the inlet concentrate solution occurs in the mixer, i.e. when the dilute flowrate is zero.

$$\eta_{ex,mixer1} = \frac{\dot{B}_{MED,in}}{\dot{B}_{H,mixer1,in} + \dot{B}_{L,mixer1,in}} \quad (6.6)$$

Mixer 2 is used to mix the distillate produced in the *MED* unit to the dilute stream exiting the *RED* unit, restoring the original concentration of the dilute solution before entering the *RED* unit. As in the previous case, the exergy efficiency of the *Mixer 2* is determined according to:

$$\eta_{ex,mixer2} = \frac{\dot{B}_{mixer2,out}}{\dot{B}_D + \dot{B}_{L,mixer2,in}} \quad (6.7)$$

In the *MED* unit, part of the inlet flow-rate coming from *Mixer 1* is vaporized to generate a concentrated stream with the original concentration and flow-rate of the concentrate solution, before entering in the *RED* unit. This component uses external heat for the thermal separation of the solute and the solvent, both with higher exergy than the feed stream. Thus, the product in the *MED* process is the increase of the exergy content of the outlet material streams ($\dot{B}_{H,MED,out} + \dot{B}_D - \dot{B}_{MED,in}$), with respect to the inlet stream, while the fuel is defined as the exergy content of the heat added to the *MED* (net value) plus the exergy of the pumping power consumed ($\dot{B}_{Q,wh,in} - \dot{B}_{Q,wh,out} + P_{pumping,MED}$). The effect of the cooling on the efficiency of the *MED* and of the whole system is included in $P_{pumping,MED}$ by calculating the pumping power required to pump the cooling water in the end condenser, according to eq. 5.19. For the cases in which the cooling solution is not available and it has to be generated on site, an additional exergy loss has to be considered in the efficiency definitions.

$$\eta_{ex,MED} = \frac{\dot{B}_{MED,out} + \dot{B}_D - \dot{B}_{MED,in}}{\dot{B}_{Q,wh,in} - \dot{B}_{Q,wh,out} + P_{pumping,MED}} \quad (6.8)$$

On overall, the global exergy efficiency ($\eta_{ex,g}$) of the integrated system is defined as the ratio between the net power produced by the *RED* unit (subtracting both pumping power in *RED* and *MED*) and the exergy content of the heat added to the *MED* unit:

$$\eta_{ex,g} = \frac{P_{RED,gross} - P_{pumping,RED} - P_{pumping,MED}}{\dot{B}_{Q,wh,in} - \dot{B}_{Q,wh,out}} \quad (6.9)$$

while, the thermal efficiency of the overall system ($\eta_{th,g}$) is calculated as:

$$\eta_{th,g} = \frac{P_{RED,net}}{Q_{wh}} = \eta_{X,g} \cdot F_{Carnot} = \eta_{X,g} \cdot \left(1 - \frac{T_{cold}}{T_{hot}}\right) \quad (6.10)$$

where F_{Carnot} is the Carnot heat factor, T_{cold} is the cold reservoir temperature (K), and T_{hot} the hot reservoir temperature (K).

Interestingly, the RED-HE requires a cooling source at temperature of

6.3 Results

The advanced *RED-MED HE* model, including the exergy analysis equations, was used to carry out sensitivity analyses in order to investigate the influence of the (i) main irreversible sources, (ii) operating and (iii) design parameters on the exergy efficiency of the system at component level (*RED* stack, *MED* unit, *Mixer 1* and *Mixer 2*).

The analysis starts considering a reference case in order to quantify the exergy potential of the system under common design and operating conditions. This scenario will be compared later on with the one obtained after the different sensitivity analyses, selecting the best obtained performing conditions for each case. The reference case considers a *RED* unit made of 1000 cell pairs with membrane area of $0.5 \times 0.5 \text{ m}^2$ (typical dimension of large-scale *RED* unit), counter current flow arrangement, inlet velocities of the two solutions equal to 1 cm/s and inlet concentration of the solutions equal to 3 M and 0.05M. The number of *MED* is set equal to 22, due to the limitation given by the particular values of the inlet concentrations and velocities (high boiling point elevation). A summary of the reference case condition is reported in *Table 6.1*.

Table 6.1 Main inputs for the base case.

Concept	Value
RED UNIT	
<u>Cell pair</u>	
Flow pattern, (-)	Counter-current
Number of cell pairs, (-)	1000
Width, b (m)	0.5
Length, L (m)	0.5
Blank resistance, R_{blank} ($\Omega \cdot m^2$)	3.27×10^{-3}
Operation temperature, T ($^{\circ}C$)	25
<u>Solutions</u>	
Concentrate inlet concentration, C_H (mol/L)	3
Dilute inlet concentration, C_L (mol/L)	0.05
Inlet concentrate velocity, v_H (cm/s)	1
Inlet dilute velocity, v_L (cm/s)	1
<u>Membranes (FujiFilm Type 10)</u>	
Thickness, δ_m (m)	1.25×10^{-4}
Water permeability ^a , P_w ($m^3/(m^2 \cdot s \cdot Pa)$)	2.222×10^{-14}
Salt permeability coefficient ^a , P_{salt} (m^2/s)	4.52×10^{-12}
<u>Spacer (Deukum)</u>	
Concentrate spacer thickness, δ_H (m)	1.5×10^{-4}
Dilute spacer thickness, δ_L (m)	1.5×10^{-4}
Relative concentrate spacer volume, ϵ_H (-)	0.175
Relative dilute spacer volume, ϵ_L (-)	0.175
Shadow factor, sf (-)	1.563
MED UNIT	
Number of effects, (-)	24
Heating steam temperature, ($^{\circ}C$)	100
Last effect temperature, ($^{\circ}C$)	27
Terminal temp. difference preheater 1, ($^{\circ}C$)	3
Terminal temp. difference end condenser, ($^{\circ}C$)	3
Intake cooling water temperature, ($^{\circ}C$)	15
Evaporators tube bundle	L: 1 m; \varnothing : 22 mm
End condenser tube bundle	L: 2 m; \varnothing : 25 mm
PUMPS	
Pumps efficiency, η_p (-)	0.8

^a Properties provided by FUJIFILM Manufacturing Europe B.V.

The global and component exergy efficiencies evaluated for the reference case are reported in Table 6.2. In the abovementioned conditions the global exergy efficiency is equal to 1.9% corresponding to a thermal efficiency of 0.4%. Analysing the exergy efficiency in each component, the lowest value is given by the RED unit (i.e. 20%), which limits the exergy

efficiency of the whole system. As it has already discussed in *Chapter 3*, the low exergy efficiency of the *RED* unit is caused by the irreversibility sources, mainly due to the membrane properties. Conversely, the *MED* unit reaches a relatively high performance, around 42%. Therefore, the exergy destruction in the *RED* stack is significant. The *Mixers 1* and *Mixer 2* have also comparatively high exergy efficiencies, respectively equal to 57.9% and 82.3%, thus suggesting that the exergy destruction in these components is low under the considered conditions.

Table 6.2 Results for the base case.

Concept	Value
Global exergy efficiency, %	1.9
Global thermal efficiency, %	0.4
RED exergy efficiency, %	20.7
MED exergy efficiency, %	41.7
Mixer 1 exergy efficiency, %	57.9
Mixer 2 exergy efficiency, %	82.3
Net power, (W)	263
Heat rate, (W)	70,260

6.3.1 Effect of irreversibility sources

The effect of the main sources of irreversibility in the *RED* process was already investigated in *Chapter 3*, where the influence of ohmic losses, membrane permselectivity, diffusive salt flux and the water flux across the *IEMs* on *RED* exergy efficiency was studied. Here the analysis is extended to all the components of the *RED-MED HE* and consider four additional scenarios to analyse also the effect of irreversibility sources due to (i) the polarisation phenomena (*case E*), (ii) *RED* and (iii) *MED* pumping power (*case F* and *G*), and (iv) the average temperature difference between vapour and brine (ΔT_{exch}) in the *MED* unit (*case H*). For this latter analysis, the same inputs fixed in the base case have been considered (0.5 m × 0.5 m, 3 – 0.05 M, 1 cm/s – 1 cm/s), while the number of *MED* effects was selected in order to maintain always for each different resistance ratio (or different *MED* inlet concentration), an effective mean temperature difference around 1°C.

The 8 investigated scenarios are described as follows:

- Scenario A. Only the internal ohmic losses are considered (ideal membrane properties): $P_w = 0 \text{ m}/(\text{Pa}\cdot\text{s})$, $P_{salt} = 0 \text{ m}/\text{s}^2$, $\theta_H = 1$, $\theta_L = 1$, and $\alpha = 1$.

- Scenario B. The effect of the non-ideal permselectivity of the membranes is considered: $P_w = 0 \text{ m}/(\text{Pa}\cdot\text{s})$, $P_{salt} = 0 \text{ m}/\text{s}^2$, $\theta_H = 1$, $\theta_L = 1$, and $\alpha \neq 1$.
- Scenario C. In this case both the non-ideal permselectivity and diffusive salt flux are added, while neglecting the water flux: $P_w = 0 \text{ m}/(\text{Pa}\cdot\text{s})$, $P_{salt} = 10^{-12} \text{ m}/\text{s}^2$, $\theta_H = 1$, $\theta_L = 1$, and $\alpha \neq 1$.
- Scenario D. This case adds the water flux: $P_w = 2.22 \cdot 10^{-14} \text{ m}/(\text{Pa}\cdot\text{s})$, $P_{salt} = 10^{-12} \text{ m}/\text{s}^2$, $\theta_H = 1$, $\theta_L = 1$, and $\alpha \neq 1$.
- Scenario E. The polarisation effect is included in this scenario: $P_w = 2.22 \cdot 10^{-14} \text{ m}/(\text{Pa}\cdot\text{s})$, $P_{salt} = 10^{-12} \text{ m}/\text{s}^2$, $\alpha \neq 1$, $\theta_H \neq 1$, and $\theta_L \neq 1$.
- Scenario F. Same assumption of the previous scenario, adding the effect of pumping power consumption in the RED unit (concentrate and dilute solution pumps).
- Scenario G. Same assumption of the previous scenario, adding the effect of pumping power consumption in the MED unit (feedwater, concentrate, distillate and cooling pumps).
- Scenario H. The influence of ΔT_{exch} on the exergy efficiency of the MED unit is investigated, fixing other conditions as in *scenario G*.

The effect of the different irreversibility sources (*A-G*) on the RED exergy efficiency is shown in *Figure 6.2-a* as a function of the resistance ratio R_{ext}/R_{int} . Of course, the same trends already discussed in Chapter 3 are obtained for the first four scenarios (*A-D*). *Scenario E* considers the effect of concentration polarisation which has a slight effect on the RED exergy efficiency, accounting for a decrease from 22.2% to 21.6%. The concentration polarisation reduces the real salinity gradient across the membranes, then, it should directly affect the power production in the RED unit. As a matter of fact, the average value of the polarisation coefficients (see *Chapter 2*) are equal to 0.99 for the concentrate and 0.83 for the dilute, producing negligible reduction of salinity gradient across the membrane and then the corresponding irreversibility source.

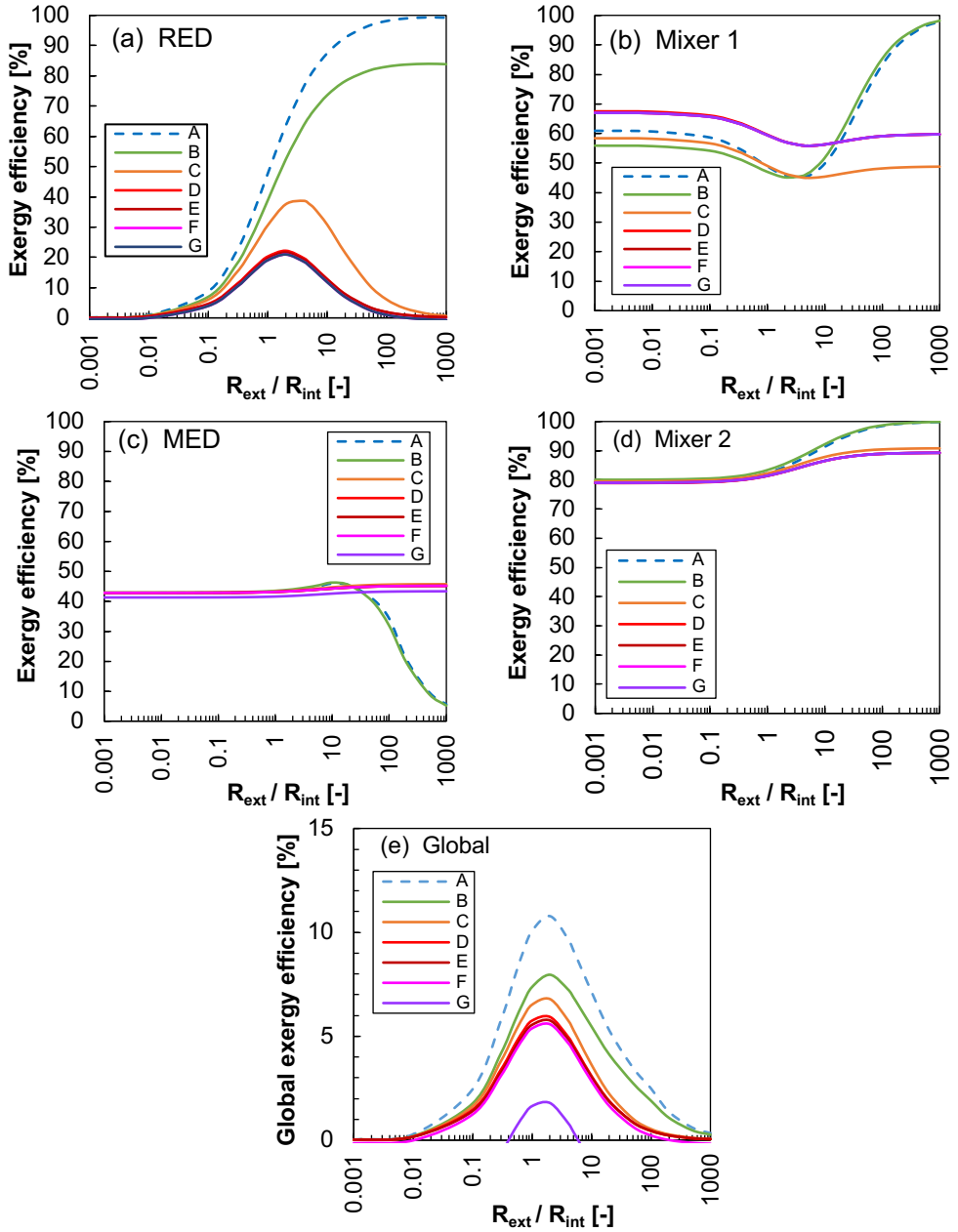


Figure 6.2. Exergy efficiency as function of the external-to-internal stack resistance ratio and the irreversibility sources, in the base case: (a) RED, (b) MED, (c) Mixer 1, (d) Mixer 2, and (e) Global. RED unit made of 1000 cell pairs $0.5 \times 0.5 \text{ m}^2$, $C_H = 3 \text{ M}$ and $C_L = 0.05 \text{ M}$, $v_H = v_L = 1 \text{ cm/s}$, MED $\Delta T_{exch} \sim 1^\circ \text{C}$.

The RED pumping power (scenario F) produces a small exergy consumption, reducing the maximum power output of about 5%. Of course, the MED pumping power consumption

(scenario G), does not affect directly the efficiency of the RED unit, but it significantly decreases the global net power of the system. The maximum power is reduced from 780 W in scenario H to 250 W in scenario G. It is worth noting that R_{ext}/R_{int} does not affect the exergy efficiency of the RED unit for the last three scenarios.

Exiting from the RED unit part of the dilute solution is added to the concentrate stream in order to re-established the original salt content of this stream, then, part of the exergy is dissipated. Figure 6.2-b shows the exergy efficiency of the Mixer 1 as a function of resistance ratio. The exergy destruction due to the mixing process is determined by two factors, i.e. (i) the concentration difference between concentrate and dilute, and (ii) the dilute flowrate added to the concentrate. In the ideal scenarios A and B, where only ohmic losses and permselectivity are the sources of irreversibility, the exergy of the Mixer 1 decreases with R_{ext}/R_{int} , reaching a minimum value for $R_{ext}/R_{int} \sim 3$. After this value, the exergy efficiency begins to increase up to approximately 100% when R_{ext}/R_{int} approaches to infinite. When R_{ext}/R_{int} approaches to zero, the ionic salt flux in the RED unit is the highest, thus the highest variation in the dilute and concentrate concentration is observed (Figure 6.3a). In this case, the exergy destruction in the Mixer 1 is mainly determined by the amount of dilute flowrate added to the concentrate (Figure 6.3.b). In this condition the dilute concentration is the highest.

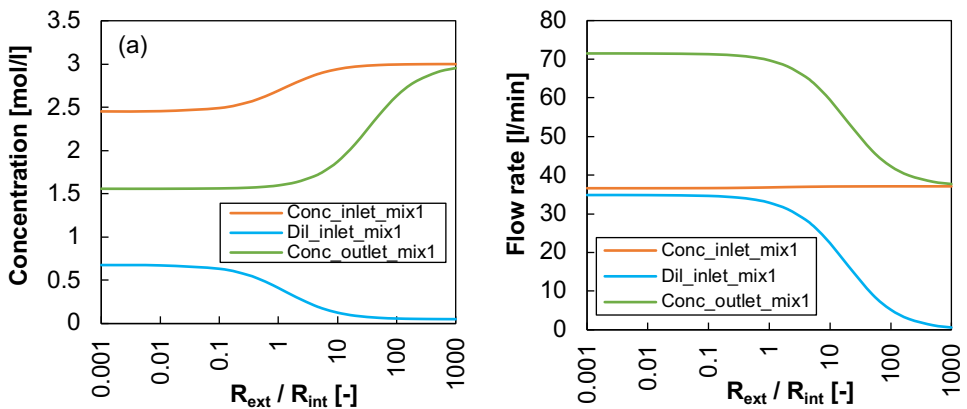


Figure 6.3. Inlet and outlet (a) concentration and (b) molar flow rate in the Mixer 1 as a function of the resistance ratio, for scenario A (only internal resistance losses). RED unit made of 1000 cell pairs $0.5 \times 0.5 m^2$, $C_H = 3M$ and $C_L = 0.05M$, $v_H = v_L = 1 cm/s$, $MED \Delta T_{exch} \sim 1^\circ C$.

Conversely, when the R_{ext}/R_{int} is increased, the ionic salt flux is reduced, tending to zero for very large R_{ext}/R_{int} and no substantial variations in the concentration of solution occur across the pile. In this case, the concentration of the dilute is the lowest, but in at the same

time the flowrate of dilute needed to integrate the salt lost in the concentrate decreases up to zero, leading to an increase of the exergy efficiency of the *Mixer 1* up to 100%. In this condition, no dilute is added to the concentrate then no exergy is dissipated during the process.

In the *scenarios C* and *D*, the uncontrolled mixing phenomena consume part of the available salinity gradient even at infinite R_{ext}/R_{int} , therefore in these cases the mixing process is always necessary. The shift in the exergy efficiency profile observed when comparing cases *C* to *D* is due to the large effect of the water flux, which increases the dilute concentration, reducing the exergy destruction in the mixers. Clearly, the other irreversibility sources do not affect the performance of the mixing process.

The resulting solution from *Mixer 1* is fed to the *MED* unit in order to restore the original concentration in the concentrate loop. The exergy efficiency of the *MED* is reported in *Figure 6.2-c*. From S.C. (i.e. $R_L/R_{int}=0.001$) up to $R_{ext}/R_{int}=1$, the exergy efficiency of the *MED* unit is almost constant, i.e. ~40% for scenarios *A-G*, due to the small variation in the inlet solution concentration. When R_{ext}/R_{int} is increased, for cases *A* and *B* the exergy efficiency of the *MED* unit starts to decrease, tending to zero for R_{ext}/R_{int} tending to infinite. In this condition, the salinity gradient between the two solutions is more and more preserved (*Figure 6.3.b*). Then, the requirement of the regeneration process is reduced with the increase of R_{ext}/R_{int} , tending to zero for $R_{ext}/R_{int} \rightarrow 0$. Hence a lower number of *MED* effects are used. For the other cases, the effect of uncontrolled mixing phenomena causes a constant consumption of the salinity gradient in the *RED* unit (the ionic flux is reduced tending to zero when the R_{ext}/R_{int} tending to infinite), then a practically constant regeneration step is required. The effect of the mean temperature difference in the *MED* unit stages on the exergy efficiency and the specific heat exchanger area is reported in *Figure 6.4*. The increase of ΔT_{exch} results in a significantly reduction of the *MED* exergy efficiency due to the reduction of the number of stages. In fact, increasing the ΔT_{exch} a large part of the available temperature difference between the first and the last effect is lost just to exchange the heat. Conversely, when low ΔT_{exch} are considered, the available temperature difference is used in the BPE to store chemical exergy in the concentrate.

On the other hand, the reduction of ΔT_{exch} causes an increase of the heat exchanger area, resulting in an increase of the capital cost of the plant. The optimal ΔT_{exch} is given by economic consideration. In the further analyses, ΔT_{exch} approximatively equal to 1°C was considered, in

order to reduce its influence on the exergy efficiency reduction and highlight the effects of the other sources of irreversibility.

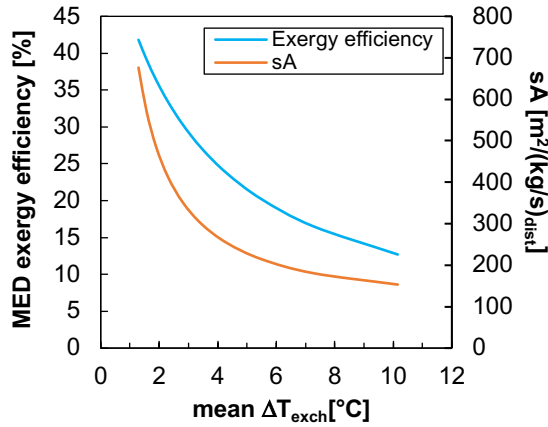


Figure 6.4 Exergy efficiency and specific heat exchanger area as a function of the mean temperature difference in the effects. RED unit made of 1000 cell pairs $0.5 \times 0.5 \text{ m}^2$, $C_H = 3M$ and $C_L = 0.05M$, $v_H = v_L = 1 \text{ cm/s}$.

The distillate extracted in the *MED* unit is added to the remaining dilute solution in *Mixer 2* to restore the original dilute stream. The exergy efficiency of *Mixer 2* is reported in *Figure 6.2-d*. For all the cases, it increases with R_{ext}/R_{int} due to the reduction in the ionic flux in the *RED* unit, which means less requirement of regeneration (and mixing). In particular, for cases *A* and *B*, the exergy efficiency tends to 100% which means that no distillate is added to the dilute solution exiting from the *RED* unit.

Finally, the global exergy efficiency is presented in *Figure 6.2-e*, where a maximum is found for R_{ext}/R_{int} between 1 and 10, as a result of combining the effects of each single component efficiency. It is interesting to highlight the significant reduction produced by the *MED* pumping power consumption on the global exergy efficiency (from 5.9% to 1.9%).

6.3.2 Current Membrane properties

In the following analyses the effect of operating and design parameters on the exergy efficiency of each component of the *RED-MED HE* is investigated by referring to the *scenario G*.

6.3.2.1 *Effect of feed solution concentration in the RED unit*

In this section, the effect of the *RED* inlet concentrations on the exergy efficiency of the system is evaluated. In particular, the exergy efficiencies of the single-component are analysed when the inlet concentrations vary between 2–5M (concentrate) and 0.01–0.1M (dilute), keeping constant the rest of parameters as in the reference case, except the number of *MED* effects, which is maximized for each different *MED* condition, keeping $\Delta T_{exch} = 1$ °C as minimum acceptable value. *Figure 6.5* shows the results of the parametric evaluation for each component (*RED* stack, *MED* unit, *Mixer 1* and *Mixer 2*) and for the overall *RED-MED* system.

The exergy efficiency of the *RED* stack (*Figure 6.5-a*) increases for lower values of the concentrate solution salinity, reaching almost 28% at $C_H=2$ M, while it is practically not affected by the dilute solution salinity in the range analysed. This behaviour is explained by the lower exergy destruction associated to the uncontrolled mixing phenomena, when the concentration difference is reduced. For the *MED* unit, the exergy efficiency increases up to 62% with the concentration of the concentrate solution (*Figure 6.5-b*). The increase in the concentration reduces the number of effect due to the *BPE*, but at the same time, more exergy is accumulated in the solution, rising the efficiency.

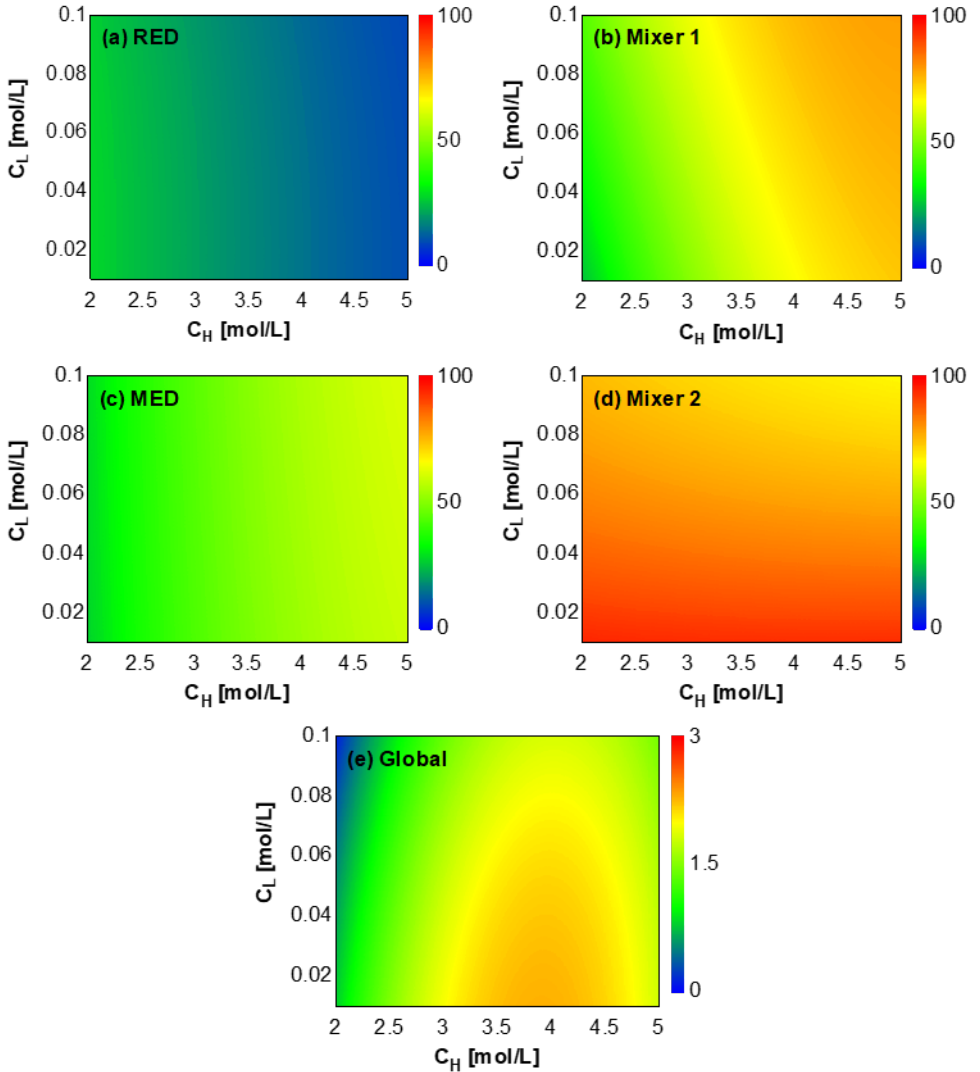


Figure 6.5. Exergy efficiency as function of the concentrate and dilute inlet concentrations to the RED stack, using current membranes: (a) RED unit, (b) MED unit, (c) Mixer 1, (d) Mixer 2, (e) Global. RED unit made of 1000 cell pairs $0.5 \times 0.5 \text{ m}^2$, $v_H = v_L = 1 \text{ cm/s}$, MED $\Delta T_{\text{exch}} \sim 1^\circ\text{C}$, scenario H.

The exergetic performance of the *Mixer 1* (Figure 6.5-b) increases when high solution concentration is considered. The highest exergy efficiency of about 80% is obtained for the highest solution concentration considered 5 M and 0.1 M. On the contrary, the exergy efficiency of the *Mixer 2*, increases up to about 95% with the decrease of the inlet dilute solution concentration (Figure 6.5-d).

Finally, as a combination of all the above-mentioned effects a maximum global exergy efficiency of 2.3% is reached at an intermediate inlet concentrations, i.e. 4M–0.01M.

6.3.2.2 *Effect of feed solution velocity in the RED unit*

In this section, the effect of the *RED* inlet velocity of concentrate and dilute solutions on the exergy efficiency is evaluated. In this analysis, the inlet concentration values leading to the maximum exergy efficiency in the previous analysis have been considered (i.e. 4–0.01 M), keeping the rest of parameters constant (except the number of *MED* effects). Results are presented in *Figure 6.6 a-e*.

The exergy efficiency of the *RED* stack is depicted in *Figure 6.6-a*. As it has already observed in *Chapter 3*, the higher exergy efficiency of *RED* unit is obtained for the higher dilute solution velocity and for the lowest concentrate velocity, reaching a maximum of 25.3% for concentrate and dilute velocities of 0.2 – 2 cm/s. The lower the inlet solution velocity, the larger the residence time of the solution within the unit, thus, the larger the concentration variation. Then, high concentrate residence times reduce the average concentration difference in the *RED* process, thus, reducing the effect of uncontrolled mixing phenomena. On the contrary, lower dilute solution residence time means lower concentration of the dilute solution which enhances the induced voltage.

The exergy efficiency of the *Mixer 1* (*Figure 6.6-b*) increases with the concentrate velocity and decreases with the dilute velocity, as the higher the concentration and flow rate of the inlet streams, the lower the exergy destruction in the mixer (almost 100% for 2 – 0.5 cm/s).

The exergy efficiency of the *MED* unit (see *Figure 6.6-c*) follows the same trend of the *Mixer 1*, due to the increase of the exergy content of the inlet stream in the *MED* unit. The inlet specific exergy is increased more than the heat rate, while the outlet flow exergy of the concentrate and distillate streams remains equal. The maximum value obtained is 54% for 2 – 1.5 cm/s

The exergy efficiency of *Mixer 2* (*Figure 6.6-d*) is not affected by the velocity of the concentrate solution, while just a small influence of the dilute solution velocity is observed, then it is constant for all the range of velocities analysed.

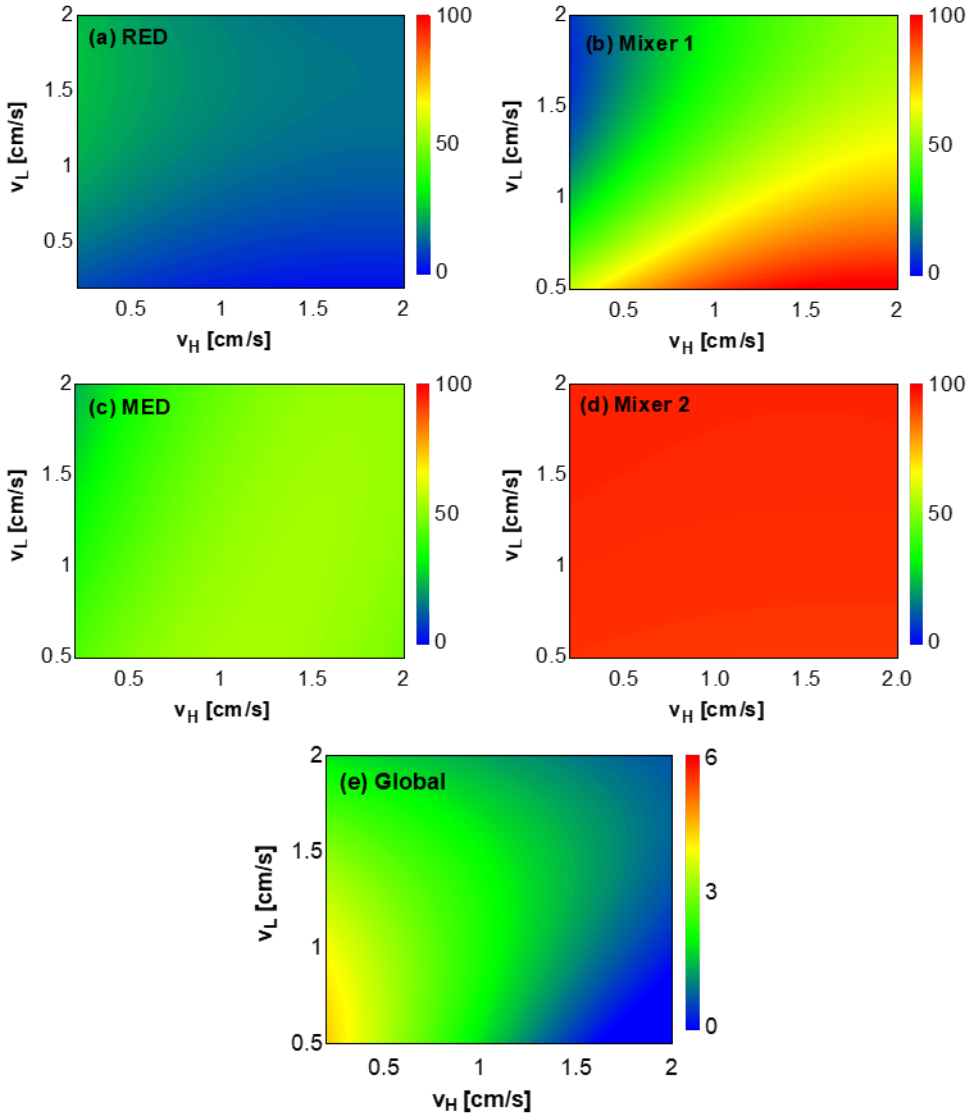


Figure 6.6. Exergy efficiency as function of the concentrate and dilute inlet velocities to the RED stack: (a) RED unit, (b) MED unit, (c) Mixer 1, (d) Mixer 2, (e) Global. RED unit made of 1000 cell pairs $0.5 \times 0.5 \text{m}^2$, $C_H = 4M$ and $C_L = 0.01M$, MED $\Delta T_{\text{exch}} \sim 1^\circ\text{C}$, scenario H.

Finally, the global exergy efficiency is depicted in (Figure 6.6-e). The maximum global exergy efficiency (4.8%) is reached for RED inlet velocities equal to 0.2 cm/s and 0.5 cm/s for concentrate and dilute, respectively.

6.3.2.3 Effect of the membrane's aspect ratio

Here, the effect of the membrane's aspect ratio (length-to-width ratio) on the global exergy efficiency is analysed. In this analysis, the concentrate and dilute concentration and velocity that led to the maximum exergy efficiency have been selected (4–0.01M and 0.2– 0.5 cm/s, respectively). Besides, a constant membrane's area of 0.25m² is assumed.

Figure 6.7 shows the evolution of the exergy efficiency. As it can be seen, intermediate values provide higher performance. This may be explained considering that the increase of the channel length (L) extends the residence time of the solutions, which it has already optimized in the analysis of the inlet velocities. Thus, the maximum exergy efficiency in the given conditions (4.8%) is reached for $R_{geom}=1$ ($b=0.5$ m, $L=0.5$ m).

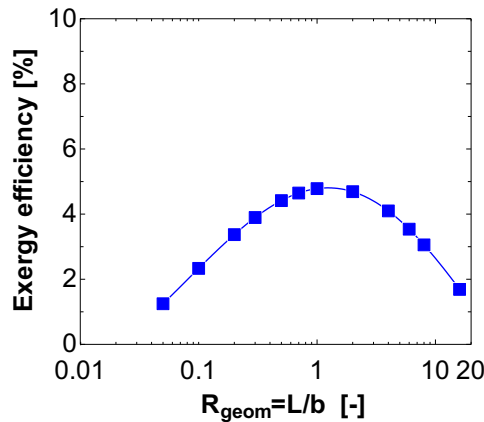


Figure 6.7. Global exergy efficiency as function of the length-to-width (R_{geom}) membrane's ratio. RED unit made of 1000 cell pairs $0.5 \times 0.5m^2$, $C_H = 4M$ and $C_L = 0.01M$, $v_H = 0.2$ cm/s $v_L = 0.5$ cm/s, MED $\Delta T_{exch} \sim 1^\circ C$, scenario H

6.3.3 Analysis with high-performing membrane properties

The membrane properties significantly affect the performance of the *RED-HE* system, as phenomena such as permselectivity, salt diffusive flux, water diffusive flux, and membrane's resistance are sources of irreversibility, which consumes part of the exergy available in the inlet solutions to the *RED* unit. The analyses performed so far, refer to the well-known properties of type 10 *Fujifilm*[®] membranes, however more performing *IEMs* are already available in the market [74], as it has already highlighted in *section 5.4.2.2*. Then, sensitivity analyses have been carried out considering the impact of improved *IEMs* on the whole *RED-HE*. The *IEM* enhancements were selected considering the findings discussed in *Chapter 3* about the effect of the membrane properties on the exergy efficiency of the system and on the basis of the literature information reported in *section 5.4.2.2*. To this aim, the permselectivity was fixed equal to 0.95, and the membrane's resistance, salt diffusive flux, and water diffusive flux, were decreased to one fourth of the current membrane values.

6.3.3.1 Effect of solutions concentration

Here, the effect of the solutions concentration on the exergy efficiency of each subsystem and global system is evaluated, for the same range of operating conditions presented in Subsection 6.3.2. The maximum global exergy efficiency (15.3%) is found for 4.5 – 0.1 M and 19 *MED* effects, with a correspondent thermal efficiency of 3%. The effect of the dilute concentration in the range analysed is almost negligible, while the influence of concentrate solution is more accused. The maximum exergy efficiencies of the different components are: *RED* 60% for 2 – 0.1 M; *Mixer 1* 68.9% for 4.5–0.1 M; *MED* 61.3% for 5 – 0.1 M, and *Mixer 2* 94.2% for 2 – 0.01 M – 2 cm/s (see *Figure 6.8*).

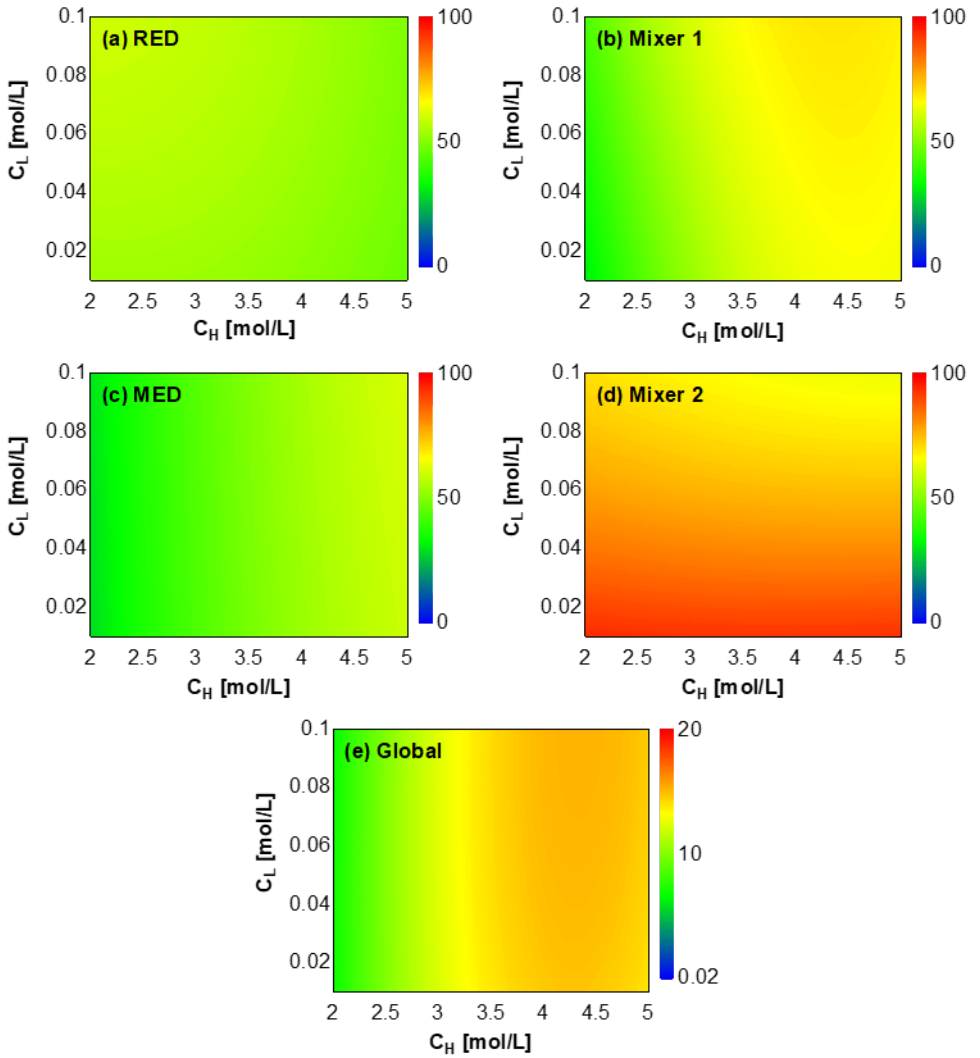


Figure 6.8 Exergy efficiency as function of the concentrate and dilute inlet concentrations to the RED stack, using high-performing membranes: (a) RED unit, (b) MED unit, (c) Mixer 1, (d) Mixer 2, (e) Global. RED unit made of 1000 cell pairs $0.5 \times 0.5 m^2$, $v_H = v_L = 1$ cm/s, MED $\Delta T_{\text{exch}} \sim 1^\circ C$.

6.3.3.2 Effect of solutions velocity

The performance of the system is assessed here as function of the RED inlet solutions velocities. In particular, using the most performing inlet solutions concentrations found in the previous subsection, the solutions velocities have been varied between 0.2–2 cm/s for both the concentrate and the dilute. Results obtained show that the highest global exergy efficiency,

25.2%, is found for 0.2 – 0.3 cm/s. For each single component the maximum exergy efficiency is equal to: *RED* 63.7% for 0.2 – 2 cm/s, *Mixer 1* 98.9% for 0.2 – 0.2 cm/s, *MED* 58.2% for 1 – 1 cm/s and *Mixer 2* 74% for 0.2 – 2 cm/s (see *Figure 6.9*).

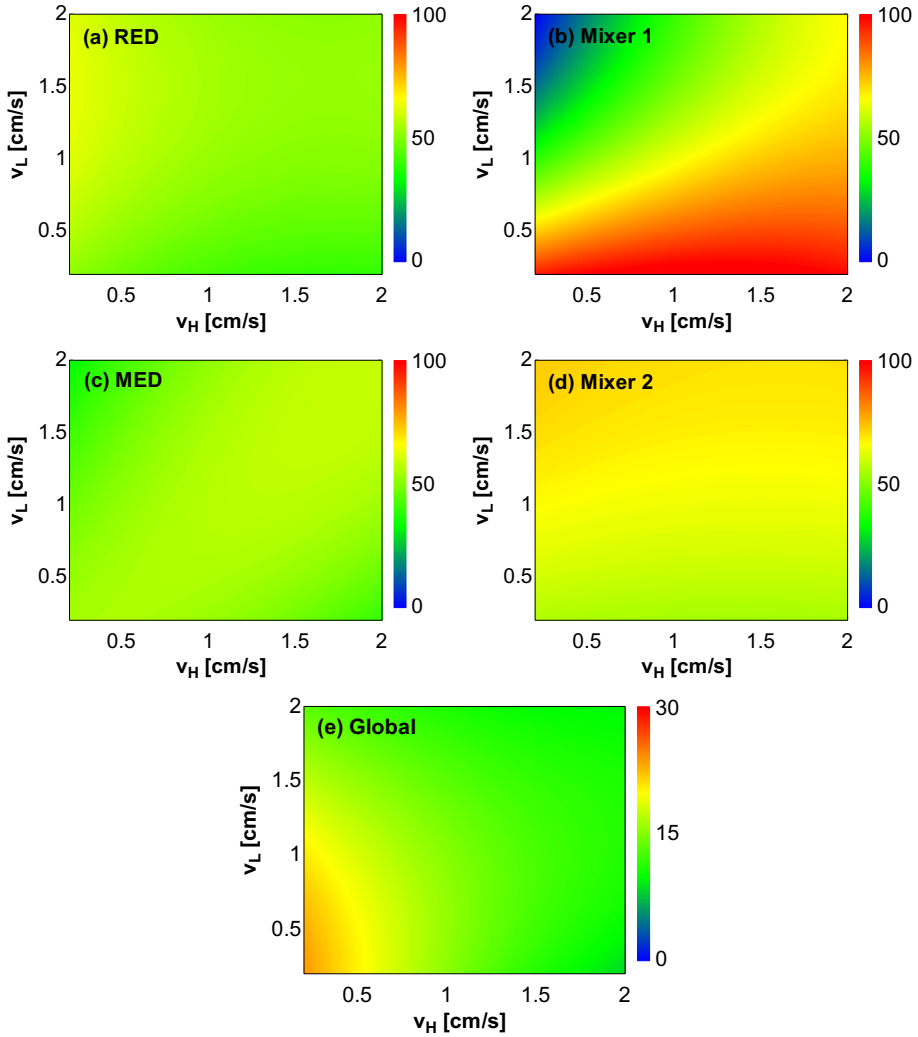


Figure 6.9. Exergy efficiency as function of the concentrate and dilute inlet velocities to the RED stack, using high-performing membranes: (a) RED unit, (b) MED unit, (c) Mixer 1, (d) Mixer 2, (e) Global. RED unit made of 1000 cell pairs $0.5 \times 0.5 \text{ m}^2$, $C_H = 4.5 \text{ M}$ and $C_L = 0.1 \text{ M}$, MED $\Delta T_{\text{exch}} \sim 1^\circ \text{C}$.

6.3.3.3 Effect of membrane's aspect ratio

Using the most-performing operating conditions identified so far, i.e. solution velocities and concentration, the exergy efficiency of the system is evaluated as function of the length-to-width membrane's ratio. To that end, a constant membrane's area is assumed, equal to 0.25 m². The maximum exergy efficiency, 25.5%, is found for $R_{geom}=2$ ($b=0.35$, $L=0.7$ m). Differently from current scenario, in the future scenario also the aspect ratio has an influence on the exergy efficiency. However, this effect is very small, increasing the R_{geom} from 1 to 2 the exergy efficiency is increased from 25.2% to 25.5% (see *Figure 6.10*)

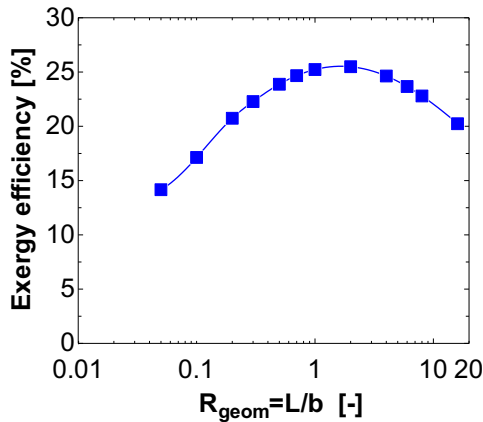


Figure 6.10. Global exergy efficiency as function of the length-to-width (R_{geom}) membrane's ratio, using future membranes. RED unit made of 1000 cell pairs $0.5 \times 0.5\text{m}^2$, $C_H=4.5\text{M}$ and $C_L=0.1\text{M}$, $v_H=0.2\text{ cm/s}$ $v_H=0.3\text{ cm/s}$, MED $\Delta T_{exch} \sim 1^\circ\text{C}$.

6.3.4 Comparative analysis

A summary of the overall improvement of the RED-MED exergy efficiency, after the different parametric analyses carried out so far (i.e. inlet concentrations, inlet velocities, stack geometry, and using high-performing membranes), is presented in *Table 6.3*. Results show the great improvement achieved with respect to the base case. In particular, after the inlet solutions concentration, velocity and membrane geometry analysis the overall exergy efficiency has more than doubled from 1.9% to 4.8%, showing that the behaviour of the global system efficiency is largely affected by the operating conditions of the RED process where larger exergy destructions are located. The highest efficiency is observed reducing the dilute solution concentration and the concentrate solution residence times. Concerning the stack geometry, symmetric stacks seem to perform better than asymmetric one.

Further, the adoption of high performing membranes in the *RED* unit lead to a huge increase in the whole system efficiency, passing from 4.9% to 25.2%. This large efficiency increase is mainly due to the improvement of the membrane properties, which are the main limiting factor of this technology.

Table 6.3 Comparison of the RED-MED performance between the base case and the different cases analysed.

Concept	Base case	Current memb.	Future memb.
Input variables			
Inlet concentrations, (mol/l)	3 – 0.05	4 – 0.01	4.5 – 0.1
Inlet velocities, (cm/s)	1 – 1	0.2 – 0.5	0.2 – 0.3
Membrane geometry, (m × m)	0.5 × 0.5	0.5 × 0.5	0.5 × 0.5
Number of MED effects	24	26	21
Mean temp. difference, (°C)	1.3	1.2	1.1
Results			
Global exergy efficiency, %	1.9	4.8	25.2
Global thermal efficiency, %	0.37	0.96	5.1
RED exergy efficiency, %	6.9	18.3	55.5
MED exergy efficiency, %	41.7	44.9	55
Mixer 1 exergy efficiency, %	57.9	62.1	95.2
Mixer 2 exergy efficiency, %	82.3	93.5	57.8
Gross power, (W)	820.3	551.9	1363
RED pumping power, (W)	24.7	3.1	1.7
MED pumping power, (W)	532.6	213.3	134
Power density, (W/m ² cp)	3.18	2.2	5.4
Heat rate, (W)	70,265	34,887	24,192
MED STEC, (kWh/m ³)	35.8	31.7	38.5

The exergy balance of the most performing case is depicted in *Figure 6.11* by means of a *Grassman's diagram*. Particularly, for each component of the system, entering and exiting exergy flows are presented along with the amount of exergy destroyed. In the *RED* unit, the exergy content of the concentrate and dilute solutions is partly consumed to generate electric power, being the remaining fraction destroyed due to the irreversibility sources of the pile.

Then, a fraction of the electric power produced is used to drive the *RED* and *MED* pumps. As shown in *Figure 6.11* the latter is considerably higher.

The exergy content of the solution exiting the *RED* unit is then partially destroyed within *Mixer 1*. To this regard, it is worth noting that its value is practically negligible compared to the exergy destruction within the *RED* and *MED* units. In the *MED* unit, the exergy supplied by the cooling process is particularly high due to the large quantity of cooling water flow rate needed at the end condenser. In addition, a great amount of waste heat exergy is supplied to the system, thus leading to a low value of the thermal efficiency. Compared to the case where conventional membranes are used, here the *MED* unit limits the overall exergy efficiency of the system. Finally, in *Mixer 2* an appreciable amount of exergy content of the distillate is destroyed.

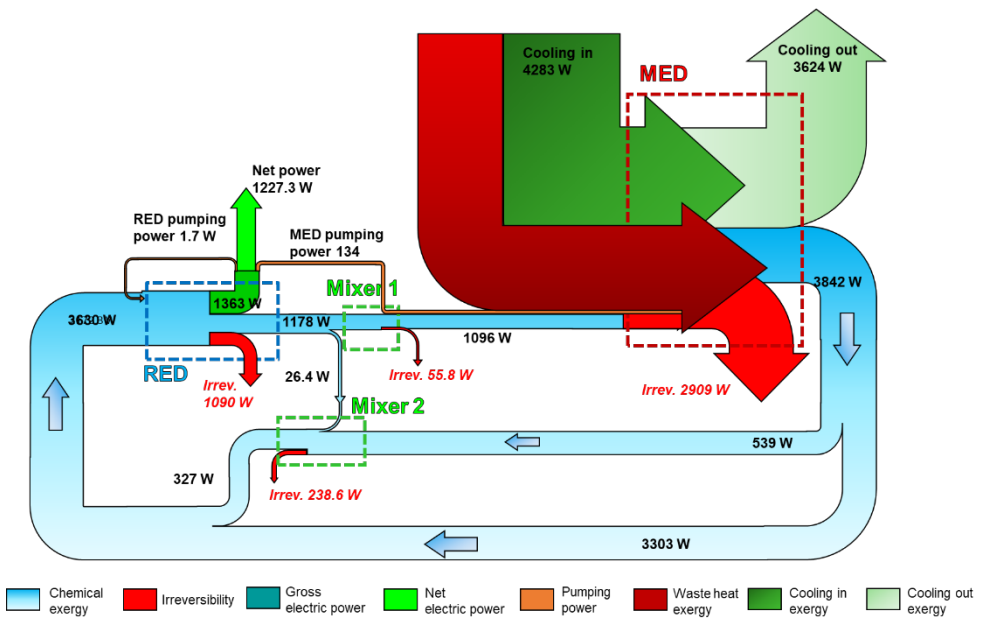


Figure 6.11. Grassmann diagram of the most performing scheme found for the RED-MED system.

6.4 Conclusions

For the first time a detailed exergy analysis at component level of a *RED-MED HE* has been carried out. *Ad-hoc* mathematical models of the *RED* and *MED* units were used, which allowed to perform sensitivity analyses regarding the main operating and design variables of the system: inlet solutions concentration, velocity, and membrane aspect ratio.

The effect of the main irreversibility sources on each component but also on the overall exergy efficiency was investigated as a function of the resistance ratio (i.e. R_L/R_{ini}) of the *RED* unit. Membrane properties strongly affect the exergy efficiency of the *RED* unit, thus determining a reduction of the global cycle efficiency. *RED* pumping power and polarisation phenomena have a small influence on the system efficiency. On the contrary, the number of effects and the ΔT_{exch} affect significantly the efficiency. If the number of effects is increased, the thermal power required by the *MED* unit decreases, but at the same time a higher pumping power is required in the *MED* unit. The higher ΔT_{exch} , the lower the number of effects and the higher the thermal efficiency of the *MED* unit. On the other hand, low ΔT_{exch} results in a large heat exchanger area. Then, the optimal value of ΔT_{exch} should be selected on the basis of economical considerations.

Furthermore, an analysis of the effects of the inlet concentrations and velocities of the solutions in the *RED* stack was carried out in order to assess at which extent they affect the exergy efficiency, considering Fujifilm type 10 membranes and future enhanced membranes. In the current scenario the maximum exergy efficiency of the integrated system is equal to 4.8% considering $C_H=4M$ $C_L=0.01M$ $C_H=0.2cm/s$ and $C_L=0.5cm/s$, while in the future scenario an exergy efficiency of 25.2% is obtained considering $C_H=4.5M$ $C_L=0.1M$ $C_H=0.2cm/s$ and $C_L=0.3cm/s$.

S SECTION III:
SALT EXTRACTION
Thermolytic salts



REGENERATION OF THERMOLYTIC SALTS SOLUTIONS

Chapter Outline

ABSTRACT	197
7.1 THERMOLYTIC SALTS IN CLOSED-LOOP APPLICATIONS.....	198
7.1.1 THERMOLYTIC SALT SOLUTIONS FOR FO DESALINATION	200
7.1.2 STATE OF THE ART OF THERMOLYTIC SGP HEAT ENGINES.....	202
7.1.3 FINAL REMARKS AND CHAPTER OUTLINE.....	203
7.2 LABORATORY-SCALE REGENERATION UNITS	205
7.2.1 REGENERATION UNIT PROCESS SCHEMES.....	205
7.2.2 AIR STRIPPING: EXPERIMENTAL SYSTEM AND EQUIPMENT	206
7.2.3 VAPOUR STRIPPING: EXPERIMENTAL SYSTEM AND EQUIPMENT.....	209
7.3 MODELING OF THE STRIPPING PROCESSES.....	212
7.4 EXPERIMENTAL RESULTS AND MODEL VALIDATION	215
7.4.1 STRIPPING COLUMN PERFORMANCES.....	215
7.4.2 VAPOUR STRIPPING COLUMN PERFORMANCES.....	217
7.5 THEORETICAL ANALYSIS OF REGENERATION PERFORMANCE.....	219
7.6 CONCEPTUAL DESIGN OF THE WHOLE REGENERATION UNIT	226
7.7 CONCLUSIONS.....	230

Paper in-preparation:

*F. Giacalone, F. Vassallo, M. Bevacqua, F. Scargiali, Cipollina, A. Tamburini, G. Micale,
“Regeneration Units for Thermolytic salts applications: Modelling and Experimental assessments”.*

Abstract

Reverse electrodialysis heat engine using a salt extraction scheme requires the knowledge of specific salt-solution properties and separation mechanisms involved in the regeneration process. Among the alternative proposed in the literature, the use of thermolytic salt solutions appears the most promising thanks to their tendency to decompose into gaseous form at low temperatures. In this chapter, two different regeneration options for thermolytic salts solutions are proposed, namely (i) air stripping and (ii) vapour stripping process. Both options have been experimentally investigated by means of lab-scale prototypes and modelled using ASPEN Plus® simulation platform. The process models have been validated by comparison with experimental results and then used to perform sensitivity analysis, investigating the performance of the two regeneration units. The modelling analysis highlighted advantages and disadvantages of the two processes, but also important operating limitations of the air-stripping/absorption process for the regeneration of ammonium bicarbonate solutions.

7.1 Thermolytic salts in closed-loop applications

In salt extraction regeneration unit, the restoring of the two solutions is obtained by transferring some solute from the dilute stream to the concentrate (*Figure 7.1*). Temperature-sensitive salts and degradation mechanisms are exploited in such processes in order to extract the solute from the dilute solution by using a separation process, where low grade heat is used as an energy source. Two main options have been proposed in literature so far: (i) *salt precipitation* and (ii) *thermolytic salt stripping* [19].

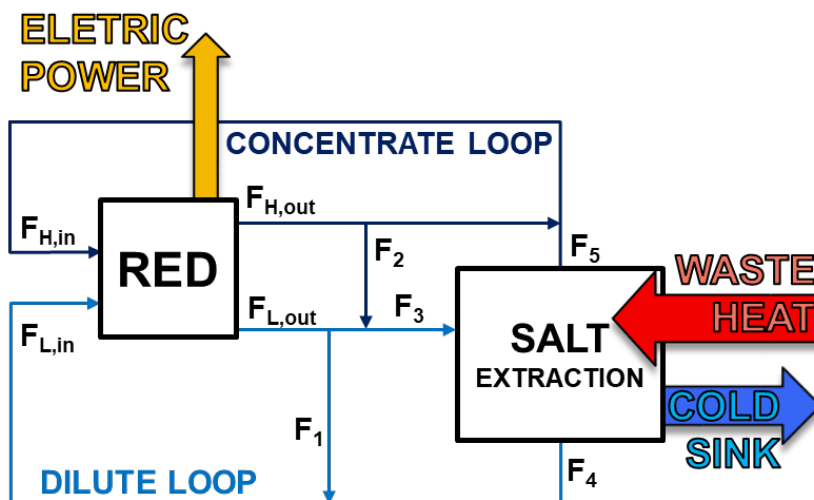


Figure 7.1 Scheme of a RED-HE with salt extraction regeneration.

In the *salt precipitation process*, two options have been explored so far: i) use of reverse-solubility salts or ii) use of anti-solvent agents. In the first case, a salt with a strong solubility reduction with temperature is adopted, so that a temperature increase of the outlet dilute stream from the SGP unit leads to the precipitation/separation of salt, which can be then re-solubilised in the concentrate loop at lower temperature [29].

In the second case, a species with anti-solvent properties is added to the dilute solution in order to achieve the precipitation of the salt. The anti-solvent agent has to be then thermally-separated from the solution and recirculated for further precipitation steps. Organic solvents such as methanol [28] or switchable-solubility compounds [178] have been proposed in the literature.

Thermolytic salts undergo a degradation process into gaseous species when the temperature is increased over a certain limit. Such degradation occurs also when salt ions are dissolved in water solutions, making possible their removal from the solution by means of a thermal stripping process. After the stripping step, the removed gaseous species can be dissolved again in the concentrate loop solution by an absorption step, resulting in a more concentrated thermolytic salt solution. The most common thermolytic salts consist of NH_3 - CO_2 -based compounds, namely ammonium bicarbonate (NH_4HCO_3), ammonium carbonate ($(\text{NH}_4)_2\text{CO}_3$) and ammonium carbamate ($\text{NH}_4\text{NH}_2\text{CO}_2$). All of them decompose into NH_3 and CO_2 at temperatures between 35-60 °C (at atmospheric pressure) [27] and can be used to convert very low temperature heat into electricity. Worth mentioning that, independently from the initial salt form, after one regeneration cycle, thermodynamic equilibria will lead to a solution composition in which NH_4^+ and HCO_3^- ions are predominant, thus allowing to consider ammonium bicarbonate (NH_4HCO_3) salt as the reference salt for this kind of applications.

For their thermally re-generable characteristic, thermolytic salts and, more in particular NH_4HCO_3 , are also used in several other applications reported in literature (a part from the SGP-HE). The most studied application is the thermolytic Forward Osmosis (*FO*) in which NH_4HCO_3 -water solutions are adopted as thermally re-generable draw agent to recover water from saline solutions. The system is constituted by two sections: (i) a forward osmosis unit, in which the osmotic pressure gradient between feed (i.e. sea or brackish water) and draw solution generates a water flux through the membrane from the feed to the drawing loop and (ii) a regeneration unit where low-temperature heat (~60 °C) is used to remove the salt (NH_4HCO_3) from the excess diluted draw solution by means of a stripping process removing gaseous NH_3 and CO_2 . The gas are separated and recovered in a distillation/stripping column, thus obtaining desalinated water and pure NH_3 and CO_2 used to regenerate the draw solution in a separate absorption (Recovery) column. An example of process scheme is reported in Figure 7.2.

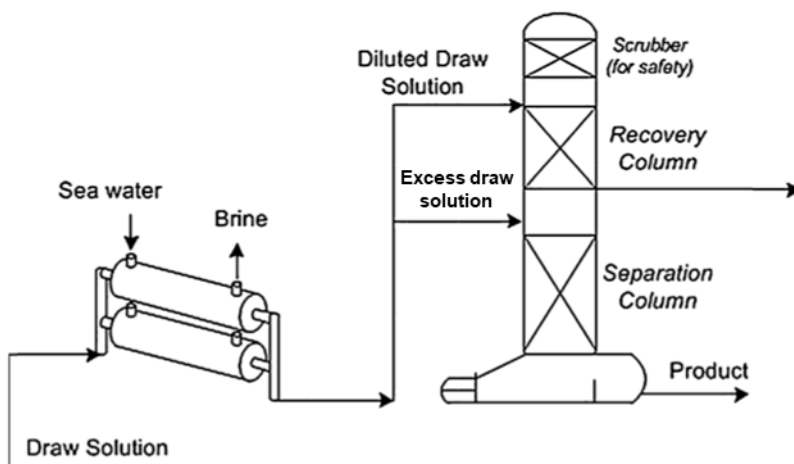


Figure 7.2. Schematic representation of the FO-thermolytic salts process. Adapted from [179].

7.1.1 Thermolytic salt solutions for FO desalination

The idea of using thermolytic salts solutions as draw agent was proposed for the first time by Neff in 1964 with the patent “solvent extractor” [27]. Since then, a number of research studies were carried out both via theoretical analysis and experimental investigation.

Theoretical analysis

With respect to theoretical analysis, McCutcheon et al. in 2005 [180] and McGinnis et al. in 2007 [181] have provided some more insight about the process. In particular, McCutcheon et al. [180] described a forward osmosis process for seawater desalination, using ammonium bicarbonate solution to extract water from a saline stream through a semipermeable osmotic membrane. However, the regeneration step in this work was described only qualitatively assuming the operation of a distillation column using waste heat. In 2007, McGinnis and Elimelech [181] continued the work, providing a simplified energetic analysis performed on Aspen Hysys® calculating the energetic requirements for the regeneration step. The authors proposed two different process diagrams: one using a single distillation column and the other using several distillation columns connected in series. The regeneration scheme was chosen on the basis of the available heat temperature. In particular, using very low-grade heat, a single distillation column, operating under vacuum, is used; while with heat temperature higher than 40°C, the possibility of using multiple columns resulted into a higher thermal efficiency.

In 2015, Zhou et al. [182] presented another modelling analysis for a closed loop *FO* process. In particular, they compared three different regeneration units: (i) distillation, (ii) stripping with steam, (iii) stripping with air. The analysis was carried out by using Aspen Plus®, adopting Electrolyte Non Random Two Liquid Redlich-Kwong (E-NRTL-RK) [183] as “*property method*”. According to the authors’ findings, the distillation system is considered the best choice. In fact, (i) the stripping with air requires a higher thermal energy demand and a larger column to obtain the same target purity, while (ii) the stripping with steam, despite requiring a thermal duty similar to the distillation process, requires an additional compressor which increases the overall costs. Worth mentioning that, no efforts were made towards thermal integration of the process, thus resulting in very high thermal consumptions, especially compared to what obtained by McGinnis and Elimelech [181] with the multiple distillation column system.

Experimental investigations

Also a number of experimental investigations were performed, presenting some preliminary results on the system performance. In particular, in 2013, McGinnis et al. [184] reported the first results of a pilot scale investigation on a NH_3/CO_2 FO desalination unit in which a forward osmosis unit is couple to a regeneration unit based on a distillation column. The pilot was tested in desalination of produced water from natural gas production in the Marcellus shale. Feed recovery higher than 60% was reported for the desalination of high salinity stream (>70.000 ppm TDS) with a thermal consumption of 275 kWh/m³ and an electrical consumption of 8.5 kWh/m³ of water produced. This work is one of the first experimental applications of the FO process based on the NH_4HCO_3 draw solutions, carried out by Oasys Water, a pioneering company in the field of FO process based on thermolytic salt draw solutions. Oasys Water has a number of patents for the recovery of fresh water from industrial wastewater sources, based on forward osmosis technologies. During the last years, Oasys Water have developed and tested other pilot plants with the aim to test the system for treating high salinity water (Parmisan Basin, salinity of 103g/l) and to match the new zero liquid discharge (ZLD) industrial policy [185].

In the same year, Shim et al. [186] carried out experiments for NH_4HCO_3 separation using for the first time a Vacuum Membrane Distillation process. Results demonstrated a salt removal efficiency around 95% and 99% when the *MD* module is fed by solutions at 50 °C

and 60° C, respectively. Conversely, at 40°C feed temperature, a lower removal efficiency of 85% was achieved.

In 2015, Kim et al. [179] installed a 3 ton/day pilot plant for thermolytic-FO desalination. The system consists of three units: (i) *FO*, (ii) thermolytic salt- water separation and (iii) draw solution regeneration. In particular, the two latter steps have been integrated in a single column. The first separation was made in a column (D=0.2m, H=3 m) with structured packing operating at ambient pressure and fed with a solution previously heated in the reboiler at temperatures up to 100 °C. The separation efficiency was equal to 99.7 % for NH₃ and 99.9 % for CO₂, while the thermal energy consumption required for producing 1 m³ of water ranged between 265 and 300 kWh.

7.1.2 State of the art of thermolytic SGP Heat Engines

Concerning the applications of thermolytic salts is in Salinity Gradient Power closed-loop systems very few works are reported in the literature. Also in this case, the system consists of two units: (i) a *power unit* where the concentration difference between two thermolytic salt solutions is converted into electricity; (ii) a *regeneration unit* where low temperature heat is used to restore the salinity gradient initially available with the two feed solutions. This idea was proposed for the first time by Loeb in 1973 who patented an heat engine based on the closed-loop *PRO* concept and in 1978 on the *RED* one [30,31]. Also with this respect, theoretical and experimental investigations were performed and presented in the literature.

Theoretical analysis

In 2007, McGinnis et al. [32] presented a theoretical study on Osmotic Heat Engine (*OHE*) where solutions of ammonium salts at high concentration (i.e. NH₄HCO₃ and NH₄OH) are used as draw agent. Simulations carried out with a simplified mathematical model indicated a theoretical power density exceeding 200 W/m², operating the *PRO* unit with the draw solution at about 100 atm. Such conditions, would lead to overall exergetic efficiency up to 16%.

In 2017 Kim et al. [187] proposed an experimentally validated model to evaluate the performance of a *RED* unit fed with ammonium bicarbonate solutions for low-grade waste heat recovery. Results have shown a maximum net power density of 0.84 W/m²_{membrane} obtained with concentrations of 2 M-0.01 M.

In the same year, Bevacqua et al [42] theoretically assessed the performance of *RED-HE* fed with ammonium bicarbonate solutions using an air stripping column as regeneration unit modelled on Aspen Plus[®], reporting exergy efficiency values up to 22%.

Experimental investigations

Experimental analysis of thermolytic salt with respect to *RED-HEs* reported in the literature are exclusively focused on the power generation unit. In particular, in 2012 Luo et al. [33] explored the potential of a *RED* unit fed with aqueous NH_4HCO_3 solutions. They obtained a power density of 0.33 W/m^2 of membrane area, at optimized feed solutions concentrations (concentrate solution 1.5 M - dilute solution 0.02 M). Similarly, Cusick et al. [34] in 2012 experimentally investigated the use a microbial *RED* unit fed with ammonium bicarbonate, reporting a maximum power density of 2.1 W/m^2 arising from *RED* unit and 3.3 W/m^2 from the substrate oxidation.

In 2015, Kwon et al. [37] focused again on the experimental characterization of the *RED* process, investigating the effect on process performance of various parameters such as: inlet flow rates and concentrations, membrane type and compartment thickness. The best finding was an optimised maximum power density of 0.77 W/m^2 of membrane area.

In 2016, Bevacqua et al. [38] presented another extensive experimental analysis on a *RED* system fed with NH_4HCO_3 solutions. Results have shown in this case that power output is maximized at 2M-0.02M concentration set, reaching a power density of 1.2 W/m^2 of membrane.

7.1.3 Final remarks and chapter outline

The literature review shows a growing interest on the application of thermolytic salts solutions closed-loop concept coupled to *FO* and *SGP* technologies. Several studies have investigated the potential of such systems mainly focused on the *generation unit*, while very little information is reported concerning the behaviour of the *regeneration unit*. In fact, very few works have experimentally analysed the applicability of thermolytic salts solutions as thermally re-generable draw agent leaving a total gap of experimentally-validated mathematical models able to reliably evaluate the real potential of such systems for closed loop *FO* and *SGP* processes.

In this chapter, two different schemes for the regeneration of ammonium bicarbonate aqueous solutions are investigated both via experiments and model analysis, namely: air-

stripping/absorption and vapour-stripping/absorption. Two experimental test rigs were built and tested through an extensive experimental campaign useful to highlight the effect of several operating conditions on the performance of ammonia and carbon dioxide stripping from thermolytic salt solutions. Furthermore, a simulation platform was developed and validated for the prediction of the operation of the two proposed stripping units by comparison with experiments. The validated process models were used to run simulations and compare the stripping performance (i.e. removal efficiency and specific energy consumption) of the two units, finally allowing to perform a thorough analysis of the overall integrated regeneration process (including the re-absorption step), thus highlighting technological limitations and perspective solution schemes.

7.2 Laboratory-scale regeneration units

As already described above, in all closed-loop applications using thermolytic salts solutions, the regeneration unit requires a “stripping stage” to remove the thermolytic salts and “regenerate” a dilute stream (i.e. drinkable water in the case of closed-loop *FO* or low concentration solution in the case of *SGP-HE*) and an “absorption stage”, where stripped gases are condensed/absorbed in order to “regenerate” the draw (concentrate) solution.

As already mentioned, the main processes proposed in the literature for the regeneration of ammonium bicarbonate solutions [182] are (i) distillation, (ii) vapour stripping and (iii) air stripping. In particular, the main focus of this chapter is the study of the above mentioned (ii) and (iii) stripping thermally regenerative processes, developing lab-scale prototypes and validated mathematical models.

7.2.1 Regeneration unit process schemes

Schematic representations of the two regeneration units, i.e. air stripping/absorption (*A-SA*) and a vapour stripping/absorption (*V-SA*) for *RED* closed-loop applications, are reported in *Figure 7.3-a* and *Figure 7.3-b* respectively.

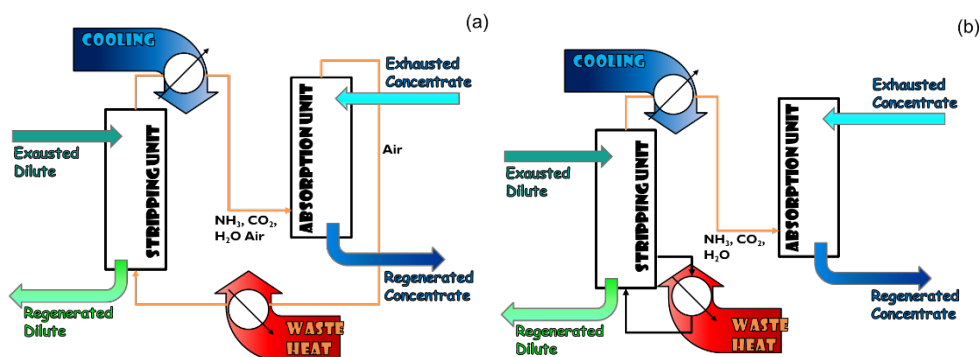


Figure 7.3 Schematic representations of the two proposed regeneration units: air stripping/absorption (*A-SA*) regeneration unit (a) and vapour stripping/absorption (*V-SA*) regeneration unit (b).

In the case of the air stripping/absorption process, hot saturated air is used as a stripping agent to promote the releasing of ammonia and carbon dioxide from the dilute solution. Then, the hot air enriched in ammonia and carbon dioxide is cooled and fed in an adsorption column where it is brought in contact with the concentrate solution in order to facilitate the absorption

of the stripped gas. The air exiting from the absorption column is heated up again and recirculated in the stripping column for a new regeneration cycle (*Figure 7.3-a*).

In the case of vapour stripping/absorption, the stripping agent is the steam produced from the vaporization of part of the exhausted dilute stream in a reboiler. The vapour allows the stripping of ammonia and carbon dioxide from the exhausted dilute. Then, the stripped gases are condensed and absorbed in the exhausted concentrate stream restoring the initial salinity gradient (*Figure 7.3-b*).

7.2.2 Air stripping: experimental system and equipment

A schematic representation of the air stripping system is reported *Figure 7.4*. The feed solution is driven by a peristaltic pump (Cellai mod. U503). The aqueous NH_4HCO_3 solution stored in a plastic tank (1) is fed into a stainless-steel coil placed in a thermal bath (3). The thermal bath is filled with hot demineralized water (T in the range 60-80°C), thus heating the NH_4HCO_3 solution up to the degradation temperature of the salt. The heated solution is fed to the top of the stripping column (6), where it falls through the packing material and enters in contact to the uprising hot saturated air. In the stripping column, the degradation of the salt is completed, and the gases generated are stripped out into the air stream. The gaseous stream of NH_3 , CO_2 and air leaves the stripping column from the top, while the regenerated NH_4HCO_3 solution leaves the column from the bottom and is stored in a plastic tank (9).

It is worth mentioning that air saturation and feed heating are needed in order to properly operate the stripping column. In fact, feeding a dry air into the column would lead to a sudden evaporation of water, which would lead to a dramatic cooling of the air and solution in the bottom of the column.

The saturation of air is achieved in a saturation column (5). Dry air from a compressor (7) (ABAC mod. PRO B6000500T7.5), whose flow rate is measured by a rotameter (8) (KEY INSTRUMENTS), enters the saturation column from the bottom and flows upwards. Deionized hot water is fed from the water thermostatic bath (3) to the top of the column by using a membrane pump (SHURFLO) (4). The counter-current flow between hot water and dry air leads to the heating and saturation of the air. Then, the hot saturated air is fed to the bottom of the stripping column, while the distilled water is fed back into the thermal bath (3).

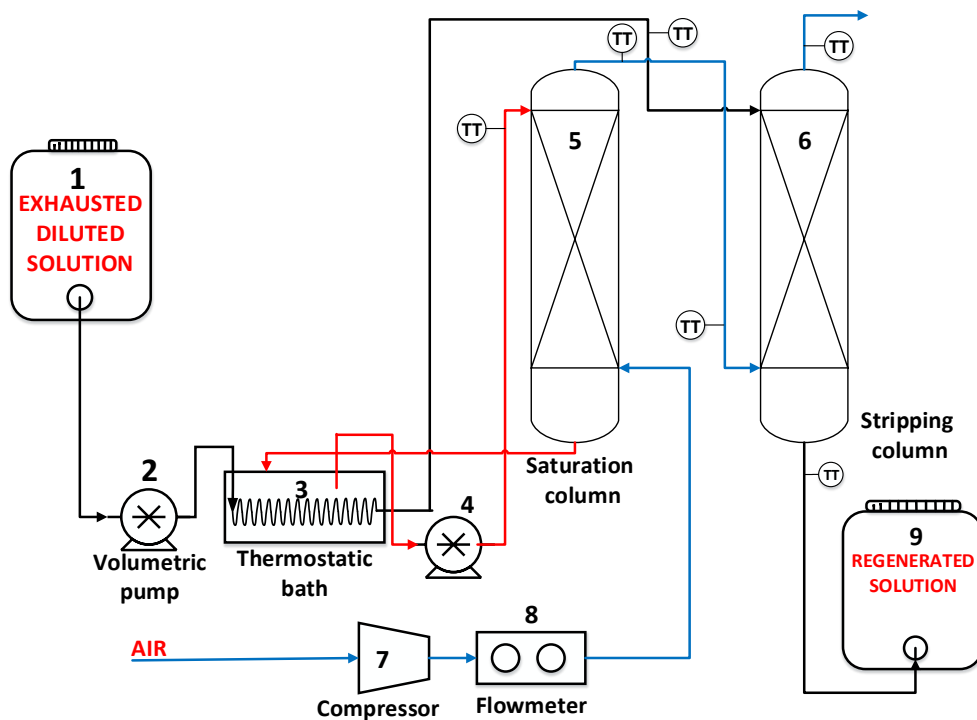


Figure 7.4 Experimental set-up of the air stripping system: 1 tank, 2 volumetric pump, 3 thermostat bath, 4 volumetric pump, 5 saturation column, 6 air stripping column, 7 air compressor, 8 flow-meter.

The saturation column is a Plexiglas tube with a height of 2 m and an inner diameter of 0.05 m. The column is filled with polyurethane Raschig rings (ID 0.01 m) for a height of 1.6 m. Gas and liquid are fed through distributors placed at the top and the bottom of the column, respectively. In order to reduce wall effects for the liquid, O-rings are used as liquid redistributors within the column.

The stripping column is a Plexiglas tube with the same dimensions as the saturation column. Two different packing materials were tested in the stripping column: metal Raschig Rings (ID 0.01m) and *FLEXIPAC 700Y* structured packing. This latter, kindly supplied by *KOCH-GLITSCH*[®], consists of corrugated stainless-steel sheets arranged in a crisscross pattern with a nominal inclination angle of 45°. Also in this case, the column was packed for a height of 1.6 meters and O-rings were placed along the column in order to redistribute the liquid.

The temperature of liquid and gaseous streams in the stripping system is measured by six thermocouples, which are placed within the tubes close to the inlets and outlets of the

columns. Thermocouples are connected to a *National Instruments* data acquisition system. A picture of the lab-scale prototype is shown in *Figure 7.5*.



Figure 7.5 Experimental air stripping system for the regeneration of aqueous NH_4HCO_3 solutions. Saturation column (1) filled with polyurethane Raschig rings; Stripping column (2) filled with metal Raschig rings.

The feed solutions were prepared dissolving anhydrous ammonium bicarbonate salt (Carlo Erba[®], purity >99.5) into deionized water.

An extensive experimental campaign was carried out, performing more than 60 experimental runs. In particular, the influence of operating conditions such as concentration and flow rate of feed solutions, air flow rates, packing materials and temperature (*Table 7.1*) on the performance of the system was investigated. In all cases, the temperature of the inlet solution (T_{sol}) was set equal to that of the saturated air (T_{air}). During each test, after the reaching of a steady state condition in the stripping column, four different samples of regenerated solution were collected every 10 min. The samples were cooled at 25 °C and characterized in terms of outlet conductivity.

Table 7.1 Experimental conditions of the air stripping system.

Packing	Air Flow [l/min]	T _{sol} [°C]	T _{air} [°C]	Inlet flow rate [l/min]				Inlet concentration [mol/l]			
				0.1	0.15	0.2	0.25	0.2	0.5	1	1.5
<i>Rashig</i>	35	60	60					0.2	0.5	1	1.5
		70	70	0.1	0.15	0.2	0.25	0.2	0.5	1	1.5
<i>Flexipac</i> [®]	35	60	60					0.2	0.5	1	1.5
		70	70	0.1	0.15	0.2	0.25	0.2	0.5	1	1.5
	70	60	60			0.15		0.2	0.5	1	1.5

7.2.3 Vapour stripping: experimental system and equipment

A schematic representation of the vapour stripping system and some pictures are reported in *Figure 7.7*. The NH_4HCO_3 solution stored in a plastic tank (1) is fed to the top of the stripping column (4) by means of a peristaltic pump (2) (Cellai mod. 503). Before entering the column, the feed solution is pre-heated in a thermal bath, which ensures the desired inlet temperature (i.e. 70°C) (3). From the top of the column, the solution falls through the packing material encountering the rising stripping vapour. The rising vapour is produced by vaporizing part of the feed solution in the reboiler placed at the bottom of the column (5). The counter-current flow between the hot solution and the water vapour guarantees the continuous degradation of the thermolytic salts into ammonia and carbon dioxide, which are eventually extracted from the top of the column. The stripping column and the reboiler work under-vacuum conditions, generated and maintained by a Venturi system (11) fed by a concentrate solution of ammonium bicarbonate. The Venturi system also performs the mixing/absorption of the stripped gasses (9-10) within the concentrate solution. The condensation/absorption step involves exothermic reactions, thus a thermal bath (8) is used to condense the stripped gas, which is subsequently absorbed in the concentrate solution.

The regenerated dilute solution is extracted from the reboiler by means of a volumetric pump (Cellai mod. U503) (6) and stored in the regenerated solution tank (7).

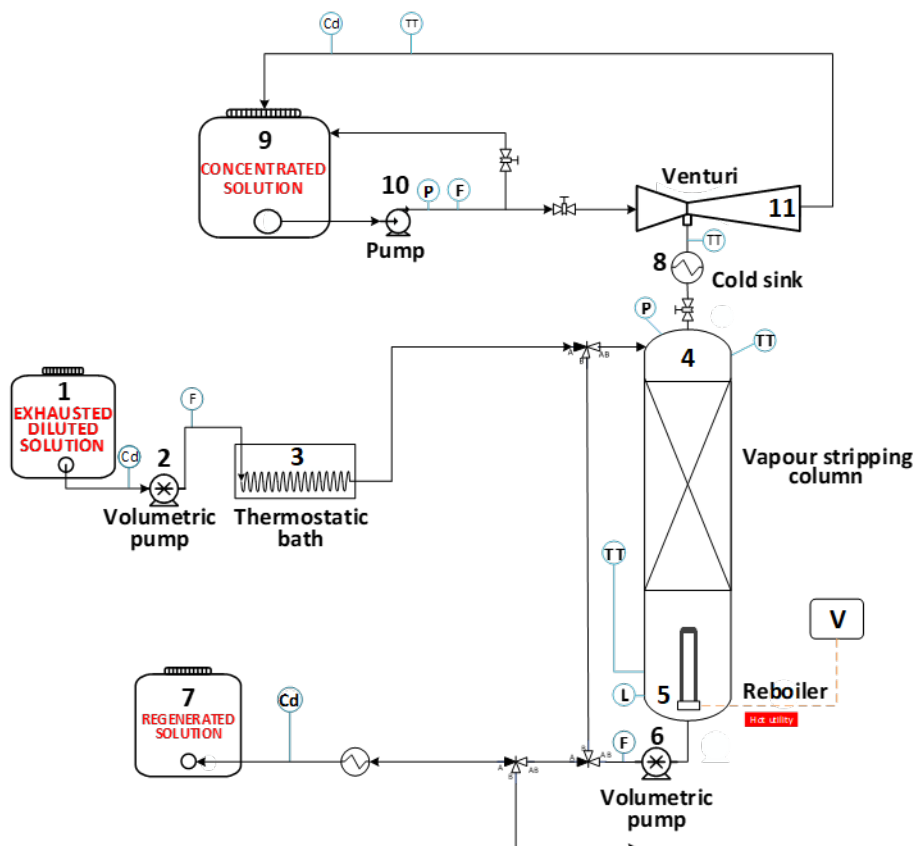


Figure 7.6 Experimental set-up of the vapour stripping system. : 1 feed tank, 2 feed pump, 3 thermostat bath, 4 stripping column, 5 reboiler, 6 regenerated solution pump, 7 regenerated tank, 8 thermal bath, 9 concentrate tank, 10 Venturi pump, 11 Venturi ejector.

The stripping column consists of a 2 m Plexiglas tube with an internal diameter of 0.05m, equipped with the Flexipac[®] structured packing kindly provided by KOCH-GLITSCH. The height of packing is 1.6 m. A liquid distributor ensures a good distribution of the solution on the packing material of the column. The reboiler consists of a Plexiglas tube with an internal diameter of 0.1 m equipped with a regulating heater with a nominal power of 2 kW. The temperature of the solution in the reboiler is monitored by a thermocouple.

As in the previous case, the temperature of liquid and gaseous streams are measured by four thermocouples. The pressure within the column is monitored using a pressure transducer. Pictures of the lab scale prototype are shown in the *Figure 7.7*.

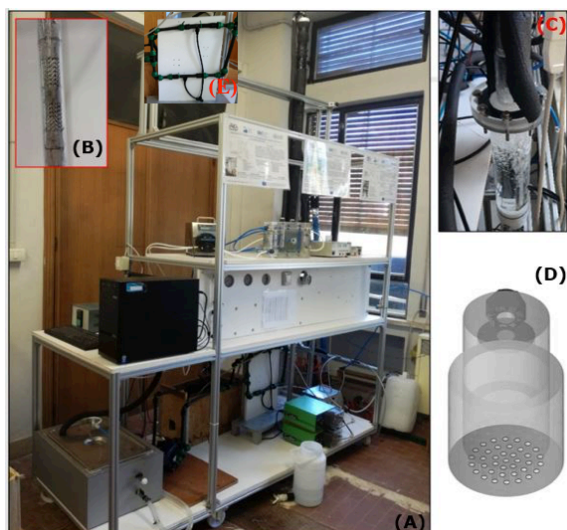


Figure 7.7 Experimental vapour stripping system for the regeneration of aqueous NH_4HCO_3 solutions. (A) test-rig, (B) structured packing, (C) reboiler, (D) sparger (E) Venturi system.

Also in this case, an extensive experimental campaign was carried out, testing the experimental set-up under different conditions (Table 7.2) and performing more than 20 experimental runs. In particular, for given inlet conditions, i.e. solution temperature ($T_{sol,in}$) and concentration (C_{in}), the concentration (or conductivity) of the regenerated solution was monitored varying the dilute inlet concentration (from 0.2 M to 0.6 M) and the thermal power provided to the reboiler (from 710 W to 1050 W). This latter was set by varying the electrical current provided to the electrical resistance. During each test, after the reaching of a steady state condition in the column, four samples of regenerated solution were collected every 10 min. The samples were cooled at 25°C and characterized in terms of outlet solution conductivity.

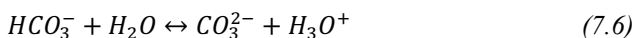
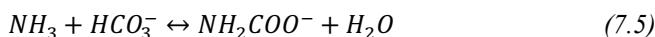
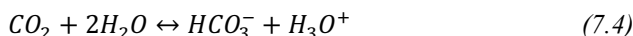
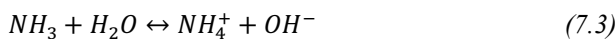
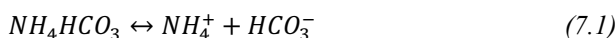
Table 7.2 Experimental conditions of the vapour stripping unit.

Packing	Inlet flow [l/min]	$T_{sol,in}$ [$^\circ\text{C}$]	C_{inlet} [mol/l]	Thermal power			$T_{reboiler}$		
				[W]			[$^\circ\text{C}$]		
Flexipac®	0.215	70	0.2	750	950		76	79	
			0.3	710	940	1050	76	78	80
			0.6	760	930	1020	77	79	80

7.3 Modeling of the stripping processes

The two different process schemes were also developed in Aspen Plus® in order to simulate the behaviour of the two experimental systems. The Aspen model was validated comparing model predictions with experimental results and they were subsequently used to analyse and compare the two regeneration systems.

The main chemical equilibrium reactions involved in ammonium bicarbonate-water solutions [23,24]:



The equilibria described in *eq.s 7.1-7.7* show a considerable complexity of the system under consideration. For this reason, a fundamental issue is to validate the thermodynamic model with experimental results in order to prove its reliability in predicting the system behaviour. A critical aspect in the implementation of the process simulator is the selection of the thermodynamic package, which describes the interactions between the different species. In the literature two thermodynamic models, i.e. Electrolyte - Non Random Two Liquid (*E-NRTL*) and *OLI System*, have been proposed to describe the equilibria involved in CO₂-NH₃-H₂O system. In particular Que et al [189] proposed the *E-NRTL* model to describe solid-liquid equilibrium of ammonia bicarbonate solutions and liquid-gas equilibrium on NH₃-CO₂-H₂O, showing a good agreement with experimental results. Zhou et al [182] used the *E-NRTL-RK* to determine the energy consumption of three different regeneration units (air stripping, steam stripping and distillation column) for FO-drawing solutions. Conversely, McGinnis et al [181] used *OLI System* to predict the energy consumption of distillation column in *FO* desalination processes. These studies did not provide any comparison with experimental results.

A first comparison between modelling and experimental results was provided by Kim et al. [179], who reported a large under-estimation of the energy consumptions given by the Aspen® model developed, stating that the thermal power consumption of the pilot was about 188–223% of that obtained by simulation.

In this work, an Aspen Plus® model was developed to simulate the behaviour of the packing columns by using a rigorous method, namely *Rad Frac*. A multi-model approach was adopted in the process simulator. In fact, while the solution properties of the liquid streams are evaluated adopting the *OLI*® Property Methods the behaviour of the columns was modelled using the *E-NRTL-RK* Property Methods. Differently from *E-NRTL*, *OLI Property Method* allows to evaluate the electrical conductivities of the salt-water solutions, facilitating the comparison with experimental results. On the other hand, *E-NRTL* predicts well the equilibria involved in the columns [189], while *OLI Property Method* alone does not provide a good enough prediction of the column operation.

The Aspen Plus® flowsheet of the two stripping processes are reported in *Figure 7.14*.

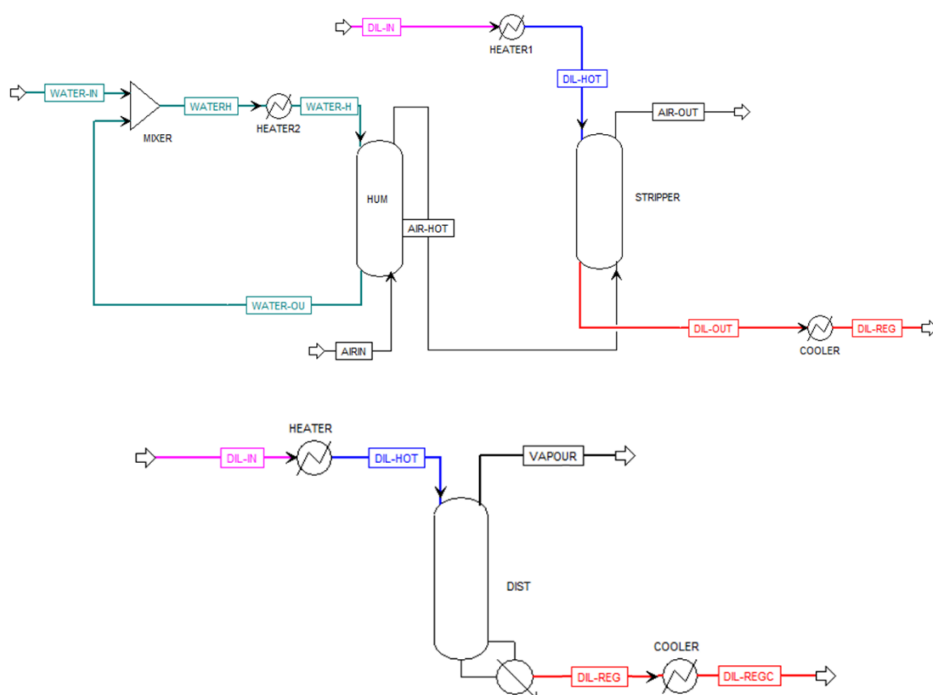


Figure 7.8 Aspen® model of the experimental setups: air-stripping column (a) and vapour stripping column (b).

In order to consider both the chemical reacting phenomena and the associated hydrodynamic, heat and mass transfer phenomena occurring within the stripping column a *rate-based* mode was chosen for the simulations, while the humidification column was set in equilibrium mode.

Once the thermodynamic conditions of the inlet streams have been fixed together with the operating conditions of the main equipment and the target of the separation (i.e. outlet conductivity of the solution), then the simulator computes the thermodynamic and electrolytic properties of the outlet streams and evaluate the thermal power (Q_{tot}) and the corresponding stripping steam/air flow rate.

The thermal power required by the regeneration step is quantified by defining a Specific Thermal Consumption (STC), defined as:

$$STC = \frac{Q_{tot}}{\Delta n_{NH_4HCO_3}} \quad (7.8)$$

where Q_{tot} is the total heat supplied to the regeneration unit, $\Delta n_{NH_4HCO_3}$ is the IN-OUT variation of ammonium bicarbonate molar flow rate in the liquid solution.

In the case of the air stripping column, also the air flow-rate is quantified as specific air-flowrate (SAF) defined as:

$$SAF = \frac{\dot{V}_{air}}{\Delta n_{NH_4HCO_3}} \quad (7.9)$$

where \dot{V}_{air} is air flow-rate required in the regeneration unit.

In order to analyse the influence of different operating conditions and compare the performance of the two stripping units, a removal efficiency was defined as:

$$\%R = \frac{\sigma_{in} - \sigma_{out}}{\sigma_{in}} \quad (7.10)$$

where σ_{in} and σ_{out} are the conductivities of the inlet and outlet solutions, respectively.

For the validation of the process models, the operating and geometrical properties were set according to the experimental columns features (see section 7.2).

7.4 Experimental results and model validation

Experimental results obtained from the two lab-scale prototypes were used to validate the model. For given operating conditions, the outlet solution conductivity from experiments is compared with the one predicted by the Aspen Plus[®] model using the combined *OLI & E-NRTL-RK* thermodynamic packages. After validation, the process models were first used to compare the removal efficiency of the two stripping units and to develop comprehensive models of the whole regeneration units, i.e. *A-SA* and *V-SA*, including also the condensation/absorption process.

7.4.1 Stripping column performances

The operating conditions adopted in the Air stripping column are summarized in *Table 7.1*. In particular, the effect of different operating conditions was analysed in terms of: (i) packing materials (Aluminium *Raschig* and *Flexipac*[®] structured packing), (ii) regeneration temperature (60°C and 70°C), (iii) air flow rate (35-70 ml/min); and (iv) inlet solution concentration (i.e. 0.2 M -1.5 M corresponding to 20 mS/cm - 94 mS/cm).

All experiments were carried out considering the impact of different parameters on the outlet conductivities of ammonium bicarbonate solutions

Figure 7.9-a and *b* show a comparison between the experimental outlet conductivities and the values predicted by the Aspen[®] model as a function of the inlet solution conductivities for the two different packing materials. Interestingly, the model predicts very well the experimental trend for both cases. In the same operating conditions, the structured packing allows to obtain a larger removal efficiency than the *Raschig* ring packing, giving an average removal efficiency equal to 44% (40% using *Raschig* rings). Therefore, in the following test, only the structured packing was considered.

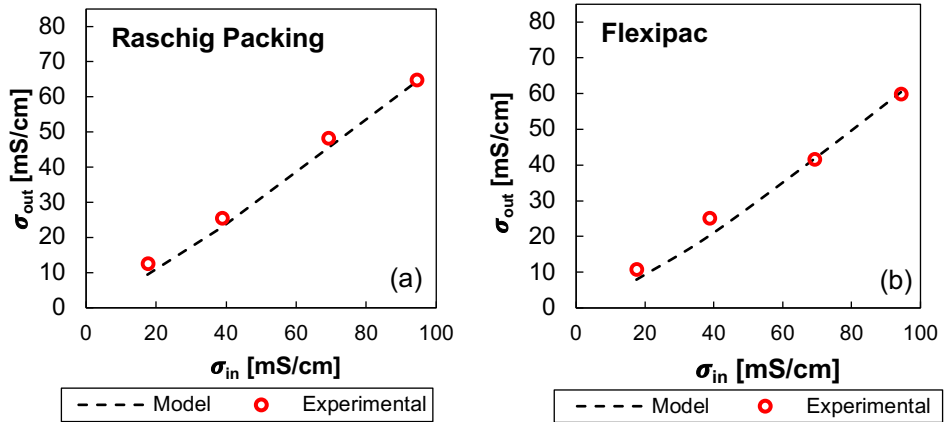


Figure 7.9 Comparison of experimental outlet solution conductivity and Aspen® model predictions for the air-stripping column considering Raschig packing (a) and Flexipac® structured packing (b) as a function of inlet solution conductivity, fixing the inlet flowrate at 0.1 l/min $T_{in}=60^{\circ}\text{C}$, air flow-rate 35 l/min.

Another interesting aspect is the effect of T_{in} on the removal efficiency. Figure 7.10 reports the experimental and predicted regenerated solution conductivities for two different regeneration temperatures, i.e. 60°C (a) and 70°C (b), keeping constant the inlet solution flowrate at 0.15 l/min and the air flow-rate at 35 l/min.

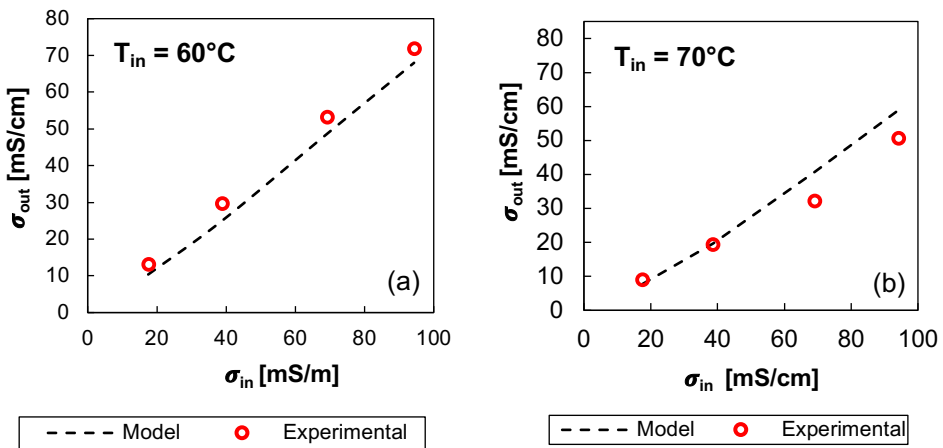


Figure 7.10 Comparison of the experimental outlet solutions conductivities and Aspen® model predictions for the air-stripping column using two different regeneration temperature (60°C (a) and 70°C (b)) as a function of inlet solution conductivity, fixing the inlet flowrate to 0.15 l/min. Air flow-rate 35 l/min, Flexipac® structured packing.

As expected, an increase of the regeneration temperature results in an increase of the amount of stripped salts with removal efficiency varying from an average value of 35% to

45% with a peak of 56% for the lowest inlet conductivities. Interestingly, the model gives good predictions also varying the inlet solution flow-rate in the investigated range 0.1 l/min (Figure 7.9) - 0.25 l/min (Figure 7.11).

The influence of the air flow rate on the performance of the air stripping column was also investigated, considering two different values of 35 l/min and 75 l/min, fixing the inlet solution flowrate at 0.25 l/min (Figure 7.11). As expected, the higher the air flow-rate, the higher the amount of gases stripped from the solution. The average removal efficiency grows from 27% to 35% increasing the air-flow rate from 35 l/min to 70 l/min.

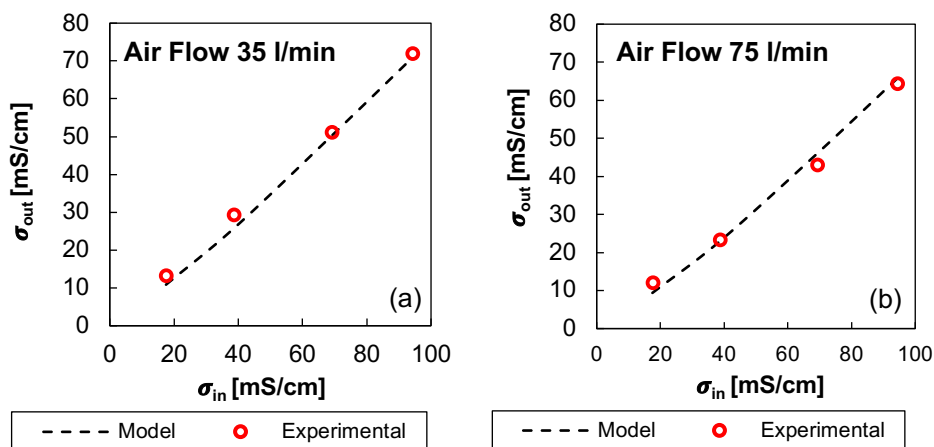


Figure 7.11 Comparison of the experimental outlet conductivities and Aspen® model predictions for the air-stripping using two different air flow rates 35 l/min (a) and 70 l/min (b), as a function of inlet solution conductivity, fixing the inlet flowrate, fixing the inlet flowrate at 0.25 l/min. $T_{in}=60^{\circ}\text{C}$, Flexipac® structured packing.

In all cases, the experimental outlet conductivities and modelling predictions from the air stripping model results in very good agreement. The maximum outlet conductivities deviations between measurements and predictions by OLI & E-NRTL-RK is around 30% for the lowest conductivity values.

7.4.2 Vapour Stripping column performances

The investigated operating conditions in the Vapour Stripping column are summarized in Table 7.2. For all the experiments, Flexipac® structured packing and a feed flow rates equal to 0.215 l/min were adopted. In all cases, the outlet solution flow rate was fixed in order to have a stable level within the reboiler.

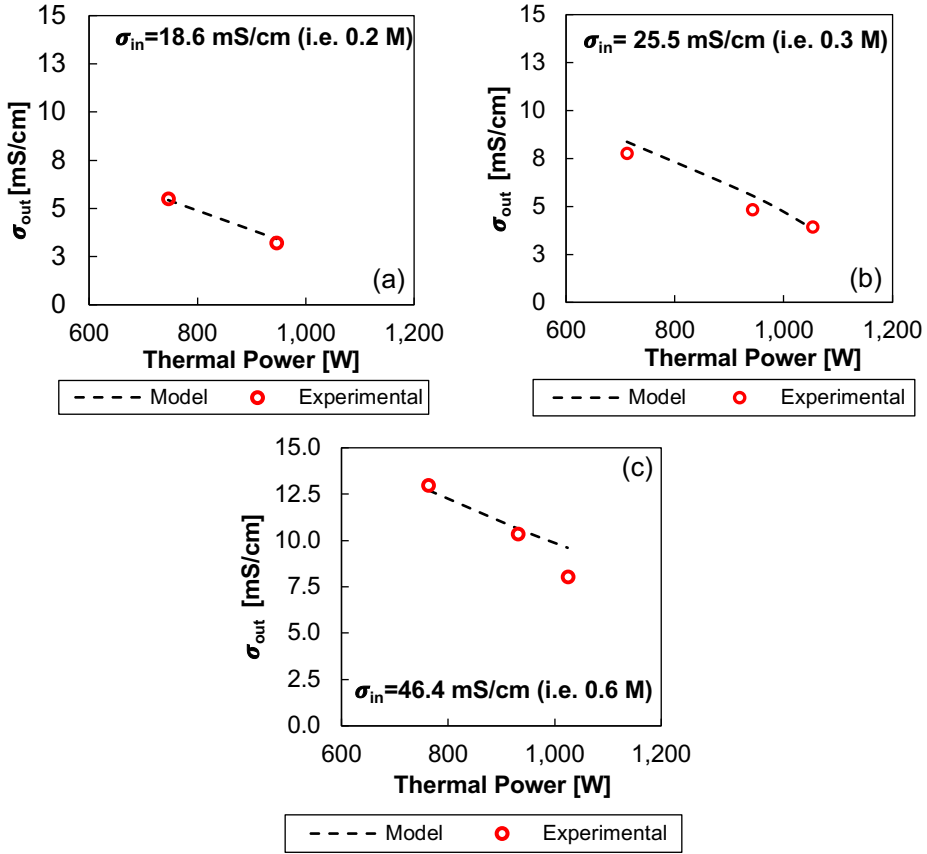


Figure 7.12 Experimental outlet solution conductivities and Aspen® model predictions from the vapour stripping column as function of the thermal power supplied to the reboiler for three different inlet solution concentration 0.2M (a), 0.3M (b), 06 M (c). Inlet flow rate equal to 0.215 l/min, Flexipac® packing material.

Figure 7.12-a,b and c report the comparison between the experimental outlet solution conductivities and the Aspen® model predictions, as a function of the thermal power provided by the reboiler. As the thermal power at the reboiler increases the stripping vapour flow rate enhances the thermolytic salt removal, thus leading to lower values of outlet conductivities and value of %R up to 85%.

In all cases, experimental results and modelling predictions are in very good agreement. with maximum deviations between model and experiments around 15%.

7.5 Theoretical analysis of regeneration performance

After validation, the simulation tool was used to investigate and compare the performance of the two stripping systems and for the conceptual design of the whole regeneration unit. Sensitivity analyses were carried-out to evaluate the *STCs* (and the *SAF* in the case of air stripping) required to perform a given separation. Same target were considered for the simulations of the two systems (i.e. same waste heat temperature, inlet and outlet concentration and inlet flow rate see *Table 7.3*).

For the modelling analysis, the two columns were specified as in the following:

- The temperature of the waste heat used as hot utility was set equal 85° C. The driving force in the heat exchangers was fixed equal to 5° C. Then, in the case of the Air Stripping system, waste heat is used to heat up the inlet solution and the saturation water at 80°C, while in the case of the Vapour Stripping system, the temperature of the solution in the reboiler is equal 80°C.
- A design factor of 70% approach to flooding was chosen to compute the column diameter. Then, the inlet flow rate was set equal to 2 l/min in order to have a reasonable ratio between column diameter and packing diameter (around $D_{\text{column}}/D_{\text{packing}} \sim 8$). Raschig ring with a diameter equal to 15 mm was adopted as packing material. Worth noting that the inlet flowrate has a negligible influence on the *STC* and *SAF*.
- The height of the columns was chosen equal to 4 m after analysing its effect on the *STC* and selecting the value which gives a good compromise between column height and power consumptions. As an example, *Figure 7.13-c* and *d* show the influence of the column height on the *STC* for the case of the air-stripping column to get a concentration target (1 ppm and 0.01 mol/l) varying the inlet solution concentration.

The Aspen® flowsheets of the two stripping systems are reported in *Figure 7.14*. Differently from the experimental setups, the new schemes include a thermal integration in order to recover part of the heat from the outlet regenerated solution and preheat the inlet solution to the stripping column, reducing the thermal power consumption of the system.

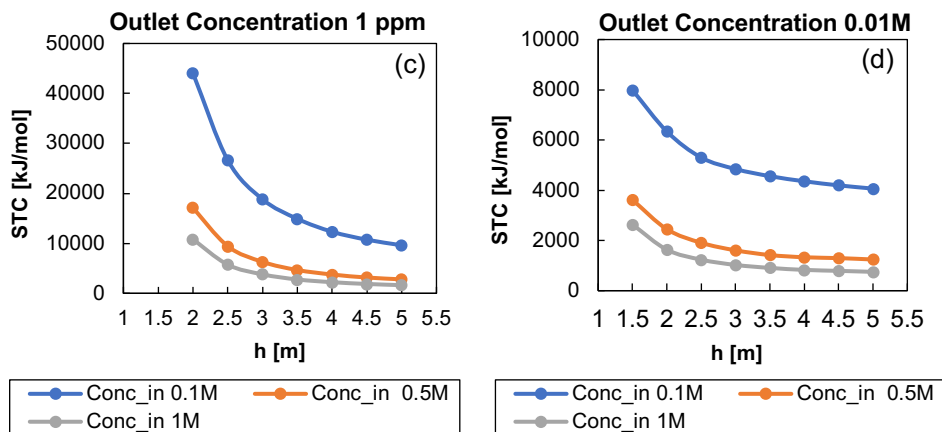


Figure 7.13 Influence of feed flow rate (0.2l/min and 1 l/min) on the specific thermal consumption (STC) (a) and specific air flow rate (SAF) (b) as function of inlet and outlet solution concentration in the air stripping column. STC of the air stripping unit as function of the column height fixing inlet flow rate at 2 l/min and outlet molar concentration equal 1 ppm (c) and 0.1 M (d).

The models were used to predict the *STC* of the two different stripping units under different inlet-outlet concentrations (see *Table 7.3*). The concentration values reported in *Table 7.3* refer to the sum of N-compounds in the solution, considering both ions (NH_4^+ , NH_2CO_2^-) and neutral (NH_3) species. In the case of *RED*-closed loop application, all inlet-outlet couples of concentrations could be operating conditions of the system. Conversely, in the case of *FO*-closed loop application, the dilute solution (i.e. drinkable water) must have a concentration of 1 ppm [181].

Table 7.3 Simulation conditions of the air and vapour stripping system.

T_{wh} [°C]	Inlet flow rate [l/min]	Inlet conc. [mol/l]	Regenerated conc. [mol/l]			
			0.01	0.05	0.1	0.2
85	2	0.1	0.01	0.05	0.1	0.2
		0.3	0.01	0.05	0.1	0.2
		0.5	0.01	0.05	0.1	0.2
		0.7	0.01	0.05	0.1	0.2
		1	0.01	0.05	0.1	0.2
		2	0.01	0.05	0.1	0.2

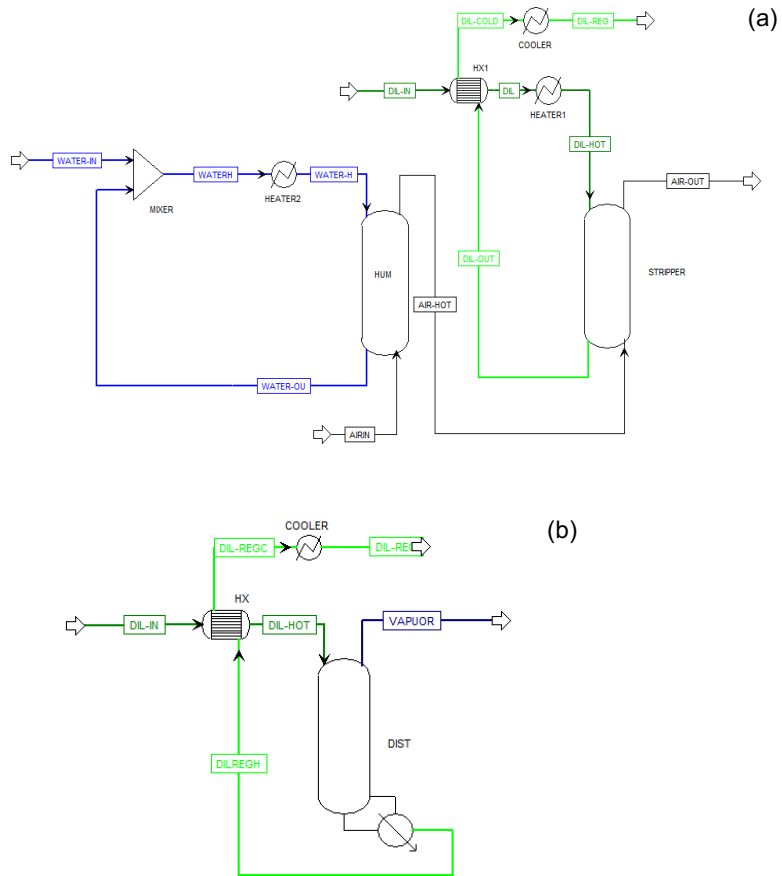


Figure 7.14 Aspen® model of air-stripping column (a) and vapour stripping column (b).

7.5.1.1 Performance analysis on the stripping process

The *STC* and the *SAF* of the air stripping column is reported in Figure 7.15 as a function of the inlet molar concentrations (i.e. concentration solution from 0.1 M to 2M) and the outlet molar concentrations (i.e. concentration solution from 0.01M to 0.2M), fixing the inlet solution flow-rate equal to 0.2 l/min. The thermal energy consumption of the air stripping process is largely determined by the thermal power required to saturate and preheat the stripping air, while only a small fraction is used to heat-up the inlet solution. Therefore, the thermal power consumption mainly depends on the air flow rate which is determined by the toughness of the separation. The higher the amount of gas to be stripped, the higher the air-flowrate required for the separation.

Both *STC* and *SAF* decrease when inlet and outlet concentration increase. For a given outlet concentration, the higher the inlet concentration, the higher the thermal power consumption. This in turn results in an increase of the air flow-rate required to reach the desired outlet concentration and in an increase of the amount of stripped gas. The lowest *STC* and *SAF* equal to 440 kJ/mol and 800 m³/mol are obtained when considering inlet ammonium bicarbonate solution of 2 M and the outlet solution concentration equal to 0.1 M. Very large *STC* characterises *FO* applications in order to get a concentration of NH₃ equal to 1 ppm, minimum acceptable concentration in drinkable water. Instead, in *SGP* application, much lower *STC* can be required due to the larger limit concentration of ammonia compounds. In fact, while the removal of the carbon dioxide is easily achieved, the ammonia is very soluble in water, demanding significant *STC* and *SAF*.

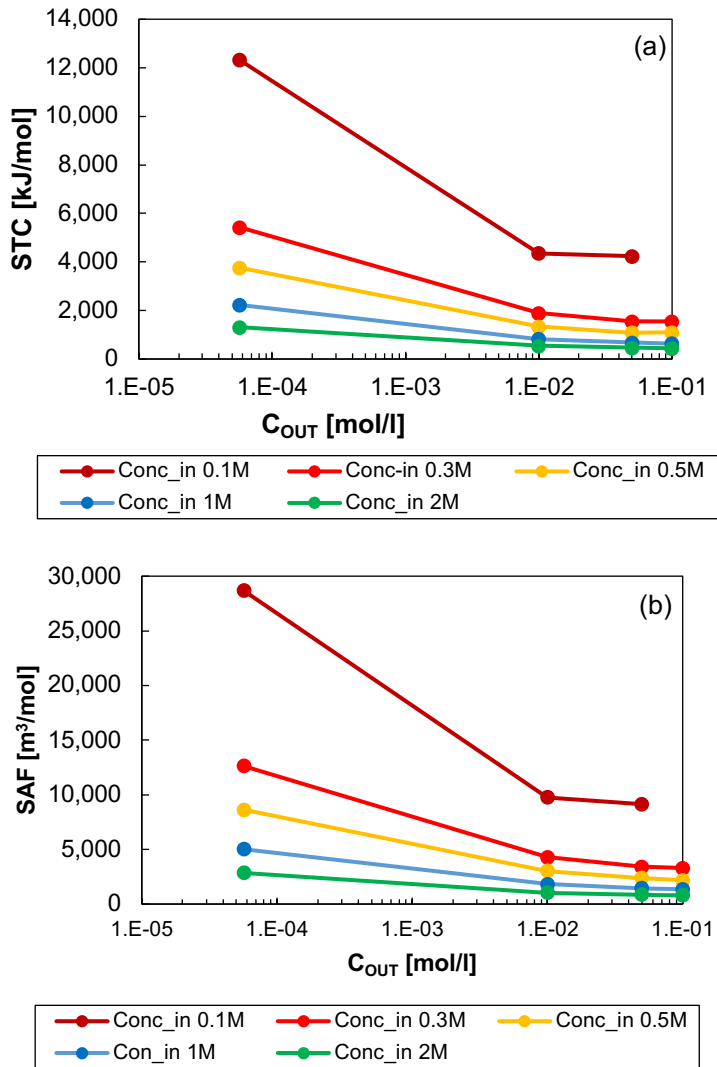


Figure 7.15 Simulation results of (a) Specific thermal Consumption (STC) and (b) Specific Air Flow Rate for the stripping column as function of molar concentration of the regenerated diluted solution.

Figure 7.16 shows the *STC* of the vapour stripping column as a function of the inlet-outlet molar concentrations, with the inlet solution flow-rate equal to 2 l/min and the column pressure equal to 0.475 bar (corresponding column temperature of 80°C). As in the case of air stripping, the lower the outlet solution concentration the larger the *STC*, on the opposite, the larger the inlet concentration the lower the *STC*. The lowest *STC* equal to 374 kJ/mol is

obtained when considering inlet ammonium bicarbonate solution of 2 M and the outlet solution concentration equal to 0.1 M.

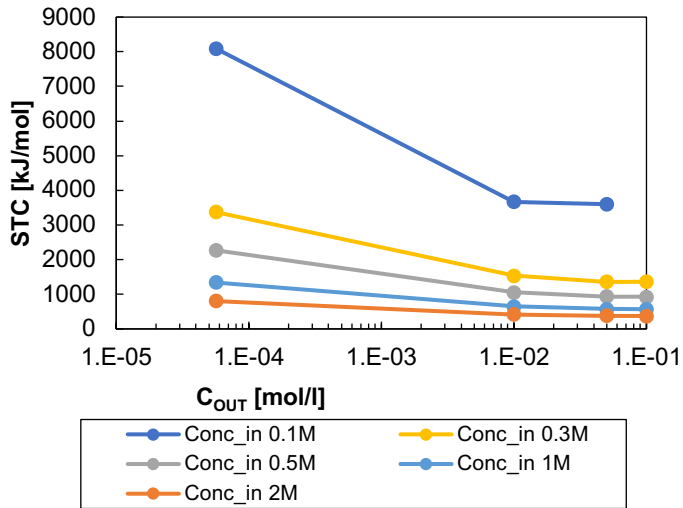


Figure 7.16 Specific Thermal Consumption of the vapour-stripping column as function of molar concentration of the regenerated dilute solution.

Comparing the two stripping systems, the vapour stripping gives lower *STC* than air stripping has already reported by [182]. The thermal consumption of the two units can be largely reduced considering further thermal integrations. Bevacqua et al. [42] reported a much lower air stripping *STC* thank to the adoption of a different process configuration (see Figure 7.17).

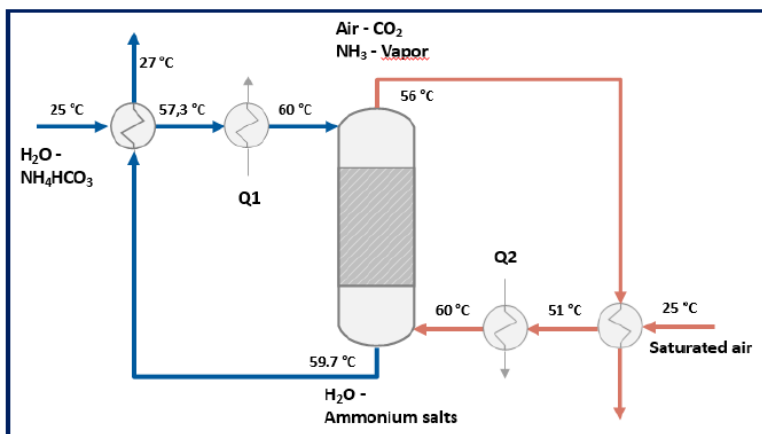


Figure 7.17 Scheme of the vapour stripping column with thermal integration [42].

exhausted concentrated solution from the *SGP* unit is fed in order to promote the absorption of the stripped gases. In the air stripping column, part of the water contained in the air, is also condensed due to the cooling, then the air exiting from the absorption column is heated and saturated again adding a fraction of the concentrate stream (water-rebalancing process), before entering in the stripping column.

In the case of vapour-stripping/absorption process the stripped gases are condensed and cooled at 25°C in a barometric condenser. Differently from the experimental set-up previously investigated, the vacuum condition in the stripping column is guaranteed by a barometric condenser where the stripped gases are condensated/absorbed in the exhausted concentrate stream. The steam is obtained vaporizing part of the dilute solution in the reboiler, then part of the concentrate is added to the inlet dilute stream to restore the original flowrate of the regenerated dilute stream (water rebalancing). In comparison to the previous regeneration unit, the absorption/condensation unit is simpler, indeed, differently from air, the stripping agent is water vapour, which is a condensable specie.

The results from the modelling analysis of the whole regeneration units (i.e. including also the absorption process) have shown that only the vapour stripping/absorption process is a viable process for the regeneration of ammonium bicarbonate solutions, due to the limitations found in the air stripping/absorption process. In fact, the use of large flow rates of air required for the stripping process (*Figure 7.15*) leads to stripped gases with a low partial pressure of NH₃ and CO₂ that strongly affect the absorption efficiency, making difficult to reach the desired regeneration in the concentrate solution. Moreover, the two different gases species NH₃ and CO₂ have really different vapour-liquid equilibrium conditions. While CO₂ is very easy to strip, the NH₃ which is very soluble in water, is hard to remove. On the opposite, the absorption of NH₃ in water results easier than the one of CO₂.

The dilution caused by air and the different thermodynamic behaviour increase the complexity of the regeneration step resulting in an accumulation of NH₃ in the dilute solution and of CO₂ in the air. An example of the regeneration working cycle for the N-compounds (i.e. NH₃, NH₂COO⁻; NH₄⁺) and for the C-compounds (i.e. CO₂, HCO₃⁻, CO₃²⁻), is shown in *Figure 7.20-a* and *b*, respectively. The results reported in this figure, consider an inlet dilute concentration equal to 0.44 M and an inlet concentrate concentration equal to 0.85 M, one of the few conditions in which the system was found feasible. The stripper operates at 1 atm a 70°C with an air flow rate of 40 l/min while the absorber at 25°C and 1 atm.

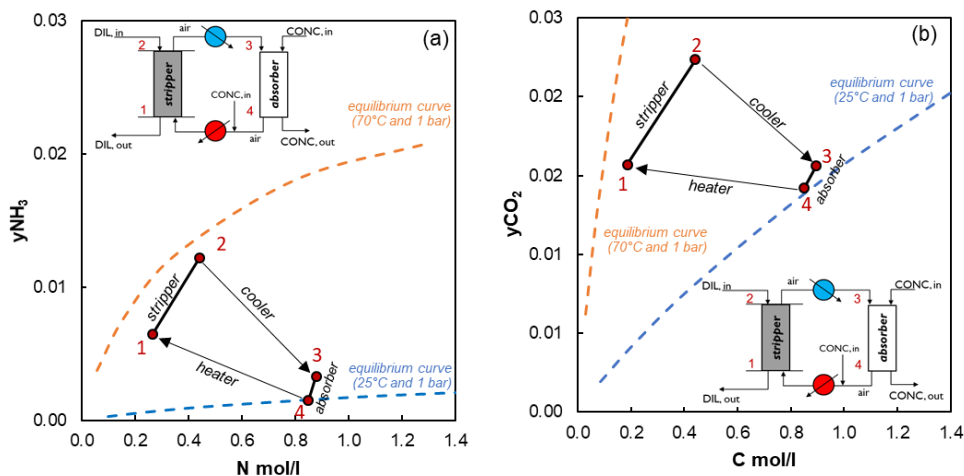


Figure 7.20 Working cycle of N -compounds (a) and C -compounds (b) within the A-SA regeneration unit. Air flow rate equal to 40 l/min, inlet dilute solution equal to 0.44 M, inlet dilute solution equal to 0.85 M, Flexipac[®] 700Y packing.

In the case shown in *Figure 7.20.a* and *b*, the regeneration process allows a partial regeneration of the two solutions decreasing the inlet concentration from 0.44 M to 0.25 M and increasing the concentrate concentration from 0.85 M to 0.9 M. However, the regenerative effect is poor, because a large amount of ammonia remains in the dilute regenerated solution. In order to increase the removal efficiency of the column a higher air flow-rate is required as shown in *Figure 7.15*. On the other hand, the increase of the flow rate reduces the partial pressure of NH_4 and CO_2 , reducing the driving force for the absorption of the gases in the absorber and in some case resulting in a further stripping of the salt stored in the concentrated solution. This latter effect is more evident when high concentration of exhausted concentrate solution is considered.

Conversely, the use of vapour as a stripping agent makes the regeneration easier. Indeed, vapour and ammonia are condensed in the barometric condenser and at the same time carbon dioxide is chemically absorbed, regenerating again the thermolytic salts ions. An eventual increase in the vapour stream required for the separation is rebalanced by the addition of a larger amount of concentrate solutions to the inlet dilute solution, which do not affect the absorption step. A qualitative description of the working cycle of the V -SA regeneration process is reported in *Figure 7.21-a*, while a quantitative analysis is shown in *Figure 7.21-b*.

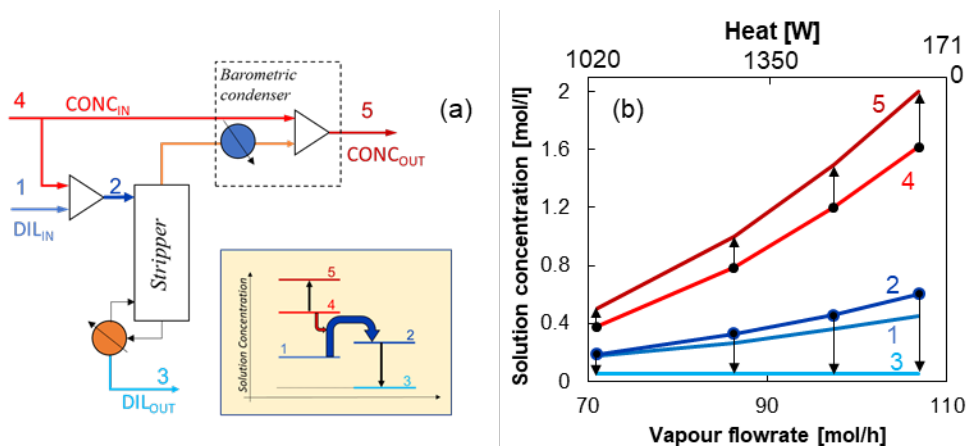


Figure 7.21 Schematic representation of the VS-A process and qualitative representation of the solution concentrations in each section of the system: (1) inlet dilute, (2) dilute solution after water balancing, (3) regenerated dilute solution, (4) inlet concentrate, (5) regenerated concentrate (a). Concentration of the solutions (1-5) during cycles of regeneration as a function of the thermal power provided to the reboiler and the corresponding vapour flowrate (b). Inlet solution (1 and 4) estimated by the RED model-based fixing for four different RED inlet concentrations (i.e., 2-0.05M, 1.5M-0.05M, 1-0M-0.05 M and 0.5M-0.05M). Inlet solution flowrate of dilute and concentrate (1 and 4) equal to 0.2 l/min. Stripping column equipped with Flexipac® 700Y packing. RED unit consisting of 50 cell pairs 0.1x0.4 m², 0.155 mm spacer.

In particular, Figure 7.21-b shows cycles of regeneration for the exhausted solution exiting from a RED unit to regenerate the original salinity gradient for four different RED inlet concentrations (i.e., 2-0.05M, 1.5M-0.05M, 1-0M-0.05 M and 0.5M-0.05M). The inlet concentrations in the Aspen® model were set on the basis of simulation results from the validated RED model presented in Chapter 2, considering a RED unit made of 50 cell pairs 0.1x0.4 m², 0.155 mm spacer, Fujifilm Type 10 membranes and inlet flowrates equal to 0.2 l/min. By regulating the heat provided to the reboiler and the mixing process for water rebalancing, it is possible to fully regenerate the two thermolytic solution in order to obtain, in all investigated cases, the desired outlet solution concentrations for both dilute and concentrate.

7.7 CONCLUSIONS

Thermolytic salts solutions are promising working solutions for *FO* closed-loop and *SGP-HE* applications. In this chapter, two different regeneration units for restoring the salinity gradient of thermolytic salts, i.e. air stripping/absorption and vapour stripping/absorption, were investigated, using experimental prototypes and modelling tools. Experimental campaigns were carried out in order to analyse the influence of different operating conditions on the performance of air and vapour stripping columns, which have experimentally demonstrated the feasibility of the removal process.

The experimental results were used to validate Aspen Plus[®] models for the two different regenerations units. Then, the two models were used to investigate the performance of the whole regeneration units, considering also the absorption process. Results have shown that air stripping/absorption process is not suitable as a regeneration unit because air dilutes the partial pressure of ammonia and carbon dioxide, reducing the efficiency of the absorption process. Conversely, the use of vapour as a stripping agent results in a viable process for the regeneration of thermolytic salts.



THE FIRST OPERATING t-RED HE

Chapter Outline

ABSTRACT	240
8.1 INTRODUCTION	234
8.2 THE FIRST OPERATING T-RED HE	236
8.2.1 PROCESS DESCRIPTION	236
8.2.2 PROTOTYPE DESCRIPTION.....	237
8.2.3 EXPERIMENTAL PROCEDURE.....	240
8.2.4 RESULTS AND DISCUSSIONS	244
8.3 THERMOLYTIC RED HEAT ENGINE (TRED-HE).....	251
8.3.1 INTEGRATED PROCESS MODEL DESCRIPTION	251
8.3.2 RESULTS	255
8.4 CONCLUSIONS.....	263

Paper in-preparation:

F. Giacalone, F. Vassallo, F. Scargiali, Cipollina, A. Tamburini, G. Micale, "Modelling Analysis of a thermolytic Reverse Electrodialysis Heat Engine".

F. Giacalone, F. Vassallo, F. Scargiali, Cipollina, A. Tamburini, G. Micale, "The first operating Thermolytic Reverse Electrodialysis Heat Engine".

Abstract

The thermolytic reverse electro dialysis heat engine (t-RED HE) is a promising technology for converting low-temperature waste heat into electricity. The construction and operation of the first world prototype are here reported. The system consists of: (i) a reverse electro dialysis unit where the concentration gradient between two solutions of thermolytic salts is converted into electricity and (ii) a thermally-driven regeneration unit where low-temperature heat is used to restore the initial conditions of the two feed streams. Regeneration is based on a degradation process of salts into an ammonia and carbon dioxide gas mixture, which can be removed almost entirely from the exhausted dilute solution by vapour stripping. Subsequently, it is reabsorbed into the exhausted concentrate solution, thus restoring the initial salinity gradient of the two streams. For the first time, the feasibility of the process was demonstrated through an experimental campaign via long-run tests and the evaluation of the system performance. Results showed a good stability of the system under different operating conditions. Maximum exergy efficiency computed on the basis of experimental measurements is equal to 1 %.

Furthermore, a mathematical model for evaluating the performance of the proposed t-RED HE was developed. After validation with experimental results from the t-RED HE prototype, the integrated model was used to perform sensitivity analysis aimed to investigate the influence of operating conditions and process configurations on the performance of the heat engine. Results showed that the current technology could achieve exergy efficiency of about 5% while, the adoption of future optimized membrane could lead to a substantial rising of the efficiency near to 10%.

8.1 INTRODUCTION

The first evidence of a closed-loop *SGP* process for the conversion of low-grade heat into electricity is due to prof. Sidney Loeb, who patented in 1974 [30] the *PRO-HE*, and in 1979 the *RED-HE* [31]. Loeb's idea did not receive significant success for decades due to both the lack of suitable membranes able to give interesting performance of the power generation unit (both for *PRO* and *RED*), and the development of suitable regeneration units. In more recent years, the interest of researchers on the field of salinity gradient power in open loop boosted the generation of knowledge about such processes, allowing to reach relevant achievements, in terms of power density but also of operating pilot plants. The important results obtained for open loop systems, has also risen the interest for closed-loop applications, giving a new perspective to Loeb's idea.

Most of the authors have been focused on modelling analysis of *SGP-HE*, proposing (i) different process configurations [32–34], (ii) the adoption of different couples salt-solvent [35,36,93,159] and (iii) the use of different regeneration units [19,39,44,190]. Further, modelling results have also demonstrated that interesting potential can be reach, obtaining exergy efficiency in the range 20-50%. Despite the interesting results of theoretical analysis reported in the literature, the main experimental works have been focused on the analysis of the performance of the single units, i.e. power generation unit [38,40,93] or solution regeneration unit [40], while no real demonstration of the process feasibility has been presented so far, due to the significant efforts required to design, construct and operate a fully integrated *RED-SGP* system.

This chapter is devoted to present the development and operation of the first reverse electro dialysis heat engine fed by ammonium bicarbonate solutions (*t-RED HE*). Based on the knowledge gained in the previous chapter on the regeneration unit for thermolytic salts, the proposed integrated prototype consists of: (i) a reverse electro dialysis unit, where salinity gradient from two ammonium bicarbonate solutions is converted into electricity; (ii) a regeneration unit with a vapour stripping column where ammonia and carbon dioxide are desorbed from the diluted stream and a barometric column where the stripped gases are absorbed into the concentrate stream, restoring the original salinity gradient. The very first experimental campaign has been carried out in order to demonstrate the feasibility of the

process during long-run tests. Further, a modelling tool was also developed, combining the Excel® *RED* process model presented in section 2 with the Aspen Plus® model of the vapour stripping/absorption regeneration unit presented in *Chapter 7*, in order to investigate the influence of the main operating conditions and system configurations on the performance of large-scale systems. Finally, a perspective investigation was carried-out to evaluate future system performance.

8.2 The first operating *t*-RED HE

This section is devoted to present the *t*-RED HE prototype, describing the process scheme, the features of the prototype components and the experimental methodology adopted, and providing the first results of the experimental assessments.

8.2.1 Process description

The thermolytic RED-HE (*t*-RED HE) prototype consists of two units: (i) a RED unit where power is produced exploiting the salinity gradient between two ammonium bicarbonate solutions (“*power unit*”) and (ii) a thermal regeneration unit where low-grade waste heat is used to restore the initial conditions of the two feed streams (“*regeneration unit*”). The concept scheme of the whole *t*-RED HE is reported in *Figure 8.1*.

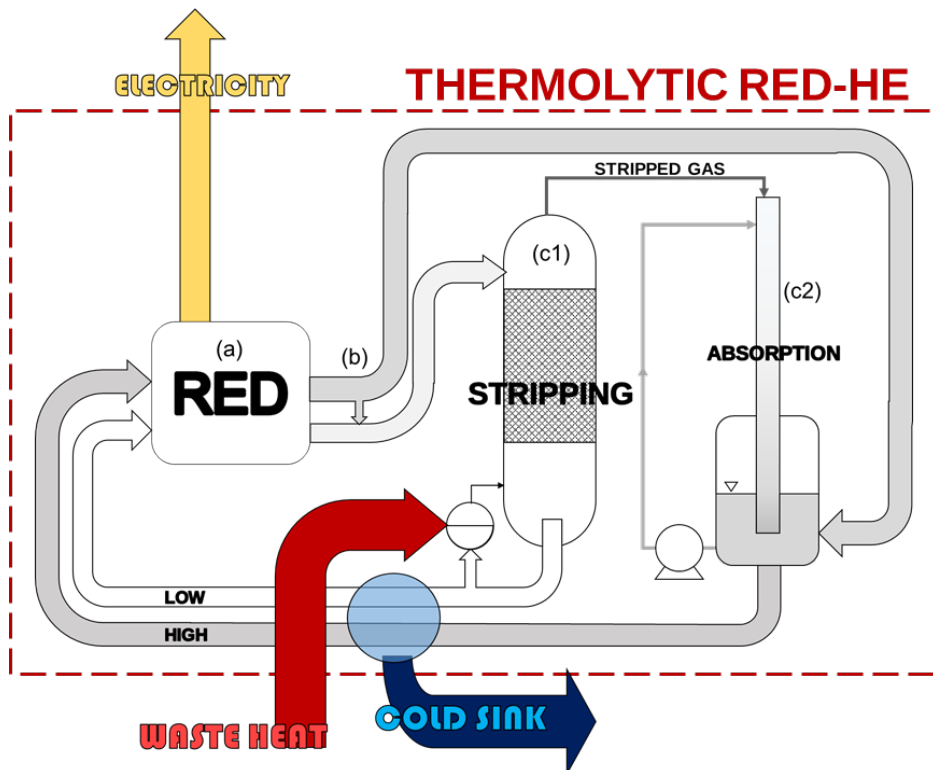


Figure 8.1 Concept scheme of the Thermolytic RED HE. (a) Power unit; (b) water rebalancing; (c₁) stripping of thermolytic salt; (c₂) condensation/absorption of the gases

The process steps can be described as follows:

(a) *Power Unit.* One diluted ammonium bicarbonate solution (*LOW*) is fed together with one concentrated ammonium bicarbonate solution (*HIGH*) in a *RED* unit to convert their salinity gradient into electricity. As a result of the controlled mixing process, the flow-rate and composition of the two streams is altered: part of the salt from the *HIGH* solution is transferred to the *LOW* solution and, due to osmotic flux, water is transferred from the *LOW* solution to the *HIGH* solution. In order to restore the initial conditions of the two streams in the regeneration unit, salt and water have to be transferred in the opposite directions.

(b) *Water rebalancing.* Before entering the regeneration unit, a by-pass stream from the exhausted *HIGH* to the *LOW* stream restores the water content in the *LOW* loop, compensating for the water losses due to osmosis in the *RED* unit and evaporation in the stripping column. The mixing process represents a source of irreversibility, dissipating part of the chemical energy of the two streams and reducing the overall energy performance.

(c) *Regeneration Unit.* The regeneration process is obtained in two steps: (c₁) stripping of thermolytic salts and (c₂) condensation-absorption of the gases. After the partial mixing, the *LOW* stream is preheated and fed on the top of the stripping column where it is distributed on the packing material and put in contact with the rising vapour. The stripping vapour is produced in a reboiler placed on the bottom of the column where part of the solution is vaporized. The mass and enthalpy exchanges between vapour and solution promotes the stripping of ammonia (NH_3) and carbon dioxide (CO_2) reducing the ions (i.e. NH_4^+ , HCO_3^- , CO_3^{2-} and $NH_2CO_2^-$) concentration in solution. The regenerated *LOW* solution exiting from the reboiler is cooled down at 25 °C and stored in the *LOW SOLUTION reservoir*.

The stripped gases are extracted from the barometric condenser connected with the top of the stripping column. Before entering the barometric column, these gases are cooled down to 25°C in order to partially condense water and ammonia and facilitate the CO_2 - NH_3 absorption operation. The barometric condenser produces the vacuum needed to operate the stripping column at low temperature (<100°C) and promotes the condensation and absorption of the stripped gases in the *HIGH* solution. The barometric condenser is operated by recirculating a cold stream from the bottom to the top of the column, where also the *HIGH* solution exiting from the *RED* unit arrives. The regenerated *HIGH* solution exiting from the bottom of the barometric column returns into the *HIGH SOLUTION reservoir*.

8.2.2 Prototype description

A schematic diagram of the prototype is reported *Figure 8.2*. The RED unit provided by REDstack BV (The Netherlands) consists of 50 cell pairs with an active membrane area of $0.1 \times 0.44 \text{ m}^2$ ⁽¹⁾. Each cell pair consists of one cation and one anion exchange membrane (Type 10 - Fujifilm Manufacturing Europe BV -The Netherlands), and two compartments, i.e. a dilute (LOW) and a concentrate (HIGH) compartment equipped with woven spacers of 155 micron (Deukum GmbH, Germany). Magnetic gear pumps (fluid-o-tech FG204) have been used to feed the unit. An electrolyte solution with a redox couple (e.g. $\text{K}_3\text{Fe}(\text{CN})_6 / \text{K}_4\text{Fe}(\text{CN})_6$) is recirculated into the electrode compartments in order to convert the ionic current into an electric current.

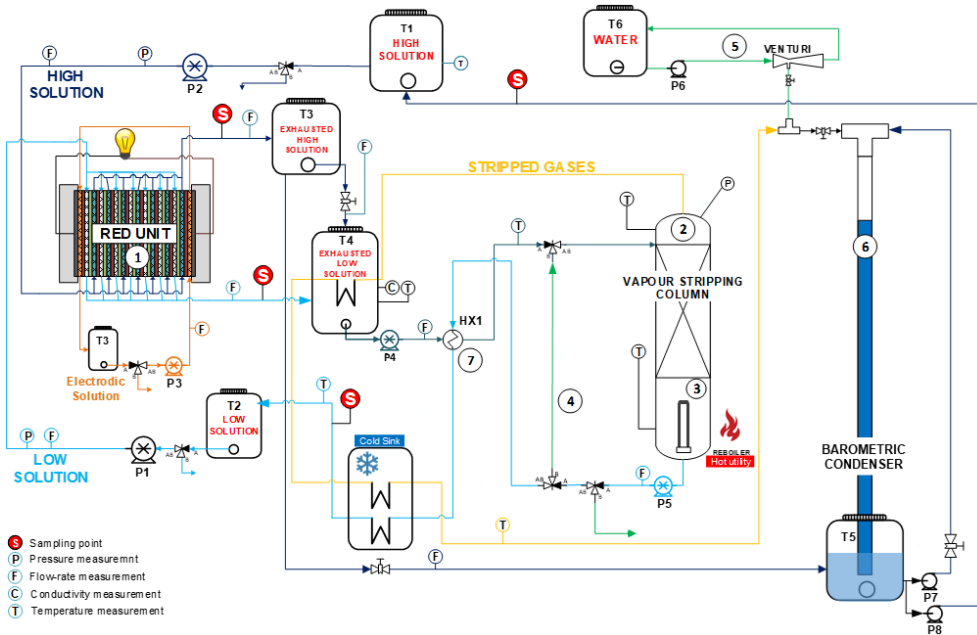


Figure 8.2 Simplified P&I diagram of the thermolytic RED-HE. Main components: (1) RED unit; (2) stripping column; (3) reboiler; (4) auxiliary circuit; (5) Venturi ejectors; (6) barometric condenser; (7) thermal integration heat exchanger; (S) sampling points.

The vapour stripping column ⁽²⁾ consists of a Plexiglas tube with an internal diameter of 50mm filled with a structured packing material (*Flexipac*[®] 700Y, KOCH-GLITSCH). The column packing height is 1.6 m. The bottom of the column is connected to a reboiler ⁽³⁾ where the stripping vapour is generated. For the purpose of the present work, the external

energy input is a low-temperature electrical resistance, which replaces the use of waste heat. The heat provided by the electrical resistance is set regulating the intensity of the electrical current supplied. A T-type thermocouple is used to measure the temperature of the solution in the reboiler. On the top of the column a liquid distributor is used to sprinkle the incoming *LOW* solution on the packing material. The top of the column is connected to an absolute pressure transducer (VEGA - VEGAbar 14) and to a T-type thermocouple. The barometric column is made of a 15 m tube (ID ½') with the bottom end submerged in the *HIGH solution tank* ⁶. A double-pipe hair-pin heat-exchanger is used for thermal integration in order to recover part of the heat from the *LOW* regenerated solution exiting from the reboiler and to preheat the solution fed to the vapour stripping column ⁷. It consists of a stainless steel *AISI 316* tube (ID 6 mm, thickness 1.5 mm) inserted in a Plexiglas tube (ID 12mm, thickness 2mm), with the cold stream flowing in the annular section.

The water balancing process is carried out by mixing part of the concentrate solution to the dilute stream in the exhausted low solution tank. The amount of mixed solution is set in order to achieve a desired concentration (or conductivity) in the outlet solution. This latter is evaluated for each different condition by using the process simulator, performing a mass balance on water. The tank of the exhausted concentrated solution is placed on the top of the prototype while the exhausted dilute solution tank on the bottom. Therefore, the concentrate flows naturally to the exhausted dilute stream. Thus, the control of the flow rate is achieved by varying the opening of the valve in the line of the exhausted concentrate solution.

Four different sampling points ^S are used to evaluate the conductivity (or concentration) of the solutions circulating in the system (WTW Cond 3320). Two sampling points are placed in the outlet pipes of the *RED* unit. The other two are placed in the bottom of the stripping and barometric columns.

During the start-up phase only, an auxiliary circuit ⁴ is used to recirculate hot solution from the reboiler to the top of the column in order to heat-up the packing material. Then air is evacuated using an auxiliary vacuum system consisting of the Venturi ejectors ⁵. A picture of the prototype system is reported in *Figure 8.3*.

A thermostatic bath is used as cold sink, where cold water (T around 15°C) is used to refrigerate the regenerated dilute solution at 25°C and to condense the stripped gases. In a real prototype this process could be achieved by using a convectional cooling stream.

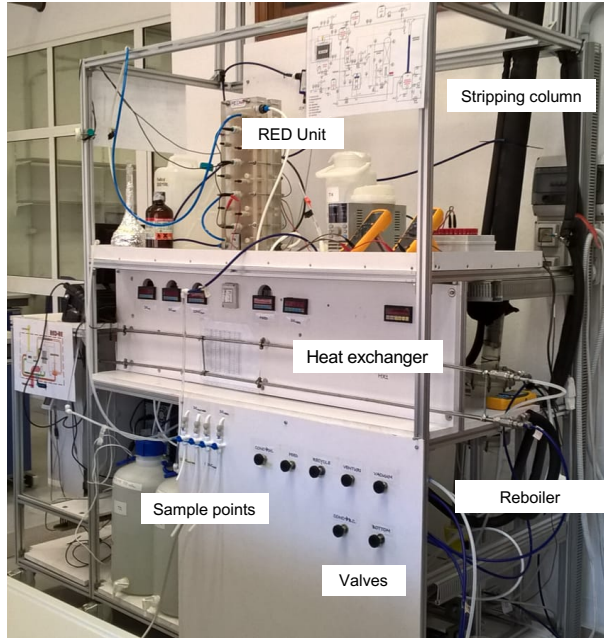


Figure 8.3 The thermolytic RED-HE prototype.

8.2.3 Experimental procedure

The two feed solutions are prepared dissolving anhydrous ammonium bicarbonate salt (Carlo Erba purity >99.5) into deionized water. The electrode rinse solution is prepared dissolving 0.1 mol/l of $K_3Fe(CN)_6$ and 0.1 mol/l $K_4Fe(CN)_6 \cdot 3H_2O$ in deionized water and adding ammonium bicarbonate at a concentration equal to the average of the two feed solutions in order to minimize osmotic fluxes.

Solution concentration was related to the measured conductivity (@ 25°C) using the equation reported in Appendix (see *Appendix 1*):

For the purpose of this work, the inlet flow-rates in the *RED* unit are fixed equal to 0.2 l/min (corresponding to a *RED* channels' velocity of 0.5 cm/s) in all cases. This value gives a good compromise between *RED* unit and vapour stripping column operability.

In order to ensure that the long run tests duration is adequate for assessing operation stability, a non-dimensional parameter (i.e. N_{RED}^C) has been introduced evaluating the number of cycles the feed solutions undergo during closed-loop operation of the *RED* unit. This parameter is defined as:

$$N_{RED}^C = \frac{t_{test}}{t_{RED}} \quad (8.1)$$

where

- t_{RED} is the residence time in the *RED* unit, defined as the ratio between the liquid hold-up in the channels (i.e. 0.28 l) and the solution flow rate (i.e. 0.2 l/min);
- t_{test} is the duration of the long run test (in minutes).

Values of N_{RED}^C close to 350 have been reached in the present investigation with time duration of the long-run test up to 8 hours.

During the continuous operation, the *RED* unit is connected to a fixed external load. The value of the external resistance is chosen in order to operate around the maximum power density condition. However, during the performed experiments, the characteristic power-output behaviour was also assessed at different operating times in order to analyse possible variations in the *RED* unit performance. Thus, the value of external resistance was varied from *O.C.* (open-circuit) to *S.C.* (short-circuit) condition, measuring both stack voltage (V_{STACK}) and current (I_{STACK}) using two multimeters (FLUKE 175). The electric power generated by the *RED* (P_{RED}) unit is given by:

$$P_{RED} = I_{STACK} \cdot V_{STACK} \quad (8.2)$$

The performance of the *RED* units is typically evaluated also in terms of maximum power density ($P_{d,max}$), i.e. the maximum power per unit of membrane area as described:

$$P_{d,max} = \frac{P_{RED,max}}{2A_m N_{cp}} \quad (8.3)$$

where $P_{RED,max}$ is the maximum power produced by the *RED* unit (for ideal stacks with short channels, corresponding to the condition $E_{stack}=OCV/2$), A_m is the active area of one membrane (i.e. $0.1 \times 0.44 \text{ m}^2$) and N_{cp} is the number of cell pairs (i.e. $N_{cp}=50$).

The pressure at the top of the stripping column varies in the range 0.41 – 0.46 bar, corresponding to a boiling temperature for the solution in the range of 78–83°C. The thermal duty of the reboiler is a growing function of the inlet solution concentration. In all investigated cases, the thermal duty is modulated in order to restore the original concentration of the solution fed to the *RED* unit. Also in this case, a non-dimensional parameter (i.e. N_{REG}^C) has been introduced to evaluate the number of cycles which the regenerated *LOW* solution undergoes during closed-loop operation in the packing material of the stripping column. This parameter is defined as:

$$N_{REG}^C = \frac{t_{lest}}{t_{RED}} \quad (8.4)$$

where

- t_{REG} is the ratio between the liquid hold-up in the stripping column (i.e. estimated as 0.10 of the column volume) and the flow rate (i.e. 0.22 l/min) entering in the stripping column;
- t_{lest} is the time duration of the long-run-test.

It is worth defining here also some important thermodynamic figures of merit, which help characterising the system performance. In particular, the maximum amount of power to be harvested from the mixing of solutions at different concentration is given by the Gibbs free power of mixing (\dot{G}_{MIX}), evaluated as the Gibbs free power of the resulting solution (\dot{G}_{mix}) minus the one of the two original streams ($\dot{G}_H + \dot{G}_L$) (*Chapter 2*):

$$\Delta\dot{G}_{mix} = \dot{G}_{mix} - (\dot{G}_H + \dot{G}_L) \quad (8.5)$$

The Gibbs free power of the generic i^{th} stream (\dot{G}_i) is evaluated considering both water and salt contributions (*Chapter 4*). The ratio between experimental electrical power and the Gibbs free power of mixing is the thermodynamic yield of the process:

$$Y = \frac{P_{RED}}{\Delta \dot{G}_{mix}} \quad (8.6)$$

The RED exergy efficiency ($\eta_{ex,RED}$) represents the fraction of the consumed chemical exergy converted into electrical power within the *RED* unit, and is defined as in the previous chapter (i.e. *Chapter 3* and *6*):

$$\eta_{ex,RED} = \frac{P_{RED}}{(\dot{G}_{H,in} + \dot{G}_{L,in}) - (\dot{G}_{H,out} + \dot{G}_{L,out})} \quad (8.7)$$

Finally, the thermal efficiency of the system (η_{th}) is defined as the ratio of the electrical power generated (P_{RED}) by the *RED* unit and the thermal power consumption (*TPC*) of the stripping column according to:

$$\eta_{th} = \frac{P_{RED}}{TPC} \quad (8.8)$$

The exergy efficiency of the system (η_{ex}) is the ratio between the thermal efficiency of the investigated heat engine (η_{th}) and the efficiency of an ideal Carnot's engine (η_C), operating in the same range of temperature. Exergy efficiency is an overall indicator to assess the performance of any heat engine. It is defined as:

$$\eta_{ex} = \frac{\eta_{th}}{\eta_C} \quad (8.9)$$

8.2.4 Results and discussions

In this section, the experimental results of the first operating *t*-RED HE are reported and critically discussed. Long-run tests (duration from 5 to 8 hours) were carried out selecting 3 different salinity gradients at the inlet of the RED unit (*Table 8.1*)

Table 8.1 Operating conditions of the 3 investigated cases.

Test	HIGH SOLUTION	LOW SOLUTION	FEED COLUMN	COLUMN CONDITIONS	
	Conc. [mol/l] (Cond. [mS/cm])	Molarity [M] (Cond. [mS/cm])	Molarity [M] (Cond. [mS/cm])	P _{TOP} [bar]	T _{BOTTOM} [°C]
A	0.6 (45.9)	0.05 (4.9)	0.21 (17.7)	0.417	78.3
B	1.0 (71.4)	0.04 (4.3)	0.38 (30.5)	0.445	79.5
C	1.6 (101.5)	0.05 (4.8)	0.48 (38.7)	0.478	82.5

8.2.4.1 Cycle analysis of process streams

The *t*-RED HE was tested in order to analyse the behaviour and stability of all components during long-run tests. The time dependent variation of the conductivity of the solutions at the inlet and at the outlet of the RED unit working close to maximum power density condition (external load resistance equal to 1.2 Ω), is reported in *Figure 8.4-a* for the case C (i.e. 1.6 M-0.05 M ammonium bicarbonate solutions). The concentration of the “HIGH” inlet solution is reduced from 1.6 M (i.e. 101.5 mS/cm at 25°C) to 1.2 M (i.e. 83.5 mS/cm at 25°C), conversely the “LOW” solution concentration is increased almost sevenfold from 0.05 M (i.e. 4.8 mS/cm at 25°C) to 0.34 M (i.e. 28.9 mS/cm at 25°C). Initial concentrations are then restored in the regeneration unit, after the water rebalancing step (see *section 8.2.2*) that produces a further increase of the LOW concentration from 0.34 M to 0.48 M (i.e. 38.7 mS/cm at 25°C). In the vapour stripping column, the thermolytic salt dissolved in the solution decomposes into ammonia and carbon dioxide. The stripped gases are then absorbed in the HIGH solution circulating in the barometric column. The relevant time dependent variation of the conductivity of the solutions at the inlet and at the outlet of the regeneration unit is reported *Figure 8.4-b*. In particular, within the stripping column the low solution conductivity is reduced from 0.48 M (i.e. 38.7 mS/cm at 25°C) to 0.05 M (i.e. 4.8 mS/cm at 25°C), while the HIGH solution conductivity is increased from 1.2 M (i.e. 83.5 mS/cm at 25°C) to 1.6 M

(i.e. 101.5 mS/cm at 25°C) in the barometric column, thus restoring the original solution concentrations.

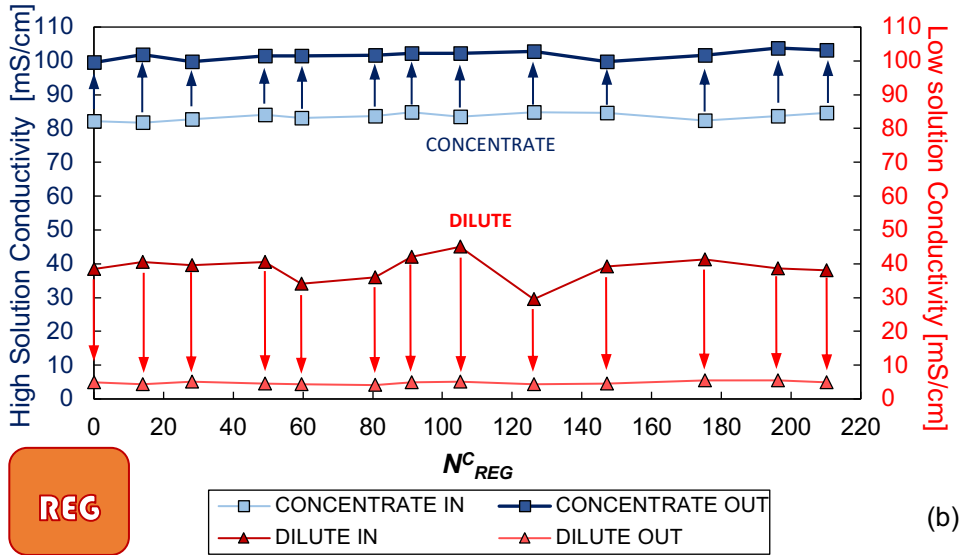
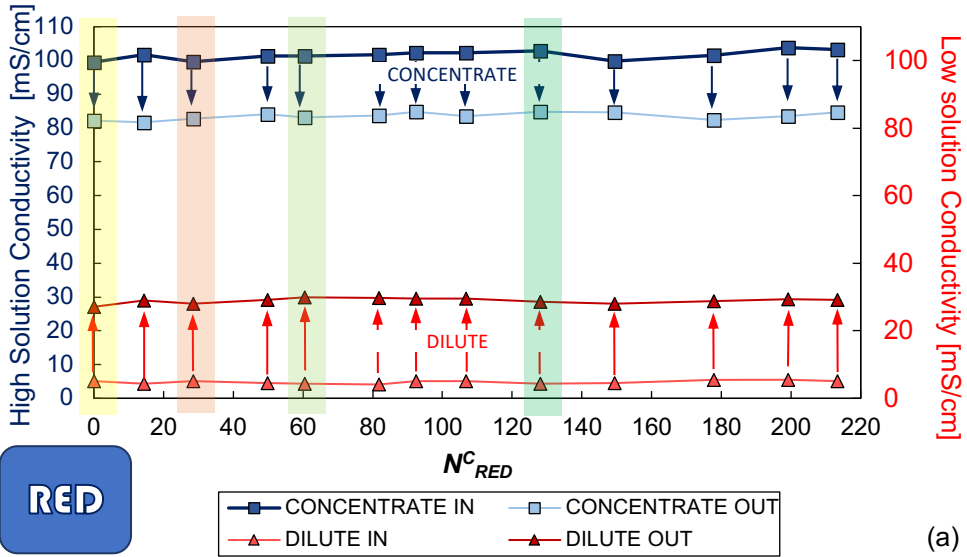


Figure 8.4 Time dependent variation of inlet/outlet conductivity of solutions in the RED generation unit (a) and in the regeneration unit (b). Vertical rectangles in figure 5.a highlight the cycles at which power density measurements were performed (as reported in **Figure 8.6**)

The stability of the operation was demonstrated during the long run tests by monitoring the solution conductivity as a function of the number of cycles (N_{RED}^C and N_{REG}^C in *Figure 8.4-a* and *b*, respectively). The conductivity of the streams was found very stable for more than 210 cycles (i.e. 5h of continuous operation), although some small variation in the inlet solution conductivity fed to the stripping column is observed. Such variation is likely due to some issues during the water rebalancing step, which was manually controlled. It is worth to noting how the result of the regeneration process is not at all affected by such variation as the result of the effectiveness and robustness of the implemented control strategy at the column outlet.

An overview of the time-variation of inlet-outlet solution conductivities from each section of the *t*-RED HE is reported in *Figure 8.5* for the 3 long-run tests performed (*Table 8.1*). In all cases, the extreme stability of operation can be observed, with the system undergoing from 200 to more than 300 cycles, corresponding to more than 8 hours of continuous operation in closed-loop conditions. Comparing the results of the three test cases, it can be easily observed that the higher concentration of the *HIGH* solution entering in the *RED* unit, the higher the outlet concentration of the *LOW* solution. This is due to the higher salinity gradient available leading to an increase of both the migrative flux across the *IEMs* (contributing to increase the power generated) and the uncontrolled mixing phenomena (i.e. detrimental salt and water fluxes). All of these fluxes contribute to increase the level of mixing achieved by the two solutions inside the unit, thus requiring a more power demanding regeneration step.

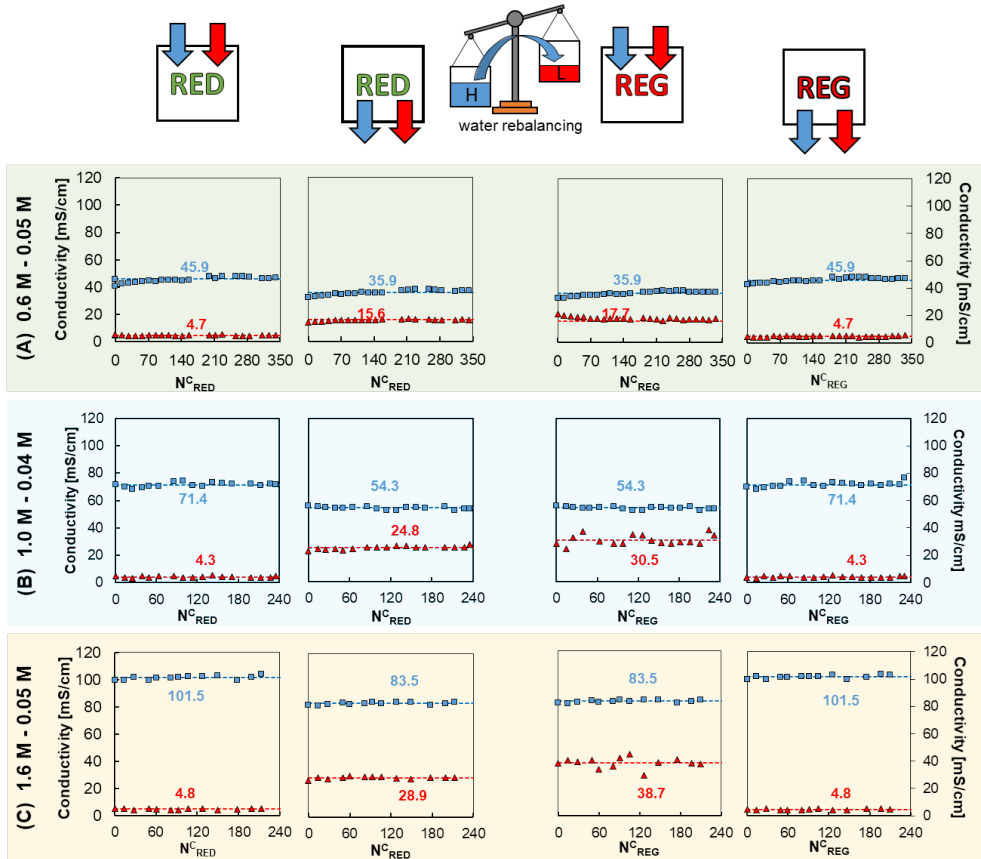


Figure 8.5 Overview of inlet-outlet solutions conductivities from RED unit and regenerated solutions conductivity for 3 long-run tests with different salinity gradient concentration: 0.6 M-0.05 M (A), 1.0 M-0.04M (B) and 1.6M-0.05M (C). Conductivity values evaluated at 25°C. Average values of conductivity are reported using dashed line and indicating their numerical values.

8.2.4.2 Power unit characterization

RED unit performance as electrical power generator is typically characterised using the so called “polarisation curve”, consisting in a plot of the electrical voltage (V_{stack}) and power density (P_d) as a function of the electrical current (I_{stack}). Results relevant to the case C are reported in Figure 8.6 at 4 different times (i.e after 0, 28, 60 and 128 cycles) corresponding to the highlighted coloured rectangles in Figure 8.6-a.

The first important evidence is the stable behaviour of the power generation unit, which guarantees the same performance in all power curves (Figure 8.6-b).

Another interesting finding is the non-ohmic behaviour of the stack, as denoted by the non-linear relationship between V_{stack} and I_{stack} (Figure 8.6-a). In fact, as a result of the

increasing electrical current, the internal stack resistance is reduced due to the larger increase in the *LOW* solution concentration. This is identified by the deviation of the voltage/current curve from the linear ohmic trend (whose slope identifies the internal stack resistance), which indicates a continuous decrease in the stack resistance. This effect is made evident in these tests thanks to the high residence times (low velocities and long channels) achieved in this study. Similar findings were already reported in the literature by Vanoppen et al. [191].

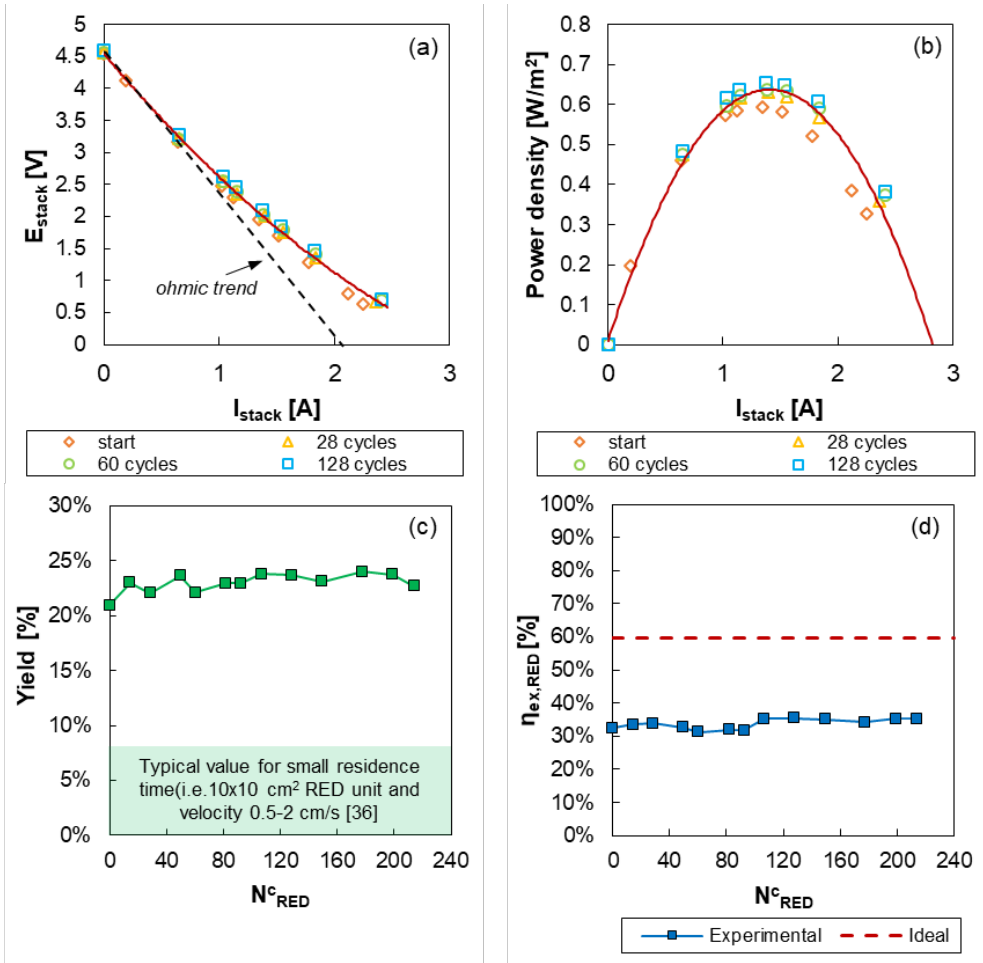


Figure 8.6 Stack voltage (a) and electrical power (b) generated by the RED unit as a function of the electrical current. Thermodynamic yield vs number of RED unit cycles (c): experimental and evaluated range for smaller stacks [38]. Exergy efficiency vs number of RED unit cycles (d): experimental and maximum value for an ideal stack (unitary permselectivity, null water and salt permeability). Experimental results refer to test case C of Table 8.1.

For the same reason, the maximum power density generated in the RED unit of 0.65 W/m^2 is lower than the highest values reported in the literature [38], on the other side, ensuring a better exploitation of the available salinity gradient. With this respect, an average yield of almost 25% (Figure 8.6-c) is obtained, which is about fivefold the value obtainable with smaller RED unit. Finally, the exergy efficiency of the RED unit is constantly maintained around 33% (Figure 8.6-d), which compares very well with the maximum value obtainable in an ideal stack provided with ideal membranes (i.e. unitary permselectivity, null water and salt permeability) operating at the same conditions (close to 60%). All that shows a satisfactory exploitation of the available salinity gradient.

8.2.4.3 Cycle analysis of unit performance

In order to analyse the cyclic behaviour of the system in terms of performance indicators, the measured power density output, specific thermal power consumption and energy efficiency are reported in Figure 8.7. As expected, the power density in the RED unit decreases when the HIGH solution concentration decreases. In particular, while a maximum power density around 0.64 W/m^2 is observed for the case 1.6-0.05 M (C), it decreases to around 0.45 W/m^2 in the case 1.0 M - 0.04 M (B) and a further reduction to 0.27 W/m^2 is observed for the case 0.6 M-0.05 M (A). On the other hand, the higher the HIGH solution concentration, the higher the specific thermal power consumption in the vapour stripping column to regenerate the two solutions, ranging from 106 kWh/m^3 to 96 kWh/m^3 and 86 kWh/m^3 for the case C, B and A, respectively.

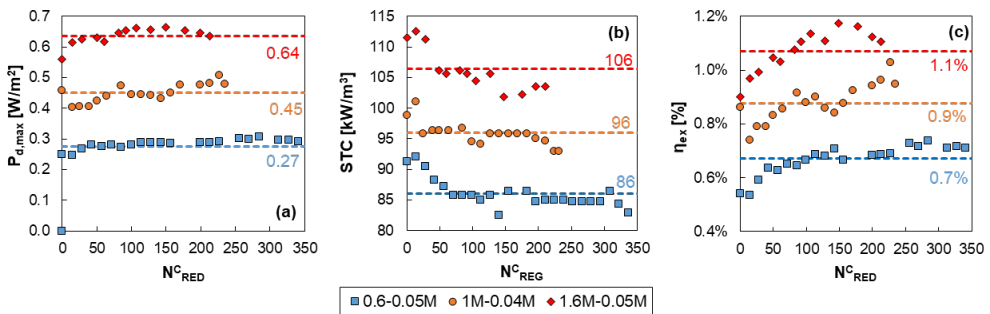


Figure 8.7 Maximum power density ($P_{d,max}$) (a), specific thermal consumption (STC) (b) and exergy efficiency (η_{ex}) (c) of the thermolytic RED-HE during long-run tests for the 3 different salinity gradient cases (A, B, and C).

However, the increase of power output with the *HIGH* solution concentration is predominant compared to the thermal power consumption increase. This results into the highest exergy efficiency value of 1.1%, observed in the case of the highest driving force considered (i.e. 1.6 M-0.05 M).

It is worth noting that despite the lower exergy efficiency obtained, the results here reported pose a relevant milestone on the field of *SGP-HE* providing the first experimental demonstration of the concept. Further, simulation results reported in Chapter 6 and 7 for *RED-MED* and *RED-MD* and in the following section for the *t-RED HE*, have already demonstrated that it is possible to achieve interesting cycle efficiencies.

8.3 Thermolytic RED heat engine (tRED-HE)

In order to evaluate the performance of reverse electro dialysis heat engine fed by ammonium bicarbonate solutions (*tRED-HE*), the vapour stripping/absorption regeneration unit model developed and validated in *Chapter 7* was coupled to the RED process model presented in *Chapter 2*. The integrated model was used to investigate the effect of operating conditions, design parameters and membrane properties on the performance of the system. Furthermore, the impact of using a multi-column regeneration unit was considered. All the analyses were performed also in order to evaluate future perspectives of such system, considering the impact of using enhanced membranes in the *RED* unit.

8.3.1 Integrated process model description

A schematic representation of the whole *tRED-HE* model is reported in *Figure 8.8*.

The two ammonium bicarbonate solutions, i.e. the dilute and the concentrate, are pumped to the *RED* unit to convert their salinity gradient into electricity. During the process part of the salt content in the concentrate solution is transferred to the dilute one and water is transferred from dilute to concentrate. In order to restore the initial conditions of the two streams in the regeneration unit, both salt and water transport have to be promoted in opposite direction (*Figure 8.8*).

After exiting from the *RED* stack, the dilute solution is mixed to a small amount of the outlet concentrate stream in *Mixer 1*. This is done to restore the water content in the dilute stream. Notably, this step is extremely important in order to restore the flow rate of the two streams since the system operates in closed loop. The second mixer (*Mixer 2*) fulfils a similar task restoring the amount of water consumed in the stripping process due to the partial vaporization of the dilute stream. In practical applications, the water-restoring step can be carried out in one mixer only. Here, two different mixers are considered because the two sub-models (i.e., one for the *RED* unit and one for the regeneration unit) are developed in different software and each of them includes a mixer.

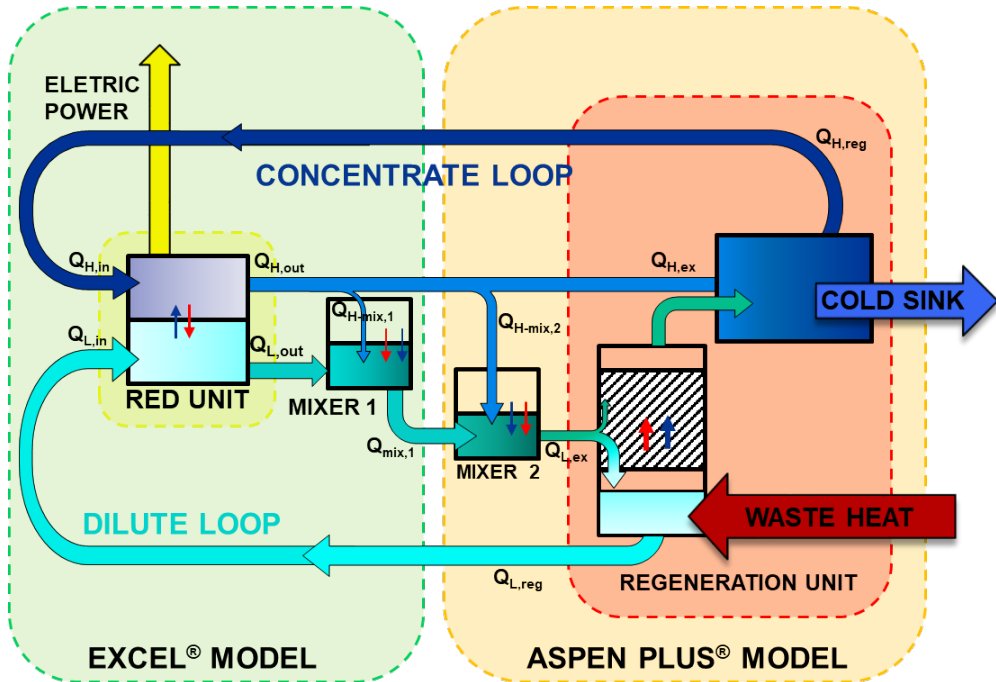


Figure 8.8 Scheme of the whole t-RED HE process simulator. Blue arrows indicate the direction of water fluxes while red arrows indicate the direction of salt fluxes.

The resulting stream from *Mixer 2* is fed to the vacuum vapour stripping column operating in vacuum conditions. Here, the ammonium bicarbonate is decomposed into ammonia and carbon dioxide, which are stripped by means of a vapour stream produced from the partial vaporization of the solution in the reboiler. Low-grade waste heat ($T \leq 100^\circ\text{C}$) is used as an energy source. The stripped gasses are absorbed again into the concentrate solution in a low temperature (25°C) absorption process. The two regenerated solutions are finally sent back to the stack where their difference in chemical potential is used again to generate electricity. The integrated process model consists of two experimentally validated sub-models (*Figure 8.8*):

- (i) The *RED* process model (presented in *Chapter 2*), including *Mixer 1*, implemented in Excel®.
- (ii) The regeneration process model (presented in section 7.4.3), including the *Mixer 2*, implemented in Aspen Plus®.

8.3.1.1 Integration of the models: mass balances in mixers

The global and salt mass balances in *Mixer 1* to restore the original water content of the two streams due to the osmotic flux in *RED* unit are reported in eq.s 8. 10-8. 11.

$$\dot{V}_{mix1} \cdot \rho_{mix1} = \dot{V}_{L,out} \cdot \rho_{L,out} + \dot{V}_{H-mix1} \cdot \rho_{H-mix1} \quad (8.10)$$

$$\dot{V}_{mix1} \cdot C_{mix1} = \dot{V}_{L,out} \cdot C_{L,out} + \dot{V}_{H-mix1} \cdot C_{H-mix1} \quad (8.11)$$

where, \dot{V}_i , ρ_i and C_i are the volumetric flowrate, density and concentration of the i^{th} generic stream respectively. The subscripts L,out , $mix1$ and $H-mix1$ refer to the dilute exiting from the *RED* unit, the stream exiting from the mixer 1 and the part of the concentrate exiting from the *RED* unit added in the mixer, respectively. The \dot{V}_{H-mix1} is evaluated from the water mass balance of the concentrate in the *RED* unit

$$\dot{V}_{H-mix1} = \frac{\dot{V}_{H,in}(\rho_{H,in} - C_{H,in} MW_{salt}) - \dot{V}_{H,out}(\rho_{H,out} - C_{H,out} MW_{salt})}{\rho_{H,out} - C_{H,out} MW_{salt}} \quad (8.12)$$

where MW_{salt} is the molecular weight of NH_4HCO_3 .

The concentration and flow rate of the stream resulting solution from *Mixer 1* are the input of the Aspen Plus® regeneration model.

The mass balances of the *Mixer 2* are implemented in the ASPEN model flow-sheet. The amount of concentrate solution to add to the dilute stream for rebalancing the water content due to the generation of the stripping vapour is evaluated using the *design spec* tool of ASPEN Plus®. This tool operates as a goal seek with the aim to set the amount of concentrate solution flowrate added to the dilute to the value which gives the same water content in the stripping gases. The thermal power required for the separation is then computed by using a second design spec (operating in parallel to the previous) which adjusts the thermal power value in order to get the desired regenerated dilute solution concentration.

8.3.1.2 Thermal and exergy efficiency

The performances of the system were investigated in terms of thermal and exergy efficiency. As already mentioned, the maximum achievable thermal efficiency of the *tRED-HE* is given by a Carnot Engine (η_c) working between the maximum operating temperature

($T_{hot}=353$ K) and the minimum temperature ($T_{cold}=293$ K). Finally, the exergy efficiency of the *t*-RED HE is the ratio between the thermal efficiency and the Carnot efficiency.

8.3.1.3 Integrated model validation

Both RED unit model and Regeneration unit model were individually validated, as already shown in *Chapter 2* for the RED unit and in *Chapter 7* for the regeneration unit. A further validation was also considered, comparing the experimental results reported in section 8.2.4 (*Figure 8.9*).

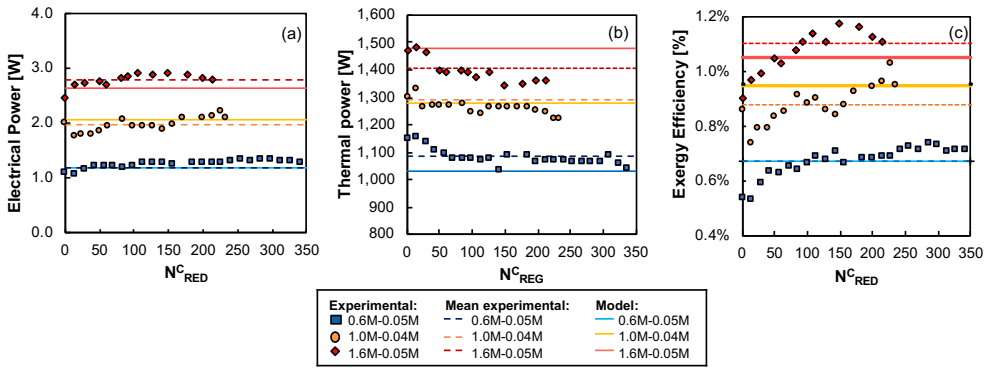


Figure 8.9 *t*-RED HE model validation

The comparison of experimental and modelling performances of the *t*RED-HE result in a good agreement validating the model.

8.3.1.4 Simulation conditions

Simulations were computed considering a RED unit consists of 1000 cell pairs (cps) with membrane area of 0.5×0.5 m² and 0.155 mm spacer thickness. Two different scenarios were analysed, i.e. (i) current scenario in which the RED unit is equipped with present membranes (Fujifilm type 10 membranes, more details in section 2.4.2) and (ii) a future scenario in which future improved membranes are considered (*Table 8.2*). As reported in [74] for the case of NaCl aqueous solutions, future membranes properties are not far from the present state of the art membranes.

The operating and geometrical properties of the column were set as follow:

- Raschig ring of 15 mm was adopted as packing material.

- The column diameter was calculated for each test case by according the sizing of the column to the steam flow-rate;

The column height was set equal to 2 m.

Table 8.2 Current and future membrane properties adopted in the analysis.

<i>Properties</i>	<i>Current</i>	<i>Future</i>
<i>Water Permeability [ml/(bar·h·m²)]</i>	6 ⁽²⁾	1.5 ⁽²⁾
<i>Permselectivity [%]</i>	85.1 ⁽¹⁾	95 ⁽²⁾
<i>Salt permeability [m²/s]</i>	4.5 10 ⁻¹²⁽²⁾	1.13 10 ⁻¹²⁽²⁾
<i>Resistance [Ω·cm²]</i>	6.01 10 ⁻⁰⁴⁽¹⁾	1.50 10 ⁻⁰⁴⁽¹⁾

⁽¹⁾reference concentration of 2 M-0.01 M NH₄HCO₃ water solutions. Property functions of solutions concentration using correlation reported in Chapter 3. ⁽²⁾assumed constant in the whole range of concentrations

8.3.2 Results

Sensitivity analyses were carried out in order to investigate the effect of inlet flow rates and inlet concentrations of the two solutions fed into the RED unit for both current and future scenarios on the performance of the whole system. Finally, the effect of using a multi-stage regeneration unit was analysed.

8.3.2.1 Influence of inlet concentration on the system performance

The first sensitivity analyses show the effect of the solution concentration on the main performance parameters of the tRED-HE for a RED unit of 1000 cell pair 0.5x0.5 m². For the first analysis, the inlet velocity of the two solutions within the channels was set to 1cm/s (typical RED unit velocity).

The influence of RED inlet concentration on the gross power density ($P_{d,max}$), is reported in Figure 8.10. As expected, the higher the salinity gradient between the two solutions, the higher the power density obtainable from the unit. As a matter of fact, when long stacks or large residence times are considered as in the present case, the detrimental effect due to the dilute solution resistance becomes less important. Conversely, if laboratory units (i.e., short stacks) or low residence times for the dilute solutions are considered, then the dilute solution resistance is the controlling factor affecting the power density [49]. In the case of current

membranes, the highest $P_{d,max}$ is equal to 2 W/m^2 while in the case of future membranes it is equal to 4.25 W/m^2 . The doubling in power density shifting from current to future scenario is due to the reduction of the irreversible phenomena occurring in the *RED* unit and responsible for the reduction of the available salinity gradient [165]

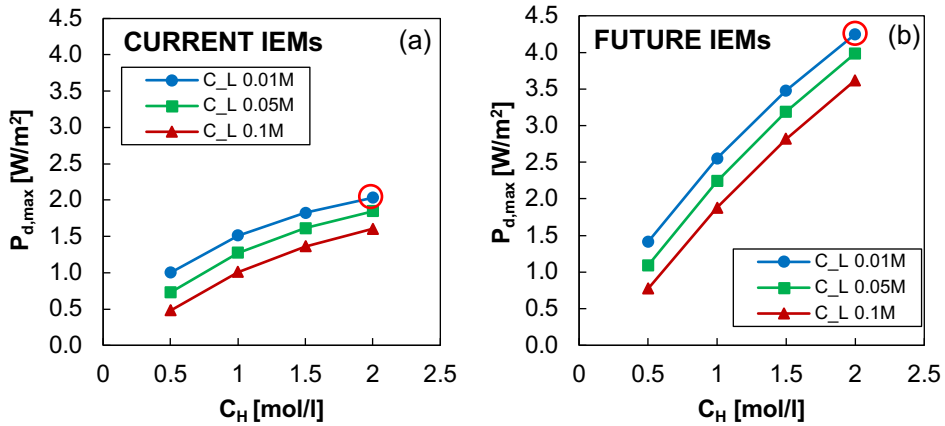


Figure 8.10 Effect of inlet concentration on *RED* unit power density for current (a) and future (b) scenarios. *RED* unit 1000 cell pairs $0.5 \times 0.5 \text{ m}^2$, inlet velocities equal to 1 cm/s . Red circle is used to highlight the conditions of the best performance.

The effect of *RED* inlet concentration on the thermal power consumption of the vapour stripping column is reported in *Figure 8.11-a* and *b* for current and future scenarios, respectively. The higher the power generated in the *RED* unit, the higher is the salinity gradient consumed, and therefore, the higher the thermal power required by the stripping column. This is why, the lowest TPC values (around 160 kW) are obtained for the smaller salinity gradient considered ($0.5\text{M}-0.1\text{M}$). Similar thermal energy consumptions are obtained for the two scenarios, i.e. current and future, due to the effect of the *Mixer 1*. It should be observed that the two solutions exiting from the *RED* unit have different concentration values for the current and future scenarios, respectively. Conversely, the two solutions entering the regeneration unit have similar concentration values for the current and future scenarios, due to the partial mixing process required for the water-rebalancing.

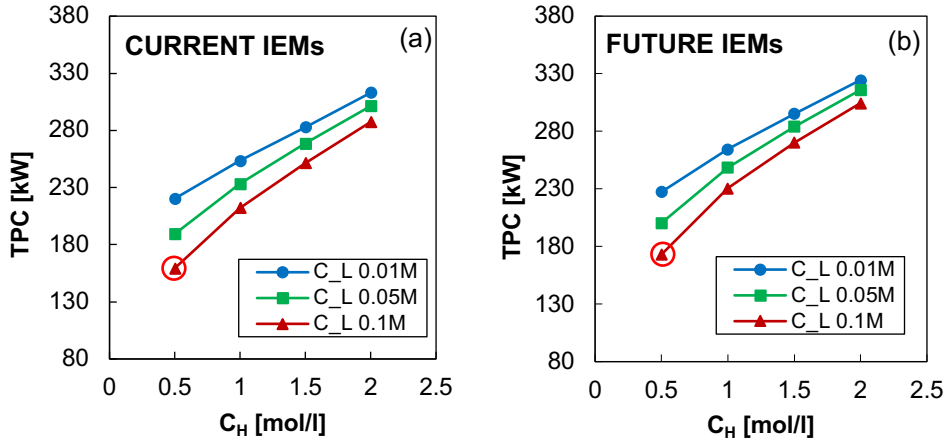


Figure 8.11 Effect of inlet concentration on Thermal Power Consumption of the vapours tripping column for current (a) and future (b) scenarios. RED unit 1000 cell pairs $0.5 \times 0.5 \text{ m}^2$, inlet velocities equal to 1 cm/s. Red circle is used to highlight the conditions for the best performance.

The ratio between the gross power output of the RED unit and the TPC of the regeneration unit is the thermal efficiency of the unit. Figure 8.12 shows the effect of inlet concentration on the thermal and exergy efficiency for both cases, i.e. current (a) and future membranes (b). In both cases the highest efficiency is achieved for the highest driving force (2M-0.01 M) because the salinity gradient affects more the power production than the TPC. As a matter of fact, considering the current scenario and $C_L=0.01\text{M}$, an increase of the concentration of the high solution from 0.5M to 2M double the power density from 1 W/m^2 to 2 W/m^2 , while the thermal energy consumption increases about 50%. This effect is more marked in the future scenario where the power density is increased almost three times ($1.5 \text{ W/m}^2 \rightarrow 4.25 \text{ W/m}^2$), while the power consumption is comparable to the one in the current scenario. As a result, the highest thermal efficiency in the current scenario is equal to 0.16 % ($\eta_{\text{ex}}=0.9\%$), while in the future one is equal to 0.32% ($\eta_{\text{ex}}=1.93\%$).

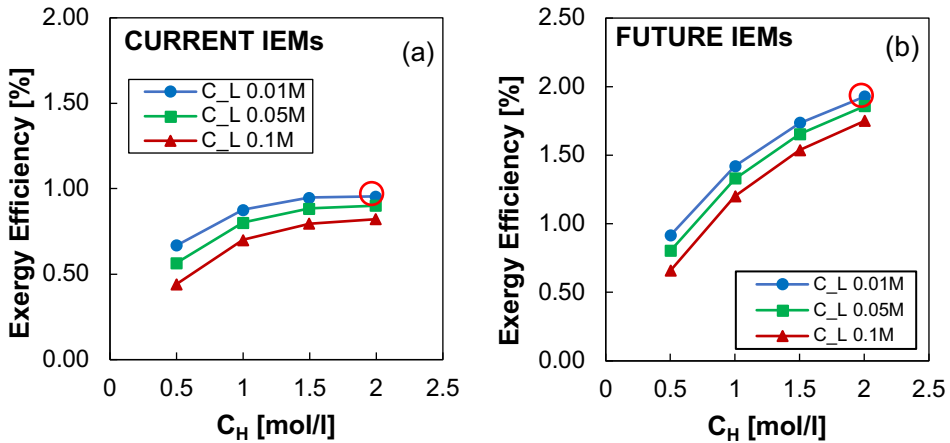


Figure 8.12 Effect of inlet concentration on Thermal and Exergy Efficiency consumption of the Thermolytic RED Heat Engine for current (a) and future (b) scenarios. RED unit 1000 cell pairs $0.5 \times 0.5 \text{ m}^2$, inlet velocities equal to 1 cm/s. Red circle is used to highlight the conditions of the best performance.

8.3.2.2 Influence of inlet velocities on the system performance

The following sensitivity analyses concerns the effect of the inlet solutions velocities on the main performance parameters of the *tRED-HE* for a RED unit consisting of 1000 cell pairs $0.5 \times 0.5 \text{ m}^2$, fixing the inlet concentration of the two solutions in the RED unit to the values that provided the highest efficiency in the previous analysis (i.e. $C_H = 2 \text{ M}$ and $C_L = 0.01 \text{ M}$).

The influence of the feed inlet velocity on $P_{d,max}$ is reported in Figure 8.13. As expected, the gross power density is a growing function of the solution velocities. In particular, the $P_{d,max}$ is affected by the dilute velocity, while only slight variations are observed with the concentrate velocity. The highest $P_{d,max}$ is equal to 2.6 W/m^2 in the current scenario. Due to the membrane improvements, the $P_{d,max}$ in the future scenario is more than the double of the current one, i.e. 5.7 W/m^2 .

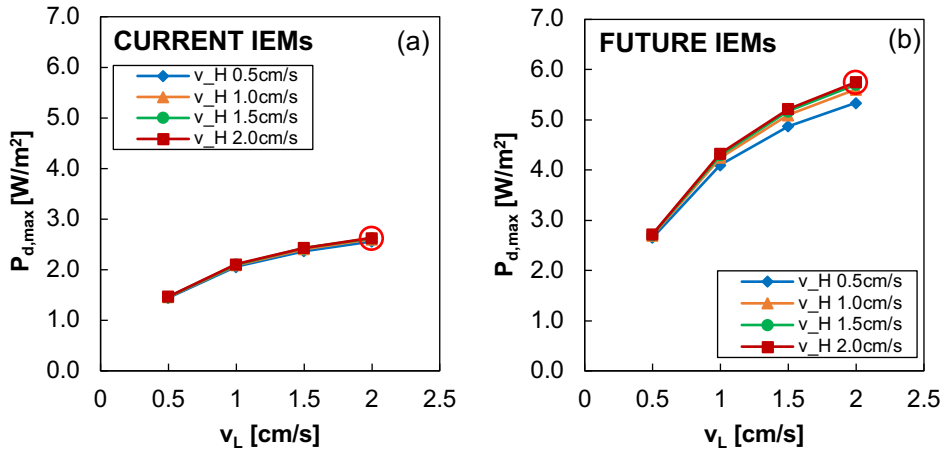


Figure 8.13 Effect of inlet velocity on RED unit power density for current (a) and future (b) scenarios. RED unit 1000 cell pairs $0.5 \times 0.5 \text{ m}^2$, inlet concentrations equal to $C_H = 2 \text{ M}$ and $C_L = 0.01 \text{ M}$. Red circle is used to highlight the conditions of the best performance.

The influence of RED inlet velocities on the TPC of the vapour stripping column is reported in Figure 8.14-a and b for current and future membranes, respectively.

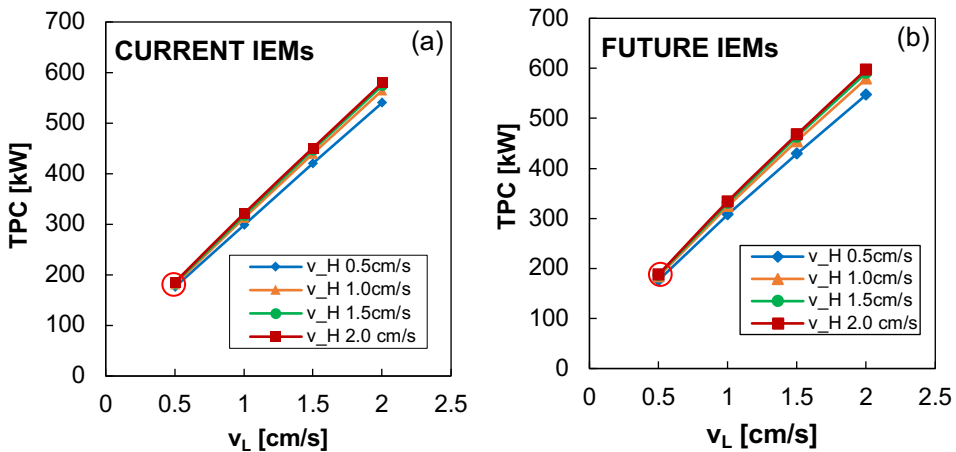


Figure 8.14 Effect of inlet velocity on Thermal power consumption for current (a) and future (b) scenarios. RED unit 1000 cell pairs $0.5 \times 0.5 \text{ m}^2$, inlet concentrations equal to $C_H = 2 \text{ M}$ and $C_L = 0.01 \text{ M}$. Single Vapour stripping column $h = 2 \text{ m}$ $T_{\text{waste-heat}} = 80^\circ\text{C}$. Red circle is used to highlight the conditions of the best performance.

The TPC linearly increases with the dilute flow-rate. The higher the dilute water flow rate fed to the stripping column, the higher the amount of stripping vapour required in the regeneration unit. The TPC is practically not affected by the velocity of the concentrate and

the adoption of either current or future membranes. The lowest *TPC* of about 180 kW is observed in the case of dilute inlet velocities of 0.5 cm/s.

The effect of *RED* inlet velocities on the exergy efficiency of the whole *tRED-HE* is depicted in *Figure 8.15-a* and *b* for current and future membranes. In both scenarios, the efficiency of the unit is dominated by the influence of the velocities on *TPC*, reaching the maximum value when the *TPC* has the lowest value (i.e. $v_H=v_L=0.5$ cm/s), notwithstanding in this condition the lowest power density is observed. The highest thermal efficiency in the current scenario is equal to 0.2%, which corresponding to an exergy efficiency of 1.1%. In the case of future enhanced membranes, the thermal efficiency is increases up to 0.36% while the exergy efficiency reaches value around 2.1%.

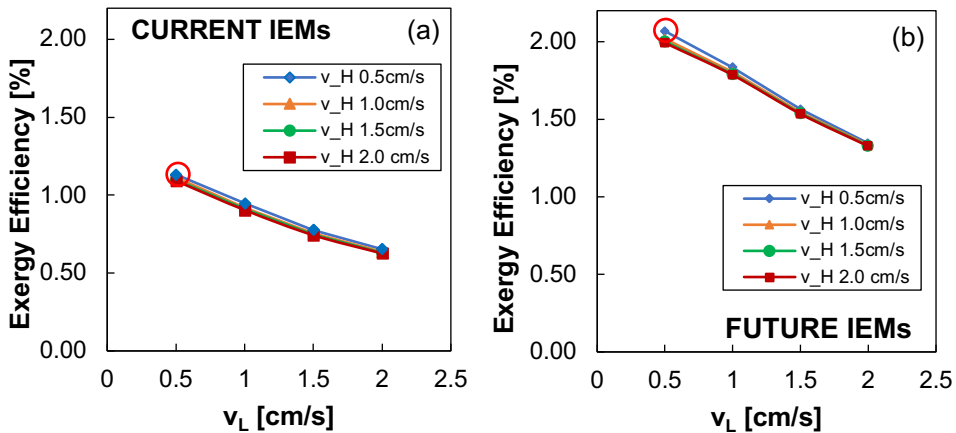


Figure 8.15 Effect of inlet velocity on the Exergy Efficiency of the integrated system for current (a) and future (b) scenarios. *RED* unit 1000 cell pairs $0.5 \times 0.5 \text{ m}^2$, inlet concentrations equal to $C_H=2$ M and $C_L=0.01$ M. Single. $T_{\text{waste-heat}}=80^\circ\text{C}$. Red circle is used to highlight the conditions of the best performance.

8.3.2.3 Multi-stage regeneration unit

The previous sensitivity analyses on the *tRED-HE* using a single stripping column has highlighted that in all the investigated conditions the thermal consumption of the vapour stripping column is the limiting factor, which leads to low efficiency values also in the case of future enhanced membranes. The high thermal power consumption is caused by the partial vaporization of the solution in the reboiler to generate the stripping steam. However, only a small part of the thermal energy contained in this stream is used to strip the gas. As a result, most of the heat supplied remains in the vapour steam exiting from the top of the column and

it is discharged in the condensation step (see *CONDENSER* in *Figure 7.19*). In order to increase the energetic efficiency of the regeneration unit this heat should be recovered and reused within the process.

A possible alternative already proposed in literature [181] for forward osmosis application, is to exploit the enthalpy of vaporization remaining in the stripping gas as an energy source for a following stripping column operating at lower pressure. In this way, a multi-column configuration is obtained, similarly to a Multi Effect Distillation (MED) unit. When a multi-column system is considered, the solution exiting from *Mixer 1* is split and feed in parallel to the columns. Only the heat supplied in the first column is coming from an external source (i.e. waste-heat), while the following columns are fed by the heat obtained from vapour condensation of the previous column as shown in *Figure 7.17*. The absorption step operates in the same way for both single and multi-stage process, as the amount of gases stripped in the two different configurations remains practically the same.

Differently from *MED* process, where a large number of effects can be adopted to increase the thermal efficiency of the process, in the present case of a multi-column arrangement, the number of columns or stages is limited due to the multi-component nature of the condensing vapour. Indeed, the condensation process takes place not at constant temperature but in a range of condensation temperature of 4-8°C, consuming rapidly the available temperature difference between the first and the last columns, and resulting in a smaller number of units. As an example, fixing the top temperature at 80°C and the lowest operating pressure equal to 0.05 bar (i.e. bottom temperature around 35 °C), the maximum number of columns is equal to 5.

The thermal and exergy efficiency of the *tRED-HE* fed by waste-heat at 80°C as a function of the number of columns in series, are reported in *Figure 8.16*. Operating conditions at the *RED* unit inlet (i.e. concentration and velocity of solutions) were fixed equal to those obtained in the previous analysis, which led to the highest efficiency (i.e. $C_H=2$ M $C_L=0.01$ M $v_H=v_L=0.5$ cm/s). The efficiency increase is not a linear function of the number of stripping columns. In fact, the efficiency is more than doubled when shifting from 1 to 2 columns ($\eta_{ex,1}=1.3\% \rightarrow \eta_{ex,2}=2.7\%$), while it is only four times higher in the case of 5 columns in series ($\eta_{ex,5}=5.1\%$). In future scenario, using a 5-column configuration the thermal and exergy efficiency are equal to 1.4% and 8.5%, respectively.

Interestingly, the temperature of the waste-heat fed into the first reboiler determines the number of stripping units placed in series. The lower the waste heat temperature, the less stripping columns can be used and thus the lower the thermal efficiency. In this work, the

temperature of waste heat was fixed at 80°C, as any further temperature increase has been proven to generate a negligible efficiency increase of the multi-column system. However, the increase of waste heat temperature can be useful to increase the temperature driving force for heat exchange in the reboilers, thus reducing the heat exchanger area and the relevant capital cost.

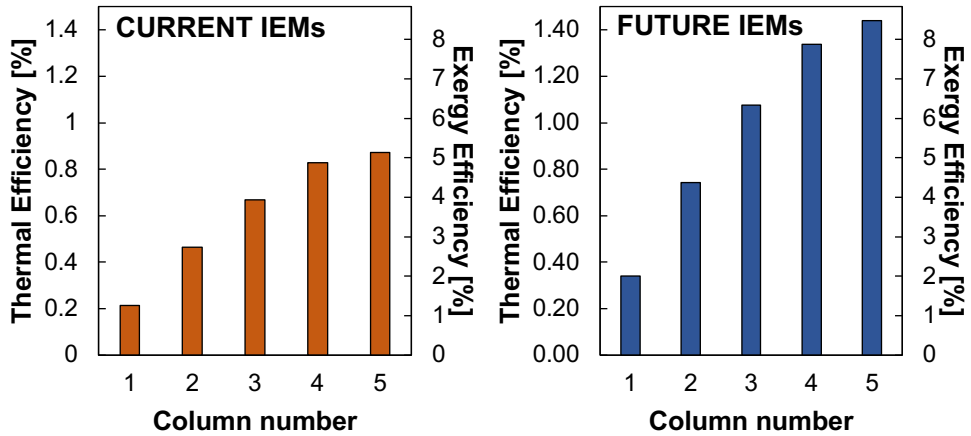


Figure 8.16 Thermal and Exergy efficiency of the t-RED HE as function of the number of stripping column adopted in the regeneration unit for current (a) and future (b) membranes. RED unit 1000 cell pairs $0.5 \times 0.5 \text{ m}^2$, $v_H = v_L = 0.5 \text{ cm/s}$, $C_H = 2M$, $C_L = 0.01M$. $T_{\text{waste-heat}} = 80^\circ\text{C}$ $T_{\text{last,column}} = 30^\circ\text{C}$.

8.4 Conclusions

In this chapter, the design, construction and operation of the first thermolytic reverse electro dialysis heat engine was presented. The thermolytic *RED-HE* consists of (i) a lab scale reverse electro dialysis unit and (ii) a thermally-driven regeneration unit made of a vapour stripping column coupled with a barometric condenser. The system stability and performance were analysed under different operating conditions via long-run tests. Experimental results have highlighted a very good stability of the process in terms of solutions properties, power generation and thermal consumption. The highest exergy efficiency computed from experimental measurements was equal to 1.1% for the case of 1.6M-0.05M ammonium bicarbonate solutions.

Furthermore, a perspective analysis was carried-out by using a purposely-developed mathematical model. To this aim, the validated Excel[®] model of the *RED* unit was coupled with the ASPEN Plus[®] model of the vapour stripping/absorption regeneration unit. After validation with experimental results, the *t-RED HE* model was used to analyse the performance of the system varying the operating conditions and system configurations. Two different scenarios, i.e. current scenario and future scenario were studied. In the current scenario, current membrane properties (i.e. Fujifilm type 10 IEMs) were considered, while in the future scenario enhanced IEM properties were taken into account. The highest exergy efficiency achieved in the current scenario is equal to 1.25% while in the future scenario the highest exergy efficiency is equal to 2%, when a simple system adopting a single stripping column is considered.

Highest efficiencies were reached by adopting a multi-stripping column regeneration unit, thanks to the higher exploitation of the external heat source. In particular, the exergy efficiency of the system is increased from 1.25% to 5.2% using 5 columns. A further increase up to 8.5% is obtainable considering enhanced future membranes.



FINAL REMARKS AND OUTLOOKS

The aim of this PhD thesis has been an in-depth study on reverse electro dialysis heat engines, providing for the first time a proof of this ground-breaking concept. To this aim, both modelling and experimental activities were carried out.

The main achievements of the research activities can be summarised as in the following:

- i. *Development of a multi-scale mathematical model for RED process.* On the basis of existing literature models, a new model for the *RED* process were developed and extensively validated against experimental results in different stack geometry and operating conditions.
- ii. *Characterization of novel solution for closed-loop applications.* Modelling and experimental activities were carried out in order to evaluate the impact of using different working solutions within the reverse electro dialysis closed-loop system.
- iii. *Conceptual development and modelling analysis of reverse electro dialysis heat engine.* New models for different *RED-HEs* were developed, validated and used to evaluate their performance and perspectives.
- iv. *Exergy analysis of reverse electro dialysis heat engines.* Exergy analysis tools were integrated in the *RED-HE* mathematical models in order to assess the rationality of the energy conversion in each unit and identify the main sources of irreversibility.
- v. *Design, construction and testing of the tRED-HE prototype.* A *tRED-HE* prototype was designed, built and tested at the University of Palermo in order to demonstrate the reverse electro dialysis closed-loop concept. This represents the first operating plant in the world for the conversion of low-grade heat into electricity using reverse electro dialysis technology.

For the above five main points, the following concluding remarks are here made.

i. Development of a multi-scale mathematical model for RED process.

The first period of this PhD thesis was dedicated to the development of a monodimensional semi-empirical mathematical model for the *RED* process, adopting a multi-scale modelling approach, considering two different scales of description: (a) a lower-scale model, describing the main phenomena involved in a single repeating unit (cell pair) and (b) a higher-scale model related to the whole system, including all cell pairs and the relevant interconnections. The model, implemented in both Engineer Equation Solver[®] and Excel[®], describes all the main phenomena involved in the process and includes: (i) thermodynamic and electrical equations, (ii) transport equations (iii) differential mass balances discretized along the solution flow path (iv) computational fluid dynamics correlations to evaluate concentration polarisation and pressure drops and (v) experimental correlations to evaluate the properties of the IEMs as a function of the concentrations of the solutions. A specific experimental campaign was carried out, during an internship at Fujifilm[®], in order to assess the average permselectivity and resistances of IEMs as a function of solution concentration, using NH_4HCO_3 .

The *RED* model was validated against experimental results for different salts (i.e. NaCl and NH_4HCO_3) and in a wide range of operating conditions, showing in all cases a good accordance with the experiments.

ii. Characterization of novel solution for closed-loop applications.

The main advantage of operating the *RED* unit in a closed-loop fashion is the possibility to select ad-hoc salt solution enhancing the process performance. The influence of the salt solutions properties on the *RED-HE* has been evaluated for the case of solvent extraction regeneration unit. Ad hoc experimental campaigns were carried out in order to characterize the behaviour of different salt-water solutions. A specific test rig was designed, built and used to evaluate osmotic and activity coefficients of salt-solutions from vapour pressure measurements, during the period at the University of Edinburgh. Novel data for caesium and potassium acetate aqueous solutions in terms of solution vapour pressure, osmotic and activity coefficients were reported, extending the range of applicability of the Pitzer's equations for both temperature, (i.e. between 20 and 90°C) and molality (i.e. 8 mol/kg), in the case of CsAc, and 9 mol/kg, in the case of KAc. On the basis of the obtained experimental results, a theoretical analysis was carried-out which has highlighted that solubility, activity and *BPE* are the three thermodynamic features mostly affecting the performance of a *RED-HE*. The higher the salt solubility, the higher the *BPE*, but the lower the partial pressure of water in

equilibrium with the solution. Thus, an optimal trade-off has to be identified between large chemical energy stored in the solution (depending on salt activity), which is released by the mixing process, and low energy requirements for the separation of the solvent for regeneration. The latter can be dramatically affected by high *BPE* where multiple-stage evaporation systems are adopted.

A theoretical analysis of the performance of an ideal *RED*-heat engine was also presented, in which a regeneration with a single stage or multi stage evaporative process is considered. Results indicate how the use of acetate salts can lead to enhanced performances with respect to NaCl solutions, thanks to higher free energy of mixing and higher solubility.

The highest thermal efficiency around 13%, corresponding to an exergy conversion efficiency of about 50%, was observed for KAc and LiCl at molality values between 15 and 17 mol/kg, though the effect of molality becomes almost negligible above 10 mol/kg. Operating at lower concentrations might lead to advantages in terms of better performance of the actual ion exchange membranes, which are known to lose significantly permselectivity when solute concentration increases above 5 e 10 M. This points to the fact that specific interactions between salt solutions-membranes can be the real controlling aspects in the performance enhancement of this technology, thus requiring a closer consideration of the most recent advances in *IEMs* technology and their future perspectives.

iii. Conceptual development and modelling analysis of reverse electro dialysis heat engines.

Reverse electro dialysis heat engines with solvent extraction regeneration units adopt thermal evaporative processes to restore the concentration of the two solutions exiting from the *RED* unit. To this aim, the main technologies proposed in the literature are membrane distillation (*MD*) and multi-effect distillation (*MED*). For each regeneration unit specific mathematical models were developed and used to carry out performance analysis and investigate the performance of such systems. In particular, a *RED-MED HE* model was developed in collaboration with the group of *CIEMAT*, coupling the *RED* model to a validated model of the *MED* process developed by *CIEMAT*. Sensitivity analyses were carried out in order to evaluate the influence of membrane properties, operating conditions and design parameters on the performance of the system. In particular, for the case of current membrane properties, the higher thermal efficiency computed optimizing the operating conditions (i.e. velocities and concentrations of the solutions) is equal to 1.4%. Assuming the adoption of

ideal membrane in the *RED* unit, the exergy and thermal efficiencies can reach values up to 31% and 6.6%, respectively.

The performance of a *RED-MD HE* lab-scale prototype were investigated by using a purposely developed mathematical model, integrating the *RED* model with correlations to evaluate the performance of commercial *MD* module provided by Aquastill®. The model was used to identify the operating conditions and the process configurations maximizing the cycle efficiency in order to drive the design of the first *RED-MD HE* prototype. Moreover, the system performances were investigated also accounting for highly performing equipment, in order to evaluate the perspectives and the room for improvements of the closed loop. As concerns the current system, exergy efficiency equal to 2.3% was achieved. Higher values can be obtained by considering improved *IEMs* and *MD* unit, resulting into an exergy efficiency of about 16.5%, which is much higher than the values reported in literature until now.

iv. *Exergy analysis of reverse electro dialysis heat engine.*

Exergy analysis represents a powerful method to identify the main sources of energy loss and quantify how much energy is effectively converted within a process. While in open-loop *RED* applications the process yield (i.e. how much energy is generated from the available salinity gradient) is the most important parameter, in closed-loop applications the exergy efficiency of salinity gradient conversion dominates the overall process efficiency. In fact, only a part of the available salinity gradient is reversibly converted into electricity, while the remaining is dissipated without producing energy, yet requiring additional effort in the regeneration stage. Exergy analysis is very useful to drive stack design and identify optimal operating conditions. In this thesis, original exergy analysis of both single *RED* process and *RED-MED HE* was carried out in order to investigate system performances in terms of exergy efficiency and power yield in a wide range of system operations. In particular, results have highlighted that phenomena often not considered in the literature as water flux and salt flux have the most detrimental effect on exergy efficiency of the *RED* process when salinity gradient above 2 M was adopted, with exergy losses (at maximum Power output conditions) accounting for 60–80% of total losses in the worst scenarios.

The effect of the main irreversibility sources on the exergy efficiency of each component but also on the whole system was investigated as a function of the resistance ratio (i.e. R_L/R_{int}) of the *RED* unit. Membrane properties strongly affect the exergy efficiency of the *RED* unit causing a reduction of the global cycle efficiency. *RED* pumping power and polarisation

phenomena have a small influence on the system efficiency. On the contrary, the number of effects and the ΔT_{exch} affect significantly the efficiency. Increasing the number of effects, the thermal power required by the *MED* unit decreases, but at the same time larger pumping power is required in the *MED* unit. The higher ΔT_{exch} , the lower the number of effects and the higher the thermal efficiency of the *MED* unit. On the other hand, low ΔT_{exch} results in a large heat exchanger area. Then, the optimal value of ΔT_{exch} should be selected based on economic aspects.

Sensitivity analysis were carried out in order to identify the effect of the inlet concentrations and velocities of the solutions to the *RED* unit on the exergy efficiency of the *RED-MED HE*, considering Fujifilm type 10 membranes and future enhanced membranes. In the current scenario, the maximum global exergy efficiency found is equal to 4.8% considering $C_H=4M$ $C_L=0.01M$ $C_H=0.2cm/s$ and $C_L=0.5cm/s$, while the future scenario exergy efficiency of 25.2% is obtained considering $C_H=4.5M$ $C_L=0.1M$ $C_H=0.2cm/s$ and $C_L=0.3cm/s$.

v. *Design, construction and testing of the tRED-HE prototype*

Reverse electrodialysis in closed-loop is a novel technology to convert low-grade heat into electricity. Promising performance have been already reported in the literature in the last years through modelling analysis showing exergy efficiency even higher than 80%. In the present PhD thesis, the first experimental assessment of the operation of a thermolytic *RED* heat engine was presented. A fully operating prototype was purposely designed and built in order to investigate the feasibility of the process. The system stability and performance were analysed under different operating conditions via long-run tests. The results collected indicate a very good stability of the process in terms of solutions properties, power generation and thermal consumption. The highest values of yield and exergy conversion efficiency were reported for the first time in the literature for *RED* units operating with thermolytic solutions. The highest exergy efficiency measured was equal to 1.1% for the case of 1.6M-0.05M ammonium bicarbonate solutions, although theoretical analysis performed using experimental validated mathematical models have highlighted that there is still room for large improvements of the whole setup, including the development of enhanced membranes suitably tailored to manage ammonium bicarbonate solutions and the design of a more efficient regeneration unit. In particular, findings of the modelling analysis have shown that the highest exergy efficiency achieved in the current scenario is equal to 1.25% while in the

future scenario the highest exergy efficiency is equal to 2%. Further, highest efficiency can be reached by adopting a multi-stage regeneration unit, thanks to the better exploitation of the external waste heat fed in the regeneration unit. The exergy efficiency of such multi-column system is increased from 1.25% to 5.2% using 5 columns. A further increase up to 8.5% is obtainable considering enhanced future membranes.

The achievement here made of the first *tRED-HE* operating prototype poses the first stone to move Loeb's idea from theory to reality.

Path-to-market

The *RED-HE* is a novel technology which is still far from immediately industrial applications. This thesis has widely contributed to the increase of the *Technological Readiness Level (TRL)* of the system up to the proof-of-the-concept level (TRL 4), although future efforts are required in order to make it competitive with other technologies. In particular, future studies should focalize on (i) the increase of the system efficiency and (ii) on the decrease of the levelized cost of electricity (LCOE). Concerning the increase of the efficiency, better performing ionic exchange membranes with high permselectivity, low electrical resistance, water and salt permeabilities especially at high concentration, have to be developed. Moreover, further studies are required in order to identify the most suitable solute-solvent couples and the optimal operating conditions including the possibility to operate the *power generation* unit at temperature higher than 25°C.

Economic analysis was performed within the framework of the *RED Heat to power* project by M. Papapetrou in his PhD thesis [192]. In particular, it has shown that the current *LCOE* is in the range of 1-2 €/kWh for the most promising scenario represented by the *RED-MED HE*. These values are far from the threshold of 0.10 €/kWh that would make the technology competitive. Notwithstanding the waste heat is for free, the current cost of ionic exchange membrane and the regeneration unit costs are the main limiting factors. Perspective analyses on the *RED-MED HE* based on economic and technological improvements, have shown that *LCOE* could be significant reduced, reaching competitive costs up to 0.10 €/kWh. Thus, future studied should be oriented on the development of new materials for both ionic exchange membranes and heat exchangers with high performance and low cost.



NOMENCLATURE

Acronyms

<i>A-SA</i>	Air Stripping/Absorption
<i>AC</i>	Alternating Current
<i>AD</i>	Adsorption Distillation
<i>AEM</i>	Anion Exchange Membrane
<i>AG-MD</i>	Air gap membrane distillation
<i>BC</i>	Base case
<i>CC</i>	Carbon Carrier
<i>CEM</i>	Cation Exchange Membrane
<i>CFD</i>	Computational Fluid Dynamics
<i>DBL</i>	Diffusion boundary layer
<i>DC</i>	Direct Current
<i>DC-MD</i>	Direct Contact Membrane Distillation
<i>E-NRTL</i>	Electrolyte - Non Random Two Liquid Model
<i>E-NRTL-RK</i>	Electrolyte - Non Random Two Liquid –Redlich Kwong Model
<i>EDL</i>	Electrical Double Layer
<i>ELCA</i>	Exergy Life Cycle Assessment
<i>FO</i>	Forward Osmosis
<i>HIGH</i>	High concentration stream or Concentrate
<i>HP</i>	High performing
<i>HT</i>	High Temperature
<i>ID</i>	Internal diameter (mm)
<i>IEM</i>	Ionic Exchange Membrane
<i>KC</i>	Kalina Cycle
<i>LCOE</i>	Levelized Cost of Electricity

<i>LGH</i>	Low Grade Heat
<i>LHS</i>	Left hand side
<i>LOW</i>	Low concentration stream or dilute
<i>LT</i>	Low Temperature
<i>MD</i>	Membrane Distillation
<i>MED</i>	Multi-Effect Distillation,
<i>MT</i>	Medium Temperature
<i>O.C.</i>	Open Circuit
<i>OHE</i>	Osmotic heat engine
<i>ORC</i>	Organic Rankine Cycle
<i>PEPG</i>	Piezo-Electric Power Generator
<i>PRO</i>	Pressure Retarded Osmosis
<i>PRO-MD HE</i>	Pressure Retarded Osmosis Membrane Distillation Heat Engine
<i>RED</i>	Reverse Electrodialysis
<i>RED-HE</i>	Reverse Electrodialysis Heat Engine
<i>RED-MD HE</i>	Reverse Electrodialysis – Membrane Distillation Heat Engine
<i>RED-MED HE</i>	Reverse Electrodialysis – Multi-Effect Distillation Heat Engine
<i>RHS</i>	Right hand side
<i>RMSE</i>	Root-mean-square error
<i>RR</i>	Recovery Ratio
<i>S.C</i>	Short Circuit
<i>SE</i>	Stirling Engine
<i>SG-MD</i>	Sweeping Gas Membrane Distillation
<i>SGE</i>	Salinity Gradient Energy
<i>SGP</i>	Salinity Gradient Power
<i>SGP-HE</i>	Salinity Gradient Power Heat Engine
<i>SRC</i>	Steam Rankine Cycle
<i>SWRO</i>	Seawater reverse osmosis
<i>t-RED HE</i>	Thermolytic Reverse Electrodialysis Heat Engine
<i>TEG</i>	Thermo-Electric Generator
<i>TRL</i>	Technological readiness level
<i>TWW</i>	Treated wastewater
<i>V-MD</i>	Vacuum Membrane Distillation

V-SA Vapour Stripping/Absorption

Symbols

a	Activity (mol/kg)
A_{cp}	Cell pair area (m ²)
A_{ϕ}	Debye-Huckel parameter
b	Width of the channel (m)
\dot{B}	Exergy stream (W)
BPE	Boiling Point Elevation (°C or K)
$b_{0i}, b_{1i}, c_i,$	fitting parameters
b_p	Universal parameter (1.2 kg ^{1/2} ·mol ^{-1/2})
C	Concentration (mol/l or mol/kg)
C_{MX}^{ϕ}	third virial coefficient
D	Diffusivity (m ² /s)
D_{eq}	Equivalent diameter (m)
E	Electrical potential (V)
\bar{e}_{ch}	Chemical specific molar flow exergy (J/mol)
E_{mix}	Exergy destruction due to uncontrolled mixing phenomena (W)
\bar{e}_{ph}	Thermomechanical specific molar flow exergy (J/mol)
\bar{e}_t	Total specific molar flow exergy (J/mol)
Ex_{cons}	Exergy consumption (W)
f	Obstruction factor
f_{Darcy}	Darcy's friction factor
f_s^0	Pure solvent fugacity (Pa or bar)
f_s	Solvent fugacity (Pa or bar)
G	Gibbs free energy (J)
g	Gravitational acceleration (m/s ²)
h	Height (m)
\bar{h}, \tilde{h}_i	Partial molar enthalpy (J/mol)
I	Electrical current (A)
$i(k)$	Electrical current in the k th branch of the circuit
I_s	ionic strength (mol/kg _{solvent})
$\dot{I}r$	Irreversibility(W)

J	Molar Flux
k	Boltzmann's constant (J/K)
L	Stack length (m)
m	Molality (mol/kg _{solvent})
MW_s	Molecular weight solvent (mol/g)
MW_{salt}	Molecular weight salt (mol/g)
N_0	Avogadro's number (kmol ⁻¹)
N_{cp}	Number of cell pair
n_{hy}	Number of hydration water molecules
N_k	Number of interval of discretization
N_{RED}^C	Number of cycles of feed solutions in the <i>RED</i> unit
N_{RED}^C	Number of cycles of feed solutions in the Stripping column
N_{stage}	Number of stage
\dot{N}	Molar flow rate (mol/s)
OCV	Open Circuit Voltage (V)
P	Membrane Permeability
p	Pressure (Pa)
$P_{condenser}$	Pumping power of cooling water
P_d	Power Density
P_{loss}	Ohmic loss in the internal resistance (W)
$P_{MED,tot}$	Total Pumping power consumption of <i>MED</i> unit (W)
$P_{pumping}$	Pumping power (W)
P_{RED}	Electrical power generated by the <i>RED</i> unit (W)
p_s^0	Pure solvent vapour pressure (Pa or bar)
p_s	Solution vapour pressure (Pa or bar)
Q	Thermal Power (W)
R	Universal Gas Constant (J/mol K)
R_{blank}	Electrode compartment resistance (Ω)
R_{cells}	Resistance of the cell pairs (Ω)
R_{ext}	Stack resistance (Ω)
R_{sol}	Electrical resistance of the solution (Ω)
Re	Reynolds number
\tilde{S}_i	Partial molar entropy (J/mol K)

SAF	Specific air-flowrate (m^3/mol)
Sc	Smidth number
SE	Specific energy (J/m^3 or kWh/m^3)
Sh	Sharwood number
SME	Specific Gibbs free energy of mixing (kJ/m^3 or kWh/m^3)
STC	Specific Thermal Consumption (kWh/m^3 of distillate)
T	Temperature (K or $^{\circ}C$)
t	Transport number
T_c	Critical temperature (K)
t_{RED}	Residence time of solution in the <i>RED</i> unit [min or h]
t_{REG}	Residence time of solution in the stripping column [min or h]
t_{test}	Duration of the long run test (min)
TEC	Thermal energy consumption (J)
t_{MD}	<i>MD</i> working time (h)
TPC	Thermal Power Consumption (W)
t_{RED}	<i>RED</i> working time (h)
V	Volume (m^3 or l)
\dot{V}	Volumetric flow rate (m^3/s or l/s)
\bar{V}	Partial molar volume (m^3/mol)
v	Velocity (m/s)
W	Electric Power (W)
w	Mass of the solution (kg)
x	Molar fraction
Y	Yield of the process
z	Number of charge
TEC	Thermal energy consumption (J)
t_{MD}	<i>MD</i> working time (h)
TPC	Thermal Power Consumption (W)
t_{RED}	<i>RED</i> working time (h)
V	Volume (m^3 or l)
v	Velocity (m/s)
W	Electric Power (W)
w	Mass of the solution (kg)

x	Molar fraction
α	Membrane Permselectivity
α_p	numerical constant
$\beta_{MX}^{(0)}$	Second virial coefficient
$\beta_{MX}^{(1)}$	Second virial coefficient
δ	Thickness
ΔE	Electrical potential difference (V)
ΔG_{mix}	Gibbs free energy of mixing (J/mol)
$\Delta \dot{G}_{mix}$	Gibbs free power of mixing (W/mol)
$\Delta n_{NH_4HCO_3}$	molar flow rate variation of ammonium bicarbonate (mol/s)
Δp	Pressure drop (Pa)
ΔT_{exch}	Driving force in the heat exchanger ($^{\circ}C$ or K)
Δx	Discretization length (m)
$\Delta \varphi_{Don}$	Donnan potential difference (V)
$\Delta \varphi_{diff}$	Diffusion potential (V)
$\Delta \pi$	Osmotic pressure difference (Pa)
ϵ_0	Permittivity of free space ($F \cdot m^{-1}$)
η	Efficiency
η_P	Pump efficiency
λ_{ev}	solvent's latent heat of evaporation (kJ/kg)
Λ	Specific molar conductivity (mS/(cm (mol/l)))
μ	Chemical potential (J/mol)
ν	number of ions
ρ	Density (kg/m^3 or g/l)
σ	Solution Conductivity (mS/cm)
φ	Electrical potential (V)
ϕ	Osmotic coefficient
θ	Polarisation coefficient
$\%R$	Removal efficiency (%)

Subscripts

-	Anion
---	-------

\pm	Average between cation and anion
ϕ	Osmotic coefficient
+	Cation
<i>A</i>	Anion
<i>av</i>	Average
<i>B</i>	Bulk
<i>C</i>	Cation
<i>cold</i>	Cold temperature
<i>corr</i>	Corrected value
<i>counter</i>	Counter-ion
<i>cp</i>	Cell pair
<i>cw</i>	Cooling water
<i>D</i>	Distillate
<i>diff</i>	Diffusive
<i>eosm</i>	Electro-osmotic
<i>ev</i>	Boiling
<i>exp</i>	Measured
<i>H</i>	High solution or Concentrate solution
<i>hot</i>	Hot temperature
<i>i</i>	Generic specie
<i>in</i>	Inlet
<i>k</i>	Number of effects
<i>L</i>	Low solution or Dilute solution
<i>lim</i>	Limiting
<i>m</i>	Membrane
<i>max</i>	Maximum value
<i>MD</i>	Membrane Distillation
<i>MED</i>	Multi-Effect Distillation
<i>mig</i>	Migrative
<i>mix</i>	Mixing solution
<i>multi</i>	Multi-effect
<i>MX</i>	Generic salt
<i>n</i>	Normal

<i>net</i>	Net
<i>out</i>	Outlet
<i>pure</i>	Pure
<i>RED</i>	Reverse Electrodialysis
<i>ref</i>	reference
<i>reg</i>	Regeneration unit
<i>s</i>	solvent
<i>salt</i>	Salt
<i>single</i>	Single effect
<i>sol</i>	Solution
<i>stack</i>	Whole stack
<i>theo</i>	Theoretical
<i>tRED-HE</i>	Thermolytic RED-HE
<i>vap</i>	Vapour
<i>w</i>	Water
<i>wh</i>	Waste heat
γ	Activity coefficient
<i>C</i>	Carnot
<i>IEM</i>	Ionic Exchange Membrane
<i>ex</i>	Exergy
<i>th</i>	Thermal
<i>0</i>	Equilibrium conditions

Superscripts

*	Restricted dead state
<i>0</i>	Standard state
<i>AEM</i>	Anionic Exchange Membrane
<i>CEM</i>	Cationic Exchange Membrane
<i>cond</i>	Condensing
<i>diff</i>	Diffusive
<i>eb</i>	Boiling
<i>in</i>	Inlet
<i>L</i>	Left side

<i>out</i>	Outlet
R	Right side
γ	Activity coefficient
<i>IEM</i>	Ionic Exchange Membrane
<i>SOL</i>	Solution
<i>th</i>	Thermal

 **REFERENCES**

- [1] R.E. Pattle, Production of Electric Power by mixing Fresh and Salt Water in the Hydroelectric Pile, *Nature*. 174 (1954) 660–660. doi:10.1038/174660a0.
- [2] F. Helfer, C. Lemckert, Y.G. Anissimov, Osmotic power with Pressure Retarded Osmosis: Theory, performance and trends - A review, *J. Memb. Sci.* 453 (2014) 337–358. doi:10.1016/j.memsci.2013.10.053.
- [3] A. Cipollina, G. Micale, Sustainable energy from salinity gradients, Elsevier Ltd, 2016. doi:10.1016/C2014-0-03709-4.
- [4] F. Giacalone, A. Cipollina, F. Grisafi, A. Tamburini, G. Vella, G. Micale, Characterization of pressure retarded osmosis lab-scale systems, *Desalin. Water Treat.* 57 (2016) 22994–23006. doi:10.1080/19443994.2016.1173379.
- [5] A. Achilli, K.L. Hickenbottom, 3 – Pressure retarded osmosis: Applications, in: *Sustain. Energy from Salin. Gradients*, 2016: pp. 55–75. doi:10.1016/B978-0-08-100312-1.00003-1.
- [6] J. Veerman, Reverse Electrodialysis design and optimization by modeling and experimentation (Doctoral dissertation), University of Groningen, (Groningen), 2010.
- [7] D.A. Vermaas, Energy Generation from Mixing Salt Water and River Water (PhD thesis), University of Twente, The Netherlands, 2014.
- [8] B. Inc, Waste Heat Recovery: Technology Opportunities in the US Industry, *Waste Heat Recover. Technol. Oppor. US Ind.* (2008) 1–112. doi:10.1017/CBO9781107415324.004.
- [9] D.B. Gingerich, M.S. Mauter, Quantity, Quality, and Availability of Waste Heat from United States Thermal Power Generation, *Environ. Sci. Technol.* 49 (2015) 8297–8306. doi:10.1021/es5060989.
- [10] R. Law, A. Harvey, D. Reay, Opportunities for low-grade heat recovery in the UK food processing industry, *Appl. Therm. Eng.* 53 (2013) 188–196. doi:10.1016/j.applthermaleng.2012.03.024.
- [11] R. Law, A. Harvey, D. Reay, A knowledge-based system for low-grade waste heat recovery in the process industries, 94 (2016) 590–599. doi:10.1016/j.applthermaleng.2015.10.103.
- [12] M. Papapetrou, G. Kosmadakis, A. Cipollina, U. LaCommare, G. Micalea, Industrial waste heat: Estimation of the technically available resource in the EU per industrial sector, temperature level and country, *Appl. Therm. Eng.* 138 (2018) 207–216. doi:10.1016/j.applthermaleng.2018.04.043.
- [13] S. Brückner, S. Liu, L. Miró, M. Radspieler, L.F. Cabeza, E. Lävemann, Industrial waste heat recovery technologies: An economic analysis of heat transformation technologies, *Appl. Energy.* 151 (2015) 157–167. doi:10.1016/j.apenergy.2015.01.147.
- [14] X. Zhang, M. He, Y. Zhang, A review of research on the Kalina cycle, *Renew.*

- Sustain. Energy Rev. 16 (2012) 5309–5318. doi:10.1016/j.rser.2012.05.040.
- [15] W. Sun, X. Yue, Y. Wang, Exergy efficiency analysis of ORC (Organic Rankine Cycle) and ORC-based combined cycles driven by low-temperature waste heat, *Energy Convers. Manag.* 135 (2017) 63–73. doi:10.1016/j.enconman.2016.12.042.
- [16] S. Karellas, A.-D. Leontaritis, G. Panousis, E. Bellos, E. Kakaras, Energetic and exergetic analysis of waste heat recovery systems in the cement industry, *Energy*. 58 (2013) 147–156. doi:10.1016/j.energy.2013.03.097.
- [17] W. He, S. Wang, L. Yue, High net power output analysis with changes in exhaust temperature in a thermoelectric generator system, *Appl. Energy*. 196 (2017) 259–267. doi:10.1016/j.apenergy.2016.12.078.
- [18] J. Karthausser, Energy generation from Waste Heat using the Carbon Carrier Thermodynamic Cycle, United States Patent Application 20160201521, 2016.
- [19] A. Tamburini, M. Tedesco, A. Cipollina, G. Micale, M. Ciofalo, M. Papapetrou, W. Van Baak, A. Piacentino, Reverse electro dialysis heat engine for sustainable power production, *Appl. Energy*. 206 (2017) 1334–1353. doi:10.1016/j.apenergy.2017.10.008.
- [20] A. Tamburini, A. Cipollina, M. Papapetrou, A. Piacentino, G. Micale, 7 – Salinity gradient engines, in: *Sustain. Energy from Salin. Gradients*, 2016: pp. 219–256. doi:10.1016/B978-0-08-100312-1.00007-9.
- [21] H.T. El-Dessouky, H.M. Ettouney, *Fundamentals of Salt Water Desalination*, Elsevier, 2002. doi:10.1016/B978-044450810-2/50008-7.
- [22] A. Cipollina, G. Micale, L. Rizzuti, *Seawater Desalination*, Springer Berlin Heidelberg, Berlin, Heidelberg, 2009. doi:10.1007/978-3-642-01150-4.
- [23] E. Curcio, E. Drioli, Membrane Distillation and Related Operations—A Review, *Sep. Purif. Rev.* 34 (2005) 35–86. doi:10.1081/SPM-200054951.
- [24] C. Olkis, G. Santori, S. Brandani, An Adsorption Reverse Electro dialysis system for the generation of electricity from low-grade heat, *Appl. Energy*. 231 (2018) 222–234. doi:10.1016/j.apenergy.2018.09.112.
- [25] Y. Cai, X.M. Hu, A critical review on draw solutes development for forward osmosis, *Desalination*. 391 (2016) 16–29. doi:10.1016/j.desal.2016.03.021.
- [26] D. Li, H. Wang, Smart draw agents for emerging forward osmosis application, *J. Mater. Chem. A*. 1 (2013) 14049–14060. doi:10.1039/c3ta12559a.
- [27] R.A. Neff, Solvent Extractor, US Patent 3130156, 1964.
- [28] G. Han, Q. Ge, T.S. Chung, Conceptual demonstration of novel closed-loop pressure retarded osmosis process for sustainable osmotic energy generation, *Appl. Energy*. 132 (2014) 383–393. doi:10.1016/j.apenergy.2014.07.029.
- [29] F.J. Arias, On osmotic heat engines driven by thermal precipitation-dissolution of saturated aqueous solutions, *Int. J. Therm. Sci.* 133 (2018) 151–161. doi:10.1016/j.ijthermalsci.2018.07.024.
- [30] S. Loeb, Method and apparatus for generating power utilizing Pressure-Retarded-Osmosis, US Patent 3906250, 1974.
- [31] S. Loeb, Method and apparatus for generating power utilizing Reverse Electro dialysis, US Patent 4171409, 1978.
- [32] R.L. McGinnis, J.R. McCutcheon, M. Elimelech, A novel ammonia–carbon dioxide osmotic heat engine for power generation, *J. Memb. Sci.* 305 (2007) 13–19. doi:10.1016/j.memsci.2007.08.027.
- [33] X. Luo, X. Cao, Y. Mo, K. Xiao, X. Zhang, P. Liang, X. Huang, Power generation by coupling reverse electro dialysis and ammonium bicarbonate: Implication for recovery of waste heat, *Electrochem. Commun.* 19 (2012) 25–28.

- doi:10.1016/j.elecom.2012.03.004.
- [34] R.D. Cusick, Y. Kim, B.E. Logan, Energy Capture from Thermolytic Solutions in Microbial Reverse-Electrodialysis Cells, *Science* (80-.). 335 (2012) 1474–1477. doi:10.1126/science.1219330.
- [35] B.E. Logan, M. Elimelech, Membrane-based processes for sustainable power generation using water, *Nature*. 488 (2012) 313–319. doi:10.1038/nature11477.
- [36] E. Shaulsky, C. Boo, S. Lin, M. Elimelech, Membrane-based osmotic heat engine with organic solvent for enhanced power generation from low-grade heat, *Environ. Sci. Technol.* 49 (2015) 5820–5827. doi:10.1021/es506347j.
- [37] K. Kwon, B.H. Park, D.H. Kim, D. Kim, Parametric study of reverse electrodialysis using ammonium bicarbonate solution for low-grade waste heat recovery, *Energy Convers. Manag.* 103 (2015) 104–110. doi:10.1016/j.enconman.2015.06.051.
- [38] M. Bevacqua, A. Carubia, A. Cipollina, A. Tamburini, M. Tedesco, G. Micale, Performance of a RED system with ammonium hydrogen carbonate solutions, *Desalin. Water Treat.* 57 (2016) 23007–23018. doi:10.1080/19443994.2015.1126410.
- [39] R. Long, B. Li, Z. Liu, W. Liu, Hybrid membrane distillation-reverse electrodialysis electricity generation system to harvest low-grade thermal energy, *J. Memb. Sci.* 525 (2017) 107–115. doi:10.1016/j.memsci.2016.10.035.
- [40] K.L. Hickenbottom, J. Vanneste, T.Y. Cath, Assessment of alternative draw solutions for optimized performance of a closed-loop osmotic heat engine, *J. Memb. Sci.* 504 (2016) 162–175. doi:10.1016/j.memsci.2016.01.001.
- [41] D. Han, B. Ho, K. Kwon, L. Li, D. Kim, Modeling of power generation with thermolytic reverse electrodialysis for low-grade waste heat recovery, *Appl. Energy*. 189 (2017) 201–210. doi:10.1016/j.apenergy.2016.10.060.
- [42] M. Bevacqua, A. Tamburini, M. Papapetrou, A. Cipollina, G. Micale, A. Piacentino, Reverse electrodialysis with NH_4HCO_3 -water systems for heat-to-power conversion, *Energy*. 137 (2017) 1293–1307. doi:10.1016/j.energy.2017.07.012.
- [43] K.L. Hickenbottom, J. Vanneste, L. Miller-Robbie, A. Deshmukh, M. Elimelech, M.B. Heeley, T.Y. Cath, Techno-economic assessment of a closed-loop osmotic heat engine, *J. Memb. Sci.* 535 (2017) 178–187. doi:10.1016/j.memsci.2017.04.034.
- [44] J. Hu, S. Xu, X. Wu, D. Wu, D. Jin, P. Wang, Q. Leng, Theoretical simulation and evaluation for the performance of the hybrid multi-effect distillation — reverse electrodialysis power generation system, 443 (2018) 172–183. doi:10.1016/j.desal.2018.06.001.
- [45] J.N. Weinstein, F.B. Leitz, Electric Power from Differences in Salinity: The Dialytic Battery, *Science* (80-.). 191 (1976) 557–559. doi:10.1126/science.191.4227.557.
- [46] R. Audinos, Electrodialyse inverse. Etude de l'énergie électrique obtenue a partir de deux solutions de salinités différentes, *J. Power Sources*. 10 (1983) 203–217. doi:10.1016/0378-7753(83)80077-9.
- [47] J. Jagur-Grodzinski, R. Kramer, Novel process for direct conversion of free energy of mixing into electric power, *Ind. Eng. Chem. Process Des. Dev.* 25 (1986) 443–449. doi:10.1021/i200033a016.
- [48] J. Veerman, M. Saakes, S.J. Metz, G.J. Harmsen, Reverse electrodialysis: Performance of a stack with 50 cells on the mixing of sea and river water, *J. Memb. Sci.* 327 (2009) 136–144. doi:10.1016/j.memsci.2008.11.015.
- [49] D.A. Vermaas, M. Saakes, K. Nijmeijer, Doubled power density from salinity gradients at reduced intermembrane distance, *Environ. Sci. Technol.* 45 (2011) 7089–7095. doi:10.1021/es2012758.

- [50] P. Długołęcki, A. Gambier, K. Nijmeijer, M. Wessling, Practical Potential of Reverse Electrodialysis As Process for Sustainable Energy Generation, *Environ. Sci. Technol.* 43 (2009) 6888–6894. doi:10.1021/es9009635.
- [51] M. Tedesco, C. Scalici, D. Vaccari, A. Cipollina, A. Tamburini, G. Micale, Performance of the first reverse electrodialysis pilot plant for power production from saline waters and concentrated brines, *J. Memb. Sci.* 500 (2016) 33–45. doi:10.1016/j.memsci.2015.10.057.
- [52] L. Gurreri, A. Tamburini, A. Cipollina, G. Micale, CFD analysis of the fluid flow behavior in a reverse electrodialysis stack, 48 (2012) 390–403. doi:10.1080/19443994.2012.705966.
- [53] O. Scialdone, C. Guarisco, S. Grispo, A.D. Angelo, A. Galia, Investigation of electrode material – Redox couple systems for reverse electrodialysis processes. Part I: Iron redox couples, *J. Electroanal. Chem.* 681 (2012) 66–75. doi:10.1016/j.jelechem.2012.05.017.
- [54] P. Długołęcki, P. Ogonowski, S.J. Metz, M. Saakes, K. Nijmeijer, M. Wessling, On the resistances of membrane, diffusion boundary layer and double layer in ion exchange membrane transport, *J. Memb. Sci.* 349 (2010) 369–379. doi:10.1016/j.memsci.2009.11.069.
- [55] A.B. Yaroslavtsev, V. V. Nikonenko, Ion-exchange membrane materials: Properties, modification, and practical application, *Nanotechnologies Russ.* 4 (2009) 137–159. doi:10.1134/S199507800903001X.
- [56] N.P. Berezina, N.A. Kononenko, O.A. Dyomina, N.P. Gnusin, Characterization of ion-exchange membrane materials: Properties vs structure, 139 (2008) 3–28. doi:10.1016/j.cis.2008.01.002.
- [57] H.J. Cassidy, E.C. Cimino, M. Kumar, M.A. Hickner, Specific ion effects on the permselectivity of sulfonated poly(ether sulfone) cation exchange membranes, *J. Memb. Sci.* 508 (2016) 146–152. doi:10.1016/j.memsci.2016.02.048.
- [58] G.M. Geise, H.J. Cassidy, D.R. Paul, B.E. Logan, M.A. Hickner, E. Logan, M.A. Hickner, Specific ion effects on membrane potential and the permselectivity of ion exchange membranes, *Phys. Chem. Chem. Phys.* 16 (2014) 21673–21681. doi:10.1039/C4CP03076A.
- [59] A. Daniilidis, D.A. Vermaas, R. Herber, K. Nijmeijer, Experimentally obtainable energy from mixing river water, seawater or brines with reverse electrodialysis, *Renew. Energy.* 64 (2014) 123–131. doi:10.1016/j.renene.2013.11.001.
- [60] M. Tedesco, A. Cipollina, A. Tamburini, G. Micale, Towards 1 kW power production in a reverse electrodialysis pilot plant with saline waters and concentrated brines, *J. Memb. Sci.* 522 (2017) 226–236. doi:10.1016/j.memsci.2016.09.015.
- [61] R.S. Kingsbury, K. Chu, O. Coronell, Energy storage by reversible electrodialysis: The concentration battery, *J. Memb. Sci.* 495 (2015) 502–516. doi:https://doi.org/10.1016/j.memsci.2015.06.050.
- [62] W.J. van Egmond, U.K. Starke, M. Saakes, C.J.N. Buisman, H.V.M. Hamelers, Energy efficiency of a concentration gradient flow battery at elevated temperatures, *J. Power Sources.* 340 (2017) 71–79. doi:https://doi.org/10.1016/j.jpowsour.2016.11.043.
- [63] Baobab Project: Blue Acid/Base Battery: Storage and recovery of renewable electrical energy by reversible salt water dissociation. European H200 project. Contract n° 73118, (2017).
- [64] M. Tedesco, A. Cipollina, A. Tamburini, I.D.L. Bogle, G. Micale, A simulation tool for analysis and design of reverse electrodialysis using concentrated brines, *Chem.*

- Eng. Res. Des. 93 (2015) 441–456. doi:10.1016/j.cherd.2014.05.009.
- [65] J. Veerman, M. Saakes, S.J. Metz, G.J. Harmsen, Reverse electro dialysis: A validated process model for design and optimization, *Chem. Eng. J.* 166 (2011) 256–268. doi:10.1016/j.cej.2010.10.071.
- [66] N.Y. Yip, M. Elimelech, Thermodynamic and energy efficiency analysis of power generation from natural salinity gradients by pressure retarded osmosis, *Environ. Sci. Technol.* 46 (2012) 5230–5239. doi:10.1021/es300060m.
- [67] G. Belfort, G.A. Guter, An experimental study of electro dialysis hydrodynamics, *Desalination*. 10 (1972) 221–262. doi:10.1016/S0011-9164(00)82001-9.
- [68] Y. Winograd, A. Solan, M. Toren, Mass transfer in narrow channels in the presence of turbulence promoters, *Desalination*. 13 (1973) 171–186. doi:10.1016/S0011-9164(00)82043-3.
- [69] J.-M. Chiapello, M. Bernard, Improved spacer design and cost reduction in an electro dialysis system, *J. Memb. Sci.* 80 (1993) 251–256. doi:10.1016/0376-7388(93)85149-Q.
- [70] J. Balster, I. Pünt, D.F. Stamatialis, M. Wessling, Multi-layer spacer geometries with improved mass transport, *J. Memb. Sci.* 282 (2006) 351–361. doi:10.1016/j.memsci.2006.05.039.
- [71] A. Campione, L. Gurreri, M. Ciofalo, G. Micale, A. Tamburini, A. Cipollina, Electro dialysis for water desalination: A critical assessment of recent developments on process fundamentals, models and applications, *Desalination*. 434 (2018) 121–160. doi:10.1016/j.desal.2017.12.044.
- [72] H. Strathmann, *Ion-Exchange Membrane Separation Processes*, Balaban Desalination Publications, 2016. doi:10.1016/j.seppur.2004.05.007.
- [73] J. Veerman, D.A. Vermaas, 4 – Reverse electro dialysis: Fundamentals, in: *Sustain. Energy from Salin. Gradients*, 2016: pp. 77–133. doi:10.1016/B978-0-08-100312-1.00004-3.
- [74] R. Ashu, S. Pawlowski, J. Veerman, K. Bouzek, E. Fontananova, S. Velizarov, J. Goulão, K. Nijmeijer, E. Curcio, Progress and prospects in reverse electro dialysis for salinity gradient energy conversion and storage, 225 (2018) 290–331. doi:10.1016/j.apenergy.2018.04.111.
- [75] T. Xu, K. Hu, A simple determination of counter-ionic permselectivity in an ion exchange membrane from bi-ionic membrane potential measurements: Permselectivity of anionic species in a novel anion exchange membrane, *Sep. Purif. Technol.* 40 (2004) 231–236. doi:10.1016/j.seppur.2004.03.002.
- [76] S. Zhu, R.S. Kingsbury, D.F. Call, O. Coronell, Impact of solution composition on the resistance of ion exchange membranes, *J. Memb. Sci.* 554 (2018) 39–47. doi:10.1016/j.memsci.2018.02.050.
- [77] X. Tuan, Concentration polarization and conductance of cation exchange membranes in sulfuric acid and alkaline sulfate media, *J. Memb. Sci.* 397–398 (2012) 66–79. doi:10.1016/j.memsci.2012.01.011.
- [78] X. Zhu, W. He, B.E. Logan, Influence of solution concentration and salt types on the performance of reverse electro dialysis cells, *J. Memb. Sci.* 494 (2015) 154–160. doi:10.1016/j.memsci.2015.07.053.
- [79] A.H. Galama, N.A. Hoog, D.R. Yntema, Method for determining ion exchange membrane resistance for electro dialysis systems, *Desalination*. 380 (2016) 1–11. doi:10.1016/j.desal.2015.11.018.
- [80] A.H. Galama, D.A. Vermaas, J. Veerman, M. Saakes, H.H.M. Rijnaarts, J.W. Post, K. Nijmeijer, Membrane resistance: The effect of salinity gradients over a cation

- exchange membrane, *J. Memb. Sci.* 467 (2014) 279–291. doi:10.1016/j.memsci.2014.05.046.
- [81] A.M. Benneker, T. Rijnaarts, R.G.H. Lammertink, J.A. Wood, Effect of temperature gradients in (reverse) electro dialysis in the Ohmic regime, *J. Memb. Sci.* 548 (2018) 421–428. doi:10.1016/j.memsci.2017.11.029.
- [82] R.W. Baker, 2 Membrane Transport Theory, in: *Membr. Technol. Appl.*, 2004: pp. 15–87. doi:10.1002/0470020393.ch2.
- [83] L. Gurreri, M. Ciofalo, A. Cipollina, A. Tamburini, W. Van Baak, G. Micale, CFD modelling of profiled-membrane channels for reverse electro dialysis, *Desalin. Water Treat.* 55 (2015) 3404–3423. doi:10.1080/19443994.2014.940651.
- [84] L. Gurreri, A. Tamburini, A. Cipollina, G. Micale, M. Ciofalo, CFD prediction of concentration polarization phenomena in spacer-filled channels for reverse electro dialysis, *J. Memb. Sci.* 468 (2014) 133–148. doi:10.1016/j.memsci.2014.05.058.
- [85] A. Cipollina, G. Micale, A. Tamburini, M. Tedesco, L. Gurreri, J. Veerman, S. Grasman, 5 – Reverse electro dialysis: Applications, in: *Sustain. Energy from Salin. Gradients*, 2016: pp. 135–180. doi:10.1016/B978-0-08-100312-1.00005-5.
- [86] L. Gurreri, A. Tamburini, A. Cipollina, G. Micale, M. Ciofalo, Flow and mass transfer in spacer-filled channels for reverse electro dialysis: a CFD parametrical study, *J. Memb. Sci.* 497 (2016) 300–317. doi:10.1016/j.memsci.2015.09.006.
- [87] L. Gurreri, A. Tamburini, A. Cipollina, G. Micale, M. Ciofalo, Pressure drop at low Reynolds numbers in woven-spacer-filled channels for membrane processes: CFD prediction and experimental validation, 61 (2017) 170–182. doi:10.5004/dwt.2016.11279.
- [88] M. Tedesco, E. Brauns, A. Cipollina, G. Micale, P. Modica, G. Russo, J. Helsen, Reverse electro dialysis with saline waters and concentrated brines: A laboratory investigation towards technology scale-up, *J. Memb. Sci.* 492 (2015) 9–20. doi:10.1016/j.memsci.2015.05.020.
- [89] L. Gurreri, A. Tamburini, A. Cipollina, G. Micale, M. Ciofalo, CFD simulation of mass transfer phenomena in spacer filled channels for reverse electro dialysis applications, *Chem. Eng. Trans.* 32 (2013) 1879–1884. doi:10.3303/CET1332314.
- [90] S. Pawlowski, V. Geraldes, J.G. Crespo, S. Velizarov, Computational fluid dynamics (CFD) assisted analysis of profiled membranes performance in reverse electro dialysis, 502 (2016) 179–190. doi:10.1016/j.memsci.2015.11.031.
- [91] F. Li, W. Meindersma, A.B. De Haan, T. Reith, Optimization of commercial net spacers in spiral wound membrane modules, 208 (2002) 289–302.
- [92] M.L. La Cerva, M. Di Liberto, L. Gurreri, A. Tamburini, A. Cipollina, G. Micale, M. Ciofalo, Coupling CFD with a one-dimensional model to predict the performance of reverse electro dialysis stacks, *J. Memb. Sci.* 541 (2017) 595–610. doi:10.1016/j.memsci.2017.07.030.
- [93] M. Micari, M. Bevacqua, A. Cipollina, A. Tamburini, W. Van Baak, T. Putts, G. Micale, Effect of different aqueous solutions of pure salts and salt mixtures in reverse electro dialysis systems for closed-loop applications, *J. Memb. Sci.* 551 (2018) 315–325. doi:10.1016/j.memsci.2018.01.036.
- [94] T. J. Kotas, *The exergy method of thermal plant analysis*, Butterworths, 1985. doi:10.1016/S0140-7007(97)85546-6.
- [95] E. Sciubba, Enrico, A Critical Interpretation and Quantitative Extension of the Sama-Szargut Second Law Rules in an Extended Exergy Perspective, *Energies.* 7 (2014) 5357–5373. doi:10.3390/en7085357.

- [96] F. Ranjbar, A. Chitsaz, S.M.S. Mahmoudi, S. Khalilarya, M.A. Rosen, Energy and exergy assessments of a novel trigeneration system based on a solid oxide fuel cell, *Energy Convers. Manag.* 87 (2014) 318–327. doi:10.1016/j.enconman.2014.07.014.
- [97] A. Vatani, M. Mehrpooya, A. Palizdar, Advanced exergetic analysis of five natural gas liquefaction processes, *Energy Convers. Manag.* 78 (2014) 720–737. doi:10.1016/j.enconman.2013.11.050.
- [98] W.J. Kostowski, J. Kalina, P. Bargiel, P. Szufleński, Energy and exergy recovery in a natural gas compressor station - A technical and economic analysis, *Energy Convers. Manag.* 104 (2015) 17–31. doi:10.1016/j.enconman.2015.07.002.
- [99] A. Noroozian, A. Mohammadi, M. Bidi, M.H. Ahmadi, Energy, exergy and economic analyses of a novel system to recover waste heat and water in steam power plants, *Energy Convers. Manag.* 144 (2017) 351–360. doi:https://doi.org/10.1016/j.enconman.2017.04.067.
- [100] L. Marletta, Luigi, Air Conditioning Systems from a 2nd Law Perspective, *Entropy*. 12 (2010) 859–877. doi:10.3390/e12040859.
- [101] N. Jain, A. Alleyne, Exergy-based optimal control of a vapor compression system, *Energy Convers. Manag.* 92 (2015) 353–365. doi:10.1016/j.enconman.2014.12.014.
- [102] B.A. Qureshi, S.M. Zubair, Exergetic efficiency of NF, RO and EDR desalination plants, *Desalination*. 378 (2016) 92–99. doi:10.1016/j.desal.2015.09.027.
- [103] B.A. Qureshi, S.M. Zubair, Exergy and sensitivity analysis of electro dialysis reversal desalination plants, *Desalination*. 394 (2016) 195–203. doi:10.1016/j.desal.2016.05.015.
- [104] N. Kahraman, Y. A. Cengel, Exergy analysis of a MSF distillation plant, *Energy Convers. Manag.* 46 (2005) 2625–2636. doi:10.1016/j.enconman.2004.11.009.
- [105] A. Piacentino, Application of advanced thermodynamics, thermoeconomics and exergy costing to a Multiple Effect Distillation plant: In-depth analysis of cost formation process, *Desalination*. 371 (2015). doi:10.1016/j.desal.2015.06.008.
- [106] C.A. Frangopoulos, Exergy, Energy System Analysis and Optimization - Volume I: Exergy and Thermodynamic Analysis, EOLSS Publications, 2009.
- [107] A. Valero, C.T. Cuadra, Thermoeconomic Analysis, in: C. Frangopoulos (Ed.), Exergy, Energy Syst. Anal. Optim., Oxford: EOLSS Publishers, 2004.
- [108] V. Verda, M. Caccin, A. Kona, Thermoeconomic cost assessment in future district heating networks, *Energy*. 117 (2016) 485–491. doi:https://doi.org/10.1016/j.energy.2016.07.016.
- [109] A. Piacentino, F. Cardona, On thermoeconomics of energy systems at variable load conditions : Integrated optimization of plant design and operation, 48 (2007) 2341–2355. doi:10.1016/j.enconman.2007.03.002.
- [110] A. Valero, L. Serra, J. Royo, Structural theory and thermoeconomic diagnosis Part I. On malfunction and dysfunction analysis, 43 (2002) 1503–1518.
- [111] J. Szargut, A. Ziębik, W. Stanek, Depletion of the non-renewable natural exergy resources as a measure of the ecological cost, *Energy Convers. Manag.* 43 (2002) 1149–1163. doi:https://doi.org/10.1016/S0196-8904(02)00005-5.
- [112] R.L. Cornelissen, G.G. Hirs, The value of the exergetic life cycle assessment besides the LCA, *Energy Convers. Manag.* 43 (2002) 1417–1424. doi:10.1016/S0196-8904(02)00025-0.
- [113] M.V. Rocco, Primary exergy cost of goods and services : an input-output approach, Springer, 2016.
- [114] M. V Rocco, A. Di Lucchio, E. Colombo, Exergy Life Cycle Assessment of electricity production from Waste-to-Energy technology: A Hybrid Input-Output approach,

- Appl. Energy. 194 (2017) 832–844. doi:<https://doi.org/10.1016/j.apenergy.2016.11.059>.
- [115] J. Veerman, R.M. de Jong, M. Saakes, S.J. Metz, G.J. Harmsen, Reverse electro dialysis: Comparison of six commercial membrane pairs on the thermodynamic efficiency and power density, *J. Memb. Sci.* 343 (2009) 7–15. doi:10.1016/j.memsci.2009.05.047.
- [116] N.Y. Yip, D.A. Vermaas, K. Nijmeijer, M. Elimelech, Thermodynamic, energy efficiency, and power density analysis of reverse electro dialysis power generation with natural salinity gradients, *Environ. Sci. Technol.* 48 (2014) 4925–4936. doi:10.1021/es5005413.
- [117] D.A. Vermaas, J. Veerman, N.Y. Yip, M. Elimelech, M. Saakes, K. Nijmeijer, High efficiency in energy generation from salinity gradients with reverse electro dialysis, *ACS Sustain. Chem. Eng.* 1 (2013) 1295–1302. doi:10.1021/sc400150w.
- [118] A. Bejan, *Advanced engineering thermodynamics*, J. Wiley & Sons, 1997. <https://books.google.co.uk/books?id=D-NSAAAAMAAJ>.
- [119] J. Szargut, *Exergy Method: Technical and Ecological Applications.*, UK: WIT Press, 2005.
- [120] K.S. Pitzer, *Activity coefficients in electrolyte solutions*, CRC Press, Boca Raton, 1991.
- [121] S. Covelli, J. Faganeli, M. Horvat, A. Brambati, Mercury contamination of coastal sediments as the result of long-term cinnabar mining activity (Gulf of Trieste, northern Adriatic sea), *Appl. Geochemistry.* 16 (2001) 541–558. doi:10.1016/S0883-2927(00)00042-1.
- [122] C. Marchina, G. Bianchini, C. Natali, M. Pennisi, N. Colombani, R. Tassinari, K. Knoeller, The Po river water from the Alps to the Adriatic Sea (Italy): new insights from geochemical and isotopic ($\delta^{18}\text{O}$ - δD) data, *Environ. Sci. Pollut. Res.* 22 (2015) 5184–5203. doi:10.1007/s11356-014-3750-6.
- [123] J.F. Ternon, C. Oudot, A. Dessier, D. Diverres, A seasonal tropical sink for atmospheric CO_2 in the Atlantic ocean: The role of the Amazon River discharge, *Mar. Chem.* 68 (2000) 183–201. doi:10.1016/S0304-4203(99)00077-8.
- [124] E.A. Ríos-Villamizar, M.T.F. Piedade, J.G. Da Costa, J.M. Adeney, W.J. Junk, Chemistry of different Amazonian water types for river classification: A preliminary review, *WIT Trans. Ecol. Environ.* 178 (2013) 17–28. doi:10.2495/WS130021.
- [125] R.A.I. Bashitialshaer, K.M. Persson, M. Aljaradin, Estimated future salinity in the Arabian Gulf, the Mediterranean Sea and the Red Sea consequences of brine discharge from desalination, *Intrenational J. Acad. Res.* 3 (2011) 133–140.
- [126] C.E. Herdendorf, Large Lakes of the World, *J. Great Lakes Res.* 8 (1982) 379–412. doi:10.1016/S0380-1330(82)71982-3.
- [127] R.A.I. Bashitialshaer, K.M. Persson, M. Larson, Mixing Time for the Dead Sea Based on Water and Salt Mass Balances, 3 (2010) 55–66.
- [128] I.N. Mohammed, Modeling the Great Salt Lake, *Statew. Agric. L. Use Baseline* 2015. 1 (2015). doi:10.1017/CBO9781107415324.004.
- [129] F. Lokiec, Sorek 150 million m^3 /year seawater desalination facility build, operate and transfer (BOT) project. Paper presented at the IDA World Congress, Perth Convention and Exhibition Centre (PCEC), Perth, 4–9 September 2011, IDA World Congr. - Perth, West. Aust. Sept. 4-9, 2011. (2011) 1–15.
- [130] A.N. Kosarev, A.G. Kostianoy, I.S. Zonn, Kara-Bogaz-Gol bay: Physical and chemical evolution, *Aquat. Geochemistry.* 15 (2009) 223–236. doi:10.1007/s10498-008-9054-z.

- [131] A.G. Pervov, A.P. Andrianov, R. V. Efremov, A. V. Desyatov, A.E. Baranov, A new solution for the Caspian Sea desalination: Low-pressure membranes, *Desalination*. 157 (2003) 377–384. doi:10.1016/S0011-9164(03)00420-X.
- [132] A. Giacalone, F. Kosmadakis, G. Papapetrou, M. Tamburini, A. Cipollina, G. Micale, R.M. de Jong, Potential of Reverse Electrodialysis in real environments, in: 13th SDEWES Conf. Palermo, 30th Sept. – 4th Oct., 2018.
- [133] D. Lide, Aqueous Solubility of Inorganic Compounds at Various Temperatures, in: *CRC Handb. Chem. Phys.*, 2005: pp. 1–6.
- [134] N.V. Sidgwick, J.A.H.R. Gentle, CCXXI.—The solubilities of the alkali formates and acetates in water, *J. Chem. Soc., Trans.* 121 (1922) 1837–1843. doi:10.1039/CT9222101837.
- [135] W.J. Hamer, Y. Wu, Osmotic Coefficients and Mean Activity Coefficients of Uni-univalent Electrolytes in Water at 25°C, *J. Phys. Chem. Ref. Data*. 1 (1972) 1047–1100. doi:10.1063/1.3253108.
- [136] R.A. Robinson, R. H. Stokes, *Electrolyte Solutions*, Dover Books on Chemistry, 1970.
- [137] Z. Meng, J.H. Seinfeld, P. Saxena, Y.P. Kim, Atmospheric Gas-Aerosol Equilibrium: IV. Thermodynamics of Carbonates, *Aerosol Sci. Technol.* 23 (1995) 131–154. doi:10.1080/02786829508965300.
- [138] T. Isono, Measurements of density, viscosity, and electrolytic conductivity of concentrated aqueous electrolyte solutions - 1. LiCl, NaCl, KCl, RbCl, CsCl, MgSO₄, ZnSO₄ AND NiSO₄., *Rika Gaku Kenkyujo Hokoku*. 56 (1980).
- [139] K.G. Weil, V. M. M. Lobo: *Physical Sciences Data 41. Handbook of Electrolyte Solutions, Part A.* V. M. M. Lobo, J. L. Quaresma: *Physical Sciences Data 41. Handbook of Electrolyte Solutions, Part B*, ISBN Vol. 41: 0-444-98847-5, Elsevier Amsterdam, Oxford, New York, T, *Berichte Der Bunsengesellschaft Für Phys. Chemie*. 95 (1991) 1305–1305. doi:10.1002/bbpc.19910951030.
- [140] M. Shahid, X. Xue, C. Fan, B.W. Ninham, R.M. Pashley, Study of a Novel Method for the Thermolysis of Solutes in Aqueous Solution Using a Low Temperature Bubble Column Evaporator, *J. Phys. Chem. B*. 119 (2015) 8072–8079. doi:10.1021/acs.jpcc.5b02808.
- [141] R.A. Robinson, The Osmotic and Activity Coefficient Data of Some Aqueous Salt Solutions from Vapor Pressure Measurements, *J. Am. Chem. Soc.* 59 (1937) 84–90. doi:10.1021/ja01280a019.
- [142] R. Robinson, The Activity Coefficients of Alkali Nitrates, Acetates and p-Toluenesulfonates in Aqueous Solution from Vapor Pressure Measurements, *J. Am. Chem. Soc.* 57 (1935) 1165–1168. doi:10.1021/ja01310a005.
- [143] D.J. Bradley, K.S. Pitzer, Thermodynamics of electrolytes. 12. Dielectric properties of water and Debye-Hueckel parameters to 350.degree.C and 1 kbar, *J. Phys. Chem.* 83 (1979) 1599–1603. doi:10.1021/j100475a009.
- [144] K.S. Pitzer, J.C. Peiper, R.H. Busey, Thermodynamic Properties of Aqueous Sodium Chloride Solutions, *J. Phys. Chem. Ref. Data*. 13 (1984) 1–102. doi:10.1063/1.555709.
- [145] H.F. Gibbard Jr, G. Scatchard, Liquid-vapor equilibrium of aqueous lithium chloride, from 25 to 100. deg. and from 1.0 to 18.5 molal, and related properties, *J. Chem. Eng. Data*. 18 (1973) 293–298. doi:10.1021/je60058a011.
- [146] K.R. Patil, A.D. Tripathi, G. Pathak, S.S. Katti, Thermodynamic Properties of Aqueous Electrolyte Solutions. Vapor Pressure of Aqueous Solutions of LiCl, LiBr, and LiI 1, *J. Chem. Eng. Data*. 35 (1990) 166–168. doi:10.1021/je00060a020.

- [147] D.G. Archer, Thermodynamic properties of the KCl + H₂O system, *J. Phys. Chem. Ref. Data.* 28 (1999) 1–16. doi:10.1063/1.556034.
- [148] W. Wagner, A. Pruss, International Equations for the Saturation Properties of Ordinary Water Substance. Revised According to the International Temperature Scale of 1990. Addendum to *J. Phys. Chem. Ref. Data* 16, 893 (1987), *J. Phys. Chem. Ref. Data.* 22 (1993) 783–787. doi:10.1063/1.555926.
- [149] R. Beyer, M. Steiger, Vapour pressure measurements and thermodynamic properties of aqueous solutions of sodium acetate, *J. Chem. Thermodyn.* 34 (2002) 1057–1071. doi:10.1006/jcht.2002.0974.
- [150] N. Hubert, Y. Gabes, J. Bourdet, L. Schuffenecker, Vapor Pressure Measurements with a Nonisothermal Static Method between 293.15 and 363.15 K for Electrolyte Solutions. Application to the H₂O + NaCl System, *J. Chem. Eng. Data.* 40 (1995) 891–894. doi:10.1021/je00020a034.
- [151] T. Rijnaarts, N.T. Shenkute, J.A. Wood, W.M. De Vos, K. Nijmeijer, Divalent Cation Removal by Donnan Dialysis for Improved Reverse Electrodialysis, *ACS Sustain. Chem. Eng.* 6 (2018) 7035–7041. doi:10.1021/acssuschemeng.8b00879.
- [152] X. Wang, A. Christ, K. Regenauer-lieb, K. Hooman, H. Tong, International Journal of Heat and Mass Transfer Low grade heat driven multi-effect distillation technology, *Int. J. Heat Mass Transf.* 54 (2011) 5497–5503. doi:10.1016/j.ijheatmasstransfer.2011.07.041.
- [153] N. Ghaffour, J. Bundschuh, H. Mahmoudi, M.F.A. Goosen, Renewable energy-driven desalination technologies: A comprehensive review on challenges and potential applications of integrated systems, *Desalination.* 356 (2015) 94–114. doi:10.1016/j.desal.2014.10.024.
- [154] S. Al-Obaidani, E. Curcio, F. Macedonio, G. Di Profio, H. Al-Hinai, E. Drioli, Potential of membrane distillation in seawater desalination: Thermal efficiency, sensitivity study and cost estimation, *J. Memb. Sci.* 323 (2008) 85–98. doi:10.1016/j.memsci.2008.06.006.
- [155] A. Ruiz-Aguirre, J.A. Andrés-Mañas, J.M. Fernández-Sevilla, G. Zaragoza, Comparative characterization of three commercial spiral-wound membrane distillation modules, *Desalin. WATER Treat.* 61 (2017) 152–159. doi:10.5004/dwt.2016.11075.
- [156] A.D. Khawaji, I.K. Kutubkhanah, J.-M. Wie, Advances in seawater desalination technologies, *Desalination.* 221 (2008) 47–69. doi:10.1016/j.desal.2007.01.067.
- [157] P. Catrini, A. Cipollina, F. Giacalone, G. Micale, A. Piacentino, A. Tamburini, Thermodynamic, Exergy, and Thermoeconomic analysis of Multiple Effect Distillation Processes, in: *Renew. Energy Powered Desalin. Handb.*, Elsevier, 2018: pp. 445–489. doi:10.1016/B978-0-12-815244-7.00012-X.
- [158] M.S. Ray, *Coulson and Richardson's Chemical Engineering Volume 6 (Design)*, 2nd Edition, by R.K. Sinnott, Pergamon Press, Oxford, UK (1993). 954 pages. ISBN 0-08-041865-1., *Dev. Chem. Eng. Miner. Process.* 2 (2008) 254–255. doi:10.1002/apj.5500020410.
- [159] A. Carati, M. Marino, D. Brogioli, Thermodynamic study of a distiller-electrochemical cell system for energy production from low temperature heat sources, *Energy.* 93 (2015) 984–993. doi:10.1016/j.energy.2015.09.108.
- [160] S.A. Klein, *Engineering Equation Solver Software (EES)*, 2013.
- [161] W. Wagner, A. Pruss, The IAPWS Formulation 1995 for the Thermodynamic Properties of Ordinary Water Substance for General and Scientific Use, *J. Phys. Chem. Ref. Data.* 31 (2002) 387–535. doi:10.1063/1.1461829.

- [162] R. Pawlowicz, R. Feistel, Limnological applications of the Thermodynamic Equation of Seawater 2010 (TEOS-10), *Limnol. Oceanogr. Methods*. 10 (2012) 853–867. doi:10.4319/lom.2012.10.853.
- [163] M.H. Sharqawy, J.H. Lienhard V, S.M. Zubair, Thermophysical properties of seawater: A review of existing correlations and data, *Desalin. Water Treat.* 16 (2010) 354–380. doi:http://dx.doi.org/10.5004/dwt.2010.1079.
- [164] B. Ortega-Delgado, L. García-Rodríguez, D.-C. Alarcón-Padilla, Opportunities of improvement of the MED seawater desalination process by pretreatments allowing high-temperature operation, *Desalin. WATER Treat.* 97 (2017) 94–108. doi:10.5004/dwt.2017.21679.
- [165] F. Giacalone, P. Catrini, A. Tamburini, A. Cipollina, A. Piacentino, G. Micale, Exergy analysis of reverse electrodialysis, *Energy Convers. Manag.* 164 (2018) 588–602. doi:10.1016/j.enconman.2018.03.014.
- [166] M. Bindels, N. Brand, B. Nelemans, Modeling of semibatch air gap membrane distillation, *Desalination*. 430 (2018) 98–106. doi:10.1016/j.desal.2017.12.036.
- [167] J.A. Andrés-Mañas, F.G. Acién, G. Zaragoza, Performance evaluation of a novel vacuum-enhanced air-gap membrane distillation module for regeneration of salinity gradients, in: *Desalin. Environ. Clean Water Energy*, 2018.
- [168] R.S. Kingsbury, S. Zhu, S. Flotron, O. Coronell, Microstructure Determines Water and Salt Permeation in Commercial Ion-Exchange Membranes, *ACS Appl. Mater. Interfaces*. 10 (2018) 39745–39756. doi:10.1021/acsami.8b14494.
- [169] A. Ruiz-Aguirre, J.A. Andrés-Mañas, J.M. Fernández-Sevilla, G. Zaragoza, Experimental characterization and optimization of multi-channel spiral wound air gap membrane distillation modules for seawater desalination, *Sep. Purif. Technol.* 205 (2018) 212–222. doi:10.1016/j.seppur.2018.05.044.
- [170] M.I. Ali, E.K. Summers, H.A. Arafat, J.H. Lienhard V, Effects of membrane properties on water production cost in small scale membrane distillation systems, *Desalination*. 306 (2012) 60–71. doi:10.1016/j.desal.2012.07.043.
- [171] M. Khayet, Membranes and theoretical modeling of membrane distillation: A review, *Adv. Colloid Interface Sci.* 164 (2011) 56–88. doi:10.1016/j.cis.2010.09.005.
- [172] P. Yazgan-Birgi, M.I. Hassan Ali, J. Swaminathan, J.H. Lienhard, H.A. Arafat, Computational fluid dynamics modeling for performance assessment of permeate gap membrane distillation, *J. Memb. Sci.* 568 (2018) 55–66. doi:10.1016/j.memsci.2018.09.061.
- [173] Y.D. Kim, L. Francis, J.G. Lee, M.G. Ham, N. Ghaffour, Effect of non-woven net spacer on a direct contact membrane distillation performance: Experimental and theoretical studies, *J. Memb. Sci.* 564 (2018) 193–203. doi:10.1016/j.memsci.2018.07.019.
- [174] A. Tamburini, M. Renda, A. Cipollina, G. Micale, M. Ciofalo, Investigation of heat transfer in spacer-filled channels by experiments and direct numerical simulations, *Int. J. Heat Mass Transf.* 93 (2016) 1190–1205. doi:10.1016/j.ijheatmasstransfer.2015.11.034.
- [175] L. Fitzsimons, B. Corcoran, P. Young, G. Foley, Exergy analysis of water purification and desalination: A study of exergy model approaches, 2015. doi:10.1016/j.desal.2014.12.033.
- [176] A. Bejan, *Advanced Engineering Thermodynamics*, John Wiley & Sons, Inc., Hoboken, NJ, USA, 2016. doi:10.1002/9781119245964.
- [177] G. Tsatsaronis, Thermo-economic analysis and optimization of energy systems, *Prog. Energy Combust. Sci.* 19 (1993) 227–257. doi:10.1016/0360-1285(93)90016-8.

- [178] S.M. Mercer, P.G. Jessop, “Switchable Water”: Aqueous Solutions of Switchable Ionic Strength, *ChemSusChem*. 3 (2010) 467–470. doi:10.1002/cssc.201000001.
- [179] Y. Kim, J.H. Lee, Y.C. Kim, K.H. Lee, I.S. Park, S.-J. Park, Operation and simulation of pilot-scale forward osmosis desalination with ammonium bicarbonate, *Chem. Eng. Res. Des.* 94 (2015) 390–395. doi:10.1016/j.cherd.2014.08.015.
- [180] J.R. McCutcheon, R.L. McGinnis, M. Elimelech, A novel ammonia—carbon dioxide forward (direct) osmosis desalination process, *Desalination*. 174 (2005) 1–11. doi:10.1016/j.desal.2004.11.002.
- [181] R.L. McGinnis, M. Elimelech, Energy requirements of ammonia-carbon dioxide forward osmosis desalination, *Desalination*. 207 (2007) 370–382. doi:10.1016/j.desal.2006.08.012.
- [182] X. Zhou, D.B. Gingerich, M.S. Mauter, Water Treatment Capacity of Forward-Osmosis Systems Utilizing Power-Plant Waste Heat, (2015). doi:10.1021/acs.iecr.5b00460.
- [183] H. Que, C.-C. Chen, Thermodynamic Modeling of the NH_3 – CO_2 – H_2O System with Electrolyte NRTL Model, *Ind. Eng. Chem. Res.* 50 (2011) 11406–11421. doi:10.1021/ie201276m.
- [184] R.L. McGinnis, N.T. Hancock, M.S. Nowosielski-Slepowron, G.D. McGurgan, Pilot demonstration of the NH_3/CO_2 forward osmosis desalination process on high salinity brines, *Desalination*. 312 (2013) 67–74. doi:10.1016/j.desal.2012.11.032.
- [185] G. Amy, N. Ghaffour, Z. Li, L. Francis, R.V. Linares, T. Missimer, S. Lattemann, Membrane-based seawater desalination: Present and future prospects, *Desalination*. 401 (2017) 16–21. doi:10.1016/j.desal.2016.10.002.
- [186] S. Shim, S. Lee, W. Kim, Experimental study on the performance evaluation of vacuum distillation process for NH_4HCO_3 removal, *J. Mech. Sci. Technol.* 27 (2013) 1171–1178. doi:10.1007/s12206-013-0304-7.
- [187] D.H. Kim, B.H. Park, K. Kwon, L. Li, D. Kim, Modeling of power generation with thermolytic reverse electro dialysis for low-grade waste heat recovery, *Appl. Energy*. 189 (2017) 201–210. doi:10.1016/j.apenergy.2016.10.060.
- [188] J.E. Pelkie, P.J. Concannon, D.B. Manley, B.E. Poling, Product distributions in the carbon dioxide-ammonia-water system from liquid conductivity measurements, *Ind. Eng. Chem. Res.* 31 (1992) 2209–2215. doi:10.1021/ie00009a018.
- [189] H. Que, C.-C. Chen, Thermodynamic Modeling of the NH_3 – CO_2 – H_2O System with Electrolyte NRTL Model, *Ind. Eng. Chem. Res.* 50 (2011) 11406–11421. doi:10.1021/ie201276m.
- [190] S. Lin, N.Y. Yip, T.Y. Cath, C.O. Osuji, M. Elimelech, Hybrid Pressure Retarded Osmosis–Membrane Distillation System for Power Generation from Low-Grade Heat: Thermodynamic Analysis and Energy Efficiency, *Environ. Sci. Technol.* 48 (2014) 5306–5313. doi:10.1021/es405173b.
- [191] M. Vanoppen, E. Criel, G. Walpot, D.A. Vermaas, A. Verliefde, Assisted reverse electro dialysis—principles, mechanisms, and potential, *Npj Clean Water*. 1 (2018) 9. doi:10.1038/s41545-018-0010-1.
- [192] M. Papapetrou, Resource, environmental and economic considerations in the development of a Reverse Electro dialysis Heat Engine (PhD thesis), University of Palermo, 2019.
- [193] E.I. Rashkovskaya, E.A.; Chernen’kaya, Densities of ammonium bicarbonate, sodium bicarbonate, and ammonium chloride and ammonia salt solutions at 20–100°C, *Zhurnal Prikl. Khimii*. 40 (1967) 301.
- [194] V. Vitagliano, P.A. Lyons, Diffusion Coefficients for Aqueous Solutions of Sodium

Chloride and Barium Chloride, *J. Am. Chem. Soc.* 78 (1956) 1549–1552.
doi:10.1021/ja01589a011.

APPENDIX

A.1. Physical properties of salt-water solutions

A.1.1. Solution Density

The density of salt-water solution is a function of temperature and salt concentration. In this thesis, constant working temperature in the RED process equal to 298.15K was assumed, then, solution density for *RED* model was estimated as a linear function of the molar concentration according to:

$$\rho = \rho_0 + \left(\frac{\Delta\rho}{\Delta C} \right) C \quad (A.1)$$

where ρ_0 is density of pure water at 298.15K, which is equal to 997 kg/m³. The slope of the function ($\Delta\rho/\Delta C$) was evaluated by fitting experimental data from literature [138,193]. For NaCl-water solution $\Delta\rho/\Delta C$ is equal to 37.4 kg/mol, while for NH₄HCO₃-water solution $\Delta\rho/\Delta C$ is equal to 35.5 kg/mol. *Figure A. 1* shows the comparison of literature experimental density for NaCl (a) and NH₄HCO₃ (b) aqueous solutions with computed value using *equation A. 1*, as function of the molar concentration at 298.15K.

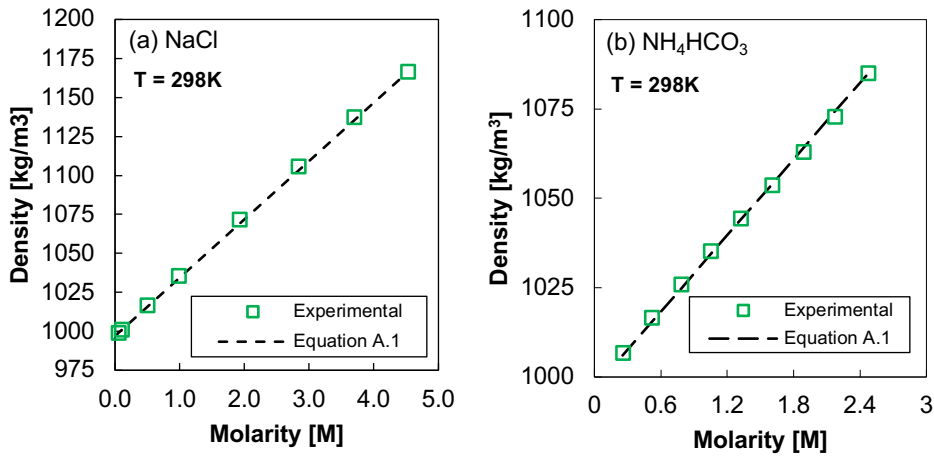


Figure A. 1 Comparison of experimental [138,193] and fitting results of NaCl (a) and NH₄HCO₃ (b) solutions density as a function of molarity at 298.15K.

A.1.2. Solution Conductivity

Solutions conductivity is another important property to be estimated, as it affects the electrical resistance of the solutions within the stack. Solutions with very low electrolyte concentration exhibit very low conductivity and high electrical resistance. The solution conductivity is a strong function of temperature and concentration. Considering a constant temperature of 298.15K, the dependence of solution equivalent electrical conductivity (Λ) on concentration was estimated according to:

$$\Lambda = \Lambda_0 - \frac{A_{\Lambda} C^{1/2}}{1 + B_{\Lambda} C^{1/2}} - C_{\Lambda} C \quad (A.2)$$

Then, the solution electrical conductivities (σ) in (mS/cm), is given by:

$$\sigma = \Lambda \cdot C \quad (A.3)$$

where Λ_0 is the equivalent conductivity of salt at infinite dilution, A_{Λ} , B_{Λ} and C_{Λ} are fitting parameters, and C is the molar concentration. The parameters for NaCl and NH₄HCO₃ water solutions were obtained fitting literature experimental results [138,140]. At 298.15K, the parameter for NaCl-water solution are $\Lambda_0=126.5$, $A_{\Lambda}=91.02$, $B_{\Lambda}=1.66$ and $C_{\Lambda}=6.80$, while for

NH_4HCO_3 -water solution are $A_0= 101.88$, $A_1= 30.32$ and $B_1=C_1=0$. Figure A. 2 shows the comparison of literature experimental conductivity for NaCl (a) and NH_4HCO_3 (b) aqueous solutions with computed value from *equation A. 3*, as function of the molar concentration at 298.15K.

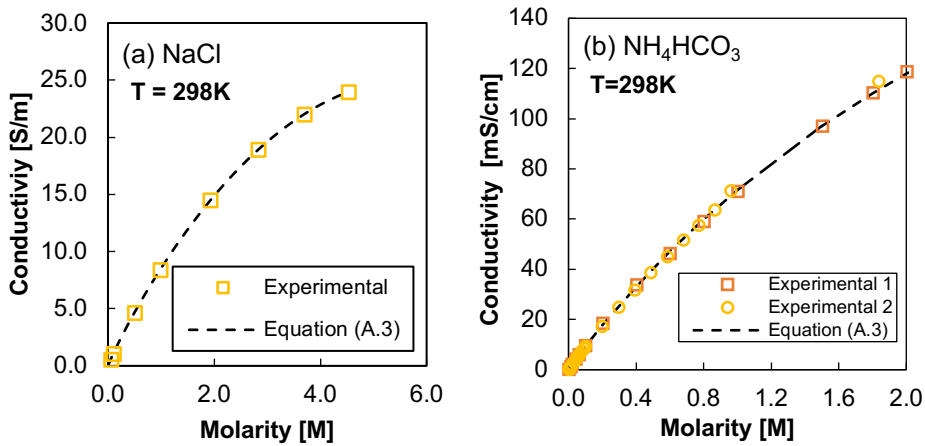


Figure A. 2 Comparison of experimental [138,140] and fitting results of the NaCl (a) and NH_4HCO_3 (b) solutions conductivity as a function of the solution molarity at 298.15K. Experimental 1 in figure b refers to homemade results while Experimental 2 to literature experimental results [140].

A.1.3. Solution viscosity

The solutions viscosity is used in the RED model to evaluate the Reynolds number of the solution flowing in the RED unit, allowing to evaluate the friction factor within the channels. The salt solution viscosity is a function of temperature and molarity. At 298.15K viscosity of salt solution can be evaluate by using a second order polynomial equation:

$$\mu = a + bC + cC^2 \quad (A.4)$$

where a , b and c are fitting parameters, and C is the molar concentration. The parameters for NaCl and NH_4HCO_3 water solutions were obtained fitting literature experimental results [138,140]. At 298.15K, the parameter for NaCl-water solution are $a=8.947*10^{-4}$, $b=5.749*10^{-5}$ and $c=1.846*10^{-5}$, while for NH_4HCO_3 -water solution are $a=8.947*10^{-4}$

$b=1.666 \cdot 10^{-4}$ and $c=1.154 \cdot 10^{-5}$. Figure A.3 shows the comparison of literature experimental viscosity for NaCl (a) and NH_4HCO_3 (b) aqueous solutions with results from equation A. 4 using the abovementioned parameters, as function of the molar concentration at 298.15K.

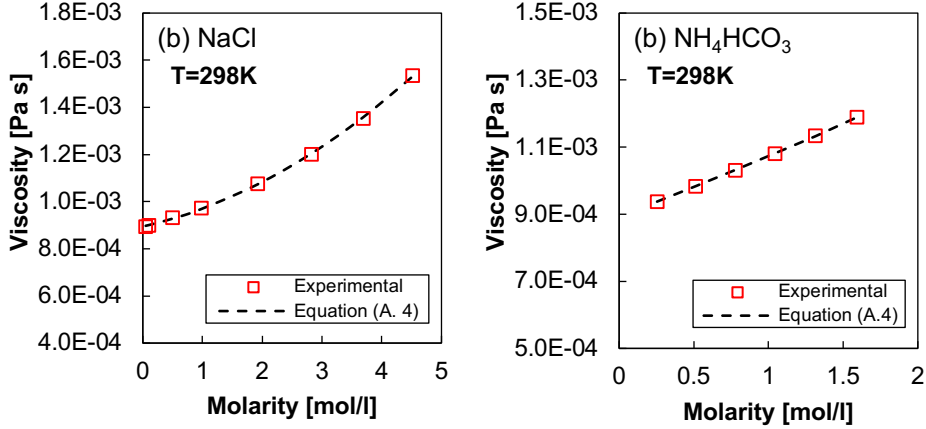


Figure A. 3 Comparison of experimental [138] and fitting results of the NaCl (a) and NH_4HCO_3 (b) solutions conductivity as a function of the solution molarity at 298.15K

A.1.4. Salt Diffusivity

The salt-solution diffusivity is used in the RED model to evaluate the Sh number and then to quantify the polarisation coefficients in the channels. The NaCl solution salt diffusivity is also a function of salt concentration. At 298.15K the diffusivity of NaCl solutions was evaluated according to eq.s A.5 and A.6, fitting data from Vitagliano and Lyons [92,194]. In particular, for molar concentration (C) lower than 0.4 mol/l, eq. A.5 is used.

$$D = 1.47 \cdot 10^{-9} + 0.13 \cdot 10^{-9} \exp\left(-\frac{C}{70}\right) \quad (A.5)$$

While, for molar concentration higher than 0.4 mol/l eq. A. 6 is used

$$D = -2.87 \cdot 10^{-21} C^3 + 2.03 \cdot 10^{-17} C^2 - 8.44 \cdot 10^{-15} C + 1.47 \cdot 10^{-9} \quad (A.6)$$

Due to the lack of literature results on salt diffusivity in the case of NH_4HCO_3 , it was estimated according to the following equations:

$$D_{\text{salt}} = \frac{\sigma kT}{2zeFc} \quad (A.7)$$

obtained combining the Einstein-Smoluchowski relation for electrical mobility (*eq. A.8*) and *eq. A.9*:

$$\bar{u} = \frac{e D_{salt}}{kT} \quad (A.8)$$

$$\sigma = F \sum_i^n |z_i| u_i C_i \quad (A.9)$$

where σ is the solution conductivity, C is the molar concentration, k is the Boltzmann's constant, T is the absolute temperature, F is the Faraday constant, e is the ion electrical charge (equal to the electron electrical charge for a monovalent electrolyte), u_i is the ion mobility and \bar{u} is the ions average mobility.

A.2. CIEMAT MED MODEL

The CIEMAT MED model is a steady state mathematical model based on mass and energy balances applied to the different elements of the plant, along with the heat transfer equations corresponding to the heat exchangers. The assumptions and approximations established in the model are the following:

- Kinetic and potential energy are neglected in comparison with the other energy terms.
- Heat losses to the environment are not considered.
- The thermodynamic losses are taken into account. These losses are referred to the boiling point elevation (*BPE*), the non-equilibrium allowance (*NEA*) and the pressure losses in the demister, connecting lines and condensation inside the evaporator tubes. The effect of the pressure drop in the vapour condensation process on the external surface of the tubes is neglected.
- The vapour entering the evaporators 2 to N is assumed to be in saturation conditions, as well as the distillate exiting all the preheaters and the evaporators.
- The vapour generated by boiling is supposed to be superheated due to the *BPE* and its temperature is assumed to be equal to the unevaporated brine ($T_{vi} = T_i$). The energy associated with the temperature increase due to the *BPE* is transferred to the solution inside the tubes of the preheaters in the condensation process.
- The effect of non-condensable gases (NGC) is not accounted.
- The produced distillate is free of salts.

The model adopts correlations for evaluating the NaCl-water solution properties (Boiling Point Elevation, latent heat density, viscosity, etc) as a function of molality, temperature and pressure. Part of these properties were obtained within this thesis by fitting literature data or Aspen Plus® (adopting *E-NRTL* thermodynamics package) results.

A brief summary of the equations of the model is reported in *Table A.1* more details can be found in [164]. Corresponding nomenclature is reported in the following

Table A. 1. Brief resume of MED-FF model. The complete model is described in [164].

Equation	Short description
$T_i = T_{V_i} = T_{V_{sat,i}} + BPE_i$	(1) Temperature of the concentrated solution and vapour in each effect
$T_{c,i} = T_{V_i} - BPE_i - (\Delta T_{demister,i} + \Delta T_{lines,i} + \Delta T_{cond,i})$	(2) Condensation temperature of the vapour generated in the effect i
$\dot{m}_F = \dot{m}_{B1} + \dot{m}_{T1}$	(3) Mass balance in the first effect
$\dot{m}_F X_F = \dot{m}_{B1} X_1$	(4) Salinity balance in the first effect
$\dot{m}_s \lambda_s + \dot{m}_F h_{preh2} = (1 - \alpha_1) \dot{m}_{T1} h'_{V1} + \alpha_1 \dot{m}_{T1} h'_{C1} + \dot{m}_{B1} h_{B1}$	(5) Energy balance in the first effect
$P_{Q1} = \dot{m}_F \bar{c}_{p1} (T_1 - t_{preh1}) + \dot{m}_{D1} \lambda_{V1} = A_1 U_{e1} (T_s - T_1)$	(6) Heat transfer equation in the first evaporator
$\dot{m}_F \bar{c}_{p,preh1} (t_{preh1} - t_{preh2}) = \alpha_1 \dot{m}_{T1} \lambda'_{V1} + \alpha_1 \dot{m}_{T1} \bar{c}_{p,BPE1} (T'_{V1} - T'_{Vsat1})$	(7) Energy balance in preheater 1
$\dot{m}_{C1} h''_{C1} + (1 - \alpha_1) \dot{m}_{T1} h_{C1} + \alpha_2 \dot{m}_{T2} h'_{C2} = \dot{m}_{FB2} h''_{V2} + \dot{m}_{C2} h''_{C2}$	(8) Energy balance in flash box 2

CIEMAT equations Nomenclature:

A	area, m ²
\bar{c}_p	average specific heat at constant pressure, J/(kg°C)
h	specific enthalpy, kJ/kg
I	electric current, A
\dot{m}	mass flow rate, kg/s
p	pressure, bar
P	power, W
Q	volumetric flow rate, m ³ /s
T or t	temperature, °C or K
U	overall heat transfer coefficient, W/(m ² ·K)
v	velocity, cm/s
X	salinity, ppm
α	fraction of vapor condensed in a preheater
λ	specific enthalpy of evaporation/condensation, kJ/kg
ρ	density, kg/m ³
BPE	Boiling Point Elevation

Subscripts

B	brine
c	condensation
$cond$	condensation
D	distillate
FB	flash box
$preh$	preheater
Q	heat
s	heating steam
sat	saturation
T	total
V	vapour

Superscripts

c	condenser
'	vapor/condensate conditions after the demister
"	vapor/condensate conditions in the flash box